COMPUTATIONAL INVESTIGATION OF TORQUE ON SPIRAL BEVEL GEARS

STEVE RAPLEY BSc MSc

Thesis submitted to the University of Nottingham

for the degree of Doctor of Philosophy

June 2009

Abstract

This thesis describes the development of a numerical modelling strategy for simulating the flow around a shrouded spiral bevel gear. The strategy is then applied to a series of parametric variations of key shroud parameters. The shroud and gear in question are generic, although based upon those employed in the internal gear box of a Rolls-Royce aeroengine. The need to shroud the gear comes from the fact that a spiral bevel gear, when rotated, acts like a fan. Work is done by the gear to move the surrounding fluid, usually air with oil particles suspended in it, which creates a parasitic loss, referred to as the windage power loss. The work within this thesis is part of a larger project which has investigated how windage power loss can be affected by geometric features of gears and shrouds. This is important as for large diameter (~ 200mm) bevel gears running at high speeds ($\Omega > 10,000$ RPM) the windage power loss forms a substantial part of the total power loss [24].

The modelling strategy has been developed in this work by studying 4 different fluid flow settings: Taylor-Couette flow, Conical Taylor-Couette flow, an unshrouded spiral bevel gear, and a shrouded spiral bevel gear. Work on Taylor-Couette flow provided a basic setting in which to trial various numerical techniques and gain familiarity with the commercial CFD program which would be used throughout this thesis (FLUENT), along with the meshing program GAMBIT. It gave an understanding of the flow, which was then used to simulate the flow in a modification of Taylor-Couette flow where the cylinders are replaced with cones, called Conical Taylor-Couette flow. Comparisons were made between 4 popular turbulence models, allowing a decision to be made on the 'best' turbulence model to use in the modelling of a shrouded gear, and to start to develop the strategy. This strategy was then applied to the more complex geometry

of an unshrouded gear, simulating experimental data which had been created on an in-house rig. To confirm the applicability of the strategy to modelling shrouded spiral bevel gears, it was applied to two shrouds for which experimental data was available [25]. It showed that numerical modelling can capture the relative performance of the shrouds well. The work then continued by considering a series of parametric variations, whereby 3 key shroud parameters are each varied in 3 manners, producing 27 variations. Each of these parameters can affect the windage power loss: an assessment of how much each parameter affects windage power loss has been given. A description of the flow field in 'good' and 'bad' cases has been given, and through approximating the flow by using the compressible form of Bernoulli's equation, reasons for a 'bad' shroud being 'bad' have been presented.

Acknowledgements

During the course of this PhD, the guidance and support of certain individuals has proved very beneficial to my completion of the work.

I would like to thank Rolls-Royce Civil Aerospace for the financial and technical support they have lent to the project as a whole. Additionally, I would like to acknowledge the support, and understanding, of Rolls-Royce Naval Marine during the writing-up period.

The PhD would not have happened without the support, guidance and encouragement of my supervisors, Dr Carol Eastwick and Dr Kathy Simmons. I would like to thank them for all that they have done to supervise my PhD.

Technical knowledge and input has also been gratefully received from Dr Colin Young of Rolls-Royce, and Dr Graham Johnson and Prof Colin Foord of the University of Nottingham.

I would like to thank my friends and colleagues at the University of Nottingham for keeping me sane over the years of study.

Finally, I wish to thank my parents and brothers for their emotional support and encouragement throughout the entire time I have spent studying for the PhD.

Contents

Nomenclature

A	Area (m^2)
C_M	Torque or Moment coefficient
C_Q	Non-dimensional throughflow rate
g	Acceleration due to gravity (ms^{-2})
h	Height of cylinder (m)
J	Mass flux ($kg\ s^{-1}$)
k	Turbulent kinetic energy
M	Moment transmitted by rotating surface (Nm)
p	Pressure (Pa)
P	Power (W)
Q	Mass flow rate ($kg\ s^{-1}$)
r	Radial coordinate (m)
R	Radius (m)
R_i	Inner radius (m)
R_o	Outer radius (m)
Ra	Rayleigh Number
$\mathrm{Re}_\phi = r^2\Omega/\nu$	Rotating Reynolds number
s	Non-dimensional Radial shroud spacing
S	General Source Terms
T	Radial gap width (m)
Ta	Taylor number
u	x velocity (ms^{-1})
u_r	Radial velocity (ms^{-1})
u_τ	Friction Velocity
u_θ	Tangential velocity (ms^{-1})
U	Mean Velocity (ms^{-1})
U^*	Non-dimensional velocity at point P
v	y velocity (ms^{-1})
v_n	Non-dimensional relative tangential velocity
v_r	Relative tangential velocity
w	z velocity (ms^{-1})
y	Distance to the wall (m)
y^*	Non-dimensional value of y_P

Table 1: Variables

η	Non-dimensional cylindrical gap width
θ	Angular coordinate (rad)
μ	Dynamic viscosity of the fluid ($kg\,m^{-1}\,s^{-1}$)
ν	Kinematic viscosity (m^2/s)
ρ	Density ($kg\,m^{-3}$)
σ	Prandtl number
ϕ	Cone vertex angle (degrees or radians)
Φ	Gear tooth pressure angle (degrees or radians)
ω	Turbulent energy production rate
Ω	Angular velocity ($rad\,s^{-1}$ or RPM)

Table 2: Greek letters

CL	Churning Loss
ML	Meshing Loss
P	Values at point P
r	Radial component
Stream	Free-stream component
WL	Windage Loss
θ	Angular component

Table 3: Subscripts

Chapter 1

Introduction

1.1 Background

This thesis describes the development of a numerical modelling strategy for simulating the flow around a shrouded spiral bevel gear. The strategy is then applied to a series of parametric variations of key shroud parameters. The shroud and gear in question are generic, although based upon those employed in the internal gear box of a Rolls-Royce aeroengine.

A spiral bevel gear is a form of gear which is used for transferring angular momentum between two shafts that are not parallel. This means that the gear has a conical form. In order to improve the momentum transfer between the two shafts, spiral bevel gears were developed. These allow more than one tooth from the crown and pinion gears to be in contact with each other, reducing the possibility of the gears slipping. They are used in the internal gear boxes of aeroengines in two key roles; firstly they allow power offtake from the mainshaft(s) of the engine, which can be used for generating electrical power for the aircraft. Additionally, the above process can be reversed so that the main shaft can be rotated by a secondary shaft to start the engine.

In order to gain a greater understanding of the flow within the gear box, it can be replicated, either on an experimental rig, or through the use of numerical models. Due to the high rotational speeds involved, experimental observation of the flow field can be difficult to resolve. Numerical modelling of the situation allows greater information on the flow field to be obtained.

The need to shroud the gear comes from the fact that a spiral bevel gear, when rotated, acts like a fan. Work is done by the gear to move the surrounding fluid, usually air with oil particles suspended in it, which creates a parasitic loss, referred to as the windage power loss. Due to the geometry of the components involved, and the changes in pressures and temperature which the engine may operate in, enclosing the gearbox in a vacuum is not practical. At first inspection, it may seem that if the volume of surrounding fluid that can interact with the gear is reduced, then the windage power loss will be reduced. It has been widely reported that as the distance between the teeth and the shroud reduces, the windage losses reduce; however there is a point at which the windage losses begin to increase [68]. Therefore, a shroud design needs to be optimised for the conditions it normally operates under, and hence reduce the windage power loss.

There are other losses which a rotating gear experiences, these are losses due to the meshing process, and losses due to churning. Meshing losses are those which can be attributed to the action of meshing, and include the mechanical losses from the torque transferral between the two shafts, and the losses due to the forces exerted on the fluid (usually a mixture of air and oil) which is trapped between, and then expelled by, the meshing teeth. Meshing losses are mechanically based, and are not considered in this thesis, as they have been widely studied elsewhere. Churning losses occur when the gear passes through a pool of lubricant. Part of the optimisation of a shroud involves preventing the build up lubricant under the shroud, by allowing 'waste' oil to exit the shroud. They also fall outside the scope of this thesis.

The work within this thesis is part of a larger project which has investigated how windage power loss can be affected by geometric features of gears and shrouds. This is important as for large diameter ($\sim$ 200mm) bevel gears running at high speeds ($\Omega >$ 10,000 RPM) the windage power loss forms a substantial part of the total power loss [24]. To date the flow field around a shrouded spiral bevel gear is one that has received little research, either experimentally or numerically, despite the widespread use of bevel gears in high speed gear boxes. This may be due, in the case of numerical modelling, to the high level of computational resources necessary to model this situation. Indeed, even now the possibility of modelling two meshing gears with a full two-phase flow field is

one that is at, or even beyond, the limit of current computational resources, even when considering the application of massively parallel clusters to the problem. Understanding the flow field can have a direct impact on reducing the power losses due to fluid dynamic effects, such as windage and churning power losses.

1.2 Aims of the thesis

The majority of previous studies on windage power loss for gears have been experimental, and the major focus has been on spur gears. It is known that effective shrouding can reduce windage power losses by approximately 60% [25, 33, 68]. Few published reports have addressed the problem of windage power loss from a spiral bevel gear [20, 25, 33, 68], and of these, only one has conducted any numerical modelling [20]. It is therefore of interest to learn whether accurate numerical modelling of this flow can be achieved, and to see what insight this modelling can give into the flow field. This can be used to inform the design of effective shrouding through much better visualisation of the flow than can be achieved experimentally. It also leads to the ability to break down the power loss over the surface in far greater detail, and hence highlight the area where designs can be improved.

Within the general scope of the project described above, the aims of the work presented in this thesis are twofold:

- develop and validate a modelling strategy for the flow around a shrouded spiral bevel gear
- Apply the developed modelling strategy to a shrouded gear, investigating parametric variation in key shroud variables to identify how windage power loss can be minimised through shroud design.

The strategy that has been described can then be taken forward and used to aid shroud design.

1.3 Development of strategy

The modelling strategy has been developed in this work by studying 4 different fluid flow settings:

- Taylor-Couette flow
- Conical Taylor-Couette flow
- an unshrouded spiral bevel gear
- a shrouded spiral bevel gear

Work on Taylor-Couette flow provided a basic setting in which to trial various numerical techniques and gain familiarity with the commercial CFD program which would be used throughout this thesis (FLUENT), along with the meshing program GAMBIT. This section of work has been included within the Appendix (§A) for completeness.

This initial work provided a basic understanding of the ability of FLUENT to model rotating flows. This understanding was then used to simulate the flow in a modification of Taylor-Couette flow where the cylinders are replaced with cones, called Conical Taylor-Couette flow (Chapter 4). Comparisons were made between 4 popular turbulence models, allowing a decision to be made on the 'best' turbulence model to use in the modelling of a shrouded gear. Insight was also obtained as to whether approximations such as rotational periodic or steady-state flow can be applied without undermining the accuracy of the model. The majority of the work presented in Chapter 4 has been published in the Journal of Fluids Engineering [49].

At this stage the strategy was reasonably well developed, so it could be applied to the more complex geometry of an unshrouded gear. Chapter 5 presents the results from a numerical simulation of the flow around a rotating unshrouded gear, simulating experimental data which had been created on an in-house rig, later published by Johnson *et al.* [25]. This work allowed further refining of the strategy, as well as producing some very interesting insights into the fluid dynamics present. The majority of the work presented in Chapter 5 was published at ASME TurboExpo 2007 [48].

To confirm the applicability of the strategy to modelling shrouded spiral bevel gears, it was applied to two shrouds which had been developed to fit the in-house rig, data from which was published by Johnson *et al.* [25]. Chapter 6 presents the results of this experimental validation, which shows that the numerical modelling can capture the relative performance of the shrouds well. The work then continued by considering a series of parametric variations, whereby 3 key shroud parameters are each varied in 3 manners, producing 27 variations. Each of these parameters can affect the windage power loss: an assessment of how much each parameter affects windage power loss has been given. A description of the flow field in 'good' and 'bad' cases has been given, and through approximating the flow by using the compressible form of Bernoulli's equation, reasons for a 'bad' shroud being 'bad' have been presented. The majority of the work presented in Chapter 6 was published at ASME TurboExpo 2007 [48] and ASME TurboExpo 2008 [47].

Chapter 2

Literature Review

The work presented in this thesis focused on four geometrical settings:

- Taylor-Couette flow
- Conical Taylor-Couette flow
- an unshrouded spiral bevel gear
- a shrouded spiral bevel gear

These progress from simple geometries, similar to a shrouded spiral bevel gear, up to a geometry that is fully representative of the shrouded gear. In this section, a review of existing literature in each of these fields will be presented. This will allow the reader to develop an understanding of the fluid mechanics involved in each setting, how these evolve as the settings become increasingly complex.

In §2.1 a review of literature on Taylor-Couette flow has been presented. Literature reviewed in this section has shown that in this relatively simple setting, there are many interesting flow phenomena. Experimental observations have been discussed, of which the paper of Bilgen & Boulos [8] provides data which has been modelled in Appendix A.

Many modifications to Taylor-Couette flow are possible, and literature on some of these has been reviewed in §2.2. This review has highlighted the far more complex flow field which is present under these modifications. The most relevant modification to Taylor-Couette flow, in terms of an approximation to a shrouded spiral bevel gear, was felt to be where the cylinders are replaced by cones. This flow has been referred

to here as Conical Taylor-Couette flow. Experimental data from Yamada & Ito [69–71], reviewed in this section, has been modelled numerically in Chapter 4.

As highlighted in the previous chapter, the losses from gears are grouped into three categories: meshing, churning, and windage. The losses that are not covered by the work in this thesis are have been considered in §2.3.2 & §2.3.1 in order to give an understanding of the contribution each of these make to the overall losses. A review of the literature in the field of windage power loss (§2.3.3) has shown the lack of any significant work in this field for spiral bevel gears.

2.1 Taylor-Couette Flow

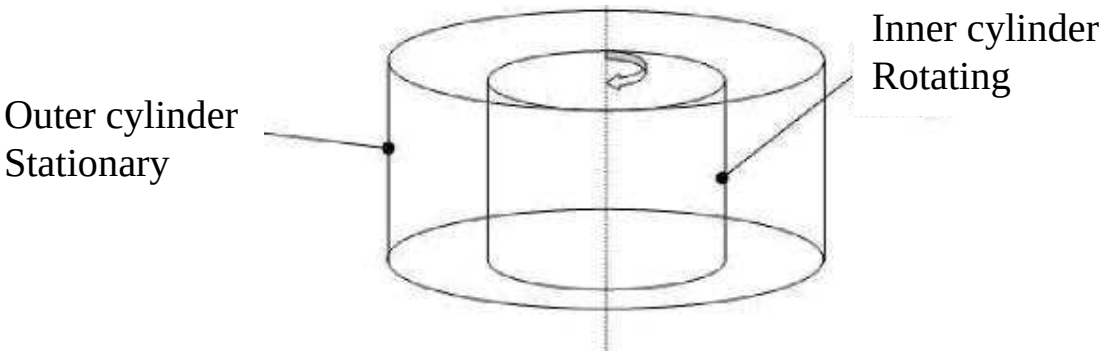

Figure 2.1: A sketch of the setting of Taylor-Couette flow

Taylor-Couette flow is the flow that occurs between two concentric cylinders where the inner cylinder rotates and the outer cylinder remains stationary. A sketch of the setting of Taylor-Couette flow is given by Fig. 2.1. The governing equations for the flow can be written in cylindrical coordinates as below (Eq. 2.1):

$$\rho\left(\frac{\partial u_r}{\partial t}+u_r\frac{\partial u_r}{\partial r}+\frac{u_\theta}{r}\frac{\partial u_r}{\partial \theta}+u_z\frac{\partial u_r}{\partial z}-\frac{u_\theta^2}{r}\right)= -\frac{\partial p}{\partial r}+\mu\left[\frac{1}{r}\frac{\partial}{\partial r}\left(r\frac{\partial u_r}{\partial r}\right)+\frac{1}{r^2}\frac{\partial^2 u_r}{\partial \theta^2}+\frac{\partial^2 u_r}{\partial z^2}-\frac{u_r}{r^2}-\frac{2}{r^2}\frac{\partial u_\theta}{\partial \theta}\right]+\rho g_r \quad (2.1a)$$

$$\rho\left(\frac{\partial u_\theta}{\partial t}+u_r\frac{\partial u_\theta}{\partial r}+\frac{u_\theta}{r}\frac{\partial u_\theta}{\partial \theta}+u_z\frac{\partial u_\theta}{\partial z}+\frac{u_r u_\theta}{r}\right)= -\frac{1}{r}\frac{\partial p}{\partial \theta}+\mu\left[\frac{1}{r}\frac{\partial}{\partial r}\left(r\frac{\partial u_\theta}{\partial r}\right)+\frac{1}{r^2}\frac{\partial^2 u_\theta}{\partial \theta^2}+\frac{\partial^2 u_\theta}{\partial z^2}+\frac{2}{r^2}\frac{\partial u_r}{\partial \theta}-\frac{u_\theta}{r^2}\right]+\rho g_\theta \quad (2.1b)$$

$$\rho\left(\frac{\partial u_z}{\partial t}+u_r\frac{\partial u_z}{\partial r}+\frac{u_\theta}{r}\frac{\partial u_z}{\partial \theta}+u_z\frac{\partial u_z}{\partial z}\right)= -\frac{\partial p}{\partial z}+\mu\left[\frac{1}{r}\frac{\partial}{\partial r}\left(r\frac{\partial u_z}{\partial r}\right)+\frac{1}{r^2}\frac{\partial^2 u_z}{\partial \theta^2}+\frac{\partial^2 u_z}{\partial z^2}\right]+\rho g_z \quad (2.1c)$$

$$\frac{1}{r}\frac{\partial}{\partial \mathrm{r}}(ru)+\frac{\partial \mathrm{w}}{\partial \mathrm{z}}=0 \quad (2.1d)$$

If the flow is assumed to be rotationally symmetric, a solution can be found to these equations, in the form:

$$u(r)=\frac{R_i^2\Omega_i-R_o^2\Omega_o}{R_i^2-R_o^2}r+\frac{R_i^2R_o^2\left(\Omega_o-\Omega_i\right)}{R_i^2-R_o^2}\frac{1}{r}, \quad (2.2)$$

The flow develops as a series of counter-rotating vortices between the two cylinders, the size of which is dependent on the gap width and the speed at which the inner cylinder is rotating. Studying and understanding Taylor-Couette flow provides a starting point for considering the flow around a shrouded bevel gear, and provides a basic approximation to the flow structure.

Stuart [54] uses hydrodynamic stability theory to investigate the disturbances which appear as Taylor-Couette flow develops from stable to unstable laminar flow. A theory based on certain assumptions about energy flow is given to describe both the growth of the disturbances and the final equilibrium state. This is achieved by assuming that the velocities can be averaged in the z direction, giving

$$u=u'=u_1(r,t)e^{\mathbf{i}\alpha z}+\tilde{u}_1(r,t)e^{-\mathbf{i}\alpha z}+u_2(r,t)e^{2\mathbf{i}\alpha z}+\tilde{u}_2(r,t)e^{-2\mathbf{i}\alpha z}+\ldots = \sum_{j=1}^{\infty}(u_j(r,t)e^{j\mathbf{i}\alpha z}+\tilde{u}_j(r,t)e^{-j\mathbf{i}\alpha z}) \quad (2.3a)$$

$$v'=v-\overline{v}(r,t)=v_1(r,t)e^{\mathbf{i}\alpha z}+\tilde{v}_1(r,t)e^{-\mathbf{i}\alpha z}+v_2(r,t)e^{2\mathbf{i}\alpha z}+\tilde{v}_2(r,t)e^{-2\mathbf{i}\alpha z}+\ldots = \sum_{j=1}^{\infty}(v_j(r,t)e^{j\mathbf{i}\alpha z}+\tilde{v}_j(r,t)e^{-j\mathbf{i}\alpha z}) \quad (2.3b)$$

$$w = w' = w_1(r,t)e^{\mathbf{i}\alpha z} + \tilde{w}_1(r,t)e^{-\mathbf{i}\alpha z} + w_2(r,t)e^{2\mathbf{i}\alpha z} + \tilde{w}_2(r,t)e^{-2\mathbf{i}\alpha z} + \ldots$$
$$= \sum_{j=1}^{\infty}(w_j(r,t)e^{j\mathbf{i}\alpha z} + \tilde{w}_j(r,t)e^{-j\mathbf{i}\alpha z}) \quad (2.3c)$$

It is shown that, by substituting equation 2.3 into Eq. 2.1, expressions for the mean motion can be derived

$$\frac{1}{r}\frac{\partial}{\partial \mathrm{r}}\left(r\overline{u'^2}\right) - \frac{1}{r}\left(\overline{v'^2} + \overline{v}^2\right) = -\frac{1}{\rho}\frac{\partial p}{\partial \mathrm{r}}, \quad (2.4a)$$

$$\frac{\partial \overline{v}}{\partial \mathrm{t}} + \frac{1}{r^2}\frac{\partial}{\partial \mathrm{r}}\left(r^2\overline{u'v'}\right) = \nu\left(\frac{\partial^2}{\partial \mathrm{r}^2} + \frac{1}{r}\frac{\partial}{\partial \mathrm{r}} - \frac{1}{r^2}\right)\overline{v}. \quad (2.4b)$$

These equations give an asymptotic expansion for the velocity components. With further work, approximate expressions for the amplitude of u_1 (Eq. 2.5) and the flow shear, which leads to an expression for the torque (Eq. 2.6), can be derived for Taylor numbers above the critical Taylor number ($Ta_c = 1708$).

$$u_1^2 = \frac{5.425 \times 10^4}{\mathrm{Re}_{\mathrm{disc}}^2}\left(1 - \frac{Ta_c}{Ta}\right) \quad (2.5)$$

$$C_M = 2\pi R_i^2 h\mu\frac{\Omega(R_i + R_o)}{2(R_o - R_i)}\left(1 + D\left(1 - \frac{Ta_c}{Ta}\right)\right) \quad (2.6)$$

The Taylor number is the ratio of inertial forces to viscous forces, and in this case is defined as

$$Ta = \frac{\Omega_i^2 R_i(R_o - R_i)^3}{\nu^2}$$

These expressions are shown to compare reasonably well with experimental data from Taylor, [55], and are shown to give good agreement for Taylor numbers up to about 10 times the critical value. They show how the moment coefficient is influenced by the speed of rotation of the cylinder, the radii of both cylinders, the Taylor number, and the kinematic viscosity of the fluid between the cylinders.

Bilgen & Boulos [8] looked at Taylor-Couette flow, presenting results from a series of experiments, which are then compared to an analytical relationship of the form $C_M = f(T/R_i, \mathrm{Re}_c)$. Their work considered the flow that occurs when a disc rotates inside a cylindrical housing, which is a form of Taylor-Couette flow. To simplify the analysis, they

do not consider the region of the experiment outside of the annular region (they discount end effects). They show that four different regimes exist (laminar, transitional, low Couette-Reynolds number turbulent ($\mathrm{Re}_C \leq 10^4$), and high Couette-Reynolds number turbulent ($\mathrm{Re}_C > 10^4$)). For laminar flow, the moment transmitted by the rotating cylinder, C_M, can be deduced from linear theory as Eq. 2.7:

$$C_M = \frac{4\pi\mu\Omega R_I^2 R_O^2 h}{R_O^2 - R_I^2}. \tag{2.7}$$

This leads to the following equation for C_M (Eq. 2.8):

$$C_M = \frac{8R_O^2\nu}{R_I^2\Omega(R_O^2 - R_I^2)}. \tag{2.8}$$

With some further work, this leads to Eq. 2.9:

$$C_M = 8\Phi(T/R_I)\mathrm{Re}_c^{-1}, \tag{2.9}$$

where

$$\Phi(T/R_I) = \frac{(1+T)^2}{2+\frac{T}{R_I}}$$

As the angular velocity increases, instabilities become apparent. Instabilities are stated as occurring when the Taylor number is greater than the critical value Ta_c. In the transitional flow regime, which is stated as being for $1708 < Ta < 160,000$, the moment coefficient on the rotating cylinder is then Eq. 2.10:

$$C_M = 2\Psi(T/R_i, \mathrm{Re}_c)\mathrm{Re}_c^{-1} \tag{2.10}$$

where Ψ is given by ($D = 1.4472$):

$$\Psi(T/R_i, \mathrm{Re}_c) = \left(2 + \frac{T}{R_I}\right)\left(1 + D\left(1 - \frac{Ta_c}{Ta}\right)\right)$$

For turbulent flow ($Ta \geq 160,000$), there are two equations given (Eq. 2.11). Firstly,

for $\mathrm{Re}_c \leq 10^4$ Eq. 2.11a holds:

$$C_M = 1.03(T/R_i)^{0.3}\mathrm{Re}_c^{-0.5}, \tag{2.11a}$$

If $\mathrm{Re}_c > 10^4$, then Eq. 2.11b is valid:

$$C_M = 0.065(T/R_i)^{0.3}\mathrm{Re}_c^{-0.2}. \tag{2.11b}$$

Overall the work demonstrates that the moment coefficient (C_M), can be expressed in the following manner (Eq. 2.12), for some constants, α, β, & c:

$$C_M = c\left(\frac{T}{R_I}\right)^{\alpha}\mathrm{Re}_c^{\beta}. \tag{2.12}$$

This is useful in that it gives numerical data that can be compared with theoretical results, and those obtained by the CFD (§A).

Wild et al., [62], presents an experimental and computational assessment of windage losses in rotating machinery, producing a model of the situation described in Bilgen and Boulos [8]. In contrast to the analysis of Bilgen and Boulos, end effects, which can be considerable, are not discounted. An assumption made to save computational time is that the flow is axi-symmetric, so that the problem need only be considered two-dimensional. Wild et al. also found that the torque obtained from their computational model was not affected by the number of Taylor vortices occurring at a given speed. However, this breaks down when the aspect ratio in the annular region is small. In this case, the Taylor vortices predicted are irregular, and the model used must be as close to the situation being modelled as possible. In this case, the use of a symmetry plane is shown to be inappropriate, even though there should be symmetry in the flow along the cylinder, as any computational model will seek to have an even number of vortices in the region between the cylinder faces and the symmetry plane whereas it is quite possible for there to be an odd amount of vortices in such a region.

Schlichting, [50], gives the moment coefficient for a disc rotating in a housing where

the flow is laminar by Eq. 2.13a, and in turbulent flow by Eq. 2.13b:

$$C_M = 2.67\mathrm{Re}^{-1/2} \tag{2.13a}$$

$$C_M = 0.0622\mathrm{Re}^{-1/5} \tag{2.13b}$$

Unlike Equations 2.7-2.12, these are theoretical expressions, not empirical formulae, for the moment coefficient, that may be used to see how the theory relates to experiment, and also to see how well the models perform in cases where there is no data available.

Other experimental relationships for the moment-coefficient are presented in Daily and Nece [11], of the form Eq. 2.14. A set of four relationships are given between the moment coefficient and flow characteristics, which depend upon the flow type (either laminar or turbulent), and the clearance. It is stated that, for a given geometry, some or all of these relationships may hold true, but no clear demarcation is given. The equations are for laminar flow (close clearance) (Eq. 2.14a), laminar flow (separate boundary layers) (Eq. 2.14b), turbulent flow (close clearance) (Eq. 2.14c), and turbulent flow (separate boundary layers) (Eq. 2.14d).

$$C_M = \frac{2\pi}{(T/R_i)\mathrm{Re}_{disc}}. \tag{2.14a}$$

$$C_M = \frac{3.70(T/R_i)^{1/10}}{\mathrm{Re}_{disc}^{1/2}}. \tag{2.14b}$$

$$C_M = \frac{0.080}{(T/R_i)^{1/6}\mathrm{Re}_{disc}^{1/4}} \tag{2.14c}$$

$$C_M = \frac{0.0102(T/R_i)^{1/10}}{\mathrm{Re}_{disc}^{1/5}} \tag{2.14d}$$

Clearly, there are many relationships that can be derived between the torque and any of a series of non-dimensional flow characteristics, due to there being no exact relationship. Dubrulle & Hersant, [17], presents another set of relationships for the torque with Reynolds number, using a non-dimensional torque, C_M (Eq. 2.16). They make an analogy with turbulent convection to classify and model the flow, giving an analogy to the

Rayleigh number, of the form Eq. 2.15:

$$\mathrm{Ra}_{DH} = 4\frac{\eta^2(1-\eta)(3+\eta)}{(1+\eta)^4}\mathrm{Re}_c^2, \tag{2.15}$$

$$C_M = \frac{M}{\rho\nu^2 h}. \tag{2.16}$$

Their relationships are of the form Eq. 2.17, which are split across 3 regions, which they classify as 'soft' turbulent ($5\times10^5 < \mathrm{Ra}_{DH} < 2\times10^7$, Eq. 2.17a), 'hard' turbulent ($2\times10^7 < \mathrm{Ra}_{DH} < 10^{11}$, Eq. 2.17b), and 'ultra-hard' turbulent, ($\mathrm{Ra}_{DH} > 10^{11}$, Eq. 2.17c)

$$C_M = 1.46\frac{\eta^{3/2}}{(1-\eta)^{7/4}}\mathrm{Re}_c^{3/2}, \tag{2.17a}$$

$$C_M = 2.12\frac{\eta^{2/3}}{(1-\eta)^{5/3}}\frac{\mathrm{Re}_c^{5/3}}{\ln[\eta^2(1-\eta)\mathrm{Re}_c^2/20]^{2/3}}, \tag{2.17b}$$

$$C_M = 0.5\frac{\eta^{2}}{(1-\eta)^{3/2}}\frac{\mathrm{Re}_c^{2}}{\ln[\eta^2(1-\eta)\mathrm{Re}_c^2/10^4]^{3/2}}, \tag{2.17c}$$

where $\eta = R_i/R_o$. These formulae are valid for the values of Ra_{DH} given above. In the work presented in §A, $7\times10^3 \leq \mathrm{Ra}_{DH} \leq 2\times10^8$, so the most appropriate formulae are Eq. 2.17a & Eq. 2.17b. These formulae will be used to compare with the data obtained in §A.4.

There exists a large transition region in Taylor-Couette flow, as the flow evolves from laminar flow to fully turbulent, with a significant quantity of research having been dedicated to its study, one such paper being that of Lathrop et al. [28]. It investigates turbulent Taylor-Couette flow at large Couette Reynolds number, $10^3 < \mathrm{Re}_c = R_i T\Omega/\nu < 10^6$. They observe a transition in the behaviour at a value of $\mathrm{Re}_c \simeq 1.3\times10^4$, above which the torque has a Reynolds number dependence similar to the drag observed in wall-bounded shear flows such as pipe flow and flow over a flat plate. Non-dimensional torque is given by Eq. 2.18, with this equation coming from the limit as $\mathrm{Re}_c \to \infty$, using Kolmogorov turbulence theory. The results this equation produces will be compared with those given by Eq. 2.17a & Eq. 2.17b in §A.4:

$$C_M = \pi\left[\frac{\eta(1+\eta)}{(1-\eta)^2}\right]\mathrm{Re}_c^2. \tag{2.18}$$

A similar approach has been taken by Eckhardt et al. [19] by looking at the Reynolds number dependence, giving the non-dimensional torque in the form Eq. 2.19:

$$C_M = 10.5\mathrm{Re}_c^{1.3725} + 0.196\mathrm{Re}_c^{1.847}. \tag{2.19}$$

In §A.4, this formula will be compared to the CFD data.

In this section it has been shown that there exist many ways of quantifying and predicting the torque in Taylor-Couette flow, with many relationships given in the form Eq. 2.20. As has been observed by Lathrop et al., [28], a value can be given for α which approximates this relationship over some range, but an exact relationship must be calculated somehow for each value of Re_c, suggesting a dependence on some other, undetermined, factors.

$$C_M \propto \mathrm{Re}_c^{-\alpha}. \tag{2.20}$$

2.2 Modified Taylor-Couette Flow

Modifications can be made to Taylor-Couette flow, which can result in much more complex flow structures, by either geometrical changes, or by inducing a flow through the domain. In this section, literature which discusses these changes and the effects that they have will be reviewed. The focus of the work presented in this section will concentrate on Conical Taylor-Couette flow, which will be defined in §2.2.2, and on the impact of inducing throughflow in Taylor-Couette and Conical Taylor-Couette flows. However, mention will be made of some work which has been conducted looking at other modifications to Taylor-Couette flow (§2.2.1). Conical Taylor-Couette flow is an approximation to a shrouded spiral bevel gear which is why the focus has moved from Taylor-Couette flow to Conical Taylor-Couette flow. The other modifications are briefly discussed here for completeness.

2.2.1 Taylor-Couette flow variants

If the geometry of either cylinder is changed, complex flows can occur. Wimmer [66] presents a comprehensive analysis of some of these variations on Taylor-Couette flow,

describing the flow between combinations of cylinders, cones or spheres, with thorough descriptions of when, where and how the Taylor vortices occur, and looking at the influence which initial and boundary conditions have on the flow.

Interesting flows also occur when only the inner cylinder is replaced with a cone. Pereira & Sousa [46] present an extensive study of this flow, looking experimentally and numerically at the confined vortex breakdown generated by a rotating cone. They demonstrate that for some combinations of Reynolds number and gap ratio a bubble type vortex breakdown can occur, and give some understanding as to the mechanism responsible for transition to transient flow.

2.2.2 Conical Taylor-Couette flow

Modifying Taylor-Couette flow by replacing right cylinders by conical cylinders, which may be known as Conical Taylor-Couette flow, produces a complex flow pattern, as has been studied by Noui-Mehidi *et al.* [40–42, 44, 65]. For vertex angles close to 0°, the flow structure is very similar to Taylor-Couette flow, but, as the angle is increased towards 180°, the classic structure of vortex pairs starts to break down and eventually disappears. The flow starts to develop characteristics akin to disc flow for a vertex angle $\phi \sim 60°$ [67]. Eventually the flow starts to show similarities to the flow over a rotating disc. In general the structure of Conical Taylor-Couette flow is a lot more complicated than basic Taylor-Couette flow, being dependent on gap width, cylinder height, rate of rotation, angle of conic, and rate of acceleration, with many different flows possible at the same angular velocities.

Wimmer [65] presents an experimental investigation of Conical Taylor-Couette flow. The influence of initial and boundary conditions on the flow is seen to be considerable, producing a wide variety of possible vortex configurations. Wimmer observes, importantly, that a system of toroidal vortices can travel through a closed flow system, without any external influence. If there exist upward travelling vortices, their velocity decreases with increasing gap width, T. Wimmer also highlights, importantly, that in 'a rare case in fluid dynamics' unstable steady and transient flows can easily co-exist in Conical Taylor-Couette flow.

Noui-Mehidi [40] looked experimentally at the effect of acceleration on transition properties in a conical cylinder system, for which the vertex angle was $\phi = 16.38°$. Noui-Mehidi observed that the rate of acceleration of the rotating inner cone, dRe/dt, had a considerable effect on the final flow. If this acceleration rate was lower than 6.8, a helical motion (a pair of counter-rotating vortex tubes winding around the inner conical cylinder) was observed, whereas for accelerations higher than 6.8, an upward motion was observed in the vortices.

The helical motion has been investigated further by Noui-Mehidi *et al.* [44]. They considered the dynamics of the helical motion, looking at the transition from laminar helical motion to turbulent helical motion, highlighting yet more variations in the flow field.

The acceleration rate can also have an influence on the number of vortices present. By looking at the mechanism of mode selection for Conical Taylor-Couette flow, Noui-Mehidi *et al.* [42] observed that if $\mathrm{dRe/dt} = 0.6$, six pairs of steady vortices develop at $\mathrm{Re} = 340$, whereas if the acceleration is $\mathrm{dRe/dt} = 1.3$, seven pairs of steady vortices develop at $\mathrm{Re} = 520$, and eight pairs of steady vortices develop at $\mathrm{Re} = 730$.

Another mechanism which will alter the number of vortices present is varying the cone vertex angle, ϕ. Noui-Mehidi *et al.* [43] performed a numerical computation of this effect, by varying the cone vertex angle over the range $0° \leq \phi \leq 8°$. This behaviour was investigated experimentally over a greater range by Wimmer and Zierep [67], varying the vertex angle over the range $0° \leq \phi \leq 180°$, that is all the way from a cylinder ($\phi = 0°$) to a disc ($\phi = 180°$). Some important observations as to the flow that has been modelled in §4 were observed. Primarily, for cones with vertex angles of $\phi = 90°$ and $\phi = 120°$, no Taylor Vortices were observed. The flow that does occur is a spiral instability, which forms regular spiral patterns, which is similar to the flow observed on a rotating disc.

The gap width is another factor that can effect the vortices present in Conical Taylor-Couette flow. Noui-Mehidi *et al.* [41] studied this effect, and found that the vortices present in such a situation can reach sizes of up to 2.4 times the gap width.

Another possibility within Conical Taylor-Couette flow is an Ekman boundary layer. An Ekman boundary layer is a boundary layer in which the forces due to the pressure

gradient across the layer, the viscous forces, and the Coriolis forces are in balance with each other. Hoffman and Busse [23] looked at the instabilities of shear flows within Conical Taylor-Couette flow, observing a transition from Taylor vortex instabilities to Ekman-type instabilities at $\phi = 45°$.

Dependence within the flow structure on the vertex angle is clear, because the flow around a cone will be somewhat similar to the flow around either a cylinder or a disc. As the vertex angle increases the moment on the cone loses its dependence on the vertex angle, and the flow becomes similar to that for a disc. Yamada & Ito, [69] looked experimentally at the frictional resistance of shrouded rotating cones for vertex angles of $30° \leq \phi \leq 270°$. They observed that, for very small spacing ratios (T/R_i), the theoretical equation, Eq. 2.21

$$C_M = \frac{\pi R_i}{T\mathrm{Re}}, \tag{2.21}$$

demonstrates good agreement with their experimental data, for any vertex angle ϕ. For $120° \leq \phi \leq 180°$, C_M shows little dependence, if any, on ϕ, however, when $\phi \leq 90°$, C_M shows strong dependence on ϕ at the region where T/R_i is comparatively large. They also report that at any of the vertex angles considered, C_M reaches a minimum at a certain value of T/R_i.

In this section the effect geometrical changes have on Taylor-Couette flow have been looked at. The main area of interest is in Conical Taylor-Couette flow. The different papers reviewed have all shown that very complex flow structures exist. Some of these are similar to those observed in Taylor-Couette flow, such as the toroidal and helical vortices observed by Wimmer [65], and Noui-Mehidi [40]. Boundary and initial conditions are shown to have a big impact on the nature of these vortices, as well as how the system evolves over time. Other flow structures are observed which show less similarity to Taylor-Couette flow as the geometrical changes progress from a Taylor-Couette system to one that resembles the flow between a stationary and a rotating disc.

2.2.3 Throughflow

Many authors have looked at the effect throughflow has on Taylor-Couette flow and on Conical Taylor-Couette flow. Throughflow effects are important in the study of a

shrouded spiral bevel gear, as the windage induces a flow through the domain. When a throughflow is introduced into Taylor-Couette flow the flow becomes a linear superposition of the Taylor-Couette flow and the imposed axial flow [59]. With Conical Taylor-Couette flow, the location and direction of the throughflow affects the resulting flow pattern. If the throughflow enters tangentially, the flow is seen to snake around the cone, partially due to the orientation of the inlet with respect to the vertex of the cone. Noui-Mehidi *et al.* [45] studied apex angle effects on the swirling flow between cones induced by means of a tangential inlet. They observed that the location of the inlet has a considerable effect on the flow, with an increase in swirl intensity if the inlet is at the point of greatest radii compared to if the inlet is at the point of least radii. The geometry of the cone, in a similar manner as discussed in §A, also has considerable effect on the swirling flow [45].

In Conical Taylor-Couette flow with throughflow, if the flow enters in an axial direction, the axial throughflow causes the transitions to unstable laminar flow and turbulent flow to occur at higher Reynolds number than for no axial throughflow. Yamada & Ito [70] investigated this phenomena. It was reported that, in the regions where the moment coefficient C_M with no throughflow is increased by the effect of Taylor type vortices, an increase in the throughflow rate C_Q results in a decrease in C_M, so long as C_Q is not too large. When the clearance ratio, T/R_i, and the Reynolds number, Re, are small, then the following relationship between C_M and Re holds:

$$C_M = \frac{\pi R_i}{T\mathrm{Re}}\left(1 + 0.186\left(C_Q\left(\frac{T}{R_i}\right)\sin\left(\frac{\phi}{2}\right)\right)^{0.8}\right).$$

A numerical study of the work of Yamada & Ito has been conducted by May *et al.* [34]. They utilize two numerical methods, a momentum-integral method, and a finite difference method. The finite difference method used simple turbulence modelling, making use of the mixing length hypothesis. It is worth highlighting that the resources available to May *et al.*, by today's standards, were extremely limited. The grid utilized in the finite difference method was two dimensional, using in the order of 4225 cells. The two dimensional results that will be presented here (§4) were conducted on grids of $\sim 20,000 \rightarrow\sim 100,000$ cells. In order to reduce the computational expense, various

assumptions about the flow were made by May *et al.* that would not necessarily be necessary today. The computational domain utilized assumed that the inflow was in a direction perpendicular to the axis of revolution. The domain was formed around a truncated cone. The outflow is through a narrow outlet, through which the flow is assumed to travel tangentially to the surface of the rotating cone. May *et al.*, when utilizing the momentum integral method, achieve good agreement with the experimental data of Yamada & Ito [69, 71] for $\phi \geq 120°$. The finite difference scheme produces good agreement, though there are some discrepancies, which may well be due to the assumptions previously mentioned. The methods used by May *et al.* do not replicate the increase in C_M as ϕ decreases.

Of a similar vintage is the work of Moureh *et al.* [39], in which a similar experiment to that of Yamada & Ito is conducted, and modelled numerically through a finite volume code. The flow was assumed laminar. Reasonable agreement between numerical predictions and experimental results is again achieved in most cases presented.

Another interesting flow structure, which is of relevance to the study of unshrouded gears, is that on a rotating cone in axial flow, as it provides a crude approximation to the flow over the unshrouded gear. Kobayashi *et al.* [27] studied the transition in the boundary-layer in such a situation. Complex flow structures are present in the transition, with spiral vortices observed as present within the boundary layer. As the rotational speed increases it is seen to provide the driving mechanism within the flow, causing these vortices to weaken and disappear as $\Omega r/U_{stream} \rightarrow \infty$

In this section the impact that throughflow has on rotational flows has been seen, predominantly in Taylor-Couette and Conical Taylor-Couette flow. As can be expected, the location and direction of the point of throughflow affects the overall flow. The throughflow has been reported by some authors [70] to cause reductions in the moment coefficient, and transitions to turbulence to occur at higher Reynolds number. The ability of previous numerical modelling to accurately replicate experimental findings has been reviewed, highlighting the short-comings that have existed.

2.3 Losses from Gears

In this section, some of the literature available which discusses losses from gears will be reviewed. Losses from rotating gears come from many sources and may be characterized into the following 2 categories: losses due to meshing, and losses due to fluid motion (churning and windage). Normally, a gear is not in isolation, it will be in contact with another gear, as it is used to transfer rotational power from one shaft to another. Meshing losses are the losses due to the interaction of the gear in consideration with another gear. The losses due to fluid motion are known as churning and windage. Churning losses are linked to lubrication. If, during the running of the gear, a quantity of lubricant develops such that it is acted upon by the rotation of the gear, this will create a retarding moment on the gear. In general it refers to losses associated with the motion of the lubricating fluid (which is a liquid), which in the multiphase environment represents the secondary phase, and not the losses encountered due to the primary phase (usually air). Windage losses refer to losses associated with the motion of the enveloping fluid (which is a gas), which in the multiphase environment represents the primary phase (usually air), and not the losses encountered due to the secondary phase.

As will be presented in this section, many models exist for the individual losses. Heingartner and Mba [22] produced a model for the losses from a helical gear mesh, incorporating models for windage (Eq. 2.22), churning (Eq. 2.24) and meshing (Eq. 2.26):

$$P_{WL} = \left(\frac{30\Omega}{\pi}\right)^{2.9} \left(0.16 d_f^{3.9} + d_f^{2.9} b^{0.75} m^{1.15}\right) \times 10^{-20} \phi \tag{2.22}$$

$$P_{CL} = \frac{1.474 f_g \nu \left(\frac{30\Omega}{\pi}\right)^3 D^{5.7}}{A_g \times 10^{26}} \tag{2.23}$$

$$P_{CL} = \frac{7.37 f_g \nu \left(\frac{30\Omega}{\pi}\right)^3 D^{4.7} b_i \left(\frac{R_f}{\sqrt{\tan(\beta)}}\right)}{A_g \times 10^{26}} \tag{2.24}$$

$$P_S(x) = 10^{-3} V_S(x) w(x) 0.0127 \log\left(\frac{29.66 w_n(x)}{L_c \mu_0 V_S(x) V_T(x)^2}\right) \tag{2.25}$$

$$P_R(x) = 9 \times 10^4 V_S(x) h(x) \phi_t L_c \tag{2.26}$$

When combined, these models compare well with their experimental findings, the numerical model being within 6.3% of experimental results.

2.3.1 Churning Power Losses

Churning Power Loss (CPL) is an important area of study in any gear system. In this section, a review of literature in this field will be presented, although, as with all the other areas of losses for gears, the majority of existing literature concentrates on spur gears. Ariura *et al.* [7] studied experimentally the churning losses in a spur gear system. It is the view of Ariura *et al.* that these losses are due to two phenomena, these are the trapping of the oil in the tooth spaces, which dominates at lower speeds; and the acceleration of the oil by the gear teeth.

Due to the significant differences in relative momentum which can occur between the air and oil, an understanding of the effect that windage can have on the flow path of oil droplets is important. If the oil is injected with a velocity that causes the oil to be too heavily influenced by the air flow, the gear may not be sufficiently well lubricated. Akin and Mross [2] presented a theory for the effect of windage on lubricant flow (in the tooth spaces of spur gears). They present two solutions (one full solution discounting windage effects (Eq. 2.27), and one approximate including windage effects (Eq. 2.28)) for the point of oil impingement on the gear surface.

$$H_v = \frac{\pi + 4\tan\Phi + B}{2P_d\left(\frac{\Omega D}{2977\sqrt{\Delta p}} + \tan\Phi\right)} \tag{2.27}$$

$$x_t = v_g - \frac{1}{\alpha}\ln(1 + v_g\alpha t) \tag{2.28a}$$

$$y_t = \frac{1}{\alpha}\ln(1 + v_j\alpha t) \tag{2.28b}$$

$$\frac{\alpha}{2P_d}(\pi + B + 4\tan\Phi) = \tan\Phi\ln(1 + v_j\alpha t) + \ln(1 + v_g\alpha t) \tag{2.28c}$$

where H_v is the vectorial impingement depth, Φ is the pressure angle, B is the backlash of mesh at 1 diametrical pitch, P_d is the diametrical pitch, Ω is the speed in RPM, x_t &

y_t are the impingement coordinates,

$$\alpha = \frac{3C_d\rho_a}{4d_o\rho_o}$$

C_D is the air drag coefficient, ρ_a & ρ_o are, respectively, the air and oil densities, d_o is the droplet diameter, v_g is the pitch-line velocity, and v_t is the oil tangential velocity, relative to the nozzle. They briefly discuss the effect of oil droplet size, showing that if the droplets are too small, the drops will be carried out of the meshing region by windage effects. For larger particles, the windage effects on the trajectory reduce, so that the two solutions provide broadly similar answers for the impingement location.

Townsend and Akin [58] studied lubricant jet flow phenomena in spur gears in the out of mesh condition, in order to determine the penetration depth onto the tooth flank of a jet of oil at different velocities pointed at the pitch line on the outgoing side of mesh. This they have achieved through both experimental and numerical analyses. They show that the impingement depth in spur gear systems is affected by the gear ratio, as well as by the ratio between oil-jet velocity and pitchline velocity. Jet angle will also affect the impingement depth, as does the location of the jet relative to the pitchline. The impingement depth is important; if it is too shallow, there may well be inadequate lubrication and cooling of the teeth, leading to the possible problem of scoring of the gear teeth. Townsend and Akin [57] considered, through experiment and numerical analysis, gear lubrication and cooling, in order to produce a gear temperature analysis model, and to validate this model with experimental data. In their experiment (and numerical model) the oil lubricant is delivered through a pressurized oil jet. It was found that increasing the pressure of this jet had a significant effect on both average and peak surface temperatures at loads above $18.95Nm^{-1}$. Significant rises in average and peak surface temperatures are also seen when the gear system is accelerated at constant load and when increasing the load whilst at a constant speed. It is also shown that most effective cooling occurs when the oil-jet pressure is such that full tooth impingement occurs. Of course, as with any fluid system, the flow behaviour will show speed dependence. Boness [10] observed that for gears partially submerged in oil, three distinct relationships can

be given between the moment coefficient and the Reynolds number as below: Laminar:

$$C_{M(\text{Boness})} = \frac{20}{\text{Re}_{\text{Boness}}} \tag{2.29a}$$

Transition:

$$C_{M(\text{Boness})} = 8.6 \times 10^{-4} \text{Re}_{\text{Boness}}^{1/3} \tag{2.29b}$$

Turbulent:

$$C_{M(\text{Boness})} = \frac{5 \times 10^8}{\text{Re}_{\text{Boness}}^2}, \tag{2.29c}$$

where

$$C_{M(\text{Boness})} = \frac{2M}{\rho\Omega^2 R^5(\theta - \sin\theta)}$$

$$\text{Re}_{\text{Boness}} = \frac{2\Omega R^2 \sin(\theta/2)}{\nu}$$

Boness attributes, for good reasons, great importance to the determination of churning losses. The work does however fail to take into account the size of the windage losses. Whilst these may be much smaller than the churning losses (approximately $1/47^{\text{th}}$ the size), it is not clear if their effect has been removed from the equations presented by Boness [10]

2.3.2 Meshing Losses

The study of meshing power loss (MPL) is an important area of consideration. This is essentially the effects that tribology[1] factors have upon meshing, though it also includes the study of the pumping of the air/oil mixture that occurs between teeth during meshing.

Tribology Effects

The study of tribology is important when considering meshing gears, as it has effects which are beyond the level of conventional CFD methods, due to the fact that they work at smaller scales than the macroscopic levels of CFD. In this section, some relevant literature from the field of tribology will be reviewed, to give an impression as to the

[1] Friction, lubrication, and wear

complexities of this interesting subject. Tevaarwerk [56] demonstrated that the traction performance of a traction drive may be predicted from the basic knowledge of two fluid parameters: the initial traction slope and the peak traction coefficient.

Pumping Effects

Anderson & Loewenthal *et al.* studied spur gear system efficiency at part and full load [4], the effect of geometry and operating conditions on spur gear system power loss [5] and studied the efficiency of nonstandard and high contact ratio involute spur gears [6]. MPL are shown to have some dependence on the torque that is transmitted through the mesh. At higher loads, the pitch of the gear has an influence on the efficiency of the gear, with fine-pitched gears being more efficient than coarse pitched gears. The pitch-line velocity also influences the gear efficiency, an improvement being seen at higher velocities. The effect of geometrical changes to the gear and their influence on MPL are considered, showing that increasing the contact ratio of the gears increases the MPL, and increasing the diameter of the gear will reduce the MPL. Milian *at al.* [37, 38], through numerical integration of Eq. 2.30, produced a model of the pumping action on the air/oil mixture that occurs between the teeth of high-speed spur and helical gears,

$$\frac{\partial}{\partial t}\int_V \rho \mathrm{d}V + \int_S \rho \mathbf{v}.\mathbf{n}\mathrm{d}S = 0, \tag{2.30}$$

where V is the volume between the teeth, S is the exit surface (the axial and radial discharge areas), and $\mathbf{v}.\mathbf{n}$ is the normal velocity to the exit surface. The numerical model developed displays reasonable agreement with experimental results, showing that, for spur and helical gears, theoretical analysis of the pumping action can be successfully performed.

2.3.3 Windage Losses from Spur Gears

One of the primary goals of this thesis has been to show that numerical modelling can be used to model the flow around a spiral bevel gear as an aid to improved shroud design. As such, it is important to present the literature that already exists in this field. A comprehensive review of this literature has been recently conducted by Eastwick &

Johnson [18], discussing some of the literature that has been reviewed here.

The majority of literature available in this field is experimental, of which the earliest are those of Dawson [12, 13], which consider gear windage on high speed (spur) gears. A formula for windage power loss was derived (Eq. 2.31):

$$P = 1.12 \times 10^{-8} C' \rho \left(\frac{\Omega \times 60}{2\pi} \right)^{2.95} \left(\frac{r}{2} \right)^{4.7} \nu^{0.15} \lambda \tag{2.31}$$

where C' is a shape factor for the gear, a constant equal to the moment coefficient, given by Eq. 2.32, for $\mathrm{Re} = 5 \times 10^5$,

$$C_M = \frac{T}{\rho \left(\frac{\Omega}{2\pi} \right)^2 R^5}, \tag{2.32}$$

and λ is a parameter denoting the influence of any shrouding, lying between 0.5 (fully shrouded) and 1 (open gear).

Diab *et al.* [14–16] looked at windage losses in high speed gears, presenting some experimental and theoretical results. Two theoretical approaches are utilized, one a dimensional analysis based upon the Reynolds number, the gear geometry and the speed, the other a quasi-analytical approach. The dimensional analysis gives the following result for the moment coefficient (Eq. 2.33):

$$C_M = 60 \mathrm{Re}^{-0.25} \left(\frac{b}{R} \right)^{0.8} Z^{-0.4} \left\{ \left(\frac{h_1}{R} \right)^{0.56} + \left(\frac{h_2}{R} \right)^{0.56} \right\}. \tag{2.33}$$

The analytical approach they derive produces equations for the moment coefficient from the front and rear faces (Eq. 2.34), and from the teeth (Eq. 2.35):

$$C_f = \frac{2 \times 1.293\pi}{5 - 2 \times 0.5} \frac{1}{\sqrt{3 \times 10^5}} \left(\frac{\sqrt{\frac{\mu 3 \times 10^5}{\rho \Omega}}}{R} \right)^5 + \ldots$$
$$\ldots + \frac{2 \times 0.074\pi}{5 - 2 \times 0.2} \left[\frac{1}{\mathrm{Re}^{0.2}} - \frac{1}{(3 \times 10^5)^{0.2}} \left(\frac{\sqrt{\frac{\mu 3 \times 10^5}{\rho \Omega}}}{R} \right)^5 \right] \tag{2.34}$$

$$C_l \simeq \xi \frac{Z}{4} \left(\frac{b}{R} \right) \left[1 + \frac{2(1 + X_A)}{Z} \right]^4 (1 - \cos\phi)(1 + \cos\phi)^3 (1 - \sin^2\beta) \tag{2.35}$$

$$C_M = C_f + C_l \tag{2.36}$$

The results obtained using both of these approaches are good, with close agreement shown with experimental data sourced from Anderson and from Dawson.

A few papers exist of numerical modelling of the flow around a spur-gear, these being the papers of Strasser [53], and Al-Shibl *et al.* [3]. Strasser [53] modelled the flow between meshing spur gears in two-dimensions. It shows the flow structure in the tooth gap spaces where no meshing is occurring is very similar to the flow structure observed by Al-Shibl *et al.*, suggesting the validity of modelling which does not involve meshing gears.

2.3.4 Windage losses from Bevel Gears

Very little previous work exists in this field; papers in the open literature are limited to those of Winfree [68], Lord [33], Farrall *et al.* [20], and Johnson *et al.* [24, 25]. Winfree [68] studied experimentally the flow around a spiral bevel gear, both unshrouded and shrouded, showing a significant reduction in windage losses when the shroud was installed. The gear used by Winfree differs from that used in Chapters 5 & 6; it has a radius of 0.381m, which is approximately 40% bigger, but has far fewer teeth (38 as opposed to 91). Some important findings with regard to shrouding design are included in [68] and these can be generalized to other spiral bevel gears. However, some conclusions appear to be specific to the gear in question. Winfree states that a gear for which the tip velocity is over $50.8ms^{-1}$ must be baffled. This equates, for the gear modelled here, to a rotational speed of 3675 RPM suggesting that a reduction in windage power loss should be seen for all shrouded cases except those at $3,000$ RPM. The flow structure was analyzed, in which it was determined that bevel gears pump fluid in the direction of increasing radius. The optimum shroud for the gear in question was determined, which was not the shroud for which the gap between teeth and shroud was the smallest. Indeed, Winfree found that it is possible to overly restrict the flow around the gear, and whilst this will reduce the windage compared to the unshrouded case, it will not produce the lowest levels of windage. The relevance of Winfree [68] to the work conducted in §5-6 is that it presents data on the flow around a spiral bevel gear. Whilst the gear in question

is quite different to that used here, it is much closer than a helical or spur gear.

A significant piece of work in the field is that of Lord [33]. Lord studied shrouded and unshrouded spur, helical and bevel gears experimentally, and matched empirical equations to the data obtained. Lord found that for a bevel gear the part of the shroud that appeared to have the greatest effect was the face shroud. This agrees with the description of the flow field given by Farrall et al. [20] in that the air flow is drawn into the gear teeth in a direction perpendicular to the gear face. If a shroud is placed across the face, it should reduce this flow. Whilst the fully shrouded configuration reduced windage power loss by 80%, Lord found that without the face shroud losses were similar to those in the unshrouded condition. Finally, Lord reports a similar finding to that of Winfree [68], that there must be some optimal shroud clearance, and that as the distance is varied from this, the windage power loss will increase.

The paper by Farrall et al. [20] is a forerunner to the work presented in this thesis. Farrall et al. studied computationally the airflow around an open bevel gear and through a shrouded bevel gear prior to experimental data becoming available. In the open case results are presented at the rotational speed of $15,000$ RPM. Due to the scope of the project, no calculations were carried out by Farrall et al. for directional dependence of this flow. A description of the flow field for the open gear is given at the speed of $15,000$ RPM. Farrall et al. report that the introduction of a shroud over the gear has a significant influence on the flow pattern near the gear, though it had little effect on the windage power loss at the mass flow rates considered.

Johnson *et al.* [25] investigated experimentally the flow around the spiral bevel gear of Chapters 5 & 6, both unshrouded and shrouded. The unshrouded gear showed directional dependence in the moment coefficient, an effect which was not reproduced with a shroud present. Directional dependence is caused by the difference in the angle of the leading edge of the tooth face relative to the flow. Further evidence, and explanation, of this will be presented from the numerical modelling in §5. The effect of shrouding was clear, reducing torque levels by 70% of their unshrouded value. An interesting analogy was made between the spiral bevel gear and a centrifugal fan, which can be used to characterize the system, allowing performance predictions to be made successfully, and

eliminating the need to test the system over large pressure ranges. The data presented by Johnson *et al.* is used in §5 and §6 to provide validation data for the numerical modelling.

As has been previously highlighted, the interaction between the air flow and any lubricant flow is significant. Recently published work by Johnson *et al.* [24] has looked at this interaction for a spiral bevel gear, incorporating meshing effects as well, and the effect that this has on power losses due to the two-phase flow. Of relevance to the work presented in Chapters 5 & 6 are their findings on the effect of adding oil into the system. It is reported that the additional torque at a given speed due to the presence of oil can be calculated via a very simple relationship (Eq. 2.37):

$$T_{\text{oil}} = \dot{m}\Omega r^2 \tag{2.37}$$

where $\dot{m}$ is the oil mass flow rate. This relationship is shown to provide a very good fit to the unshrouded experimental data presented. In the shrouded cases the fit is not as good, though this may well be due to churning losses, as the authors report a build-up of oil observed between the shroud and the gear. These are important results, as they allow the effect of changes in oil injection rate upon torque levels to be calculated readily. Additionally, if numerical modelling is used to predict the windage losses due to air alone, this can then be combined with Eq. 2.37 to predict the total torque due to the air and oil. This is of benefit to the numerical modeller, as it eliminates the need to perform computationally expensive two-phase modelling. Additionally, eliminating the need to model oil injection gives the domain around a single gear rotational periodicity, which allows smaller models of just a few teeth to be constructed. This would allow an increase in near-wall resolution and/or reduce computing time compared to a full-gear model.

In this section, literature dedicated to windage power loss from Bevel Gears has been reviewed. The ability of shrouding to reduce this loss has been discussed, with all sources highlighting this aspect. Reductions in windage power loss due to shrouding quoted vary from 40% to 80%. All sources highlight that there exists an optimum shroud clearance for reducing windage power loss and that away from this clearance windage power loss

will increase.

2.4 Summary

In this chapter, existing literature in the open-press has been discussed. A description of the first of the flows modelled in this thesis, Taylor-Couette flow, has been given (§2.1). The many interesting features present within this flow, such as the contra-rotating vortices which are present, have been described. Numerical modelling has been utilized by many authors to simulate this flow, with varying degrees of success. Experimental analysis has shown that the flow is one that lacks any over riding global characterization.

Extensions and modifications of Taylor-Couette flow have also been reviewed (§2.2). These have again highlighted the subtle complexity of Taylor-Couette flow, with any slight modification in boundary conditions leading to significant changes in flow structure. Again, numerical modelling by many authors has been reviewed which has shown the possibility of using accurate simulation techniques to understand the driving mechanisms behind the complex flow structures that are present.

A review of some of the literature related to gear power losses. These losses can be grouped into losses due to fluid motion (churning and pumping during meshing), and mechanical losses due to tribological effects. The fluid effects all interact together (along with windage) so understanding of one must be obtained whilst at the same time considering the effects that it can have on the others. Depending on the system, the fraction that each of these losses represents of total system losses varies. Existing literature in the field of Windage Power Loss has been discussed, and has highlighted the lack of any significant previous work in this field.

Chapter 3

CFD Methodology

3.1 Introduction

In this chapter, a description of the theoretical grounding of the numerical models which have been used in this thesis will be given. To start with the fundamental equations of fluid dynamics will be given (Eq. 3.1). A description of how the commercial CFD code FLUENT solves these equations has been given, with details of the numerical discretisation schemes that have been applied given in Section 3.3. Descriptions of some of the 'extra' physical phenomena that need to be considered when modelling fluid flow, such as turbulence and boundary layers, has been presented (§3.4-§3.7). After this, the generation of the meshes used in the simulations has been described (§3.10). A description of how the simulations are conducted on these meshes has been given as well (§3.12). By presenting these models along with some implicit assumptions, an understanding of how the work in this thesis has been produced can be arrived at.

3.2 Computational Fluid Dynamics (CFD)

A mathematical description of the mechanics of fluid flow was first proposed by both Navier and Stokes in the 19^{th} century, which can be written in many forms. This system of equations is known as the Navier-Stokes equations. In three-dimensions in a cartesian

coordinate system they can be written as follows:

$$\rho\left(\frac{\partial u}{\partial \mathrm{t}}+u\frac{\partial u}{\partial x}+v\frac{\partial u}{\partial \mathrm{y}}+w\frac{\partial u}{\partial \mathrm{z}}\right)=-\frac{\partial p}{\partial x}+\ldots \\ \cdots+\mu\left[\frac{\partial^2 u}{\partial \mathrm{x}^2}+\frac{\partial^2 u}{\partial \mathrm{y}^2}+\frac{\partial^2 u}{\partial \mathrm{z}^2}\right]+\rho g_x+\frac{\mu}{3}\left(\frac{\partial u}{\partial \mathrm{x}}\right) \quad (3.1a)$$

$$\rho\left(\frac{\partial v}{\partial \mathrm{t}}+u\frac{\partial v}{\partial \mathrm{x}}+v\frac{\partial v}{\partial \mathrm{y}}+w\frac{\partial v}{\partial \mathrm{z}}\right)=-\frac{\partial p}{\partial \mathrm{y}}+\ldots \\ \cdots+\mu\left[\frac{\partial^2 v}{\partial \mathrm{x}^2}+\frac{\partial^2 v}{\partial y^2}+\frac{\partial^2 v}{\partial z^2}\right]+\rho g_y+\frac{\mu}{3}\left(\frac{\partial v}{\partial \mathrm{y}}\right) \quad (3.1b)$$

$$\rho\left(\frac{\partial w}{\partial \mathrm{t}}+u\frac{\partial w}{\partial \mathrm{x}}+v\frac{\partial w}{\partial \mathrm{y}}+w\frac{\partial w}{\partial \mathrm{z}}\right)=-\frac{\partial p}{\partial \mathrm{z}}+\ldots \\ \cdots+\mu\left[\frac{\partial^2 w}{\partial \mathrm{x}^2}+\frac{\partial^2 w}{\partial y^2}+\frac{\partial^2 w}{\partial z^2}\right]+\rho g_z+\frac{\mu}{3}\left(\frac{\partial w}{\partial \mathrm{z}}\right) \quad (3.1c)$$

The momentum equations (Eq. 3.1a, Eq. 3.1b & Eq. 3.1c) describe the change in momentum with time and space. They do not conserve mass, for this reason, it is also necessary to consider the mass continuity equation

$$\frac{\partial \rho}{\partial t}+\frac{\partial}{\partial \mathrm{x}}(\rho u)+\frac{\partial}{\partial \mathrm{y}}(\rho v)+\frac{\partial}{\partial \mathrm{z}}(\rho w)=0 \quad (3.1d)$$

There is one major issue with solving Navier-Stokes equations: the ability to find an analytical solution to the equations. Apart from a few simple cases, it is generally not possible to find a global analytical solution to the Navier-Stokes equations in a given setting. Therefore, it is necessary to solve the equations numerically at specific points within the flow. The numerical solution of the Navier-Stokes equations is known as Computational Fluid Dynamics (CFD). In this thesis, the Navier-Stokes equations have been solved in 4 settings (Taylor-Couette flow (Appendix A), Conical Taylor-Couette flow (Chapter 4), an unshrouded gear (Chapter 5), and a shrouded gear (Chapter 6)) using the commercial CFD program FLUENT [1]. Due to the nature of the domains in question, in all 4 settings the flow has been solved using the rotational or cylindrical form of the Navier-Stokes equations (Eq. 3.1): however, the theory and equations are presented

easier in a cartesian format. The implications of solving in a (moving) rotational frame will be discussed further on.

FLUENT solves the Navier-Stokes equations (Eq. 3.1) using a finite-volume method, where the computational domain is sub-divided into a series of finite volumes or cells. The Navier-Stokes equations are integrated over these volumes, resulting in a series of discretized equations, which can be linearized (§3.3). These linear algebraic equations can then be solved to give an approximate solution to the Navier-Stokes equations. Two types of solver are available in FLUENT: a pressure based solver, and a density based solver. The pressure based solver has been used throughout this thesis. It seeks to solve the continuity equation (Eq. 3.1d) via a pressure correction equation. An iterative process is followed, whereby the fluid properties (including turbulent viscosity) are first 'updated', either using the initial values (for the very first iteration) or from the previous iteration. The momentum equations are then solved to give the velocity field within the domain, using either the initial pressure field (for the very first iteration) or the previously calculated pressure field, and the fluid properties. This 'new' velocity field is then used in the pressure correction equation to update the pressure field. Equations for additional variable quantities, such as the turbulence parameters, are then solved. The additional models for turbulence, boundary layers, and compressibility will be discussed in Sections 3.5, 3.6, & 3.7, respectively.

3.3 Discretisation

Upon integration over the control-volume (the cells), the Navier-Stokes equations (Eq. 3.1) are then discretized. The unsteady conservation equation for transport of a variable quantity ψ, integrated over a control volume V is given as follows:

$$\int_V \frac{\partial \rho\psi}{\partial t} dV + \oint \rho\psi\vec{v} \cdot d\vec{A} = \oint \Gamma_\psi \nabla\psi \cdot d\vec{A} + \int_V S_\psi dV \tag{3.2}$$

The equation is discretized as below:

$$\frac{\partial \rho\psi}{\partial t} V + \sum_f^{N_{\text{faces}}} \rho_f \vec{v}_f \psi_f \cdot \vec{A}_f = \sum_f^{N_{\text{faces}}} \Gamma_\psi \nabla\psi_f \cdot \vec{A}_f + S_\psi V \tag{3.3}$$

where N_{faces} = number of faces enclosing cell, ψ_f = value of ψ convected through face f, $\rho_f \vec{v}_f \cdot \vec{A}_f$ = mass flux through the face, $\vec{A}_f$ = area of face f, $\nabla\psi_f$ = gradient of ψ at face f, and V= cell volume. The discretized equation (Eq. 3.3) contains an unknown variable, ψ. In general the equation will be non-linear, but it can be linearized as

$$a_P \psi = \sum_{\text{nb}} a_{\text{nb}} \psi_{\text{nb}} + b. \tag{3.4}$$

This results in a set of linear equations for each cell in the grid, which results in a set of algebraic equations with a sparse coefficient matrix. For variable equations, FLUENT solves this linear system using a point implicit (Gauss-Seidel) linear equation solver in conjunction with an algebraic multigrid (AMG) method. In the setting which has been used in this thesis, variable quantities are stored for cell-centre values, and not for the faces of the cells. Thus, an approximation to these values must be used. This is the spatial discretisation, of which 4 variants are available in FLUENT: 1$^{\text{st}}$ order upwind, 2$^{\text{nd}}$ order upwind, power law, and Quadratic Upwind Interpolation for Convective Kinetics (QUICK). The power law model has not been used in this thesis; descriptions of the other three models are given below.

The simplest of these models is the 1$^{\text{st}}$ order upwind model. It assumes that the value of a variable is the same throughout the cell, so the face-value is the same as the cell-centre value.

3.3.1 2$^{\text{nd}}$ order upwind

The 2$^{\text{nd}}$ order upwind calculates the face value of ψ through a Taylor series expansion of the cell-centred solution about the cell centroid

$$\psi_f = \psi + \nabla\psi \cdot \vec{r}. \tag{3.5}$$

The gradient of ψ, $\nabla\psi$, needs to be calculated. It is given as follows

$$(\nabla\psi)_{c0} = \frac{1}{\mathcal{V}} \sum_f \overline{\psi}_f \vec{A}_f \tag{3.6}$$

where

$$\overline{\psi}_f = \frac{\psi_{c0} + \psi_{c1}}{2}$$

3.3.2 QUICK

The QUICK scheme uses a weighted average of the 2nd order upwind scheme and a 2nd order central-differencing scheme. For face e in Figure 3.1, the value of ψ is as given by equation 3.3.2:

$$\psi_e = \theta \left[\frac{S_d}{S_c + S_d}\psi_P + \frac{S_c}{S_c + S_d}\psi_E \right] + (1 - \theta) \left[\frac{S_u + 2S_c}{S_u + S_c}\psi_P - \frac{S_c}{S_u + S_c}\psi_W \right] \tag{3.7}$$

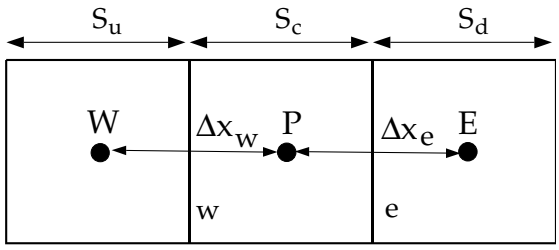

Figure 3.1: One-dimensional control volume [1].

3.3.3 Temporal Discretisation

In the case of transient (unsteady) simulations, the time-derivative of a variable is given by either a 1st order or a 2nd order discretisation. The 1st order discretisation is given by Eq. 3.8:

$$\frac{\psi^{n+1} - \psi^n}{\Delta t} = F(\psi) \tag{3.8}$$

3.3.4 Discretisation of the Momentum Equations

The momentum equations are discretized spatially in the manners previously described. However, in the linearized x-momentum equation, for example (Eq. 3.9), the pressure field and the mass-fluxes through the faces of each cell are not known:

$$a_P u = \sum_{\text{nb}} a_{\text{nb}} u_{\text{nb}} + \sum p_f \text{A} \cdot \hat{\imath} + S \tag{3.9}$$

The default option in Fluent interpolates the value of pressure at the cell face from the cell-centre value using the coefficients in the momentum equation, as below:

$$p_f = \frac{\frac{p_{c_0}}{a_{p,c_0}} + \frac{p_{c_1}}{a_{p,c_1}}}{\frac{1}{a_{p,c_0}} + \frac{1}{a_{p,c_1}}}$$

The alternative that has also been used in this thesis is the pressure staggering option (PRESTO!). This solves the discrete continuity balance about a 'staggered' control volume centred upon the cell face. This calculates the pressure in the staggered volume, which is of course equal to the pressure on the face of the original volume.

3.3.5 Discretisation of the Continuity Equation

The discretized form of the continuity equation (Eq. 3.1d) over a control volume is as below:

$$\sum_{f}^{N_{\text{faces}}} J_f A_f = \sum_{f}^{N_{\text{faces}}} \rho v_n A_f = 0 \tag{3.10}$$

This can lead to problems of 'checker-boarding' in the pressure if the face velocities are linearly interpolated from the cell centred values. For this reason, FLUENT uses a momentum averaged approach to calculate the face values, using the coefficients from the discretized momentum equation (3.9) to give the mass flux as below:

$$J_f = \rho_f \frac{a_{p,c_0} v_{n,c_0} + a_{p,c_1} v_{n,c_1}}{a_{p,c_0} + a_{p,c_1}} + d_f((p_{c_0} + (\nabla p)_{c_0} \cdot \vec{r_0}) - (p_{c_1} + (\nabla p)_{c_1} \cdot \vec{r_1})) \tag{3.11}$$

where p_{c_0}, p_{c_1} and v_{n,c_0}, v_{n,c_1} are the pressures and normal velocities, respectively, within the two cells on either side of the face, and $\hat{J}_f$ contains the influence of velocities in these cells. The term d_f is a function of the average of the momentum equation a_p

3.3.6 Pressure-Velocity Coupling

As mentioned previously, using an iterative pressure based solver necessitates the use of a coupling between the pressure field and the velocity field solutions. Many methods are available for this coupling, for the purposes of this work the SIMPLE algorithm has been used. The SIMPLE algorithm uses a relationship between velocity and pressure

corrections to enforce mass conservation and to obtain the pressure field. When the momentum equation is solved using a guessed pressure field, p^*, the resulting mass fluxes, J_f^*, do not satisfy the continuity equation. For this reason, a correction term is computed, to satisfy continuity. The SIMPLE algorithm suggests that the correction can be calculated from the pressure values using the function d_f:

$$J_f' = d_f(p_{c0}' - p_{c1}') \tag{3.12}$$

This is then substituted into the discrete continuity equation (Eq. 3.10), giving an equation for the pressure in each cell

$$a_P p' = \sum_{\text{nb}} a_{\text{nb}} p_{\text{nb}}' + \sum_{f}^{N_{\text{faces}}} J_f^* A_f \tag{3.13}$$

This then leads to 'final' values for the pressure and mass flux as below:

$$p = p^* + \alpha_p p' \tag{3.14}$$

$$J_f = J_f^* + d_f(p_{c0}' - p_{c1}') \tag{3.15}$$

where α_p is the pressure under-relaxation factor.

3.4 Turbulence

Turbulence in fluid dynamics is a flow regime which is characterized by stochastic property changes, although it is often wrongly thought of as chaotic. In turbulent flow, all fluid properties are time-dependent, even though in steady flow the mean values are constant. If all of the variables in the Navier-Stokes equations are considered to have a mean component and a fluctuating component (ie $u = \overline{u} + u'$), this leads to the following:

$$\rho\left(\frac{\partial\overline{u}}{\partial \mathrm{t}}+\overline{u}\frac{\partial\overline{u}}{\partial x}+\overline{v}\frac{\partial\overline{u}}{\partial \mathrm{y}}+\overline{w}\frac{\partial\overline{u}}{\partial \mathrm{z}}\right)=-\frac{\partial p}{\partial x}+\ldots$$
$$\cdots+\mu\left[\frac{\partial^2\overline{u}}{\partial \mathrm{x}^2}+\frac{\partial^2\overline{u}}{\partial \mathrm{y}^2}+\frac{\partial^2\overline{u}}{\partial \mathrm{z}^2}\right]+\rho g_x+\frac{\mu}{3}\left(\frac{\partial\overline{u}}{\partial \mathrm{x}}\right)-\ldots$$
$$\cdots-\rho\frac{\partial}{\partial \mathrm{x}}\left(\overline{u'u'}\right)-\rho\frac{\partial}{\partial \mathrm{y}}\left(\overline{u'v'}\right)-\rho\frac{\partial}{\partial \mathrm{z}}\left(\overline{u'w'}\right)+\frac{\mu}{3}\left(\frac{\partial u'}{\partial \mathrm{x}}\right) \quad (3.16a)$$

$$\rho\left(\frac{\partial\overline{v}}{\partial \mathrm{t}}+\overline{u}\frac{\partial\overline{v}}{\partial \mathrm{x}}+\overline{v}\frac{\partial\overline{v}}{\partial \mathrm{y}}+\overline{w}\frac{\partial\overline{v}}{\partial \mathrm{z}}\right)=-\frac{\partial p}{\partial \mathrm{y}}+\ldots$$
$$\cdots+\mu\left[\frac{\partial^2\overline{v}}{\partial \mathrm{x}^2}+\frac{\partial^2\overline{v}}{\partial y^2}+\frac{\partial^2\overline{v}}{\partial z^2}\right]+\rho g_y+\frac{\mu}{3}\left(\frac{\partial\overline{v}}{\partial \mathrm{y}}\right)-\ldots$$
$$\cdots-\rho\frac{\partial}{\partial \mathrm{x}}\left(\overline{v'u'}\right)-\rho\frac{\partial}{\partial \mathrm{y}}\left(\overline{v'v'}\right)-\rho\frac{\partial}{\partial \mathrm{z}}\left(\overline{v'w'}\right)+\frac{\mu}{3}\left(\frac{\partial v'}{\partial \mathrm{y}}\right) \quad (3.16b)$$

$$\rho\left(\frac{\partial\overline{w}}{\partial \mathrm{t}}+\overline{u}\frac{\partial\overline{w}}{\partial \mathrm{x}}+\overline{v}\frac{\partial\overline{w}}{\partial \mathrm{y}}+\overline{w}\frac{\partial\overline{w}}{\partial \mathrm{z}}\right)=-\frac{\partial p}{\partial \mathrm{z}}+\ldots$$
$$\cdots+\mu\left[\frac{\partial^2\overline{w}}{\partial \mathrm{x}^2}+\frac{\partial^2\overline{w}}{\partial y^2}+\frac{\partial^2\overline{w}}{\partial z^2}\right]+\rho g_z+\frac{\mu}{3}\left(\frac{\partial\overline{w}}{\partial \mathrm{z}}\right)-\ldots$$
$$\cdots-\rho\frac{\partial}{\partial \mathrm{x}}\left(\overline{w'u'}\right)-\rho\frac{\partial}{\partial \mathrm{y}}\left(\overline{w'v'}\right)-\rho\frac{\partial}{\partial \mathrm{z}}\left(\overline{w'w'}\right)+\frac{\mu}{3}\left(\frac{\partial w'}{\partial \mathrm{z}}\right) \quad (3.16c)$$

3.5 Turbulence Modelling

There are 12 'additional' terms which appear on the right hand side of Eq. 3.16: $\rho\frac{\partial}{\partial \mathrm{x}}\left(\overline{u'u'}\right)$, $\rho\frac{\partial}{\partial \mathrm{y}}\left(\overline{u'v'}\right)$, $\rho\frac{\partial}{\partial \mathrm{z}}\left(\overline{u'w'}\right)$, $\frac{\mu}{3}\left(\frac{\partial u'}{\partial \mathrm{x}}\right)$, $\rho\frac{\partial}{\partial \mathrm{x}}\left(\overline{v'u'}\right)$, $\rho\frac{\partial}{\partial \mathrm{y}}\left(\overline{v'v'}\right)$, $\rho\frac{\partial}{\partial \mathrm{z}}\left(\overline{v'w'}\right)$, $\frac{\mu}{3}\left(\frac{\partial v'}{\partial \mathrm{y}}\right)$, $\rho\frac{\partial}{\partial \mathrm{x}}\left(\overline{w'u'}\right)$, $\rho\frac{\partial}{\partial \mathrm{y}}\left(\overline{w'v'}\right)$, $\rho\frac{\partial}{\partial \mathrm{z}}\left(\overline{w'w'}\right)$, & $\frac{\mu}{3}\left(\frac{\partial w'}{\partial \mathrm{z}}\right)$. Of these, the 6 terms of the form

$$\rho\frac{\partial}{\partial \mathrm{x}_i}\left(\overline{u_i'u_i'}\right)$$

are known as the Reynolds stresses. If the mesh is fine enough to use a direct numerical simulation, then the Reynolds stresses should not need to be modelled. However, direct numerical simulations are extremely computationally expensive. In any other numerical

model, therefore the Reynolds stresses need to be computed. This creates then the problem of closure of the Navier-Stokes equations, there are more unknowns (3 velocity components, 6 Reynolds stresses, pressure and density) than equations (4). It leads to the field of turbulence modelling. Two popular forms of turbulence modelling are Reynolds stress modelling (RSM) and the family of two-equation models using energy and frequency. The latter includes the $k-\epsilon$ turbulence models, which have transport equations for the turbulent kinetic energy, k, and its dissipation rate, ϵ, and the $k-\omega$ turbulence models, which have transport equations for the turbulent kinetic energy, k, and its production rate, ω.

Turbulence modelling has been used throughout this thesis, with a significant section of the work looking at comparisons between the performances of different turbulence models when simulating experimental data from the open literature. In this section, a basic overview of the 5 turbulence models used within this thesis will be given. These are the Standard $k-\epsilon$ turbulence model, the Renormalized Group (RNG) $k-\epsilon$ turbulence model, the Realizable $k-\epsilon$ turbulence model, the Shear Stress Transport (SST) $k-\omega$ turbulence model, and the Reynolds Stress Model. All 5 turbulence models are used in Chapter 4, with just the RNG $k-\epsilon$ turbulence model used in Chapters 5 & 6. Assessments are made in Chapter 4 as to the optimum turbulence model for modelling Conical Taylor-Couette flow. This forms an approximation to the flow around a shrouded spiral bevel gear, and so the chosen model is then used in Chapters 5 & 6.

3.5.1 $k-\epsilon$ Turbulence Models

As stated previously, the $k-\epsilon$ turbulence models have transport equations for the turbulent kinetic energy, k, and its dissipation rate, ϵ. Two key assumptions are made

- the turbulent behaviour is isotropic
- The Boussinesq hypothesis holds true

The Boussinesq hypothesis states that an effective (turbulent) viscosity can be used to relate the stress in a fluid element to the rate of strain it experiences. The implication of

these assumptions is that the Reynolds Stresses can be given by the following equation:

$$-\rho\overline{u_i'u_j'} = \mu_t\left(\frac{\partial u_i}{\partial \mathrm{x}_j} + \frac{\partial u_z}{\partial \mathrm{x}_i}\right) - \frac{2}{3}\left(\rho k + \mu_t\frac{\partial u_i}{\partial \mathrm{x}_i}\right)\delta_{ij} \tag{3.17}$$

where

$$\mu_t = \rho C_\mu \frac{k^2}{\epsilon} \tag{3.18}$$

$$k = \frac{1}{2}\left(\overline{u_r'^2} + \overline{u_\theta'^2} + \overline{u_z'^2}\right)$$

$$\epsilon = 2\nu\overline{e_{ij}'e_{ij}'}$$

δ_{ij} is the Kronecker delta function: $\delta_{ij} = 1$ if $i = j$, $\delta_{ij} = 0$ if $i \neq j$. e' is the fluctuating component of the rate of deformation of a fluid element. There are many forms of the transport equations which have been proposed for the evolution of k and ϵ, these allow the turbulent form of the Navier-Stokes equations (Eq. 3.16) to be 'solved'.

Standard $k-\epsilon$ Turbulence Model

The Standard $k-\epsilon$ turbulence model was developed by Launder and Spalding [31]. The transport equations for the turbulent kinetic energy, k, and its dissipation rate, ϵ are:

$$\frac{\partial}{\partial t}(\rho k) + \frac{\partial}{\partial x_i}(\rho k u_i) = \frac{\partial}{\partial x_j}\left[\left(\mu + \frac{\mu_t}{\sigma_k}\right)\frac{\partial k}{\partial x_j}\right] + G_k - \rho\epsilon - Y_M + S_k, \tag{3.19a}$$

$$\frac{\partial}{\partial t}(\rho \epsilon) + \frac{\partial}{\partial x_i}(\rho \epsilon u_i) = \frac{\partial}{\partial x_j}\left[\left(\mu + \frac{\mu_t}{\sigma_\epsilon}\right)\frac{\partial \epsilon}{\partial x_j}\right] + C_{1\epsilon}\frac{\epsilon}{k}G_k - C_{2\epsilon}\rho\frac{\epsilon^2}{k} + S_\epsilon. \tag{3.19b}$$

In these equations, G_k represents the generation of turbulent kinetic energy due to the mean velocity gradients. From the exact equation for the transport of k,

$$G_k = -\rho\overline{u_i'u_j'}\frac{\partial u_j}{\partial \mathrm{x}_i}. \tag{3.20}$$

To ensure consistency with the Boussinesq hypothesis, the following is used for the evaluation of G_k

$$G_k = \mu_t S^2, \tag{3.21}$$

$$S \equiv \sqrt{2S_{ij}S_{ij}},$$

$$S_{ij} = \frac{1}{2}\left(\frac{\partial u_j}{\partial x_i} + \frac{\partial u_i}{\partial x_j}\right) \tag{3.22}$$

In this thesis, gravitational effects have not been included, due to the assumption (in almost all cases) of rotational periodicity and dominance within the flow. For this reason, the usual buoyancy term G_b has not been included. Y_M represents the contribution of compressibility effects to the overall dissipation rate. If the dilatation dissipation is neglected, the observed decrease in spreading rate with increasing Mach number for compressible mixing and other free shear layers is not predicted:

$$Y_M = 2\rho\epsilon \mathrm{M}_t^2,$$

where M_t is the turbulent Mach number, defined as:

$$\mathrm{M}_t = \sqrt{\frac{k}{a^2}}.$$

$C_{1\epsilon}$ and $C_{2\epsilon}$ are constants. σ_k and σ_ϵ are the turbulent Prandtl numbers for k and ϵ, respectively. Their values are: $C_{1\epsilon} = 1.44$, $C_{2\epsilon} = 1.92$, $C_\mu = 0.09$, $\sigma_k = 1.0$, $\sigma_\epsilon = 1.3$. The standard $k-\epsilon$ turbulence model has been used in Chapter 4 and Appendix A.

RNG $k-\epsilon$ Turbulence Model

The RNG $k-\epsilon$ turbulence model [26] has a very similar form to the standard $k-\epsilon$ turbulence model (Eq. 3.19), with the addition of an additional term in the ϵ equation, and a change in the viscosity term on the right hand side of the equations. These equations are as below:

$$\frac{\partial}{\partial t}(\rho k) + \frac{\partial}{\partial x_i}(\rho k u_i) = \frac{\partial}{\partial x_j}\left(\alpha_k \mu_{\text{eff}} \frac{\partial k}{\partial x_j}\right) + G_k - \rho\epsilon - Y_M + S_k, \tag{3.23a}$$

$$\frac{\partial}{\partial t}(\rho \epsilon) + \frac{\partial}{\partial x_i}(\rho \epsilon u_i) = \frac{\partial}{\partial x_j}\left(\alpha_\epsilon \mu_{\text{eff}} \frac{\partial \epsilon}{\partial x_j}\right) + C_{1\epsilon}\frac{\epsilon}{k}G_k - C_{2\epsilon}\rho\frac{\epsilon^2}{k} - R_\epsilon + S_\epsilon. \tag{3.23b}$$

The additional terms (compared to the standard $k-\epsilon$ turbulence model) are R_ϵ, α_k, α_ϵ, and μ_{eff}. The effective viscosity, μ_{eff}, comes from Eq. 3.18, with $C_\mu = 0.0845$. The

inverse effective Prandtl Numbers (α_k and α_ϵ) are calculated from the following equation:

$$\left|\frac{\alpha - 1.3929}{0.3929}\right|^{0.6321} \left|\frac{\alpha + 2.3929}{3.3929}\right|^{0.3679} = \frac{\mu_{\text{mol}}}{\mu_{\text{eff}}}.$$

Finally, the additional term R_ϵ is given below:

$$R_\epsilon = \frac{C_\mu \rho \eta^3 (1 - \eta/\eta_0)}{1 + \beta\eta^3} \frac{\epsilon^2}{k}, \tag{3.24}$$

where $\eta \equiv Sk/\epsilon$, $\eta_0 = 4.38$ and $\beta = 0.012$. The other constants are $C_{1\epsilon} = 1.42$ and $C_{2\epsilon} = 1.68$.

It is claimed in many sources [1] that due to the greater fidelity shown by the development of the RNG model to the flow physics, compared to the standard $k-\epsilon$ turbulence model, it should perform better. It has been used in this thesis in Chapters 4, 5, & 6, as well as in Appendix A. Work which will be presented in Chapter 4 will support this claim for rotational flow.

Realizable $k - \epsilon$ Turbulence Model

The Realizable $k - \epsilon$ turbulence model [51] again seeks to improve upon the standard model. As with all $k - \epsilon$ turbulence models, it works by introducing two turbulent variables k, the turbulent kinetic energy, and ϵ, the turbulence dissipation rate, and gives transport equations for both of these. These equations are as below:

$$\frac{\partial}{\partial t}(\rho k) + \frac{\partial}{\partial x_i}(\rho k u_i) = \frac{\partial}{\partial x_j}\left[\left(\mu + \frac{\mu_t}{\sigma_k}\right)\frac{\partial k}{\partial x_j}\right] + G_k - \rho\epsilon - Y_M + S_k, \tag{3.25a}$$

$$\frac{\partial}{\partial t}(\rho \epsilon) + \frac{\partial}{\partial x_i}(\rho \epsilon u_i) = \frac{\partial}{\partial x_j}\left[\left(\mu + \frac{\mu_t}{\sigma_\epsilon}\right)\frac{\partial \epsilon}{\partial x_j}\right] + \rho C_{1\epsilon} S_\epsilon - C_{2\epsilon}\rho\frac{\epsilon^2}{k + \sqrt{\nu\epsilon}} + S_\epsilon, \tag{3.25b}$$

where $C_1 = \max\left[0.43, \frac{\eta}{\eta+5}\right]$, and $\eta = S\frac{k}{\epsilon}$. As with previous models, the effective viscosity comes from Eq. 3.18. However, in this case, C_μ is not a constant.

$$C_\mu = \frac{1}{A_0 + A_s \frac{kU^*}{\epsilon}}, \tag{3.26}$$

where

$$U^* \equiv \sqrt{S_{ij}S_{ij} + \tilde{\Gamma}_{ij}\tilde{\Gamma}_{ij}}$$

and

$$\begin{aligned} \tilde{\Gamma}_{ij} &= \Gamma_{ij} - 2\epsilon_{ijk}\omega_k, \\ \omega_{ij} &= \overline{\Gamma_{ij}} - \epsilon_{ijk}\omega_k. \end{aligned}$$

where $\overline{\Gamma_{ij}}$ is the mean rate-of-rotation tensor viewed in a rotating reference frame with the angular velocity Ω. The model constants A_0 and A_s are given by $A_0 = 4.04$, $A_s = \sqrt{6}\cos\psi$ where

$$\psi = \frac{1}{3}\cos^{-1}(\sqrt{6}W), \quad W = \frac{S_{ij}S_{jk}S_{ki}}{\tilde{S}^3}, \quad \tilde{S} = \sqrt{S_{ij}S_{ij}}, \quad S_{ij} = \frac{1}{2}\left(\frac{\partial u_j}{\partial x_i} + \frac{\partial u_i}{\partial x_j}\right).$$

It has also been claimed that the Realizable $k-\epsilon$ turbulence model performs better than the standard model. Work presented in Appendix A supports this claim, although it shows no improvement over the RNG $k-\epsilon$ turbulence model. The Realizable $k-\epsilon$ turbulence model has only been used in Appendix A. For completeness it has been included here.

3.5.2 $k-\omega$ Turbulence Models

In the family of $k-\omega$ Turbulence Models [61], the turbulence behaviour is again assumed to be isotropic. They again seek to solve equation 3.17. The difference is now in the equation for the turbulent viscosity, which is computed from the following equation:

$$\mu_t = \alpha^* \frac{\rho k}{\omega}. \tag{3.27}$$

where the term α^* is a low Reynolds number damping coefficient on the turbulent viscosity, which will be given later.

The standard $k-\omega$ model is an empirical model based on model transport equations for the turbulence kinetic energy (k) and the specific dissipation rate (ω), which can also be thought of as the ratio of ϵ to k. The turbulence kinetic energy, k, and the specific

dissipation rate, ω, are obtained from the following transport equations:

$$\frac{\partial}{\partial t}(\rho k) + \frac{\partial}{\partial x_i}(\rho k u_i) = \frac{\partial}{\partial x_j}\left(\gamma_k \frac{\partial k}{\partial x_j}\right) + G_k - Y_k + S_k, \tag{3.28a}$$

and

$$\frac{\partial}{\partial t}(\rho \omega) + \frac{\partial}{\partial x_i}(\rho \omega u_i) = \frac{\partial}{\partial x_j}\left(\gamma_\omega \frac{\partial \omega}{\partial x_j}\right) + G_\omega - Y_\omega + S_\omega. \tag{3.28b}$$

In these equations, γ_k and γ_ω represent the effective diffusivity of k and ω, respectively. They are given by

$$\gamma_k = \mu + \frac{\mu_t}{\sigma_k}, \tag{3.29}$$

$$\gamma_\omega = \mu + \frac{\mu_t}{\sigma_\omega}, \tag{3.30}$$

where σ_k and σ_ω are the turbulent Prandtl numbers for k and ω, respectively. The term α^* is given by the following equation:

$$\alpha^* = \alpha^*_\infty \left(\frac{\alpha^*_0 + \mathrm{Re}_t/R_k}{1 + \mathrm{Re}_t/R_k}\right), \tag{3.31}$$

where

$$\mathrm{Re}_t = \frac{\rho k}{\mu \omega}, \tag{3.32}$$

$$R_k = 6, \tag{3.33}$$

$$\alpha^*_0 = \frac{\beta_i}{3}, \tag{3.34}$$

$$\beta_i = 0.072. \tag{3.35}$$

G_k represents the generation of turbulence kinetic energy due to mean velocity gradients, calculated as in Eq. 3.21, with the turbulent viscosity as given by Eq. 3.27. G_ω represents the generation of ω, and is given by Eq. 3.36:

$$G_\omega = \alpha \frac{\omega}{k} G_k, \tag{3.36}$$

where G_k is given by Eq. 3.21. The coefficient α is given by

$$\alpha = \frac{\alpha_\infty}{\alpha^*}\left(\frac{\alpha_0 + \mathrm{Re}_t/R_\omega}{1 + \mathrm{Re}_t/R_\omega}\right), \tag{3.37}$$

where $R_\omega = 2.95$. α^* and Re_t are given by Eq. 3.31 and Eq. 3.32, respectively. Y_k and Y_ω represent the dissipation of k and ω due to turbulence.

The dissipation of k is given by

$$Y_k = \rho\beta^* f_{\beta^*} k\omega, \tag{3.38}$$

where

$$f_{\beta^*} = \begin{cases} 1 & \chi_k \leq 0 \\ \frac{1+680\chi_k^2}{1+400\chi_k^2} & \chi_k > 0 \end{cases}, \tag{3.39}$$

where

$$\chi_k \equiv \frac{1}{\omega^3}\frac{\partial k}{\partial x_j}\frac{\partial \omega}{\partial x_j}, \tag{3.40}$$

and

$$\beta^* = \beta_i^*\left[1 + \zeta^* F(\mathrm{M}_t)\right], \tag{3.41}$$

$$\beta_i^* = \beta_\infty^*\left(\frac{4/15 + (\mathrm{Re}_t/R_\beta)^4}{1 + (\mathrm{Re}_t/R_\beta)^4}\right), \tag{3.42}$$

$$\zeta^* = 1.5, \tag{3.43}$$

$$R_\beta = 8, \tag{3.44}$$

$$\beta_\infty^* = 0.09, \tag{3.45}$$

where Re_t is given by Eq. 3.32.

The dissipation of ω is given by

$$Y_\omega = \rho\beta f_\beta \omega^2, \tag{3.46}$$

where

$$f_\beta = \frac{1+70\chi_\omega}{1+80\chi_\omega}, \tag{3.47}$$

$$\chi_\omega = \left|\frac{\Gamma_{ij}\Gamma_{jk}S_{ki}}{(\beta^*_\infty\omega)^3}\right|, \tag{3.48}$$

$$\Gamma_{ij} = \frac{1}{2}\left(\frac{\partial u_i}{\partial \mathrm{x}_j} - \frac{\partial u_j}{\partial \mathrm{x}_i}\right). \tag{3.49}$$

The strain rate tensor, S_{ij} is defined in Eq. 3.5.1. Also,

$$\beta = \beta_i\left[1 - \frac{\beta^*_i}{\beta_i}\zeta^* F(\mathrm{M}_t)\right]. \tag{3.50}$$

β^*_i and $F(\mathrm{M}_t)$ are defined by Eq. 3.42 and Eq. 3.51, respectively.

The compressibility function, $F(\mathrm{M}_t)$, is given by

$$F(\mathrm{M}_t) = \begin{cases} 0 & \mathrm{M}_t \leq \mathrm{M}_{t0} \\ \mathrm{M}_t^2 - \mathrm{M}_{t0}^2 & \mathrm{M}_t > \mathrm{M}_{t0} \end{cases}, \tag{3.51}$$

where

$$\mathrm{M}_t^2 \equiv \frac{2k}{a^2}, \tag{3.52}$$

$$\mathrm{M}_{t0} = 0.25, \tag{3.53}$$

$$a = \sqrt{\gamma RT}. \tag{3.54}$$

S_k and S_ω are user-defined source terms. The constants used in the model are: $\alpha^*_\infty = 1$, $\alpha_\infty = 0.52$, $\alpha_0 = \frac{1}{9}$, $\beta^*_\infty = 0.09$, $\beta_i = 0.072$, $R_\beta = 8$.

The standard $k-\omega$ turbulence model has not been used in this thesis, as it has been widely reported to only be acceptable for low-Reynolds number flow, whereas in this thesis the flows are for $1\times10^4 < \mathrm{Re} < 2\times10^6$. It has been presented however in order to provide the basis of a description of the Shear Stress Transport (SST) $k-\omega$ turbulence model, which is given in the following section.

SST $k-\omega$ Turbulence Model

There are some known draw backs of the standard $k-\omega$ turbulence model, primarily for flows with a high Reynolds number [36]. To overcome these, the SST $k-\omega$ turbulence model [35] was developed. It blends the standard $k-\omega$ turbulence model with the standard $k-\epsilon$ turbulence model, essentially using the $k-\omega$ turbulence model as a wall function. The SST $k-\omega$ turbulence model uses the two equations given below:

$$\frac{\partial}{\partial t}(\rho k) + \frac{\partial}{\partial x_i}(\rho k u_i) = \frac{\partial}{\partial x_j}\left(\gamma_k \frac{\partial k}{\partial x_j}\right) + \tilde{G}_k - Y_k + S_k, \tag{3.55a}$$

$$\frac{\partial}{\partial t}(\rho \omega) + \frac{\partial}{\partial x_i}(\rho \omega u_i) = \frac{\partial}{\partial x_j}\left(\gamma_\omega \frac{\partial \omega}{\partial x_j}\right) + G_\omega - Y_\omega + D_\omega + S_\omega. \tag{3.55b}$$

Apart from the addition of the cross diffusion term, D_ω, this equation is, at first inspection, the same as the standard $k-\omega$ turbulence model. The major difference comes through in the equation for the turbulent viscosity, μ_t, which is computed from the following equation:

$$\mu_t = \frac{\rho k}{\omega} \frac{1}{\max\left[\frac{1}{\alpha^*}, \frac{SF_2}{a_1 \omega}\right]}, \tag{3.56}$$

where S is the strain rate magnitude (other variables are given below). With some work, it can be shown that for small values of α^*, which will occur in the near-wall flow, this will be identical to Eq. 3.27, giving the standard $k-\omega$ model. Alternatively, it can also be shown that for large values of $\frac{SF_2}{a_1 \omega}$, the equation for the turbulent viscosity takes the form from the $k-\epsilon$ turbulence model family Eq. 3.18.

In these equations, $\tilde{G}_k$ represents the generation of turbulence kinetic energy due to mean velocity gradients, calculated as described by Eq. 3.66. G_ω represents the generation of ω, calculated as described by Eq. 3.67. Γ_k and Γ_ω represent the effective diffusivity of k and ω, respectively, which are given by

$$\Gamma_k = \mu + \frac{\mu_t}{\sigma_k}, \tag{3.57}$$

$$\Gamma_\omega = \mu + \frac{\mu_t}{\sigma_\omega}, \tag{3.58}$$

where σ_k and σ_ω are the turbulent Prandtl numbers for k and ω, respectively, and

$$\sigma_k = \frac{1}{F_1/\sigma_{k,1} + (1-F_1)/\sigma_{k,2}}, \tag{3.59}$$

$$\sigma_\omega = \frac{1}{F_1/\sigma_{\omega,1} + (1-F_1)/\sigma_{\omega,2}}. \tag{3.60}$$

α^* has been previously defined (Eq. 3.31). The blending functions, F_1 and F_2, are given by

$$F_1 = \tanh\left(\Phi_1^4\right), \tag{3.61}$$

$$\Phi_1 = \min\left[\max\left(\frac{\sqrt{k}}{0.09\omega y}, \frac{500\mu}{\rho y^2 \omega}\right), \frac{4\rho k}{\sigma_{\omega,2} D_\omega^+ y^2}\right], \tag{3.62}$$

$$D_\omega^+ = \max\left[2\rho\frac{1}{\sigma_{\omega,2}}\frac{1}{\omega}\frac{\partial k}{\partial x_j}\frac{\partial \omega}{\partial x_j}, 10^{-10}\right], \tag{3.63}$$

$$F_2 = \tanh\left(\Phi_2^2\right), \tag{3.64}$$

$$\Phi_2 = \max\left[2\frac{\sqrt{k}}{0.09\omega y}, \frac{500\mu}{\rho y^2 \omega}\right], \tag{3.65}$$

where y is the distance to the next surface, and D_ω^+ is the positive portion of the cross-diffusion term (Eq. 3.74).

The term $\tilde{G}_k$ represents the production of turbulence kinetic energy, and is defined as:

$$\tilde{G}_k = \min(G_k, 10\rho\beta^* k\omega), \tag{3.66}$$

where G_k is defined in the same manner as in the standard $k-\omega$"> model Eq. 3.21. The term G_ω represents the production of ω and is given by

$$G_\omega = \frac{\alpha}{\nu_t} G_k. \tag{3.67}$$

For the SST $k-\omega$ model, α_∞ is given by

$$\alpha_\infty = F_1 \alpha_{\infty,1} + (1-F_1)\alpha_{\infty,2}, \tag{3.68}$$

where

$$\alpha_{\infty,1} = \frac{\beta_{i,1}}{\beta^*_\infty} - \frac{\kappa^2}{\sigma_{w,1}\sqrt{\beta^*_\infty}}, \tag{3.69}$$

$$\alpha_{\infty,2} = \frac{\beta_{i,2}}{\beta^*_\infty} - \frac{\kappa^2}{\sigma_{w,2}\sqrt{\beta^*_\infty}}, \tag{3.70}$$

where κ is 0.41.

The term Y_k represents the dissipation of turbulence kinetic energy

$$Y_k = \rho\beta^* k\omega. \tag{3.71}$$

The term Y_ω represents the dissipation of ω, and is defined as

$$Y_\omega = \rho\beta\omega^2. \tag{3.72}$$

Instead of a having a constant value, β is given by

$$\beta = F_1\beta_{i,1} + (1 - F_1)\beta_{i,2}, \tag{3.73}$$

and F_1 is obtained from Eq. 3.61.

In order to blend the the standard $k-\epsilon$ and $k-\omega$ turbulence models together, the standard $k-\epsilon$ turbulence model is 're-written' in a $k-\omega$ formulation. This gives rise to the cross-diffusion term D_ω in Eq. 3.55b, which is given by the following:

$$D_\omega = 2\left(1 - F_1\right)\rho\sigma_{\omega,2}\frac{1}{\omega}\frac{\partial k}{\partial x_j}\frac{\partial \omega}{\partial x_j}, \tag{3.74}$$

S_k and S_ω are user-defined source terms. The other constants are: $\sigma_{k,1} = 1.176$, $\sigma_{\omega,1} = 2.0$, $\sigma_{k,1} = 1.176$, $\sigma_{\omega,1} = 2.0$, $\sigma_{k,2} = 1.0$, $\sigma_{\omega,2} = 1.168$, $\sigma_{k,2} = 1.0$, $\sigma_{\omega,2} = 1.168$ $a_1 = 0.31$, $\beta_{i,1} = 0.075$, $\beta_{i,2} = 0.0828$.

3.5.3 Reynolds Stress Model (RSM)

Mathematically it is better to model the Reynolds Stress directly, instead of assuming that the turbulence is isotropic, approximating and modelling turbulent kinetic energy

and its production or dissipation rate. This form of modelling is more computationally expensive than 'two-equation' turbulence models, but it can produce far more accurate results, in some cases. The transport equation for the Reynolds stress transport is as below (Eq. 3.75).

$$\begin{aligned}\frac{\partial}{\partial t}(\rho\overline{u_i'u_j'}) + \frac{\partial}{\partial x_k}(\rho u_k\overline{u_i'u_j'}) = -\frac{\partial}{\partial x_k}\left[\rho\overline{u_i'u_j'u_k'} + \overline{p\left(\delta_{kj}u_i' + \delta_{ik}u_j'\right)}\right] + \dots \\ \cdots + \frac{\partial}{\partial x_k}\left[\mu\frac{\partial}{\partial x_k}(\overline{u_i'u_j'})\right] - \rho\left(\overline{u_i'u_j'}\frac{\partial u_j}{\partial x_k} + \overline{u_j'u_k'}\frac{\partial u_i}{\partial x_k}\right) - \rho\beta(g_i\overline{u_j'\theta} + g_j\overline{u_i'\theta}) + \dots \\ \cdots + \overline{p\left(\frac{\partial u_i'}{\partial x_j} + \frac{\partial u_j'}{\partial x_i}\right)} - 2\mu\overline{\frac{\partial u_i'}{\partial x_j}\frac{\partial u_j'}{\partial x_i}} - 2\rho\Gamma_k\left(\overline{u_j'u_m'}\epsilon ikm + \overline{u_i'u_m'}\epsilon jkm\right) \quad (3.75)\end{aligned}$$

It is traditionally described as Local Time Derivative + Convection = Turbulent Diffusion + Molecular Diffusion + Stress Production + Buoyancy Production + Pressure Strain + Dissipation + Production by System Rotation. Apart from the Buoyancy Production, the terms on the right hand side of this equation will be dealt with in turn below. Due to gravitational effects not being modelled in this thesis, the buoyancy production will be zero.

Turbulent Diffusion

The turbulent diffusion term is modelled using the following equation

$$-\frac{\partial}{\partial x_k}\left[\rho\overline{u_i'u_j'u_k'} + \overline{p\left(\delta_{kj}u_i' + \delta_{ik}u_j'\right)}\right] = \frac{\partial}{\partial x_k}\left(\frac{\mu_t}{\sigma_k}\frac{\partial\overline{u_i'u_j'}}{\partial x_k}\right) \quad (3.76)$$

The effective viscosity is modelled in the same manner as in the standard $k-\epsilon$ turbulence model, with the same constants (§3.5.1). The turbulent Prandtl number, σ_k, takes a value of 0.82.

Pressure-Strain

The Pressure-Strain term is modelled using the following equation

$$\overline{p\left(\frac{\partial u_i'}{\partial x_j} + \frac{\partial u_j'}{\partial x_i}\right)} = \psi_{ij,1} + \psi_{ij,2} + \psi_{ij,w} \quad (3.77)$$

The three terms on the right hand side of the equation are called the slow pressure-strain (or return to isotropy) term, the rapid pressure-strain term, and the wall reflection term. Slow pressure-strain, $\psi_{ij,1}$, is given by the following equation:

$$\psi_{ij,1} \equiv -C_1 \rho \, \frac{\epsilon}{k} \left[\overline{u_i' u_j'} - \frac{2}{3} \delta_{ij} k \right]. \tag{3.78}$$

where $C_1 = 1.8$. Rapid pressure-strain, $\psi_{ij,2}$, is given by the following equation:

$$\psi_{ij,2} \equiv -C_2 \left[(P_{ij} + F_{ij} - C_{ij}) - \frac{2}{3} \delta_{ij} (P - C) \right] \tag{3.79}$$

where $C_2 = 0.60$.

$$P_{ij} = -\rho \left(\overline{u_i' u_j'} \frac{\partial u_j}{\partial x_k} + \overline{u_j' u_k'} \frac{\partial u_i}{\partial x_k} \right)$$

$$F_{ij} = -2\rho\Gamma_k \left(\overline{u_j' u_m'} \epsilon ikm + \overline{u_i' u_m'} \epsilon jkm \right)$$

$$C_{ij} = \frac{\partial}{\partial x_k} (\rho u_k \overline{u_i' u_j'})$$

$P = \frac{1}{2} P_{kk}$, $G = \frac{1}{2} G_{kk}$, and $C = \frac{1}{2} C_{kk}$. The wall-reflection term, $\psi_{ij,w}$, is responsible for the redistribution of normal stresses near the wall. It tends to damp the normal stress perpendicular to the wall, while enhancing the stresses parallel to the wall. This term is modelled as

$$\psi_{ij,w} \equiv C_1' \frac{\epsilon}{k} \left(\overline{u_k' u_m'} n_k n_m \delta_{ij} - \frac{3}{2} \overline{u_i' u_k'} n_j n_k - \frac{3}{2} \overline{u_j' u_k'} n_i n_k \right) \frac{C_\ell k^{3/2}}{\epsilon d} \tag{3.80}$$

$$+ C_2' \left(\psi_{km,2} n_k n_m \delta_{ij} - \frac{3}{2} \psi_{ik,2} n_j n_k - \frac{3}{2} \psi_{jk,2} n_i n_k \right) \frac{C_\ell k^{3/2}}{\epsilon d} \tag{3.81}$$

where $C_1' = 0.5$, $C_2' = 0.3$, n_k is the x_k component of the unit normal to the wall, d is the normal distance to the wall, and $C_\ell = C_\mu^{3/4} / \kappa$ where κ is the von Kármán constant ($= 0.4187$).

3.6 Boundary Layers and their Modelling

As the name would suggest, a boundary layer in fluid flow is the layer of fluid near to a bounding surface. It is how the bulk flow interacts with solid objects, and vice-versa.

Fluid very close to the object will be moving at the same velocity as the object due to the no-slip condition. As consideration moves away from the boundary, the fluid velocity will tend to the bulk velocity. A boundary layer can either be laminar, transitional, or turbulent. A turbulent boundary layer is traditionally described as having a laminar sub layer, buffer region, and fully-turbulent outer region.

If a simulation is being run with some form of turbulence modelling, then a mechanism is needed for modelling the near-wall behaviour. The problem here lies in the fact that the flow near the wall is laminar; using a turbulence model to simulate this flow will cause inaccurate predictions of the near-wall behaviour. This can cause the overall flow structure to be incorrectly predicted. For this reason, various models for the near wall behaviour have been developed which work in conjunction with the turbulence models to correctly capture the boundary layer, and its effects. Two near-wall flow models have been used in this thesis. Arguably the SST $k-\omega$ turbulence model, Eq. 3.55, is a standard $k-\epsilon$ turbulence model which uses the $k-\omega$ turbulence model to capture the near wall flows. For the purposes of this section though it will not be referred to as a near-wall flow model.

For the work presented in this thesis, the resolution of the near-wall flow is of fundamental importance. The primary variable of concern is the torque on the rotating surface, which is due to the interaction between the fluid and the moving surface of either a cylinder (Appendix A), a cone (Chapter 4), or a gear (Chapters 5 & 6). If the model for the near-wall flow is not able to correctly predict the near-wall flow it will not only skew the flow structures seen, but also, more importantly, it will cause the predictions of the torque to be incorrect, undermining the validity of the results.

Before looking at the two wall functions specifically, it is necessary to explain how the two wall functions act on the turbulent variables. In the $k-\epsilon$ model, the k equation is solved in the whole domain including the wall-adjacent cells. The boundary condition for k imposed at the wall is:

$$\frac{\partial k}{\partial \vec{\mathbf{n}}} = 0 \tag{3.82}$$

where $\vec{\mathbf{n}}$ is the local normal to the wall. The production of turbulent kinetic energy, G_k, and its dissipation rate, ϵ, at the wall-adjacent cells, which are the source terms in

the k equation, are computed on the basis of the local equilibrium hypothesis. Under this assumption, the production of turbulent kinetic energy and its dissipation rate are assumed to be equal in the wall-adjacent control volume. Thus, the production of G_k is computed from

$$G_k \approx \tau_w \frac{\partial U}{\partial y} = \tau_w \frac{\tau_w}{\kappa \rho C_\mu^{1/4} k_P^{1/2} y_P}, \tag{3.83}$$

and ϵ is computed from

$$\epsilon_P = \frac{C_\mu^{3/4} k_P^{3/2}}{\kappa y_P}. \tag{3.84}$$

3.6.1 Standard Wall Functions

The standard wall functions in Fluent are based on the proposal of Launder and Spalding [32]. Two formulae for the stress-strain relationship are utilized depending on the value of y^*, one a log-law for the mean velocity (the so-called 'law of the wall', Eq. 3.85),

$$U^* = \frac{1}{\kappa} \ln(E y^*) \tag{3.85}$$

the other a laminar stress-strain relationship Eq. 3.86,

$$U^* = y^*, \tag{3.86}$$

where E is the energy of the fluid. The log-law is employed when $y^* > 11.225$, the laminar law when $y^* < 11.225$. Reynolds analogy between momentum and energy transport gives a similar logarithmic law for mean temperature. The standard wall functions work reasonably well for a broad range of wall-bounded flows. However, they tend to become less reliable when the flow situation departs too much from the ideal conditions that are assumed in their derivation. Among others, the constant-shear and local equilibrium hypotheses are the ones that most restrict the universality of the standard wall functions.

The standard wall functions have been successfully used throughout this thesis. It is known that if the mesh in the near-wall region produces $y^* \leq 80$, the standard wall function produces reasonable results, which is of benefit, as it means the near-wall mesh doesn't need to be as highly resolved as would be needed (ideally) for an enhanced wall treatment. The drawbacks of having to assume constant-shear and local equilibrium in

the wall adjacent cells will be expanded upon in the relevant chapter later (Chapter 5).

3.6.2 Enhanced Wall Treatment

To have a method that can extend its applicability throughout the near-wall region (i.e., laminar sub layer, buffer region, and fully-turbulent outer region) it is necessary to formulate the law-of-the wall as a single wall law for the entire wall region. Fluent achieves this by blending linear (laminar) and logarithmic (turbulent) laws-of-the-wall using a function suggested by Kader [26]:

$$u^+ = e^{\Gamma} u^+_{\text{lam}} + e^{\frac{1}{\Gamma}} u^+_{\text{turb}} \tag{3.87}$$

where the blending function is given by:

$$\Gamma = -\frac{a(y^+)^4}{1 + by^+} \tag{3.88}$$

and $a = 0.001$ and $b = 5$. Similarly, the general equation for the derivative $\frac{du^+}{dy^+}$ is:

$$\frac{du^+}{dy^+} = e^{\Gamma} \frac{du^+_{\text{lam}}}{dy^+} + e^{\frac{1}{\Gamma}} \frac{du^+_{\text{turb}}}{dy^+} \tag{3.89}$$

This approach allows the fully turbulent law to be easily modified and extended to take into account other effects such as pressure gradients or variable properties. This formula also guarantees the correct asymptotic behaviour for large and small values of y^+ and reasonable representation of velocity profiles in the cases where y^+ falls inside the wall buffer region ($3 < y^+ < 10$). The velocity components, u_{lam} and u_{turb}, are found by integrating the following equations:

$$\frac{du^+_{\text{lam}}}{dy^+} = 1 + \alpha y^+ \tag{3.90}$$

$$\frac{du^+_{\text{turb}}}{dy^+} = \frac{1}{\kappa y^+} \left[S'(1 - \beta u^+ - \gamma (u^+)^2) \right]^{1/2} \tag{3.91}$$

where

$$S' = \begin{cases} 1 + \alpha y^+ & \text{for } y^+ < y_s^+ \\ 1 + \alpha y_s^+ & \text{for } y^+ \geq y_s^+ \end{cases} \tag{3.92}$$

and

$$\alpha \equiv \frac{\nu_w}{\tau_w u^*} \frac{dp}{dx} = \frac{\mu}{\rho^2 (u^*)^3} \frac{dp}{dx} \tag{3.93}$$

$$\beta \equiv \frac{\sigma_t q_w u^*}{c_p \tau_w T_w} = \frac{\sigma_t q_w}{\rho c_p u^* T_w} \tag{3.94}$$

$$\gamma \equiv \frac{\sigma_t (u^*)^2}{2 c_p T_w} \tag{3.95}$$

where y_s^+ is the location at which the log-law slope will remain fixed. By default, $y_s^+ = 60$. An important difference between the standard wall function and the enhanced wall treatment is that the standard wall function does not directly resolve the pressure gradient close to the wall in its calculations.

The enhanced wall treatment has been used in this thesis in Chapters 4 & 5. It has the draw-back of needing much higher resolution in the near-wall region, creating the need for much larger meshes. The direct resolution of the pressure gradients is an aspect of the model which has proved beneficial to some of the work presented here (see Chapter 5).

3.6.3 Boundary conditions for SST $k - \omega$ turbulence Model

In the SST $k - \omega$ model, the boundary conditions for k are the same as in the $k - \epsilon$ model. In Fluent the value of ω at the wall is specified as

$$\omega_w = \frac{\rho (u^*)^2}{\mu} \omega^+ \tag{3.96}$$

The asymptotic value of ω^+ in the laminar sublayer is given by

$$\omega^+ = \min \left(\omega_w^+, \frac{6}{\beta_i (y^+)^2} \right) \tag{3.97}$$

where

$$\omega_w^+ = \begin{cases} \left(\frac{50}{k_s^+}\right)^2 & k_s^+ < 25 \\ \\ \frac{100}{k_s^+} & k_s^+ \geq 25 \end{cases} \tag{3.98}$$

where

$$k_s^+ = \max\left(1.0, \frac{\rho k_s u^*}{\mu}\right) \tag{3.99}$$

and k_s is the roughness height.

In the logarithmic (or turbulent) region, the value of ω^+ is

$$\omega^+ = \frac{1}{\sqrt{\beta_\infty^*}} \frac{du_{\text{turb}}^+}{dy^+} \tag{3.100}$$

which leads to the value of ω in the wall cell as

$$\omega = \frac{u^*}{\sqrt{\beta_\infty^*}\kappa y} \tag{3.101}$$

3.7 Compressibility and Thermal Effects

An important physical concept which occurs in fluid dynamics is that of compressibility. A simple description of compressibility is that as a fluid travels faster it takes up more volume, becoming less dense. If the flow is isentropic, the density of the fluid varies as below:

$$\rho = \rho_0 \left[1 + \frac{(k-1)\text{Ma}^2}{2}\right]^{1/(1-k)},$$

where ρ_0 is the isentropic stagnation density of the fluid (the density of the fluid when brought isentropically to rest), k is the ratio of specific heats, and Ma is the Mach number [60]. Up to Ma = 0.3 the flow can be considered incompressible. For 0.3 < Ma density effects start to become more important. For liquids such as water this means that unless the speeds in the fluid being considered are very high, then the flow can be considered to be incompressible, as the speed of sound in water is $\sim$ 1497 m/s. If the fluid in question is a gas, such as air, compressibility effects need to be considered at much slower speeds: a Mach number of 0.3 equates to a velocity of approximately 100 m/s. The work presented in this thesis considers flows in water and air. Those

in water (Chapter 4 and Appendix A) are at sufficiently low speeds to be considered incompressible (Ma << 0.3). However, those modelled in air (Chapters 5 & 6), although still subsonic, experience Mach numbers of up to 0.8, due to the high angular velocities and the size of the gear. For this reason, some of the work presented in Chapters 5 & 6 is modelled compressible. This is indicated within these chapters.

Numerical modelling of compressibility is relatively straight forward, but it has wide ranging effects on the solution. The model used for the density of the fluid in compressible flow is given by Eq. 3.102:

$$\rho = \frac{p}{\frac{R}{M_w}T} \tag{3.102}$$

where p is the absolute pressure, R is the universal gas constant, and M_w is the molecular weight. The temperature, T, is computed from the energy equation (Eq. 3.103), which forces the use of models for heat transfer in the fluid. The transport of total energy, E, is given by the energy equation (Eq. 3.103):

$$\frac{\partial}{\partial t}(\rho E) + \nabla \cdot (\vec{v}(\rho E + p)) = \nabla \cdot (k_{\text{eff}} \nabla T) \tag{3.103}$$

where k_{eff} is the effective conductivity ($k + k_t$, where k_t is the turbulent thermal conductivity, defined according to the turbulence model being used),

$$E = h - \frac{p}{\rho} + \frac{v^2}{2}, \tag{3.104}$$

h is the enthalpy.

3.8 Moving Reference Frames

When solving the Navier-Stokes equation around a complex, moving geometry, it can prove easier to solve the equation in a reference frame that moves with the geometry. For example, in the case of the models of the gear (Chapters 5 & 6), the solutions are solved within a reference frame that rotates with the gear, eliminating the problem of a mesh that would need to deform around the gear teeth. Additionally, by solving in a reference frame which moves with the gear, then the flow can be considered as steady,

whereas in a stationary reference frame the flow appears transient. Solving in a rotating reference frame causes extra terms to 'appear' in the momentum equation. In cylindrical coordinates the momentum equation (in a stationary reference frame) is

$$\frac{\partial}{\partial t}\rho\vec{v} + \nabla\cdot(\rho\vec{v}_r\vec{v}) = -\nabla p + \nabla\overline{\overline{\tau}} + \vec{F} \tag{3.105}$$

FLUENT allows velocities to be solved that are either relative to the reference frame or absolute velocities. In the first case the momentum equation becomes:

$$\frac{\partial}{\partial t}(\rho\vec{v}_r) + \nabla\cdot(\rho\vec{v}_r\vec{v}_r) + \rho(2\vec{\Omega}\times\vec{v}_r + \vec{\Omega}\times\vec{\omega}\times\vec{r}) = -\nabla p + \nabla\overline{\overline{\tau}}_r + \vec{F} \tag{3.106}$$

For absolute velocities, the momentum equation is:

$$\frac{\partial}{\partial t}\rho\vec{v} + \nabla\cdot(\rho\vec{v}_r\vec{v}) + \rho(\vec{\Omega}\times\vec{v}) = -\nabla p + \nabla\overline{\overline{\tau}} + \vec{F} \tag{3.107}$$

The extra term on the left hand side of Eq. 3.106, $\rho(2\vec{\Omega}\times\vec{v}_r + \vec{\Omega}\times\vec{\omega}\times\vec{r})$ is due to the Coriolis acceleration ($2\vec{\Omega}\times\vec{v}_r$) and the centripetal acceleration ($\vec{\Omega}\times\vec{\Omega}\times\vec{r}$). In the absolute formulation (Eq. 3.107) these terms collapse to give the extra term $\rho(\vec{\Omega}\times\vec{v})$.

3.9 Temporal Effects

In this thesis, simulations have been conducted using both steady-state and transient calculations. In each section of the thesis, it will be made clear as to whether the flow has been assumed steady-state or transient.

Assuming the flow is steady-state makes the solution of the Navier-Stokes equations slightly easier, with an implicit solution of the equations relatively easy to find. However, as has been suggested in previous sections, it is possible for the flow that is being resolved to vary in time, whatever reference frame it is being solved in. Whilst the overall flow may possess a steady-state, some features of the flow may be time dependent. This leads to the need to solve the Navier-Stokes equations in time as well as space. Temporal effects are shown to be of importance in two chapters of this thesis (Chapters 5 & 6).

Through the use of transient simulations, both sections show flows which have a transient nature within a quasi steady-state. The first of these is vortices being shed from the teeth of an unshrouded gear, the latter being recirculations under the shroud in some of the shrouded cases.

3.10 Mesh Generation and Independence

This thesis covers the modelling of the fluid flow in four different settings which vary greatly. Greater detail of the individual meshes used will be given in each chapter. Structured and unstructured meshes were used during the course of the work presented in this thesis. In this section a description of what these terms mean will be given.

A structured mesh in two or three dimensions has grid lines in 2 or 3 coordinate directions which are orthogonal in the computational space, making each cell a rectangle or hexahedron. Unstructured meshes are not restricted to being orthogonal and are formed of cells that can take any shape. When the geometry of the domain in question is complex, it can be difficult to fit a structured mesh throughout the entire domain, whereas an unstructured mesh, by its very nature, can fit to any geometry.

The decision to use an unstructured mesh instead of a structured mesh can be due to necessity, due to the time necessary to subdivide a domain into sections that can be meshed in a structured manner. The numerical implications of using a structured mesh are that it is possible for the solution to 'align' to the grid structure. Unstructured meshes allow smoother changes in the mesh density to be built into the solution, allowing the mesh to 'grow', whereas a structured mesh can have significant changes in size. It is also easier to manage the aspect ratio of cells in an unstructured mesh due to this ability for growth. This growth is managed through size functions. A size function specifies how the distance between nodes varies within the mesh. With an unstructured mesh, they are a mechanism for increasing the mesh density in the boundary layer.

Another issue that needs to be considered with the meshes, be they structured or unstructured, is that of mesh independence. Mesh independence can be said to have been achieved when changes in mesh density have no effect on the flow structure or the bulk properties. It does not imply that the solution will be an accurate prediction of the

flow structure, but is a necessary condition.

3.11 Boundary Conditions

In this section, a description of the boundary conditions which have been applied in this thesis will be given. These include walls, pressure inlets, pressure outlets, mass-flow inlets, axis, and periodic boundaries.

3.11.1 Walls

A wall represents a solid surface, such as the cone and conical shroud in Chapter 4; the gear, stub-shaft and back-wall in Chapter 5; and the gear, stub-shaft, shroud and back-wall in Chapter 6. In all the simulations conducted in this thesis, walls have been used to form some of the boundaries to the domain. They fall into two categories (stationary and moving), but their effect on the solution is identical. The turbulence boundary conditions at a wall have been given in Section 3.6. Velocities on a wall node are the same as the wall velocity. In cylindrical coordinates this means that for wall nodes on a surface that is rotating with angular velocity Ω rad $s^{-}1$ (but not moving in either the axial or radial directions) the nodes will have velocity components of $u_r = 0$, $u_\theta = \Omega$, and $u_z = 0$.

3.11.2 Pressure Inlets and Outlets

A pressure inlet represents a non-physical boundary to the domain, that are often used to simulate a pressure source linked to the simulation, such as the room the unshrouded gear is situated in in Chapter 5. They can be used to create a pressure difference across the domain. Generally they are used in areas where it is known that flow will enter the domain, although they do allow flow to leave the domain. In Chapters 5 & 6 pressure inlets have been used to simulate atmospheric conditions. Numerically, a pressure boundary works in two ways. For a pressure inlet, a total pressure is defined at the inlet, along with turbulent quantities, such as the turbulence intensity and hydraulic diameter. A 'dummy' layer of cells, equal in size to the layer of cells at the boundary is extruded in the normal direction the boundary. Using the pressure and turbulent

quantities defined at the inlet and the pressure and turbulent quantities that have been calculated at the first set of nodes inside the domain, an iterative process is used to calculate the mass flux across the inlet.

A pressure outlet is very similar to a pressure inlet, differing in two manners. Instead of specifying a total pressure, a static pressure, relative to the operating pressure in the domain, is given. Additionally, it is possible to target a mass flow out of the domain, through the outlet. In the same way as for a pressure inlet, a 'dummy' layer of cells, equal in size to the layer of cells at the boundary is extruded in the normal direction the boundary. Using the pressure, turbulent quantities, and desired mass flux defined at the outlet and the pressure and turbulent quantities that have been calculated at the first set of nodes inside the domain, an iterative process is used to calculate the mass flux across the outlet.

3.11.3 Mass Flow Inlet

Mass flow inlets allow the mass flux across a boundary to be specified, whilst the pressure varies. In a similar manner to the pressure inlet, a 'dummy' layer of cells, equal in size to the layer of cells at the boundary is extruded in the normal direction the boundary. Using the mass flow and turbulent quantities defined at the inlet and the mass flow and turbulent quantities that have been calculated at the first set of nodes inside the domain, an iterative process is used to calculate the total pressure at the inlet.

3.11.4 Periodic Boundary

A periodic boundary is another non-physical boundary that can be used. In settings where there is translational or rotational symmetry, it allows the domain to be simplified by imposing this symmetry upon the domain. Periodic boundaries have been used throughout the work in this thesis: for example, in Chapter 6 the domain has been simplified to model the domain around one tooth, reducing the computational volume to a 91^{st} of the full domain, by using a pair of rotationally periodic boundaries. Numerically they work by linking one 'side' of the domain to the other. The restriction they apply upon the meshes generated is that the mesh on each side of the boundary must

be identical, so that the join between the two sides of the domain is seamless.

3.11.5 Axis

An axis boundary condition is used where an axis of revolution is included in the computational domain. It has been used in Chapters 4 & 5. They are a form of symmetry boundary, in that the values of all the solution variables on the axis are given by the values in the adjacent cell.

3.12 Solution Technique and Convergence Criteria

During the course of this work, experience has been gained as to how to run the simulations, leading to a solution technique. This is as follows.

To simulate the transient flow (not all of the simulations have been conducted unsteady) in any of the settings, the flow field must first be initialized in one of four ways. It can be set to be absolutely stationary, or set to be stationary relative to the moving reference frame. Other possibilities which help in developing a solution are to temporarily set the rotational speed of the reference frame to some fraction of the desired speed, initializing the flow to this speed, and then re-set the reference frame to the desired speed. Alternatively, in a situation where there already exists data for an identical domain produced using a different mesh, FLUENT allows an initial flow field to be extrapolated from the pre-existing solution. This means that the initial flow-field is very close to the converged solution.

After initialization in one of the four forms described above, the model is then run in a steady-state formulation, with the flow assumed incompressible. Once the solution is deemed to have converged, the flow is then set to be compressible, and again run on to convergence. From this point the simulation can then be run transient. If the Enhanced Wall Treatment is to be used, it has been found easier to achieve a converged solution if initial calculations are started with the Standard Wall Functions, the solution is converged, and then switched to Enhanced Wall Treatment, usually before switching from incompressible to compressible flow.

At this point, if a mass-flow through the domain is to be imposed, if desired it can

be increased. Similarly, if the angular velocity needs to be increased, this is again a good time for changing this, though it usually helps to return to a steady-state setting at this point.

Solution convergence has been monitored in two manners. Primarily, the values of residuals (continuity, velocities, and turbulent quantities) have been monitored in order to observe whether they are reducing, staying constant, fluctuating steadily or increasing. Fluent utilizes so called 'scaled' residuals. The residual of continuity is the sum over all cells of the absolute mass flux in each cell after N iterations, divided by the sum over all cells of the positive mass flux in each cell after 5 iterations. In the first 5 iterations the residual of continuity is reported as being 1. The residual of, respectively, the velocity components and the turbulent quantities is the sum over all cells of the imbalance of, respectively, the velocity components and turbulent quantities in each cell, divided by the sum over all cells of, respectively, the velocity components and turbulent quantities in each cell. The convergence has also been monitored by monitoring the torque levels on the rotating surfaces. In the steady-state cases convergence has been deemed to be achieved when the torque levels over 200 iterations vary by less than 3% and all the residuals have values less than 10^{-4}, with the residuals of the turbulent quantities have values less than 10^{-6}. In transient cases a similar approach has been used to see whether the models have reached a quasi steady-state by monitoring the torque levels over many time steps, though the amount depends on the time step size, and how that relates to the flow dynamics.

3.13 Summary

In this chapter, the theoretical grounding of the numerical models which have been used in this thesis has been given. This started by looking at the fundamental equations of fluid dynamics, the Navier-Stokes equations (Eq. 3.1). These equations describe the variation of pressure and velocity across the domain and over time. Few solutions exist for these equations, leading to the field of CFD. A description of how the commercial CFD code FLUENT solves the Navier-Stokes equations is given, with details of the numerical discretisation schemes that have been applied given in Section 3.3. The concept

of turbulence (stochastic fluctuations in the flow variables) has been introduced (§3.4). In simulations of turbulent flow, modelled in manners other than direct numerical simulation, the turbulence has to then be modelled. Descriptions of the turbulence models that have been used in this thesis have been given (§3.5). Within this thesis, through the development of a modelling strategy, answers to the following question will be sought to be presented. The flow needs to be modelled using some form of turbulence modelling, but which model should be used? Should a two-equation $k-\epsilon$ or $k-\omega$ turbulence model be used, or should an attempt be made to use the more complex Reynolds Stress Model? The two-equation models impose certain assumptions on the flow which whilst being reasonable assumptions, may turn out to be physically incorrect. An assessment of this question will be made in Chapter 4.

If turbulence must be modelled, then consideration must also be made to the resolution of the boundary layers which exist in the flow. A short description of boundary layers, and how they are modelled, has been given in Section §3.6. This leads to another question, how to resolve the near-wall flow? Again, it needs to be seen whether a numerically simpler model can produce results of sufficient accuracy to eliminate the need to use more complex, potentially more accurate model. This question has not been fully answered within this thesis, with arguments supporting both types of near-wall model presented.

The problems of compressibility and thermal effects have been discussed in section §3.7. It is clear that in some cases compressibility will indeed need to be modelled, which forces the modelling of the energy equation, giving rise to thermal effects. Throughout this thesis, all cases involving water have been modelled incompressible. For cases where the working fluid is air, it has been stated whether the flow has been modelled compressible or not.

Another pair of questions which this thesis will attempt to answer are due to the resolution of the solution in space and time. Should the settings be modelled using structured meshes, or can unstructured meshes be used? The former should give swifter convergence; the latter can be easier to create, especially for complex geometries like a spiral bevel gear. Throughout this thesis examples will be seen of both styles of meshes.

A related question is whether the flow needs to be resolved using a transient solver, or can the flow be assumed steady-state? The ability to model the flow as steady-state will allow much shorter computational times, but features that are inherently transient, such as vortices being shed from a gear tooth, may be difficult to capture, unless a transient formulation is used. A description of the style of meshes used has been given (§3.10), and the importance of temporal resolution has been discussed (§3.9).

The first aim of this thesis is develop and validate a modelling strategy for the flow around a shrouded spiral bevel gear. As this has been developed with each stage of work presented in this thesis, the development of the strategy has been given in Chapter 7.

Chapter 4

Computational Investigation of Torque on a Shrouded Rotating Cone

4.1 Introduction

A shrouded rotating cone represents an approximation to the geometry of a shrouded spiral bevel gear. In this chapter, a computational study of the flow around a shrouded rotating cone is presented and the data is compared to available experimental data [69–71][1]. The models are generated using a basic modelling strategy, developed in Appendix A. Results are compared for combinations of varying throughflow rates, cone vertex angles, non-dimensional gap widths, and angular velocities with experimental data. Good agreement of the computational data with the experimental data is obtained. The effect of different turbulence models and computational wall treatments is examined. Comparisons are made between two-dimensional and three-dimensional models, in order to assess the effect of imposing rotational periodicity on the flow. The work allows the first steps in the development of the strategy for modelling a shrouded spiral bevel gear to be made.

A description of the physical background to the work is presented in §4.2, with a

[1] Most of the work contained in this chapter has been published in the Journal of Fluids Engineering [49]

summary of the methodology that has been used given in §4.3, with results and discussion in §4.4. Conclusions are presented in §4.6.

4.2 Physical Background

The geometry in the physical setting is identical (except for an assumption on the inlet size) to that used by Yamada & Ito [69–71], and is shown in Fig. 4.1. It involves a cone of varying vertex angle rotating inside a conical shroud. The fluid used by Yamada & Ito was water. The water enters through an inlet, before impacting on the apex of the rotating inner cone. The physical cases modelled are described in Table 4.1.

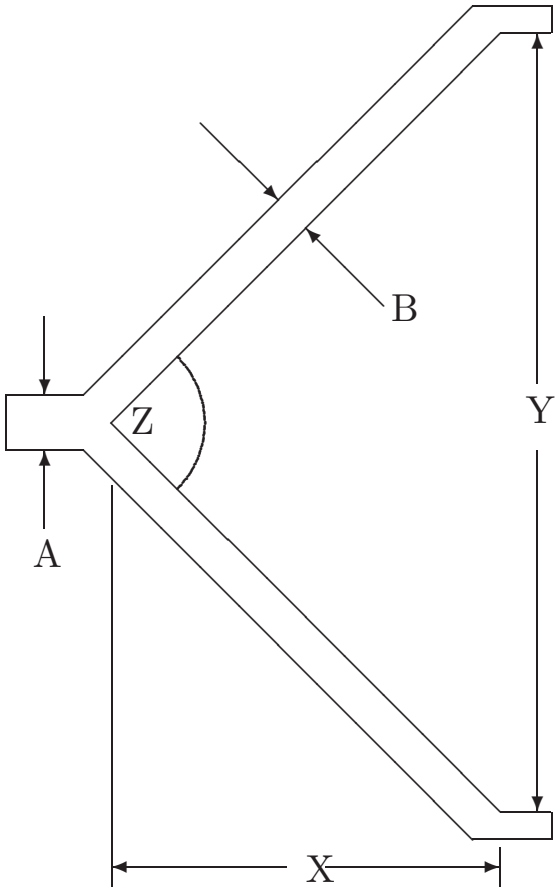

Figure 4.1: Schematic of Rotating Cone Geometry.

Case	X (m)	Y (m)	Z (rad)	A (mm)	B	Data Source
1	0.06275	0.125	$\pi/2$	4	0.008	[69–71]
2	0.06275	0.125	$\pi/2$	4	0.016	[69–71]
3	0.03623	0.125	$2\pi/3$	4	0.016	[69, 70]

Table 4.1: Physical Settings. Dimensions are as in Fig. 4.1

4.3 CFD Methodology

Calculations of the fluid flow field (the fluid in question being water) and associated torques are obtained for a shrouded cone. The geometrical information for the shrouded cones used in the study is given in Table 4.1. The study uses two and three-dimensional computational fluid dynamics (CFD) to calculate the fluid flow and subsequent friction and turbulence losses for three configurations of shrouded cone. Computations have been carried out using two-dimensional and three-dimensional models. The two-dimensional models assume axisymmetry within the flow. Two different three-dimensional models were developed, one representing a rotationally periodic volume incorporating a 6° wedge on the shroud and cone, whilst the other represented the entire three-dimensional setting. The geometry (Fig. 4.1) matches that used in Yamada & Ito [71], although some assumptions were necessary regarding the diameter of the inlet, as no information is given in the paper. By scaling drawings on the apparatus contained in [69–71], it was assumed that the inlet was of diameter 4 mm, as this dimension is not given in these papers. Steady state solutions for the single-phase fluid flow field have been obtained using the commercial CFD codes FLUENT 6.2.16 & 6.3.17. Simulations are performed using a rotating frame of reference and the absolute velocity formulation. Computations correspond to rotation rates, Ω, within the range 3 rad $s^{-1} \leq \Omega \leq 112$ rad s^{-1}. Turbulence is modelled using the standard $k-\epsilon$ model [31], as well as the RNG version [63, 64], the SST $k-\omega$ model [61], and the Reynolds Stress Model [21, 29, 30]. The governing equations were discretized using a second order upwind differencing scheme. Near-wall behaviours were captured through the standard wall function and the enhanced wall treatment, with comparisons made between the performances of each. Descriptions of all these models, and the theory behind them, is given in Chapter 3.

As will be shown later, an apparent transition from laminar to turbulent flow exists

in the experimental data of Yamada & Ito. Due to the geometry of the cone, the rotating flow (ignoring throughflow effects temporarily) near the inlet has a low rotating Reynolds number, suggesting laminar flow. At the outer radius of the cone, near the outlet, the flow has a high rotating Reynolds number, suggesting turbulent flow. In order to model the entire domain without artificially imposing a laminar solution on part of the domain, the entire flow has been modelled as turbulent.

4.3.1 Boundary, Operating Conditions and Meshes

In all cases, the flow is assumed to be steady state and isothermal. The fluid is assumed incompressible, as the tip velocity of the cone, even at the highest rotational rate, is only 0.0097 Mach.

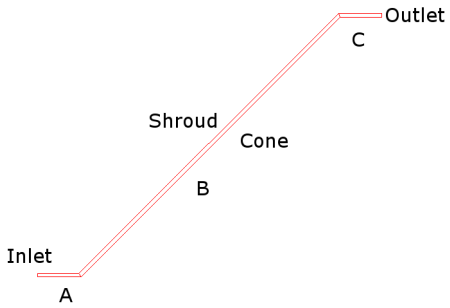

Figure 4.2: Schematic Diagram, Showing a Cross Section of the Model.

A cross sectional view of the geometry is shown in Fig. 4.2. Water enters through a stationary, cylindrical, inlet duct, passes through the shrouded cone, and exits axially through the outlet. A mass flow inlet, located 0.0214 m upstream of the cone vertex, is used at the upstream axial boundary to prescribe the flow entering the system. Turbulence quantities are calculated by turbulence intensity and hydraulic diameter. The intensity is chosen as 10%, the hydraulic diameter comes from the diameter of the inlet pipe, which is 4 mm. A pressure outlet is specified at the outlet. This is used as it allows fluid to enter or leave the domain only due to the pressure difference across this boundary, so any flow across this boundary will be due to either the imposed throughflow rate and/or possible recirculations in the outlet region induced by the rotation of the cone upon the fluid. The cone is modelled as a rotating wall with a no-slip condition applied. The shroud is modelled as a stationary wall with a no-slip condition applied.

Name	ϕ	s	A	B	C	Cell count
Mesh 1	90°	0.016	Triangular	Quadrilateral, with boundary layer	Triangular	25,740
Mesh 2	90°	0.016	Triangular	Triangular, with boundary layer	Triangular, with boundary layer	24,482
Mesh 3	90°	0.008	Triangular	Triangular, with boundary layer	Triangular, with boundary layer	106,604
Mesh 4	90°	0.008	Quadrilateral	Quadrilateral, with boundary layer	Quadrilateral, with boundary layer	56,223
Mesh 5	120°	0.016	Triangular	Triangular, with boundary layer	Triangular, with boundary layer	36,324
Mesh 6 (3D, 6° wedge shape Slice)	90°	0.016	Tetrahedral	Tetrahedral Hybrid, with Hexahedral Core	Hexahedral Map	1,343,856
Mesh 7 (3D, 360°)	90°	0.016	Hexahedral Wedge	Tetrahedral Hybrid, with Hexahedral Core	Hexahedral Wedge	1,800,000

Table 4.2: CFD meshes used

The geometry is shown schematically in Fig. 4.2.

4.3.2 Mesh Structure

Different meshes were used in order to demonstrate grid independence. These were as described in Table 4.2.

A series of 5 cases where run, as detailed below

1. $\phi = 120°$, $s = 0.016$, $C_Q = 0$, varying Ω (Mesh 5)
2. $\phi = 90°$, $s = 0.016$, $C_Q = 0$, varying Ω (Mesh 1)
3. $\phi = 90°$, $s = 0.008$, $C_Q = 0$, varying Ω (Mesh 3)
4. $\phi = 90°$, $s = 0.008$, $C_Q = 1500$, varying Ω (Meshes 3 & 4)
5. $\phi = 90°$, $s = 0.016$, $C_Q = 1500$, varying Ω (Mesh 1, 2, 6 & 7)

For all cases, the flow is initialized to be stationary. The throughflow rate is defined as $C_Q = Q/R_i\nu$. For the cases where $C_Q = 0$, the mass-flow rate through the inlet

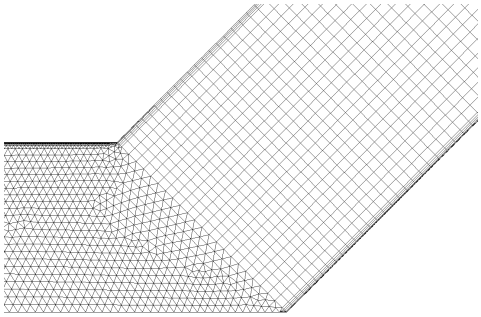

Figure 4.3: Close up of mesh structure near cone vertex.

is specified to be zero. Whilst the apex of the inner cone appears to be a singularity point within the domain (Fig. 4.3), and caused numerous problems in meshing the three-dimensional models, it is not a problem numerically. The equations are solved in a rotating frame, so the flow over the apex becomes akin to flow round a corner. All the simulations, except those for Mesh 7, were computed on a computer with a Pentium 4, 3.40GHz with 2.0 GB of RAM. Calculations for Mesh 7 were computed on the High Performance Cluster installed at the University of Nottingham, running Fluent in parallel on up to 18 computing nodes. Each node is a dual Opteron 248 processer, 2.2GHz with 2.0GB of RAM.

Mesh independence has been checked in two ways. Firstly, the mesh is adapted on y^* until it is within acceptable levels ($0 < y^* < 4$) for the use of enhanced wall functions, whilst checking whether the refinement has any effect on the moment reported. Secondly, to check that the solutions are independent of the style of grid used, for each mesh an individual throughflow rate has been chosen for which some of the work has been conducted using the two different meshes and the results compared. In each case, the overall difference between the different meshes has been negligible, so mesh independence has been achieved.

4.4 Results

In this section, results will be presented, describing the various parameters used, and demonstrating the effect changing each parameter has on the moment coefficient. The

parameters which have been changed are the cone vertex angle (ϕ), the non-dimensional gap width (s), the throughflow (C_Q), and the angular velocity (Ω). The results are split into four sections, those where the effect of throughflow has not been considered (§4.4.1), and those where their effect has been considered, firstly in two dimensions (§4.4.2), and then three dimensionally (§4.4.3). The final section presents details of the flow structure (§4.5).

4.4.1 No throughflow

This section presents the results for which no throughflow was present. All the work in this section is from two-dimensional simulations. The parameter that has been varied in this section is the cone vertex angle, in order to see the ability of different turbulence models to replicate the experimental data available for these two cases. Both cases are presented with varying angular velocity.

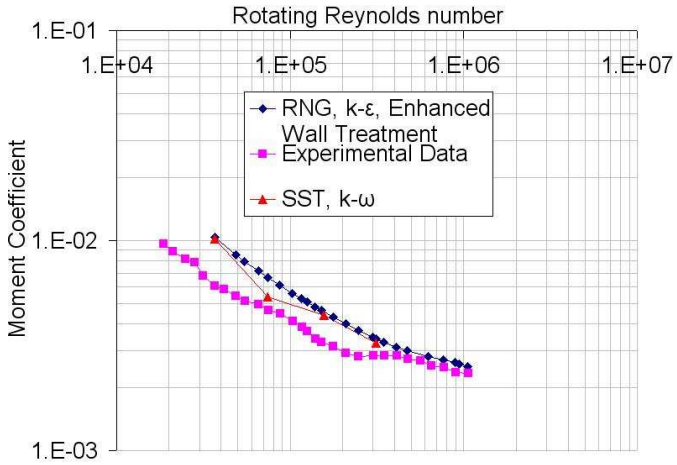

Figure 4.4: Graph of Rotating Reynolds Number (Re) against Moment Coefficient (C_M), for a Vertex Angle of $\phi = 120°$, Non-dimensional Gap Width $s = 0.016$, and no Throughflow ($C_Q = 0$).

Figure 4.4 presents a graph of rotating Reynolds number (Re) against moment coefficient (C_M), for a vertex angle of $\phi = 120°$, a non-dimensional gap width $s = 0.016$ and no throughflow ($C_Q = 0$), calculated on Mesh 5.

A transition is visible in the experimental data over the range $249,000 \leq \text{Re} \leq 475,000$. Before the transition the quantitative agreement between the RNG $k - \epsilon$ turbulence model, with enhanced wall treatment, and the experimental data is weak,

with the moment coefficient being consistently over estimated. The best agreement is found for Re $= 248,000$, where the percentage difference, $C_{\%} = 33\%$. The worst agreement is found for Re $= 37,000$, where the percentage difference is 70%. Before the transition, the quantitative agreement between the $k-\omega$ turbulence model and the experimental data is better than with the RNG $k-\epsilon$ turbulence model, with the moment coefficient being consistently over estimated. The best agreement is found for Re $= 75,000$, where the percentage difference is 16%. The worst agreement is found for Re $= 37,000$, where the percentage difference is 67%.

After the transition, the quantitative agreement between the RNG $k-\epsilon$ turbulence model, with enhanced wall treatment, and the experimental data greatly improves. The best agreement is found for Re $= 1,057,000$, where the percentage difference is 7.8%. The worst agreement is found for Re $= 893,000$, where the percentage difference is 11%. The $k-\omega$ turbulence model was not used for calculations after the transition in this case. As there is no experimental data available from Yamada & Ito [69–71] for the case of $\phi = 120°$ with throughflow, results are only presented for the case with no throughflow.

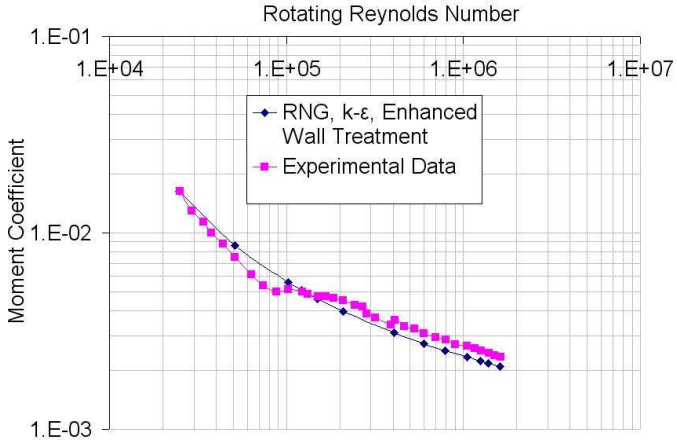

Figure 4.5: Graph of Rotating Reynolds Number (Re) against Moment Coefficient (C_M), for a Vertex Angle of $\phi = 90°$, Non-dimensional Gap Width $s = 0.008$, and no Throughflow ($C_Q = 0$).

Figure 4.5 presents a graph of rotating Reynolds number (Re) against moment coefficient (C_M), for a vertex angle of $\phi = 90°$, non-dimensional gap width $s = 0.008$, and no throughflow ($C_Q = 0$), calculated on Mesh 3. A transition is visible in the experimental data over the range $88,000 \leq \text{Re} \leq 210,000$, in the same manner as that seen in Fig. 4.4. Across the entire range of the experimental data the quantitative agreement between the

RNG $k-\epsilon$ turbulence model, with enhanced wall treatment, and the experimental data is good. The best agreement is found for $\mathrm{Re} = 25,000$, where the percentage difference is 0.6%. The worst agreement is found for $\mathrm{Re} = 406,000$, where the percentage difference is 14%.

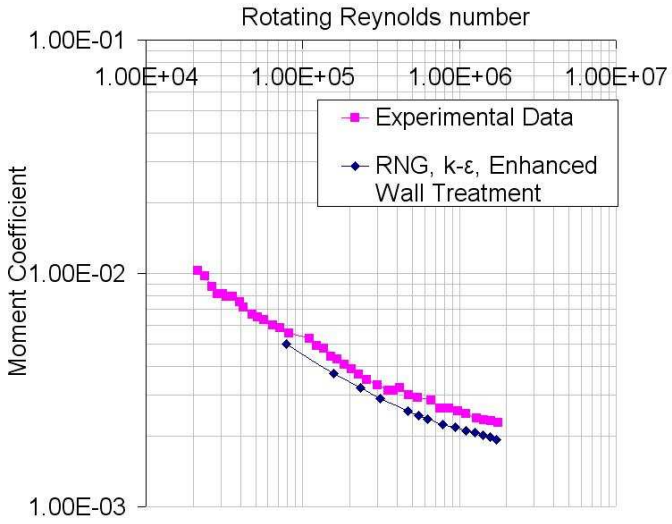

Figure 4.6: Graph of Rotating Reynolds Number against Moment Coefficient, for a Vertex Angle of $\phi = 90°$, Non-dimensional Gap Width $s = 0.016$ and no Throughflow ($C_Q = 0$).

Figure 4.6 shows a graph of rotating Reynolds number (Re) against moment coefficient (C_M), for a vertex angle of $\phi = 90°$, non-dimensional gap width $s = 0.016$, and no throughflow ($C_Q = 0$), calculated on Mesh 1. A transition is visible in the experimental data over the range $47,000 \leq \mathrm{Re} \leq 110,000$. Across the entire range of the experimental data the quantitative agreement between the RNG $k-\epsilon$ turbulence model, with enhanced wall treatment, and the experimental data is good. The best agreement is found for $\mathrm{Re} = 47,000$, where the percentage difference is 2.7%. The worst agreement is found for $\mathrm{Re} = 627,000$, where the percentage difference is 17%.

To summarize, it has been shown that, for the cases with no throughflow and a 90° vertex angle, there is good numerical agreement between the CFD and the experimental data, with torque levels predicted to within 17% by the RNG $k-\epsilon$ turbulence model, with enhanced wall treatment. The agreement at the wider vertex angle is not so good, with torque levels predicted by the RNG $k-\epsilon$ turbulence model, with enhanced wall treatment, within 70% of the experimental data.

4.4.2 Throughflow, Two Dimensional Models

This section presents the results for which throughflows were present, and is followed by a section where the same cases were computed in three dimensions.

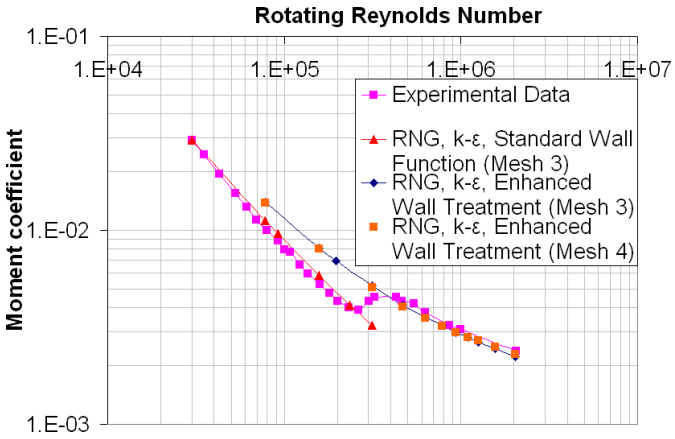

Figure 4.7: Graph of Moment Coefficient (C_M) against Rotating Reynolds Number (Re), for a Vertex Angle of $\phi = 90°$, Non-dimensional Gap Width $s = 0.008$ and Non-dimensional Throughflow $C_Q = 1500$.

Figure 4.7 presents a graph of moment coefficient (C_M) against rotating Reynolds number (Re), for a vertex angle of $\phi = 90°$, non dimensional gap width $s = 0.008$ and non-dimensional throughflow $C_Q = 1500$, calculated on meshes 3 and 4. A transition, more marked than in the cases without throughflow, is visible in the experimental data over the range $200,000 \leq \text{Re} \leq 464,000$. Before the transition the quantitative agreement between the RNG $k - \epsilon$ turbulence model, with enhanced wall treatment, and the experimental data is weak, with the moment coefficient being consistently over estimated. The best agreement is found for $\text{Re} = 78,000$, where the percentage difference is 39%. The worst agreement is found for $\text{Re} = 196,000$, where the percentage difference is 62%. Before the transition the quantitative agreement between the RNG $k - \epsilon$ turbulence model, with standard wall functions, and the experimental data is strong. The best agreement is found for $\text{Re} = 30,000$, where the percentage difference is 0.6%. The worst agreement is found for $\text{Re} = 78,000$, where the percentage difference is 12%.

After the transition, the quantitative agreement between the RNG $k - \epsilon$ turbulence model, with enhanced wall treatment, and the experimental data greatly improves. The best agreement is found for $\text{Re} = 470,000$, where the percentage difference is 4%. The worst agreement is found for $\text{Re} = 1,567,000$, where the percentage difference is 9.4%.

The RNG $k-\epsilon$ turbulence model, with standard wall functions, was not used for calculations after the transition in this case.

In order to see if the results are independent of the mesh used (Mesh 3), an alternative mesh (Mesh 4) was used to replicate the work performed by the original mesh (Mesh 3), using the RNG $k-\epsilon$ turbulence model, with enhanced wall treatment. It can be observed that the behaviour of these models is very similar, with the difference between the moment coefficient predicted by the two meshes being $\pm 3\%$.

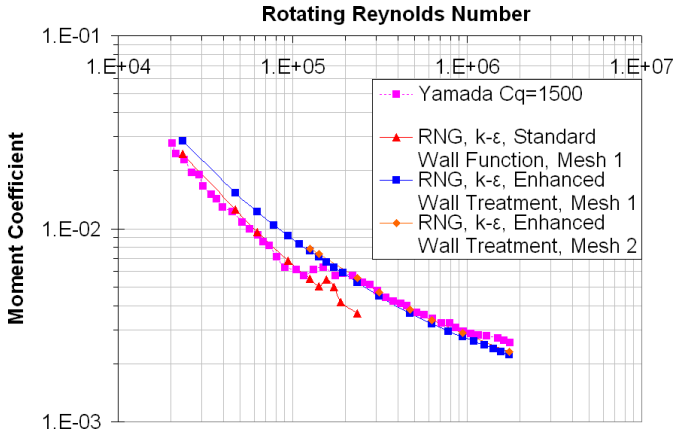

Figure 4.8: Graph of Moment Coefficient (C_M) against Rotating Reynolds Number (Re), for a Vertex Angle of $\phi = 90°$, Non-dimensional Gap Width $s = 0.016$, and Non-dimensional Throughflow $C_Q = 1500$.

Figure 4.8 presents a graph of moment coefficient (C_M) against rotating Reynolds number (Re), for a vertex angle of $\phi = 90°$, this time with a larger non dimensional gap width of $s = 0.016$ and non-dimensional throughflow $C_Q = 1500$, calculated on meshes 1 and 2. A transition is visible in the experimental data over the range $117,000 \leq \mathrm{Re} \leq 221,000$. As in Fig. 4.7, before the transition the quantitative agreement between the RNG $k-\epsilon$ turbulence model, with enhanced wall treatment, and the experimental data is weak, with the moment coefficient being consistently over estimated. The best agreement is found for $\mathrm{Re} = 24,000$, where the percentage difference is 25%. The worst agreement is found for $\mathrm{Re} = 78,000$, where the percentage difference is 45%. Before the transition the quantitative agreement between the RNG $k-\epsilon$ turbulence model, with standard wall functions, and the experimental data is strong. The best agreement is found for $\mathrm{Re} = 63,000$, where the percentage difference is 4.1%. The worst agreement is found for $\mathrm{Re} = 94,000$, where the percentage difference is 13%.

After the transition, as before, the quantitative agreement between the RNG $k-\epsilon$ turbulence model, with enhanced wall treatment, and the experimental data greatly improves. The best agreement is found for $\mathrm{Re} = 470,000$, where the percentage difference is 4.6%. The worst agreement is found for $\mathrm{Re} = 1,746,000$, where the percentage difference is 14%. The RNG $k-\epsilon$ turbulence model, with standard wall functions, was not used for calculations after the transition in this case.

Again, for the purposes of mesh independence, an alternative mesh (Mesh 2) was used to replicate the work performed by the original mesh (Mesh 1), using the RNG $k-\epsilon$ turbulence model, with enhanced wall treatment. It can be observed that the behaviour of these models is very similar, with a maximum percentage difference in moment coefficient of 5%.

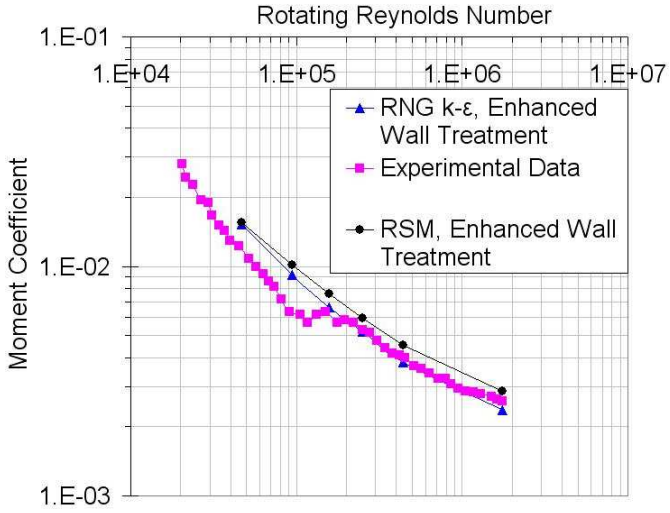

Figure 4.9: Graph of Moment Coefficient (C_M) against Rotating Reynolds Number (Re), for a Vertex Angle of $\phi = 90°$, a Non-dimensional Gap Width of $s = 0.016$ and a Non-dimensional Throughflow of $C_Q = 1500$, showing the Effect of using Different Turbulence models.

In Fig. 4.9 the relative performance of the Reynolds Stress Model and the RNG $k-\epsilon$ turbulence model, with enhanced wall treatment, is presented, calculated on mesh 1, for the same case presented in Fig. 4.8. Over the entire range of the experimental data, it can be observed that RSM model, with enhanced wall treatment, does not perform as well as the RNG $k-\epsilon$ turbulence model, with enhanced wall treatment. Before the transition the quantitative agreement between the RSM model, with enhanced wall treatment, and the experimental data is weak, with the moment coefficient being consistently over

estimated. After the transition, the quantitative agreement between the RSM model, with enhanced wall treatment, and the experimental data greatly improves. The best agreement is found for Re $= 1,746,000$, where the percentage difference is 10%. The worst agreement is found for Re $= 439,000$, where the percentage difference is 14%. Its performance, in terms of accuracy, over the speed range considered, is similar to the RNG $k-\epsilon$ turbulence model, though it can also be observed that with increasing Reynolds number (Re), the performance of the RSM model improves.

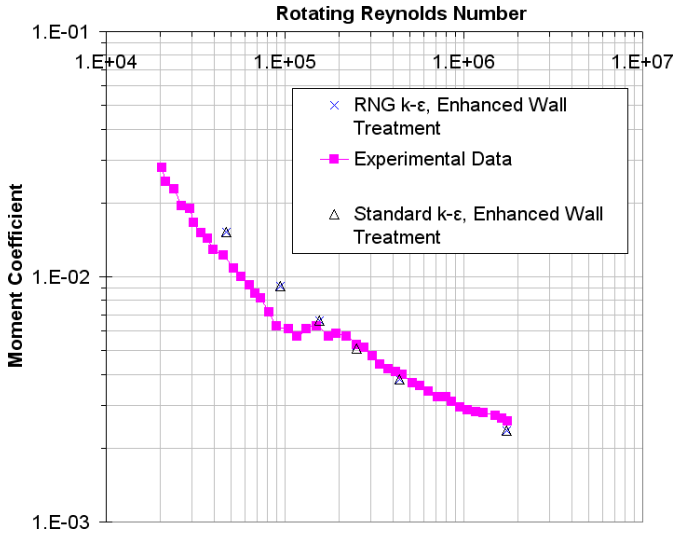

Figure 4.10: Graph of Moment Coefficient (C_M) against Rotating Reynolds Number (Re), for a Vertex Angle of $\phi = 90°$, a Non-dimensional Gap Width of $s = 0.016$ and a Non-dimensional Throughflow of $C_Q = 1500$, showing the Effect of using Different Turbulence models.

In Fig. 4.10 the relative performance of the standard $k-\epsilon$ and the RNG $k-\epsilon$ turbulence models, with enhanced wall treatment, is presented. As will be shown in Fig. 4.11, there is little difference in the results obtained with the two models.

Overall, little difference is observable between the results obtained with the two different version of the $k-\epsilon$ model, as can be observed by looking at the percentage difference between the two cases (Fig. 4.11). A similar lack of difference between the performance of these two different versions of the $k-\epsilon$ model has been reported in modelling other variations on Taylor-Couette flow by Shiomi *et al.* [52].

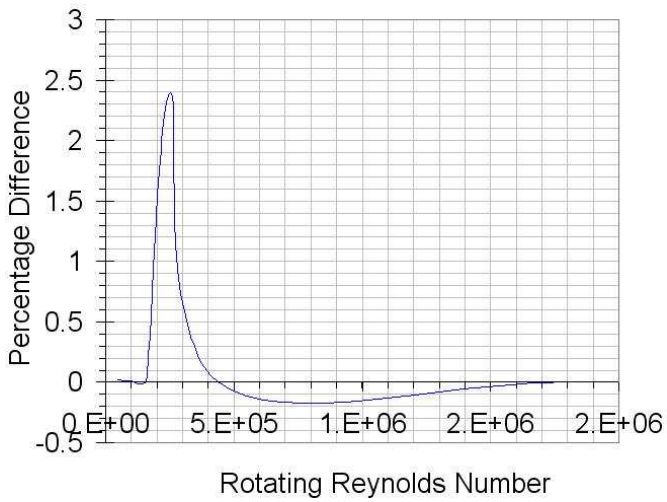

Figure 4.11: Graph of Percentage Difference between Standard and RNG $k-\epsilon$ Turbulence models, for a Vertex angle of $\phi = 90°$, Non-dimensional Gap Width $s = 0.016$ and Non-dimensional Throughflow $C_Q = 1500$.

Summary

To summarize, it has been demonstrated that, with the presence of throughflow, the numerical modelling can produce results that agree well with the experimental data, but neither of the wall treatments used performs consistently across the speed range. A transition that is present in the experimental data has not been captured numerically, but the torque levels before and after this transition can be predicted using (respectively) the standard wall function or the enhanced wall treatment. The RNG $k-\epsilon$ turbulence model, with standard wall functions predicts the torque levels to within 13% before the transition, and with enhanced wall treatment predicts the torque levels to within 14% after this transition. In a latter section (Section 4.5) the flow structures present within the flow will be looked at.

Due to the inability of the two-dimensional models to capture the transition, consideration must be raised as to whether any of the assumptions that have been used are the root of this issue. A transition could be caused by instability in the solution, either in time or space. In the following section, the flow will be modelled in three dimensions, to see whether imposing complete axi-symmetry upon the flow is responsible for not being able to predict this transition.

4.4.3 Throughflow, Three Dimensional Models

Torque Levels

A two dimensional model, by its very nature, cannot capture three-dimensional flow features. Therefore, in order to establish if there were any three-dimensional effects, two three-dimensional models were created, the initial model representing a six degree wedge shape section. Subsequently, due to the inability of this model to capture the transition, a fully three-dimensional model was developed. In this section a comparison with experimental torque values is discussed, whilst the flow structure is discussed in §4.5

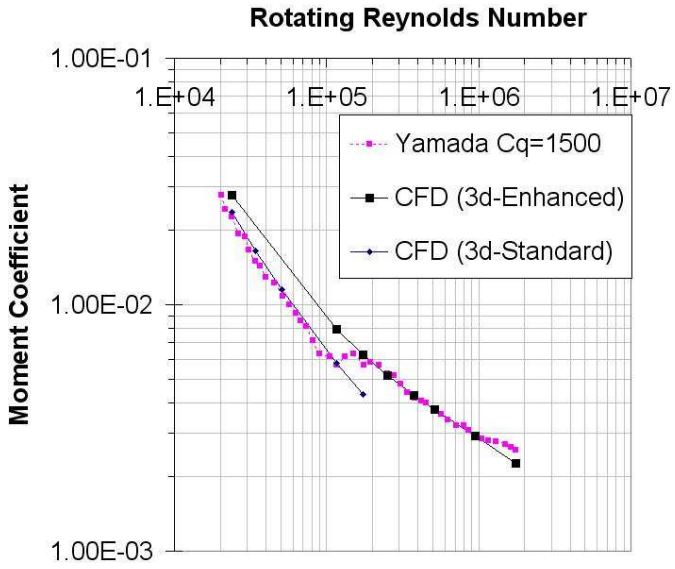

Figure 4.12: Graph of Moment Coefficient (C_M) against Rotating Reynolds Number (Re), to show the Performance of the Three Dimensional (Wedge Shaped) Model (Mesh 6), for a Vertex angle of $\phi = 90°$, Non-dimensional Gap Width $s = 0.016$ and Non-dimensional Throughflow $C_Q = 1500$.

In Fig. 4.12 the results from the wedge shaped model are shown, which is equivalent to Fig. 4.8 in §4.4.2. A transition is visible in the experimental data over the range $117,000 \leq \text{Re} \leq 221,000$. Before the transition, as for the two dimensional cases, the quantitative agreement between the RNG $k-\epsilon$ turbulence model, with standard wall function, and the experimental data is strong. The best agreement is found for $\text{Re} = 24,000$, where the percentage difference is 4.9%. The worst agreement is found for $\text{Re} = 34,000$, where the percentage difference is 10%.

After the transition, again, as for the two dimensional cases, the quantitative agreement between the RNG $k-\epsilon$ turbulence model, with enhanced wall treatment, and the experimental data is good. The best agreement is found for $\mathrm{Re} = 946,000$, where the percentage difference is 0.2%. The worst agreement is found for $\mathrm{Re} = 1,747,000$, where the percentage difference is 11%.

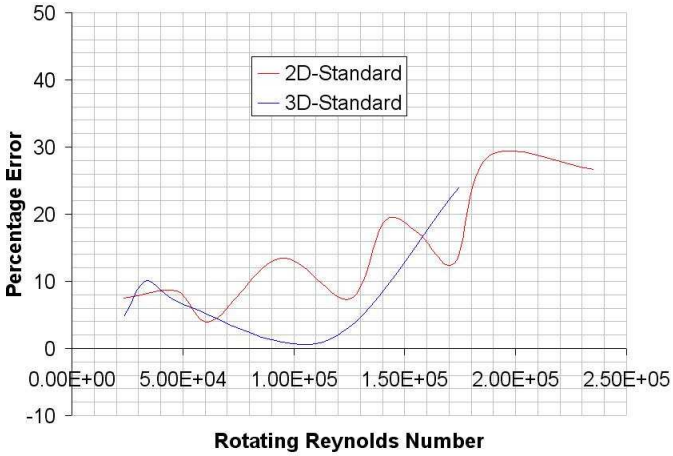

Figure 4.13: Graph of Rotating Reynolds Number against Percentage Error, to show the performance of the (Wedge Shaped) three-dimensional model, relative to that of the two dimensional model, using the RNG $k-\epsilon$ turbulence model, with Standard Wall Function.

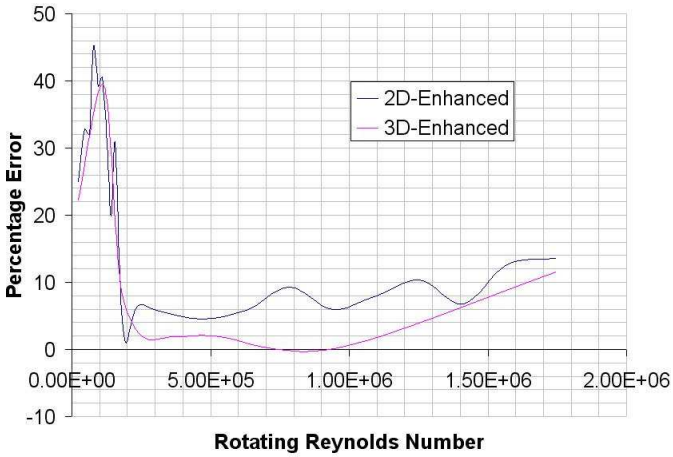

Figure 4.14: Graph of Rotating Reynolds Number against Percentage error, to show the performance of the (Wedge Shaped) three-dimensional model relative to that of the two dimensional model, using the RNG $k-\epsilon$ turbulence model, with Enhanced Wall Treatment.

Overall, the three-dimensional wedge model is more accurate than the two dimensional model, as can be seen in Figures 4.13 & 4.14. Fig. 4.13 shows the percentage error (relative to the experimental data) in the 2D and 3D Models, using the standard

wall functions. Fig. 4.14 shows the percentage error (relative to the experimental data) in the 2D and 3D Models, using the enhanced wall treatment. The increase in the accuracy of the predictions produced by the three-dimensional wedge model, over the two dimensional model, compared with the experimental data of Yamada & Ito [71], is of the order of between 5% and 7%. This level of increase in accuracy must be balanced against the increase in computational resources needed, as the mesh has increased in size by a factor of ~ 50, the governing equations have extra terms in them, and an extra equation is needed. In this case, the results have shown little gain for the increase in resources needed.

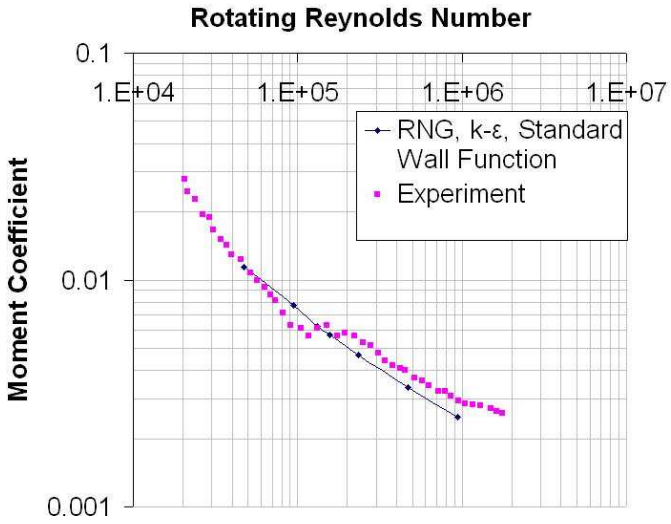

Figure 4.15: Graph of Rotating Reynolds Number against moment coefficient, to show the performance of the full three-dimensional model (Mesh 7).

In Fig. 4.15 the results from the fully three-dimensional model are presented. A transition is visible in the experimental data over the range $117,000 \leq \mathrm{Re} \leq 221,000$. In a notable change from the two dimensional model results, it can be observed that, across the entire experimental range, the quantitative agreement between the RNG $k-\epsilon$ turbulence model, with standard wall function, and the experimental data is strong. The best agreement is found for $\mathrm{Re} = 132,000$, where the percentage difference is 2.0%. The worst agreement is found for $\mathrm{Re} = 12,000$, where the percentage difference is 22%. Whilst the transition seen in the experimental data is not replicated, the results show significant differences from the two-dimensional models (§4.4.2) and the three-dimensional wedge model.

4.5 Flow Structure

This section looks at the flow structure and its dependence on rotational speed and throughflow conditions. Firstly the two dimensional flow fields with throughflow are looked at, and then the full three-dimensional flow field is considered.

4.5.1 Two Dimensional Flow Structure

The first case considered is at a rotational speed of $\Omega = 28$ rad s^{-1}, $C_Q = 750$, with Figure 4.16(a) depicting streamlines between the shroud and the cone, coloured by radial velocity, showing a vortex contained between the shroud and the cone near to the inlet pipe. This is present for all rotation speeds where throughflow is present, giving clear evidence of the behaviour Pereira & Sousa described [46], with a vortex trapped between the outer cone and the more dominant throughflow. As the rate of throughflow is increased the size of the vortex is seen to increase, with its centre being seen to travel away from the inlet (in the positive axial direction), as can be seen in Figures 4.16(b) and 4.16(c). Figure 4.17 shows the effect of increasing the angular velocity upon the flow structure near the inlet. It shows that increasing the rate of rotation whilst maintaining the throughflow rate at a constant value causes the length of the vortex to remain constant, but the thickness of the vortex reduces, which could explain the decrease in moment coefficient as Ω increases.

Before the transition, three additional vortices are present toward the outlet of the domain, as seen in 4.18. These form a pair of counter rotating vortices, which it can be safely assumed are created by the mechanisms which cause Taylor cells to occur in classic Taylor-Couette flow. A third vortex is then present between this pair and the inlet vortex, though it is not connected to it. These can be seen in Figure 4.18, which shows streamlines between the shroud and cone, coloured by velocity magnitude. Beyond the transition, this trio of vortices has disappeared entirely, as can be seem in Figure 4.19.

Summary

In this section the two-dimensional flow structures which exist have been looked at. Clear behavioural differences have been seen before and after the torque transition, which is

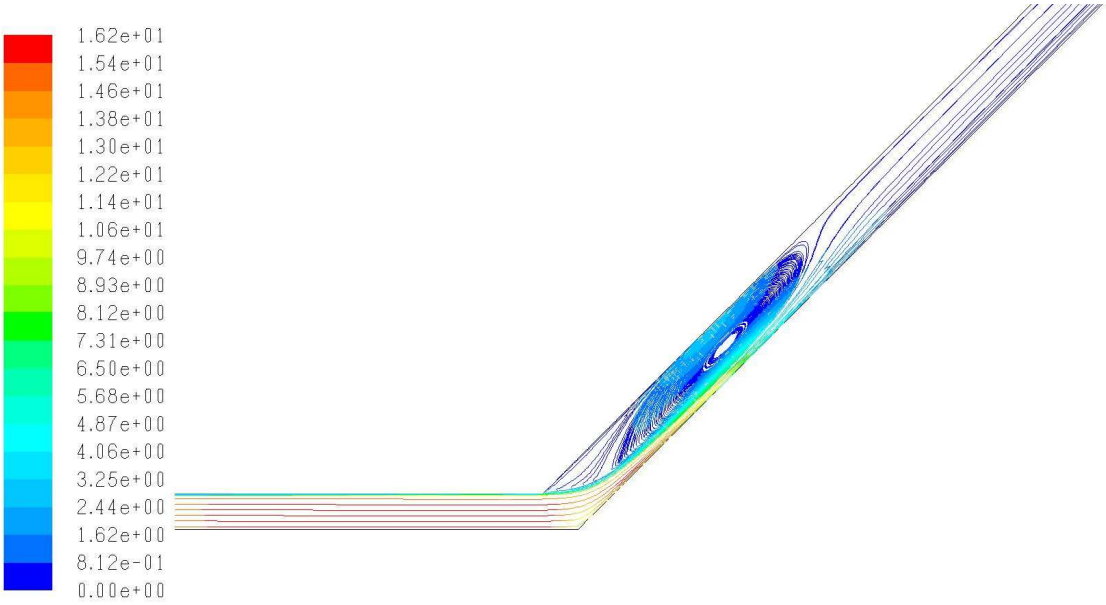

(a) $C_Q = 750$

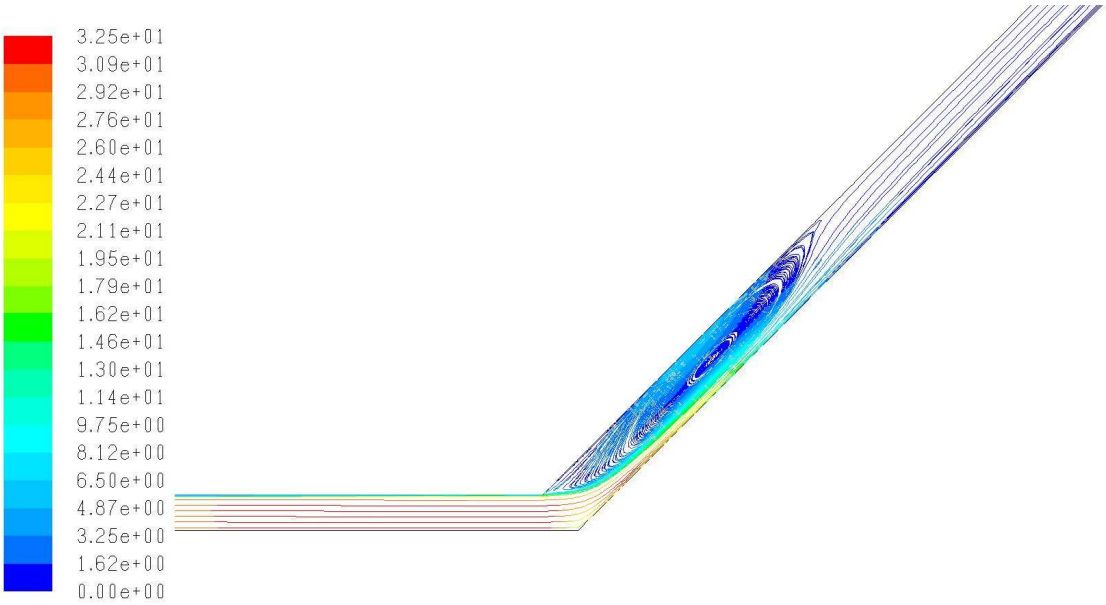

(b) $C_Q = 1500$

Figure 4.16: Streamlines, between the Shroud and the Cone, Coloured by Velocity Magnitude ($m\ s^{-1}$), to show vortex. Computed using Mesh 3, $\Omega = 15$ rad s^{-1}, varying values of C_Q. Fig. 4.16 continues

governed by increasing the angular velocity. The effect of changing the throughflow rate has also been shown. Now consideration will move on to consider the full three-dimensional flow structures.

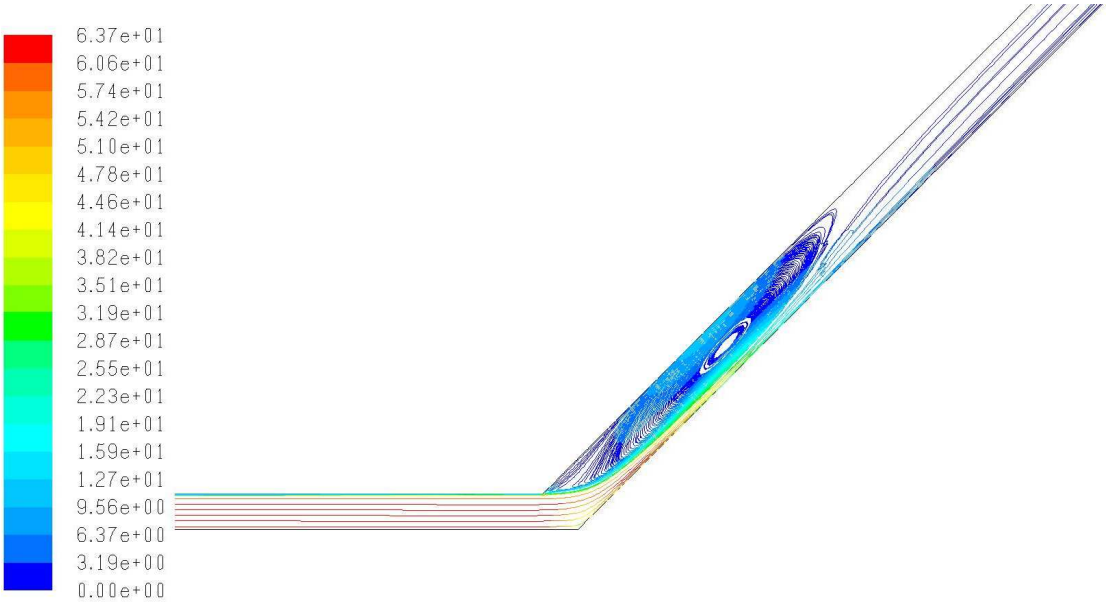

(c) $C_Q = 3000$

Figure 4.16: Streamlines, between the Shroud and the Cone, Coloured by Velocity Magnitude ($m\ s^{-1}$), to show vortex. Computed using Mesh 3, $\Omega = 15$ rad s^{-1}, varying values of C_Q

4.5.2 Three Dimensional Flow Structure

In this section, the three-dimensional flow structure which exists between the cone and the shroud shall be investigated.

In Figures 4.20(a)-4.20(c), the effect of increasing rotation on the flow structure can be seen. It can be seen that the increasing rotation is having a noticeable effect on the axial flow. By looking at how the flow structure changes with increasing rotational speed in the fully three-dimensional model, it can be seen that the flow is not axisymmetric in nature, although there is clear rotational periodicity in the flow (as with all simulations in this chapter, these simulations were conducted using a steady-state formulation). Indeed, the spiral patterns described by Wimmer & Zierep [67] appear to be occurring.

By studying the velocity magnitude in the annulus, it can be observed that with increasing rotational velocity, the velocity magnitude in the annulus increases. Figure 4.21(a) shows a plot of velocity magnitude against 'chordal length', for a range of rotational speeds, from the full three-dimensional model. The 'chordal length' is a chord situated in the middle of the annulus, parallel to the surface of the cone. Figure 4.21(b)

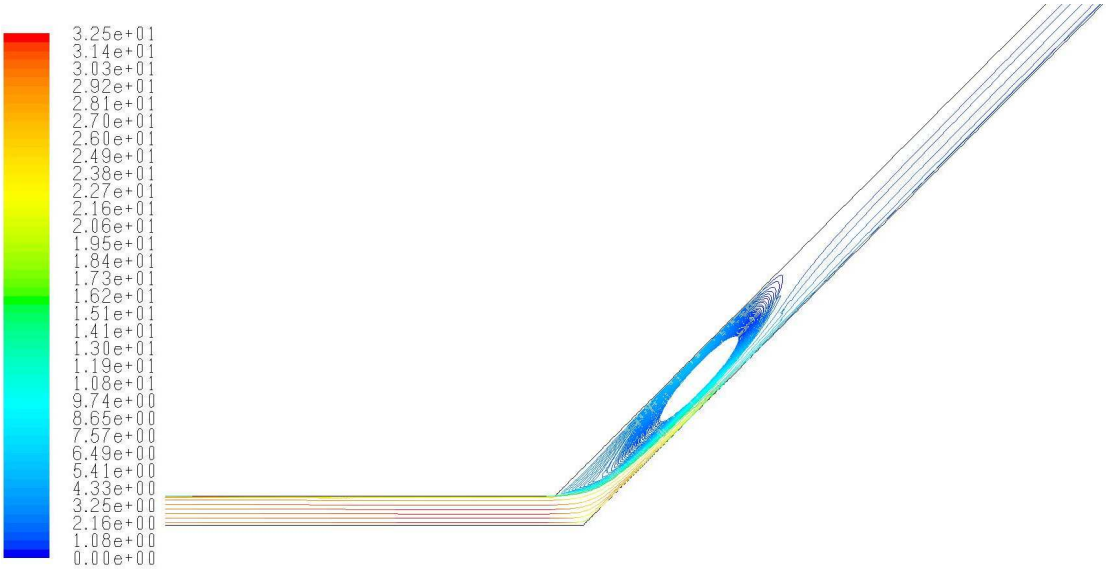

(a) $\Omega = 50$ rad s^{-1}

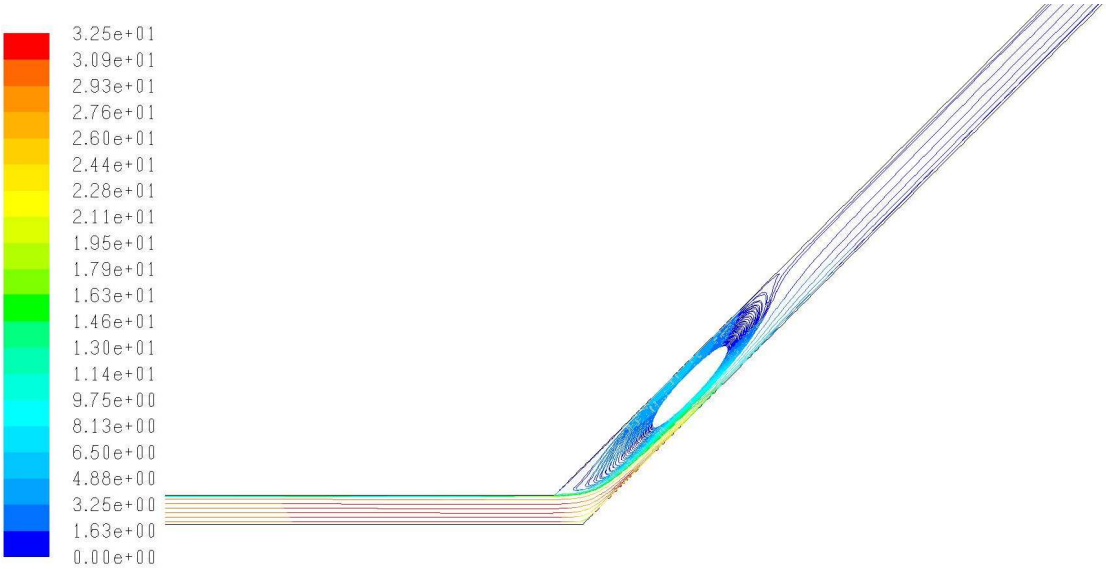

(b) $\Omega = 70$ rad s^{-1}

Figure 4.17: Streamlines, between the Shroud and the Cone, Coloured by Velocity Magnitude ($m\ s^{-1}$), to show vortex. Computed using Mesh 3, varying values of Ω, $C_Q = 1500$. Fig. 4.17 continues

shows a plot of tangential velocity against chordal length, for a range of rotational speeds, from the full three-dimensional model. A similar behaviour can be observed to that shown in Fig. 4.21(a). It is more interesting to look at the tangential velocity relative to the rotating surface. It can be observed from Fig. 4.21(c) that as the rotational rate is

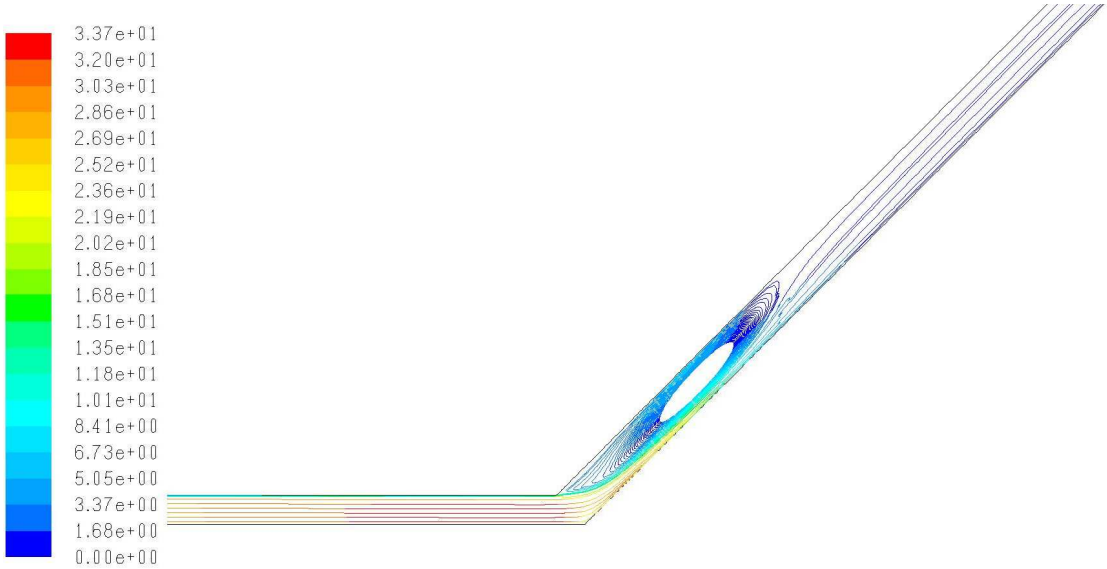

(c) $\Omega = 100$ rad s^{-1}

Figure 4.17: Streamlines, between the Shroud and the Cone, Coloured by Velocity Magnitude ($m\ s^{-1}$), to show vortex. Computed using Mesh 3, varying values of Ω, $C_Q = 1500$

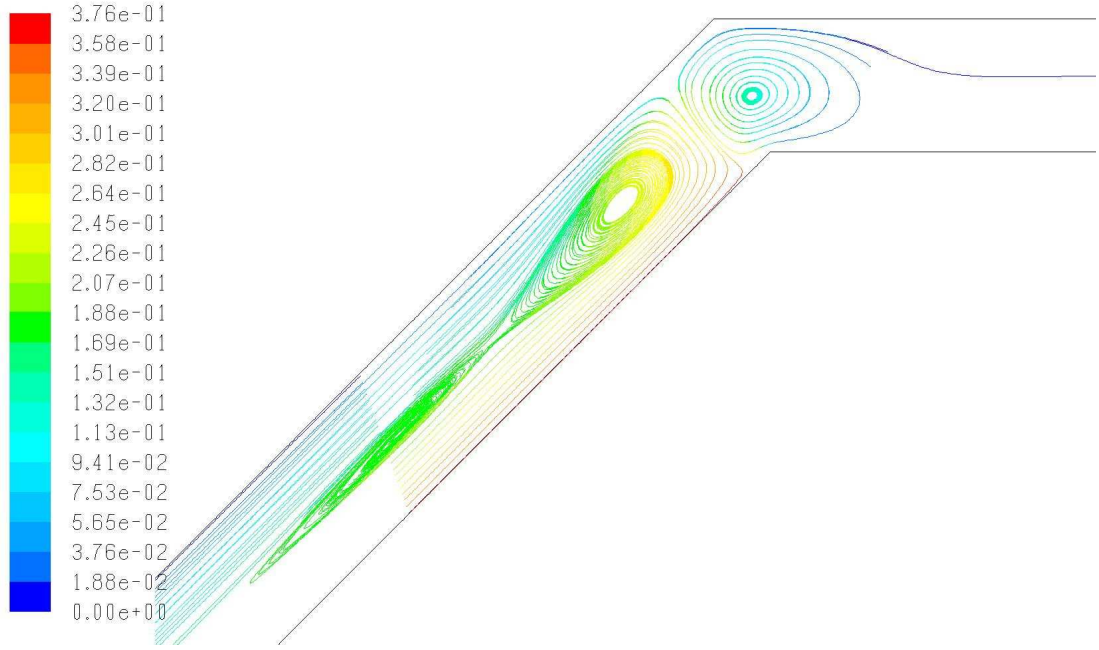

Figure 4.18: Streamlines, between the Shroud and the Cone, Coloured by Velocity Magnitude ($m\ s^{-1}$), to show secondary vortices present at low speed. Computed using Mesh 3, $\Omega = 3$ rad s^{-1}, $C_Q = 1500$

increased, the relative tangential velocity decreases. Through non-dimensionalisation of the relative tangential velocity as in Eq. 4.1, the curves shown in Fig. 4.21(d) & 4.21(e)

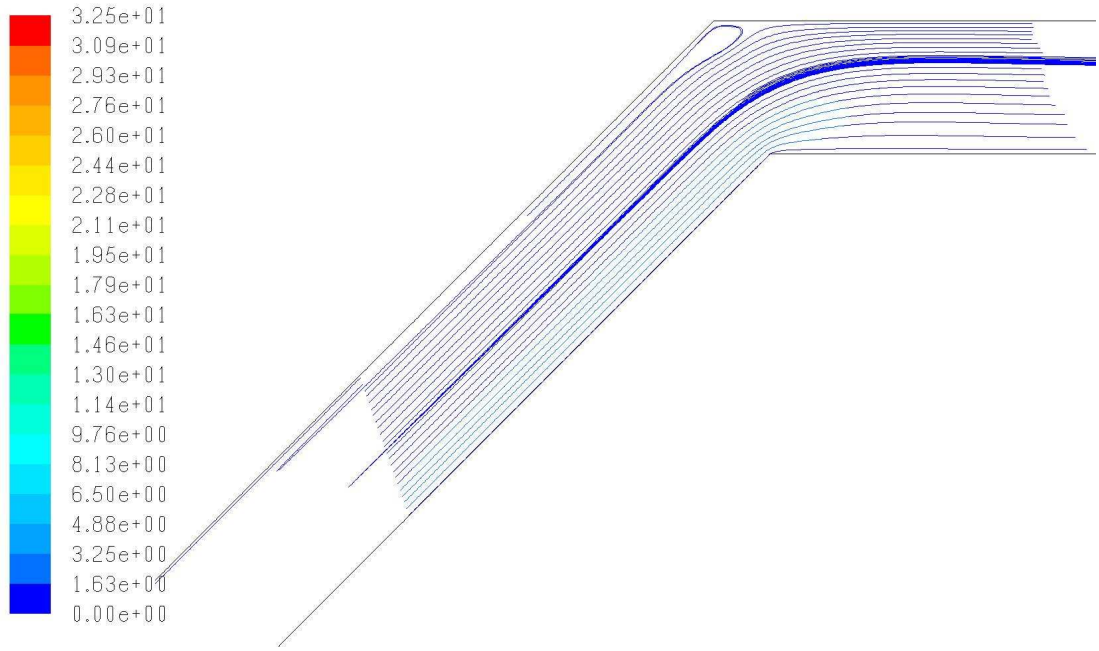

Figure 4.19: Streamlines, between the Shroud and the Cone, Coloured by Velocity Magnitude ($m\ s^{-1}$), to show lack of secondary vortices present after transition. Computed using Mesh 3, $\Omega = 28$ rad s^{-1}, $C_Q = 1500$

can be obtained:

$$v_{\mathrm{n}} = \frac{v_{\mathrm{r}}}{\Omega R_i}. \tag{4.1}$$

From these figures an explanation for the difference in the behaviour before and after the transition can be approached at. Before the transition the relative tangential velocity is positive for at least the first third of the cone, whereas after the transition the relative tangential velocity is negative for most of the region. If the relative velocity is positive, this means the flow is rotating slightly faster than the cone, whereas if it is negative, the flow is rotating slower. If the flow is slower than the cone, then it will be retarding the cone, which will create a greater moment about the cone-surface.

Summary

To summarize, in this section it has been shown that three-dimensional modelling, either when rotationally periodicity is applied on the solution domain or the entire situation is modelled, results in greater accuracy compared with two-dimensional models. Physically the flow is expected to be non-axi-symmetric [67], which has been replicated numerically

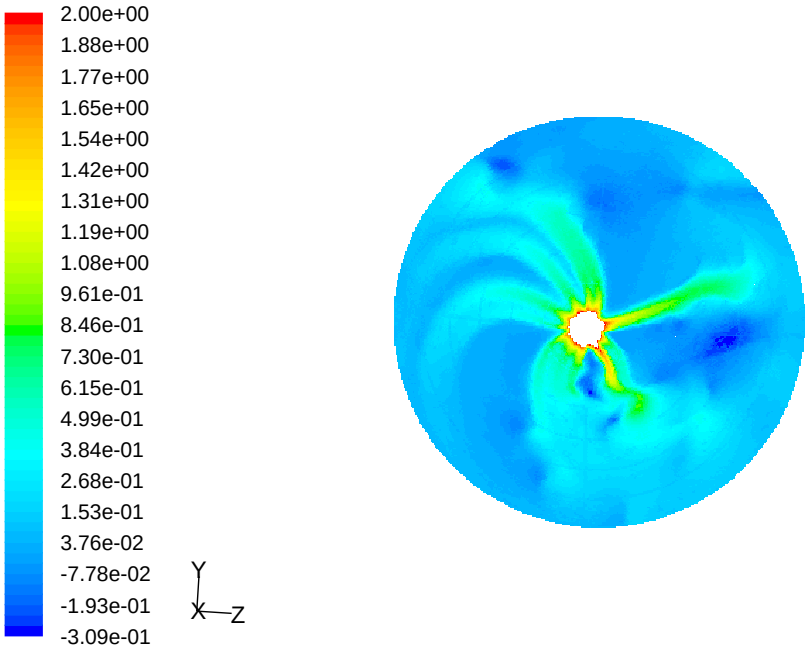

(a) Contours of Axial Velocity ($m\ s^{-1}$) on the cone surface, for $\Omega = 3$ rad s^{-1}.

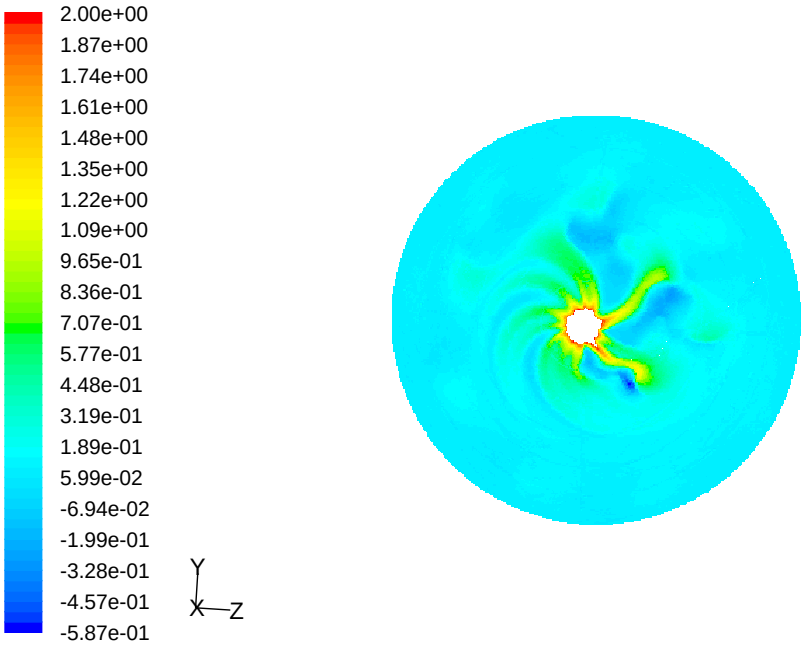

(b) Contours of Axial Velocity ($m\ s^{-1}$) on the cone surface, for $\Omega = 10$ rad s^{-1}.

Figure 4.20: Contours of Axial Velocity ($m\ s^{-1}$) on the cone surface, for 3 rad $s^{-1} \leq \Omega \leq 30$ rad s^{-1}. Figure 4.20 continues.

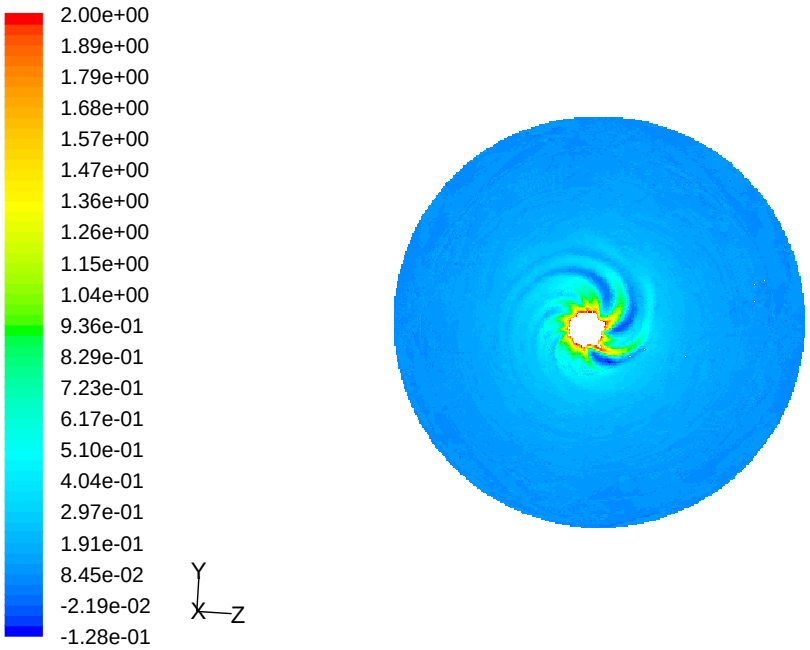

(c) Contours of Axial Velocity ($m\ s^{-1}$) on the cone surface, for $\Omega = 30$ rad s^{-1}.

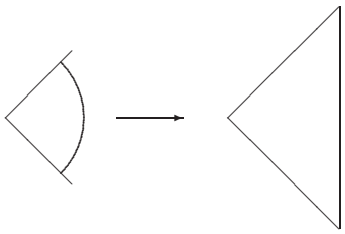

(d) Orientation of view in Figures 4.20(a)-4.20(c).

Figure 4.20: Contours of Axial Velocity ($m\ s^{-1}$) on the cone surface, for 3 rad $s^{-1} \leq \Omega \leq 30$ rad s^{-1}.

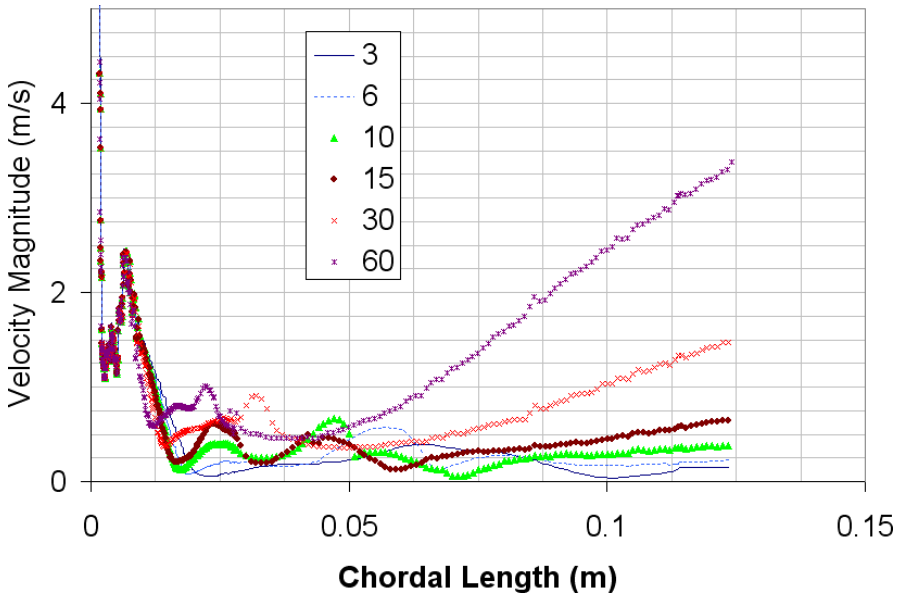

(a) Velocity Magnitude

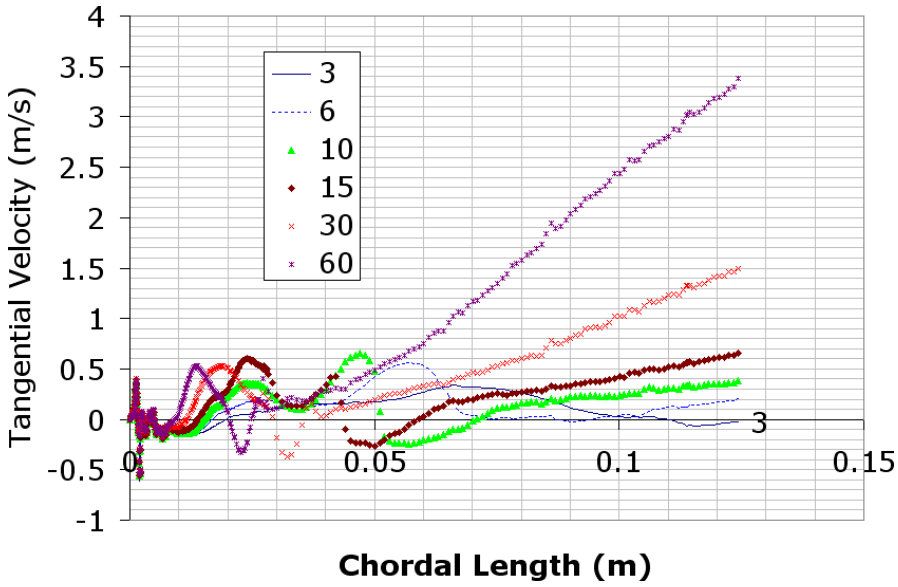

(b) Tangential Velocity

Figure 4.21: Graphs of various velocity components against Chordal Length (along a chord situated in the middle of the annulus) within the flow, for a range of Ω (shown in legend, units rad s^{-1}). Fig. 4.21 continues.

(Fig. 4.20), and so modelling the situation in its entirety (i.e. a full three-dimensional model) is the only way of capturing such phenomena.

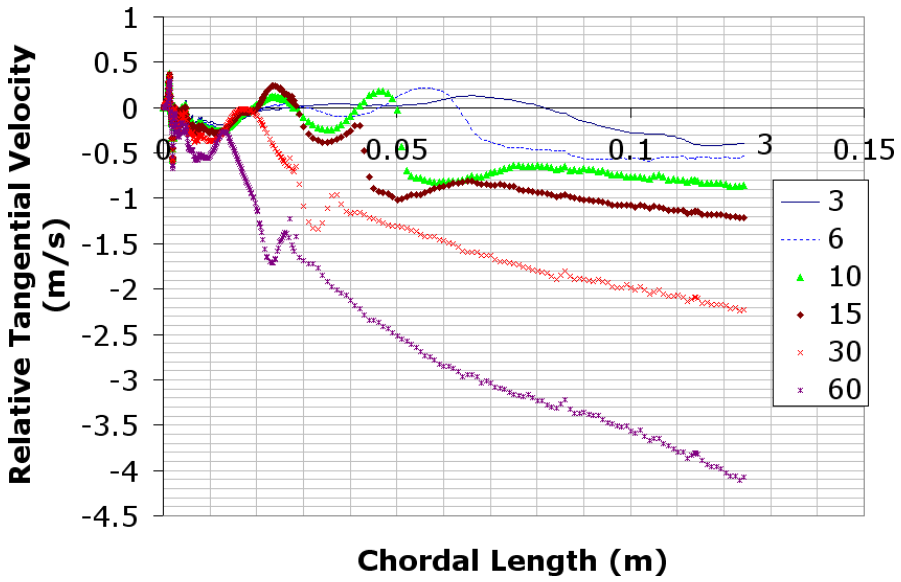

(c) Relative Tangential Velocity

Figure 4.21: Graphs of various velocity components against Chordal Length (along a chord situated in the middle of the annulus) within the flow, for a range of Ω (shown in legend, units rad s^{-1}). Fig. 4.21 continues.

4.5.3 Overall Effects of Increasing Throughflow and Geometrical Changes

Figure 4.22 presents a graph of moment coefficient (C_M) against rotating Reynolds number (Re), for a vertex angle of $\phi = 90°$ and a non-dimensional gap width $s = 0.016$, for increasing non-dimensional throughflow rates (C_Q). In Fig. 4.22 it can be observed that increasing the through flow rate causes an increase in the moment coefficient calculated by the CFD, which is consistent with the experimental data of Yamada & Ito [71]. So as to be consistent, all of these data points were calculated using the RNG $k-\epsilon$ turbulence model, with enhanced wall treatment.

Figure 4.23 presents a graph of moment coefficient (C_M) against rotating Reynolds number (Re), for a non-dimensional throughflow rates (C_Q), a non-dimensional gap width $s = 0.016$, and increasing vertex angle ϕ. In Fig. 4.23 it can be observed that increasing the vertex angle causes an increase in the moment coefficient calculated by the CFD, which is consistent with the experimental data of Yamada & Ito [71]. So as to be consistent, all of these data points were calculated using the RNG $k-\epsilon$ turbulence model, with enhanced wall treatment.

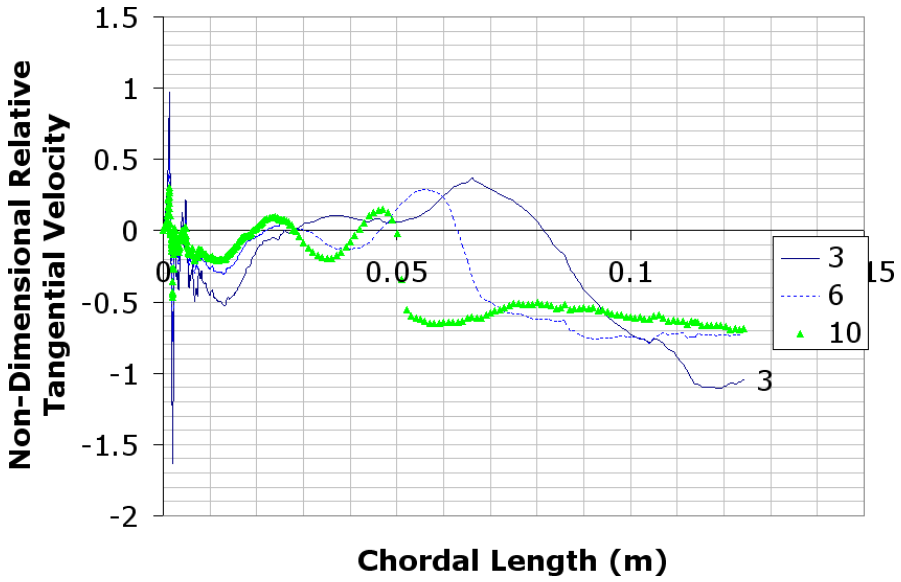

(d) Non-dimensional Relative Tangential Velocity

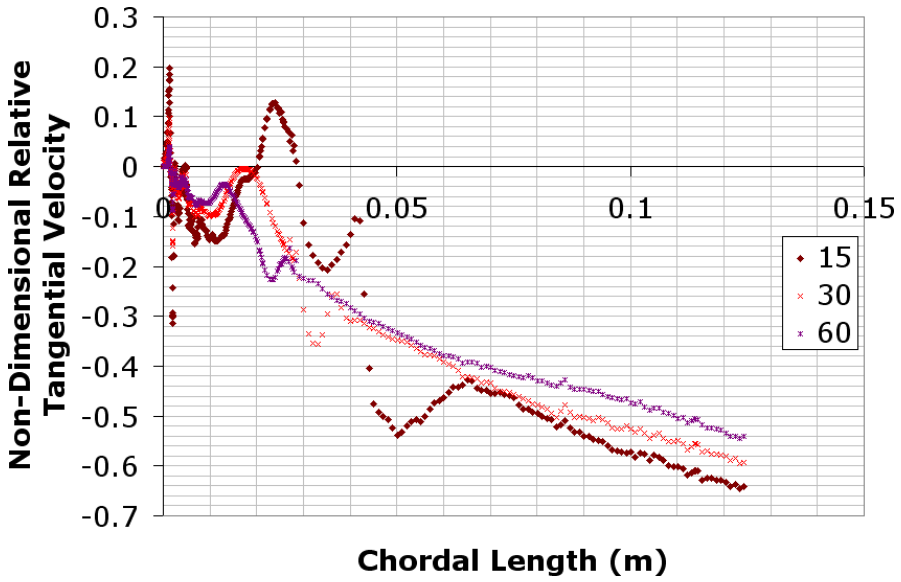

(e) Non-dimensional Relative Tangential Velocity

Figure 4.21: Graphs of various velocity components against Chordal Length (along a chord situated in the middle of the annulus) within the flow, for a range of Ω (shown in legend, units rad s^{-1}).

Figure 4.24 presents a graph of moment coefficient (C_M) against rotating Reynolds number (Re), for a non-dimensional throughflow rates (C_Q), a vertex angle ϕ, and increasing non-dimensional gap width s. In Fig. 4.24 it can be observed that increasing the gap width causes a decrease in the moment coefficient calculated by the CFD, which

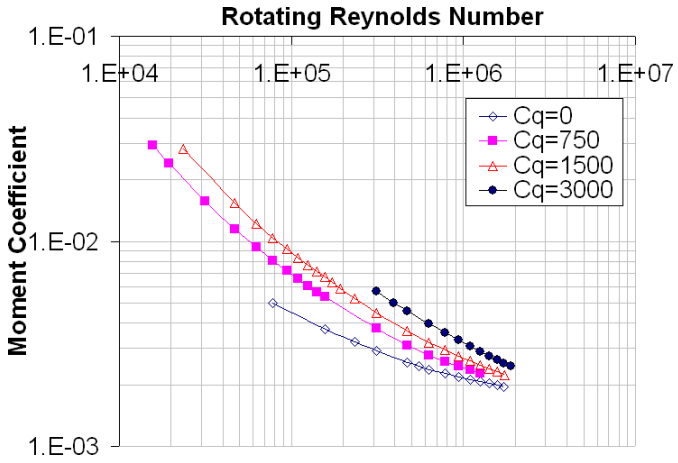

Figure 4.22: Graph of Moment Coefficient (C_M) against Rotating Reynolds Number (Re), for a Vertex Angle of $\phi = 90°$ and a Non-dimensional Gap Width $s = 0.016$, for increasing Non-dimensional Throughflow Rates (C_Q).

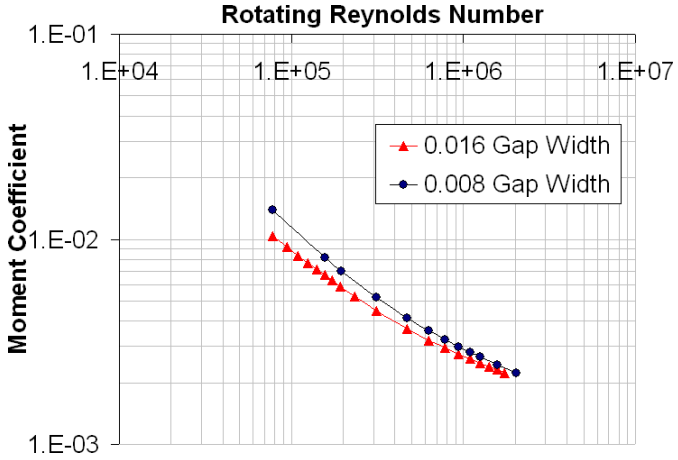

Figure 4.23: Graph of Moment Coefficient (C_M) against Rotating Reynolds Number (Re), to show the Effect of Increasing Vertex Angle (ϕ) for a Constant, Non-dimensional Gap Width ($s = 0.016$).

is consistent with the experimental data of Yamada & Ito [71].

To summarize, it has been shown that the numerical modelling is showing that increasing C_Q, increasing the vertex angle ϕ, or decreasing the gap width s lead to increases in the moment coefficient, which agrees with the experimental trends observed by Yamada & Ito [69–71]. This is a useful result, as it shows the ability of the numerical modelling style to capture trends shown in experimental data. In chapter 6 the relative performance of different shrouds will be looked at, so this gives confidence that the modelling strategy being developed can replicate these differences.

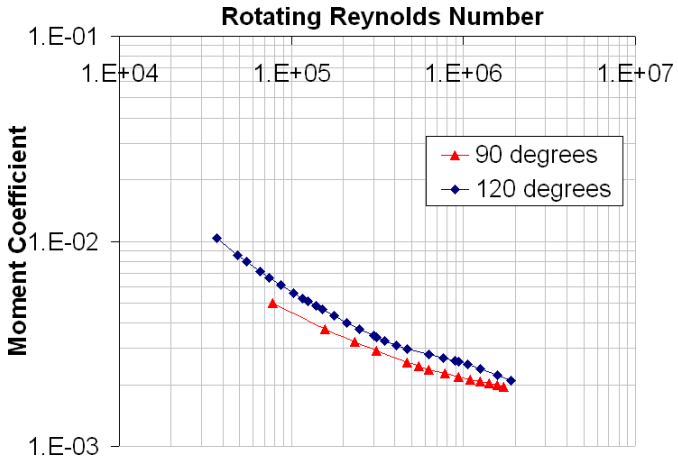

Figure 4.24: Graph of Moment Coefficient (C_M) against Rotating Reynolds Number (Re), to show the Effect of Increasing Gap Width (s), for a Constant Vertex Angle ($\phi = 90°$), and a Constant, Non-dimensional Throughflow ($C_Q = 0$).

4.6 Conclusions

In simulations of the flow where no forced throughflow is present, calculations from two dimensional models computed using the RNG $k-\epsilon$ or SST $k-\omega$ turbulence models have been presented for different vertex angles and gap widths. These show good agreement with the experimental data of Yamada & Ito [69–71] for a vertex angle of $\phi = 90°$. The transition that is present in all the cases is relatively weak when there is no throughflow, and as such the enhanced wall treatment is seen to predict the torque levels consistently across the speed range in these cases. For the cases with a larger vertex angle ($\phi = 120°$), the performance of the model is far worse, with torque levels consistently over predicted by between 33% and 70% in comparison with the experimental data. Additionally, computation were conducted using the SST $k-\omega$ turbulence model, which was seen to perform slightly better, though still over predicting torque levels by between 16% and 67%.

The effect of throughflow on the flow has also been considered in both two dimensional and three-dimensional simulations. In these cases, the transition is far more distinct. Again, these show good agreement with the experimental data of Yamada & Ito, except for in the transitional regime. Three different treatments for viscosity effects were utilized, and comparisons made between their performances, the RNG $k-\epsilon$ turbulence model, the Standard $k-\epsilon$ turbulence model, and the Reynolds Stress Model. Little

difference was found between the results from the RNG $k-\epsilon$ turbulence model and the Standard $k-\epsilon$ turbulence model, nor between the RNG $k-\epsilon$ turbulence model and the Reynolds Stress Model. More significant differences were found by varying the wall function utilized in each case. The two dimensional models have been unable to offer any insight into the mechanism behind the transition. This is due to the fact that whilst the two different wall approaches (standard wall functions and enhanced wall treatment) give very good agreement before and after the transition (respectively), neither approach performs with equal accuracy both sides of the transition when used in these models.

The situation has been modelled in three dimensions for one geometrical setting ($\phi = 90°$, $s = 0.016$), utilizing a rotationally periodic, 6° wedge shaped model and also a full 360° simulation. Turbulence modelling in these models has concentrated on utilizing the RNG $k-\epsilon$ model. Similarly to the two dimensional simulations the transition is not well captured by the rotationally periodic model. This supports the notion that the mechanism behind the transition is incorporated in the non-axi-symmetry of the flow, as discussed in §4.5.3. The full simulations still fail to capture the transition. However the performance of the turbulence model used (RNG $k-\epsilon$ with Standard Wall Function) is consistent with the experimental data across the speed range.

The consistency shown by the models to the effects of increasing the vertex angle, throughflow, and gap width (§4.5.3), replicating trends shown experimentally is encouraging. This allows confidence to be had in the strategy developed to capture the effect changing the geometry has on the flow structure and torque levels.

This investigation has produced a strategy for the modelling of the flow around a bevel gear, and has highlighted some shortcomings in the two dimensional numerical modelling. To summarize, the (preliminary) strategy is

- model turbulence using an RNG $k-\epsilon$ turbulence model
- model as much of the domain as computational resources allow

The work has also shown that using a three-dimensional model produces more accurate results. However, to clearly see whether a flow is axisymmetric or not, the entire situation needs to be modelled. In doing this, a much clearer understanding of the flow has been obtained, and it is possible to use the CFD to explain differences in the flow field. Moving

forward, in the following Chapters, the flow around a spiral bevel gear will be looked at, in unshrouded (Chapter 5) and shrouded (Chapter 6) configurations. Whilst the work shown in this chapter suggests the need to model the gear in its entirety, lack of resources has precluded this approach.

Chapter 5

Unshrouded Gear

In this chapter a computational study of the flow around a spiral bevel gear is presented and the data is compared to available experimental data[1]. The overall application of the modelling strategy which this thesis is developing is a gear pair operating in an aeroengine with oil and shrouds present. However, this final setting is beyond the scope of this thesis. Modelling a single unshrouded gear is a logical next step in the progression towards the ultimate situation following the work in the previous chapter. Additionally, experimental data exists for this setting [25], allowing the results produced to be validated. Results are presented for clockwise and anticlockwise rotation for an unshrouded configuration. The effect of different computational wall treatments on the predicted torque levels is presented, as well as the effect of modelling the flow using a transient simulation compared to the use of a steady-state simulation.

5.1 Experimental Setting

The spiral bevel gear used in this study is shown in Fig. 5.1. It has 91 teeth, an outer radius of 133.5mm, and a module of 2.92mm. In this study, the fluid surrounding the gear is air, operating at atmospheric pressures, with no lubrication. Rotational speeds vary from 0 to 15,000 RPM, in either rotational direction, giving tip velocities of up to $210ms^{-1}$. On the experimental test facility, illustrated in Fig. 5.2, the gear is mounted on a shaft which is connected through a series of bearings and a gearbox to a motor. The

[1] Parts originally published within [48]

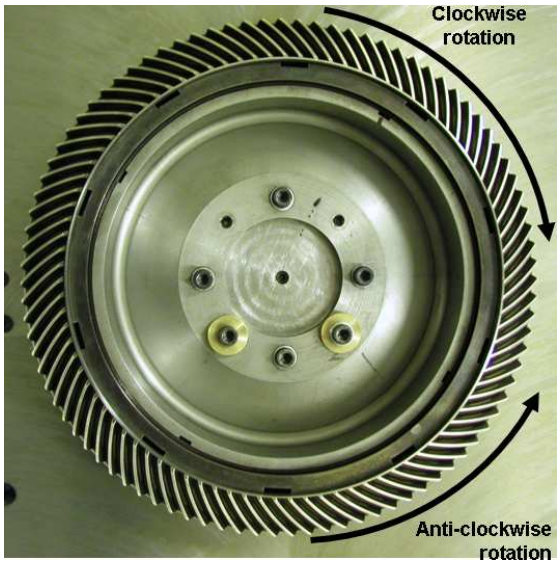

Figure 5.1: The spiral bevel gear, illustrating rotation directions

shaft passes through a back plate that isolates the test region from the driving section. Data from the experiment that is logged includes the rotational speed of the shaft, and the torque that the gear experiences. Further details are given in the papers of Johnson *et al.* [24, 25].

5.2 CFD Geometry, Boundary Conditions and Methodology

In this section, details of the Geometry Modelled will be given (§5.2.1), as well as the Mesh (§5.2.2), Boundary Conditions (§5.2.3), Assumptions (§5.2.4), and Numerical Methods (§5.2.5) used. Details will then be given of the cases that have been computed (§5.3).

5.2.1 Geometry

The geometry modelled computationally was chosen to be as close as possible to that investigated experimentally. A definition of rotational direction as used in this chapter is given in Fig. 5.1. In the modelled configuration, illustrated in Fig. 5.3, the gear and shaft rotate freely, and the gear is able to draw in air from the test cell. A plot of velocity magnitude on the gear surface and back wall is shown in Fig. 5.4. It highlights

Figure 5.2: Experimental test facility

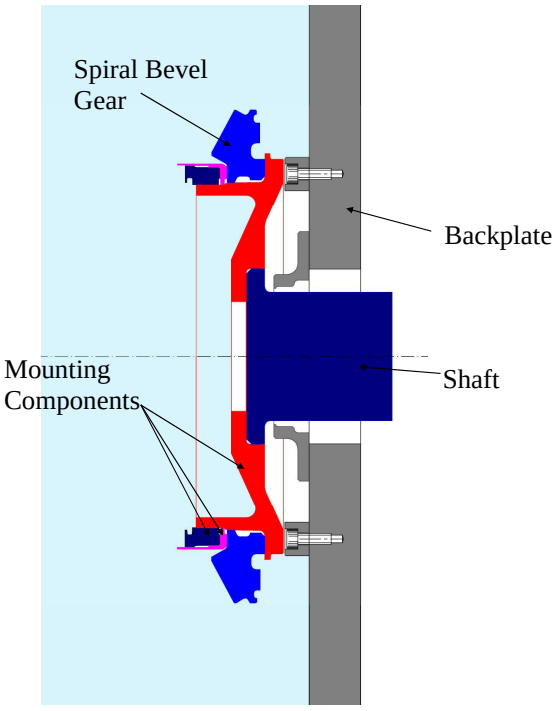

Figure 5.3: Illustrating the unshrouded gear

the shape of the domain that has been modelled, which follows the curvature of the teeth. Additionally, the stationary walls are apparent, as they have zero velocity magnitude. A cross-sectional view of the geometry and the boundaries are shown in Fig. 5.5.

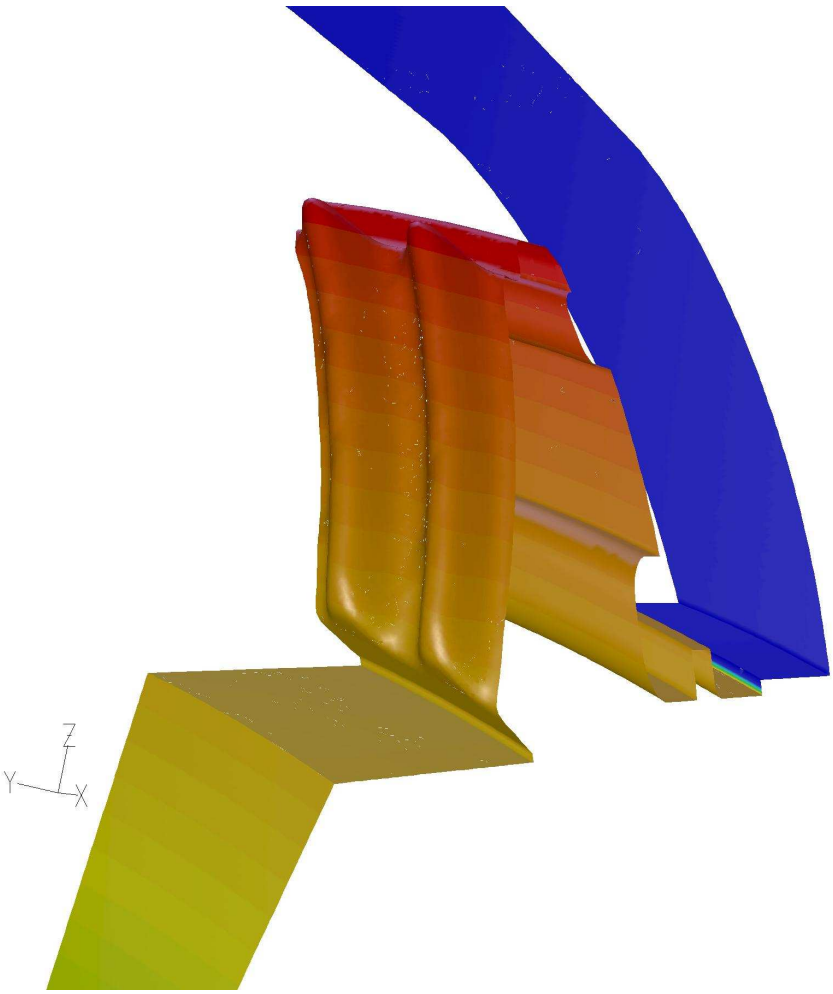

Figure 5.4: Illustrating two-tooth geometry

Referring to Fig. 5.5, air enters the computational domain through the pressure inlet located 0.1m upstream of the gear in the axial direction. Ambient conditions are approximated by specifying a zero total gauge pressure. The air, deflected radially outwards by the back plate leaves the computational domain through the pressure outlet.

5.2.2 Mesh

Two CFD models have been created, one two-dimensional and one three-dimensional. A two-dimensional model of the gear was created to provide some understanding in the

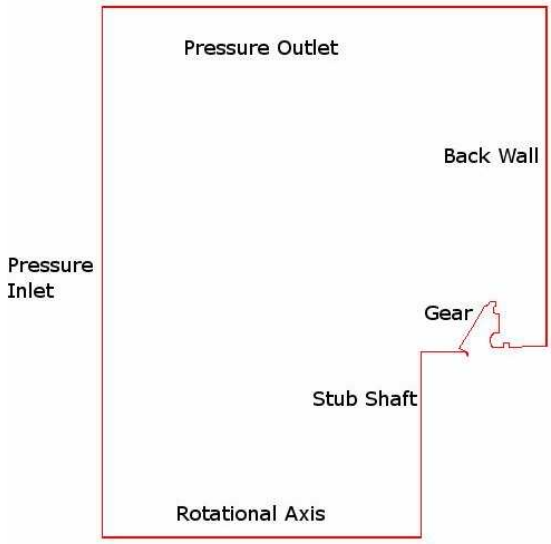

Figure 5.5: Boundary conditions

basic flow structure. The geometry of the three-dimensional setting was approximated, so that the 2D model captures the silhouette of the gear, making it essentially a cone. It was meshed with a triangular meshing scheme, using a size function attached to the gear to control the size and growth rate of the cells in the mesh. The two dimensional model of the gear contained $5,543$ triangular cells. An overall view of the two-dimensional mesh is given in Fig. 5.6, with a close up of the section close to the 'teeth' given in Fig. 5.7. The three-dimensional two-tooth model contained $961,751$ cells. An overall view of this three-dimensional mesh is given in Fig. 5.8, with a close up of the section close to the teeth given in Fig. 5.9. The three-dimensional model uses unstructured, tetrahedral meshes, with hex cores, in the region close to the gear teeth, with structured mesh through the rest of the domain. Figure 5.10 shows a plot of the cell-type on the rotating boundaries. Blue represents tetrahedral cells, red triangular prisms, and green cuboidal cells. All the meshes were constructed using the commercial meshing program Gambit. The use of unstructured meshes in the region close to the gear teeth was due to the ease of producing meshes in this style around such a complex geometry. In order to capture the boundary layer, a size function was used to increase the mesh density in the near-wall region.

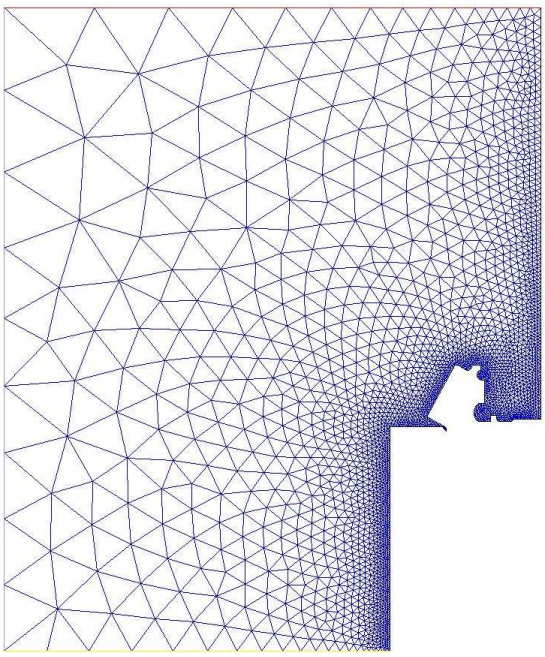

Figure 5.6: Two-dimensional mesh

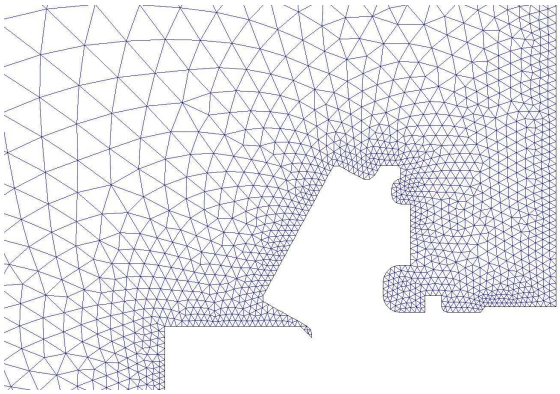

Figure 5.7: Two-dimensional mesh, close up of mesh around gear.

5.2.3 Boundary Conditions

The gear teeth were not fully modelled in the two-dimensional study. The turbulence quantities at the pressure inlets and outlets (for backflow) are calculated from an imposed turbulence intensity of 10% (typical of room conditions) and a hydraulic diameter appropriate to the inlet geometry. The face of the gear is modelled as a rotating wall with a no-slip condition applied. Stationary walls also have a no-slip condition imposed.

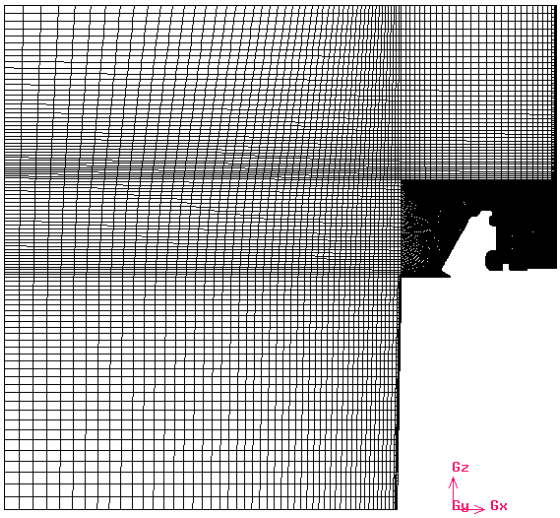

Figure 5.8: Mesh on rotating boundary

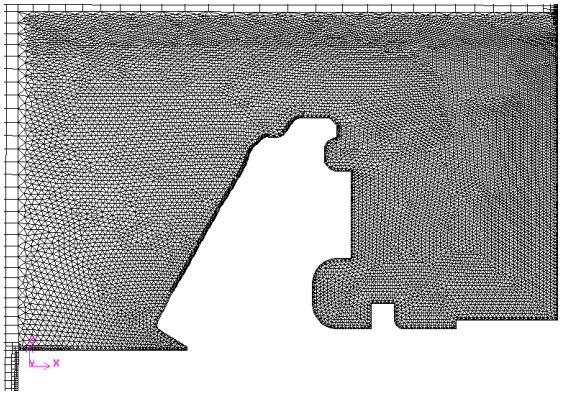

Figure 5.9: Mesh on rotating boundary-close up of section close to gear

5.2.4 Assumptions used

The two-dimensional computations were conducted assuming the flow was two-dimensional and axi-symmetric. The three-dimensional computations have been carried out using a rotationally periodic volume. Simulations are performed using a rotating reference frame and an absolute velocity formulation. Computations correspond to shaft speeds between 3000 RPM and 15,000 RPM, resulting in a Mach number in the vicinity of the gear teeth reaching values of the order of 0.7. For this reason, at the higher rotational rates (shaft speed $\geq 10,031$ RPM) a compressible calculation has been performed taking air as an ideal gas, whilst for lower rotation rates the fluid is assumed incompressible.

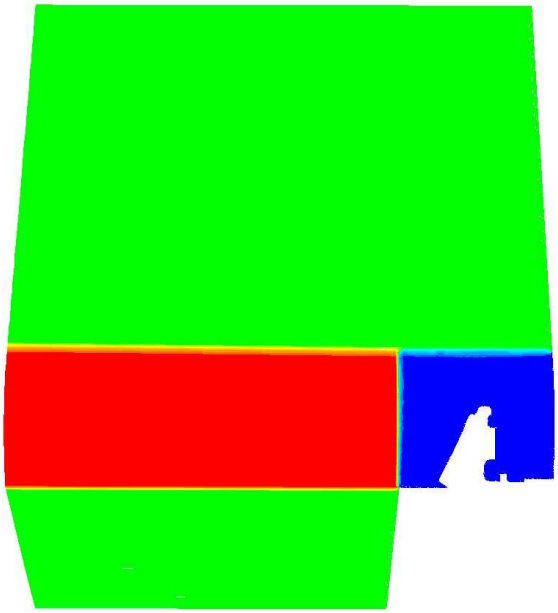

Figure 5.10: Cell types on rotating boundary. Blue represents tetrahedral cells, red represents triangular prisms, and green represents cuboidal cells.

5.2.5 Numerical Method

Single phase calculations of the air flow field and associated torques are obtained for a single crown gear using the commercial CFD code FLUENT (releases 6.2.16 & 6.2.17) in two and three-dimensional forms. Due to the findings presented in the previous chapter (Chapter 4), turbulence is modelled using the RNG $k-\epsilon$ model [63, 64]. The governing equations have been discretized using the QUICK formulation, with the pressure equation discretized using the PRESTO formulation. Pressure-velocity coupling is conducted using the SIMPLE algorithm. Details of these models are given in sections 3.3.2, 3.3.4 and 3.3.6, respectively.

5.3 Results

In this section, details of the results that have been produced will be presented, and discussed. The first group of results are those produced using a steady-state assumption, and demonstrate the ability of the code to simulate the flow around the gear, in both rotational directions. After this, results that have been presented for anti-clockwise rotation using a transient formulation are looked at, using both three-dimensional (§5.3.2) and two-dimensional models (§5.3.3). Descriptions of the flow structure are presented

for cases in both rotational directions.

5.3.1 Steady State

Experimental data obtained on the test rig in Fig. 5.1 will be used for validation of the CFD models [25]. The primary variable that can be compared is the windage torque. On the test rig a torque transducer was mounted on the gear shaft such that there was one roller bearing and the gear contributing to measured torques. The bearing and other losses have been accounted for in the data as presented here. For the remainder of this chapter, unless stated otherwise, all results are obtained using the RNG $k-\epsilon$ turbulence model, with enhanced wall treatment, and are steady state, isothermal, and incompressible. Steady state results were obtained for a range of shaft speeds with the gear rotated in both the clockwise and anticlockwise directions. Data will be presented on two graphs, separated by rotation direction. These graphs plot 3 sets of data; these are as follows: *CFD: RNG* $k-\epsilon$*, Standard Wall Function* (computations conducted using the RNG $k-\epsilon$ turbulence model with a Standard Wall Function), *CFD: RNG* $k-\epsilon$*, Enhanced Wall Treatment* (computations conducted using the RNG $k-\epsilon$ turbulence model with an Enhanced Wall Treatment), and *Experimental Data*. The data is non-dimensionalised using a Rotating Reynolds Number (Re) and a Moment Coefficient, C_M. There exist fixed uncertainties in the experimental data. Due to the scaling on C_M, these uncertainties dominate for lower rotational rates, $\text{Re} \leq 8.3 \times 10^5$, so experimental data is only presented above this value.

Fig. 5.11 shows a plot of Rotating Reynolds Number against Moment Coefficient, rotating in the clockwise direction, comparing experimental data to CFD simulations. The CFD simulations are split into two groups: those produced using a standard wall function, and those produced using an enhanced wall treatment. Results produced with the RNG $k-\epsilon$ model with standard wall function are looked at first, in which it can be seen that the best agreement is at $\text{Re} = 1.3 \times 10^6$, which corresponds to a shaft speed of $10,031$ RPM, for which the percentage difference in the torque levels (referenced to the experimental value) is 23%, and the worst is at 8.4×10^5, which corresponds to a shaft speed of $6,708$ RPM, for which the percentage difference is 26%. The predictions

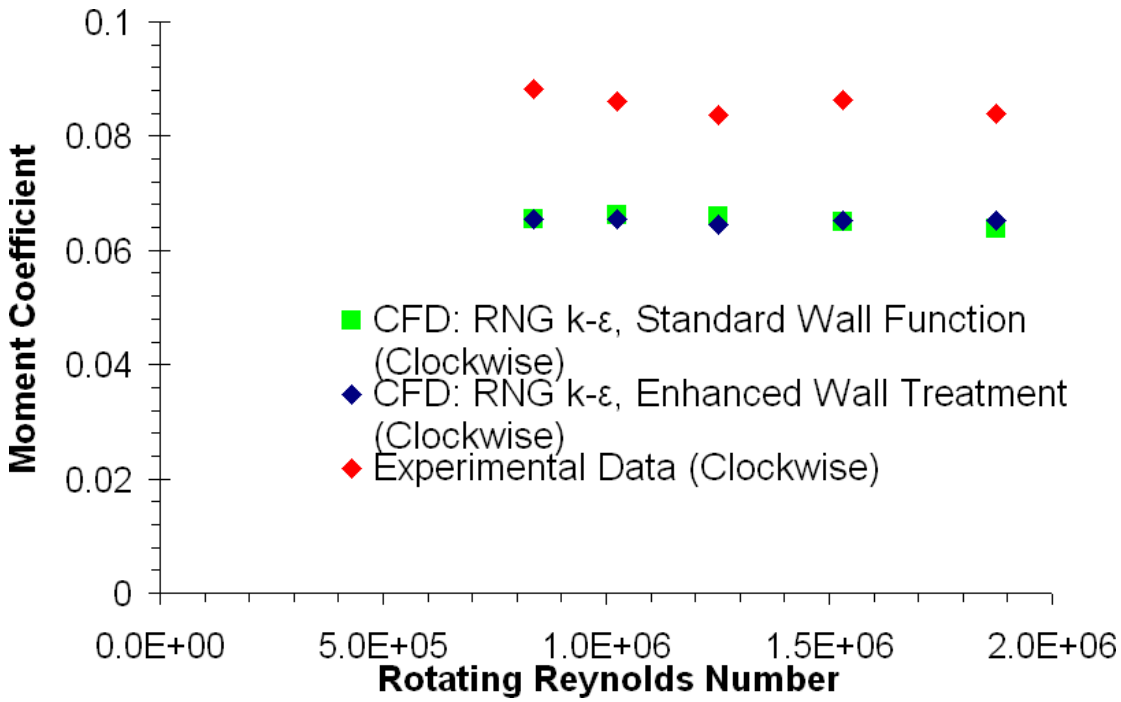

Figure 5.11: Graph of Moment Coefficient against Rotating Reynolds Number, gear rotating in the clockwise direction

made using the RNG $k-\epsilon$ model with enhanced wall treatment show the same trend as the standard wall function, with the quantitative agreement for the CFD consistently under predicting the torque levels. The best agreement is at Re $= 1.9 \times 10^6$, which corresponds to a shaft speed of 15,000 RPM, for which the percentage difference in the torque levels (referenced to the experimental value) is 22%, and the worst is at 8.3×10^5, which corresponds to a shaft speed of 6,708 RPM, for which the percentage difference is 26%. Overall, it can be observed that the results from the two methods are very similar, varying by less than 10%. The difference between the numerical predictions and the experimental data is discussed further after the results from the anti-clockwise rotation have been presented.

Fig. 5.12 shows a plot of Rotating Reynolds Number against Moment Coefficient, rotating in the anticlockwise direction, comparing experimental data to CFD simulations. The CFD simulations are split into two groups: those produced using a standard wall function, and those produced using an enhanced wall treatment. In the case of enhanced wall treatment, true convergence was not obtained but a situation arose where there was consistent fluctuation in the value of C_M with the code 'hunting' for a solution. This

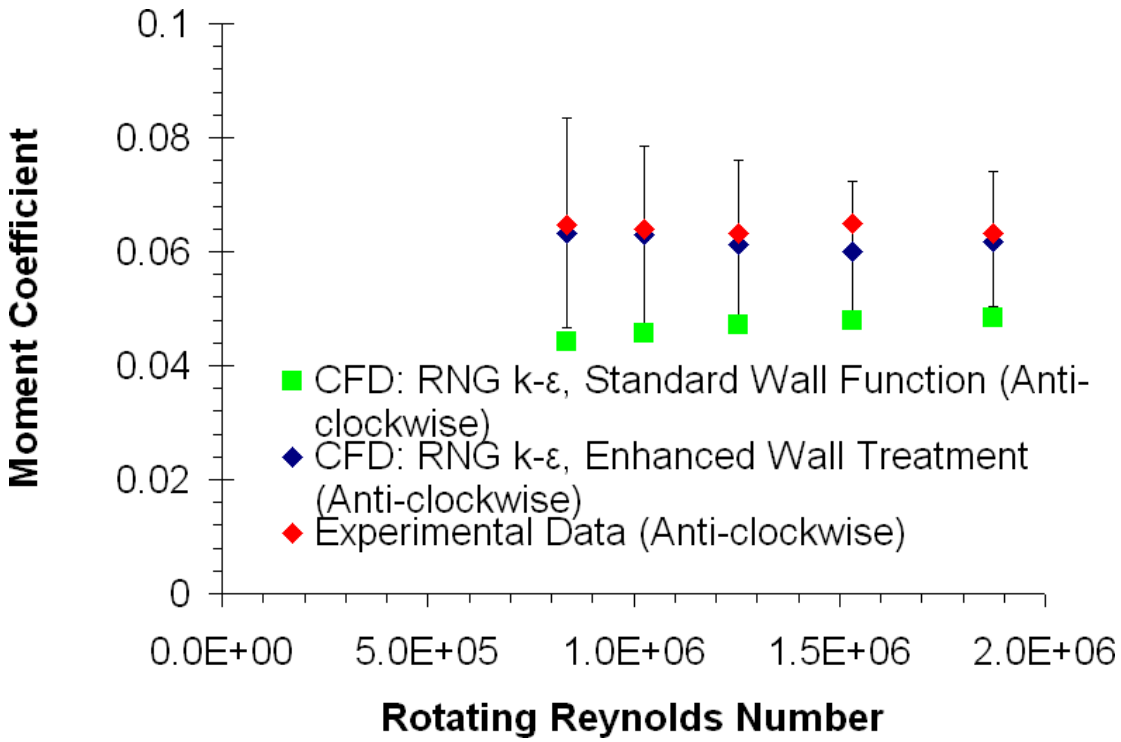

Figure 5.12: Graph of Moment Coefficient against Rotating Reynolds Number, gear rotating for anti-clockwise rotation

often occurs when a transient solution should be sought. The values presented here are steady-state, with the average of the torque values over 5000 iterations given, as well as the minimum and maximum values. For standard wall functions it can be seen that both qualitative and quantitative agreement between the predictions and the experimental data is not so good in this case. C_M is under predicted in all cases by between 21% and 40%. It can be seen that there is now very good agreement between the averaged results from the enhanced wall treatment and the experimental torque values; C_M is predicted to between 1.2% and 6.4% of the experimental level. The difference between the results obtained from the two near-wall flow models may be due to a number of reasons. However, it will be shown later on in this chapter that the enhanced model predicts vortices to be present within the flow, being seen transiently shedding from the outer radii of the gear teeth. Part of the mechanism which generates these can be linked back to the pressure gradient near the walls, which is something which is not directly resolved by the standard wall function. The enhanced wall treatment is however capable of resolving these gradients, which explains why it is able to capture these vortices.

Overall, it has been seen that whilst the CFD captures trends in the experimental data, the torque levels are being under-predicted. Concentrating on the results obtained using the standard wall function, their behaviour is consistent, showing the same directional bias as seen experimentally. There are many things that can be contributing to the under-predictions. The key assumptions that have been made are:

1. Flow is rotationally periodic
2. Fluid is isothermal/incompressible
3. Flow is not transient

To eliminate the first of these assumptions, a model of the full gear could be produced to see what difference this produces in the flow field and torque levels. The second assumption, that of incompressibility, has not been made in all cases, and yet the results show no change in trend above the speed where this effect has been included, so it can safely be concluded that this effect is not significantly affecting the predictions. The grid density in the near-wall region may also be affecting the results. Mesh adaptation can be performed, decreasing the cell-size in the near-wall region in order to better model the near-wall flow. Meshes in this chapter were developed and adapted so that y^* was sufficiently small (< 4) to give mesh independence, reducing the possibility of mesh density affecting the solution. The final assumption, that the flow is steady-state, is a crucial one. The anti-clockwise results with enhanced wall treatment suggest that transience is present in this direction. In order to investigate further the time-varying nature of the torque obtained for anti-clockwise rotation, various transient calculations were performed, for shaft speeds of 8203 RPM and 15000 RPM, and this is reported in section 5.3.2.

5.3.2 Transient Flow

Transient calculations were conducted for rotational speeds of 8203 RPM and $15,000$ RPM anticlockwise rotation. Time steps of $\simeq 8\mu$s and $\simeq 3\mu$s (respectively) were chosen with the RNG $k-\epsilon$ model, using the enhanced wall treatment. These timestep sizes give 10 timesteps per toothpass. A timestep of this size was chosen in order to obtain

a solution that was independent of the timestep size. The transient calculations were started from the steady state, incompressible case, but compressibility was included as the calculation progressed. Figure 5.13(a) shows a plot of torque against time for a rotational speed of 8203 RPM. The experimental value shown is the average value obtained from the experimental data equipment, over a long timescale. Equipment used for measuring the torque levels is not capable of sampling at a high enough frequency to be able to capture the frequencies shown numerically. The experimental torque level is under-predicted by the average of the CFD value by just 2%. As Fig. 5.13(a) shows, there is clearly periodicity within the torque levels. By performing a Fourier analysis Figure 5.13(b) is obtained, which shows a plot of frequency against magnitude. The enhanced wall treatment produces dominant frequencies of approximately 730 Hz and 1216 Hz. As tooth passing frequency is $12,441$, it can be seen that these equate to $\simeq 1/17^{\text{th}}$ and $1/10^{\text{th}}$ tooth passing frequency, respectively. A transient calculation was conducted for a rotational speed of 15000 RPM anticlockwise rotation. A time step of $3\mu s$ was chosen with the RNG $k-\epsilon$ model and enhanced wall treatment. Fig. 5.14(a) shows a plot of torque against time, for this case. The average torque level is under-predicted by 11%. As Fig. 5.14(a) shows, there is clearly periodicity within the torque levels. By performing a Fourier analysis Fig. 5.14(b) is obtained, which shows a plot of frequency against magnitude. There are two dominant frequencies present, of approximately 1300 Hz and 1960 Hz. Again it can be seen that these equate to $\simeq 1/17^{\text{th}}$ and $1/10^{\text{th}}$ tooth passing frequency, respectively, suggesting that these frequencies scale linearly with Ω.

5.3.3 Two-dimensional Transient Model

To understand in greater detail the mechanism behind this transience, a two dimensional model of the gear has been produced, using the full tooth profile (so this replicates a 'conic' of the same geometry as the gear without teeth cut into it). Whilst this is an approximation, it was felt that this could lead to a greater understanding of the basic behaviour involved. This modelling was conducted as a way of producing some quick insight as to some of the basic flow structures. It is important to note that this work should not be seen as a replacement to full three-dimensional models of the gear-as

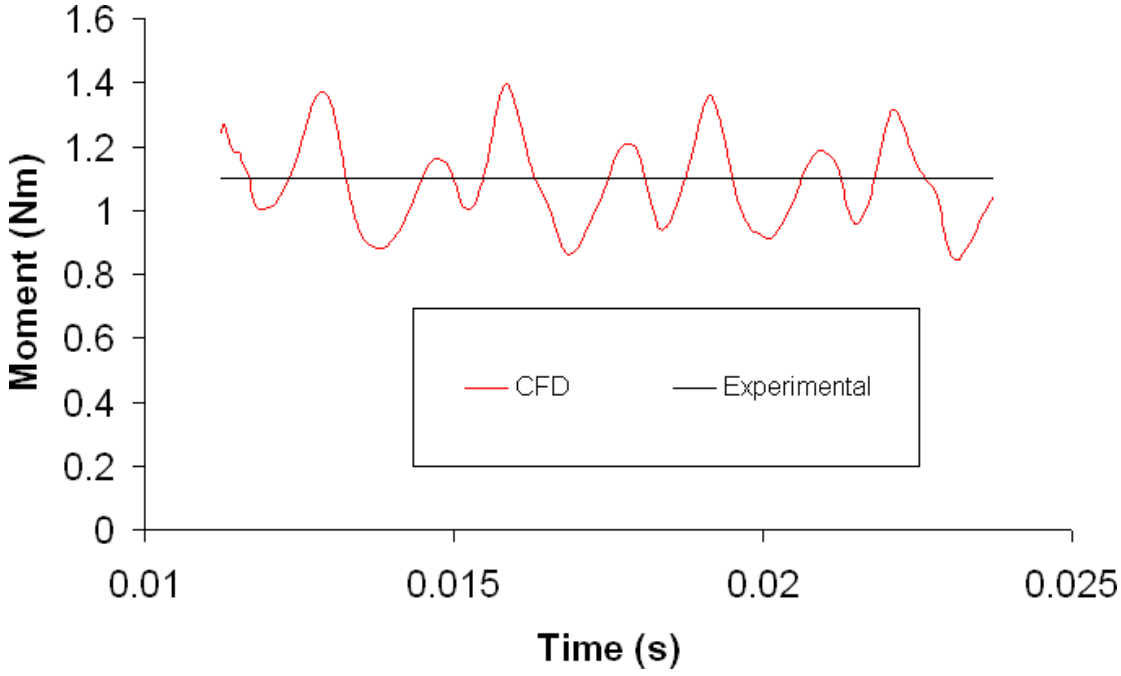

(a) Moment against time

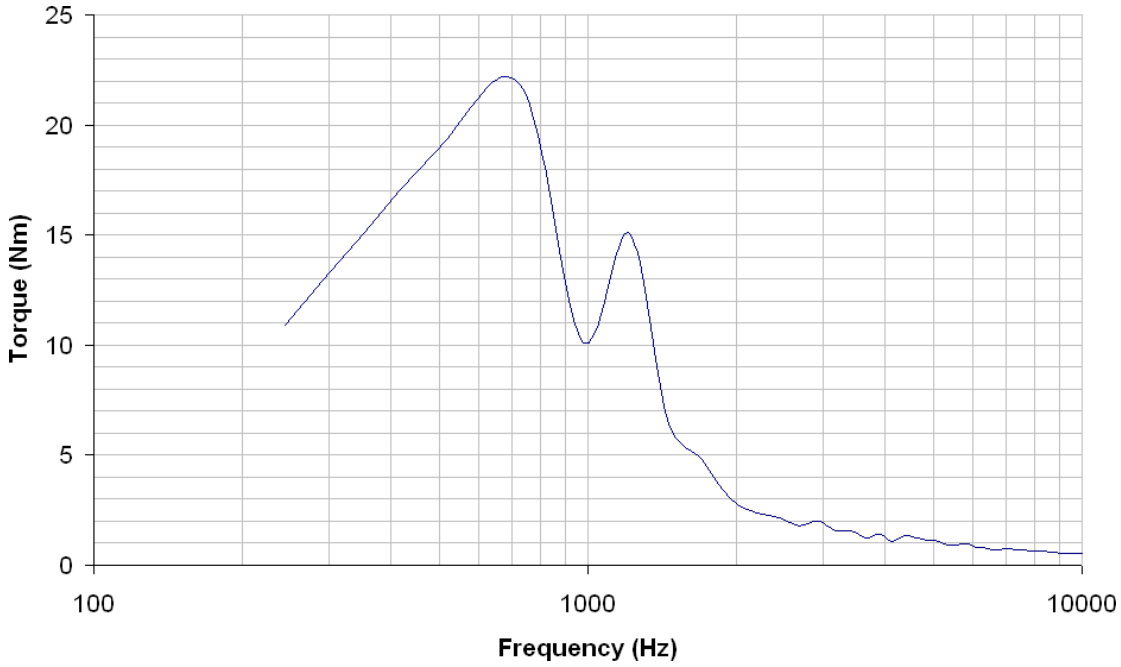

(b) Signal Frequency against Magnitude

Figure 5.13: Time variation in Moment Coefficient for a transient anti-clockwise rotation case (8203 RPM)

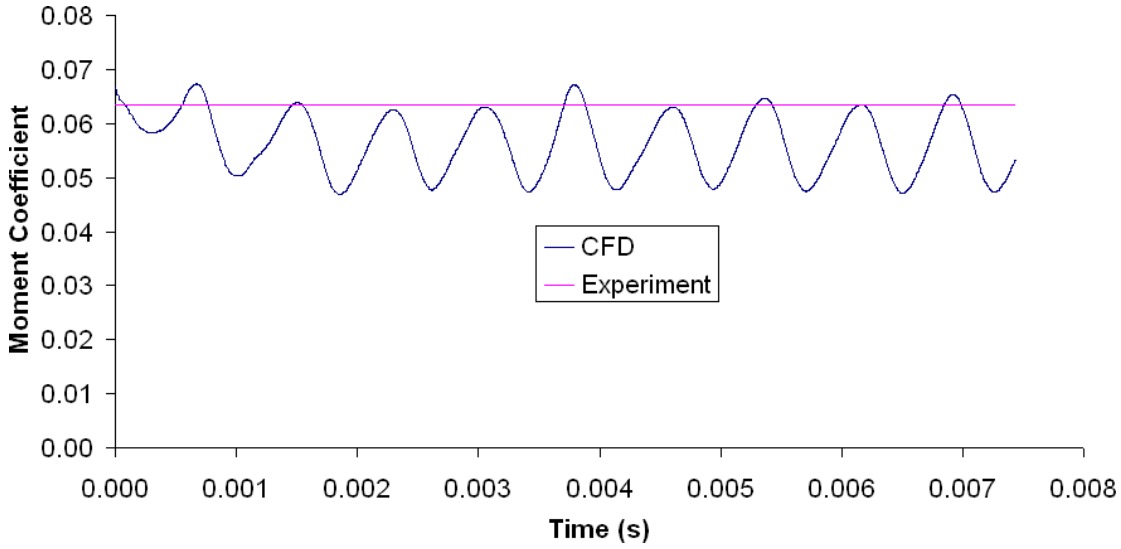

(a) Moment against time

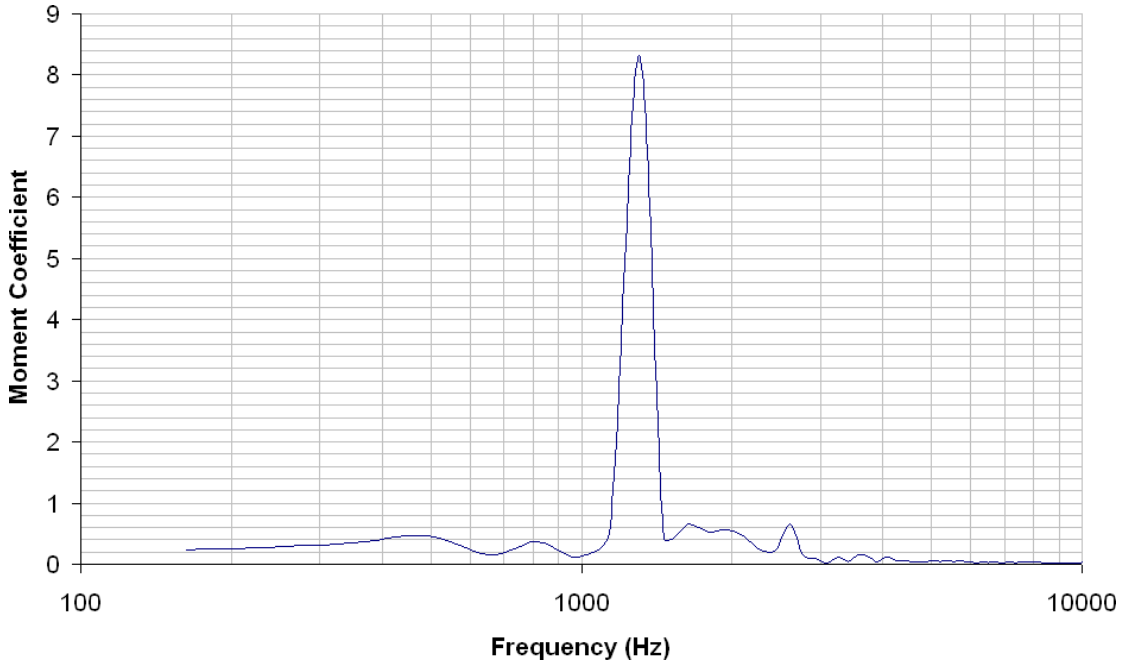

(b) Signal Frequency against Magnitude

Figure 5.14: Time variation in Moment Coefficient for a transient anti-clockwise rotation case (15000 RPM)

has been concluded previously (§4), to get a full-understanding of the flow, it must be modelled three-dimensionally. This model was initially run steady-state, in order to setup the basic flow structure, and then run transient.

In Fig. 5.15(a) the results obtained from this transient solution are presented. One dominant frequency is apparent in the torque levels shown. By performing Fourier analysis on this data, the frequency spectrum shown in Fig. 5.15(b) is obtained. The dominant frequency is at approximately 93 Hz, or around a $1/131^{st}$ of TPF. The variation in torque levels on the 2D simulation of the toothless gear, and the frequency of these variations, are much less than for the toothed gear, being in the order of 1% for the toothless gear, and 20% for the toothed gear in anti-clockwise rotation.

5.3.4 Flow structures

In this section, details of the flow structures present will be discussed. Due to the different velocity ranges present, there is a need to non-dimensionalize the velocities that are plotted. One way of doing this is through the use of a swirl coefficient, defined as

$$S_w = \frac{u_\theta}{r\Omega}. \tag{5.1}$$

This gives the ratio of the tangential velocity to the grid tangential velocity, and is non-dimensional, allowing comparisons between the flow structure at different values of Ω to be made more readily. Fig. 5.16 presents plots of the swirl coefficient on the plane that runs through the centre of the tooth valley, at three rotational speeds, for clockwise rotation, using the three-dimensional model. Essentially this figure shows that the region in which there is significantly swirling flow is very similar at all three shaft speeds. There is slightly higher swirl coefficient between the gear and the back plate at higher rotation speeds although this is not particularly significant. The bulk flow can be ascertained from these plots: air is being drawn in perpendicularly to the forward facing rotating surfaces, and is then being ejected parallel to the valley until impinging on the back wall. Figure 5.17 shows swirl coefficient contours for the anticlockwise direction of rotation, again on the plane that runs through the valley. The bulk flow structure is similar to that for clockwise rotation, but areas of higher velocities are present away from the gear teeth,

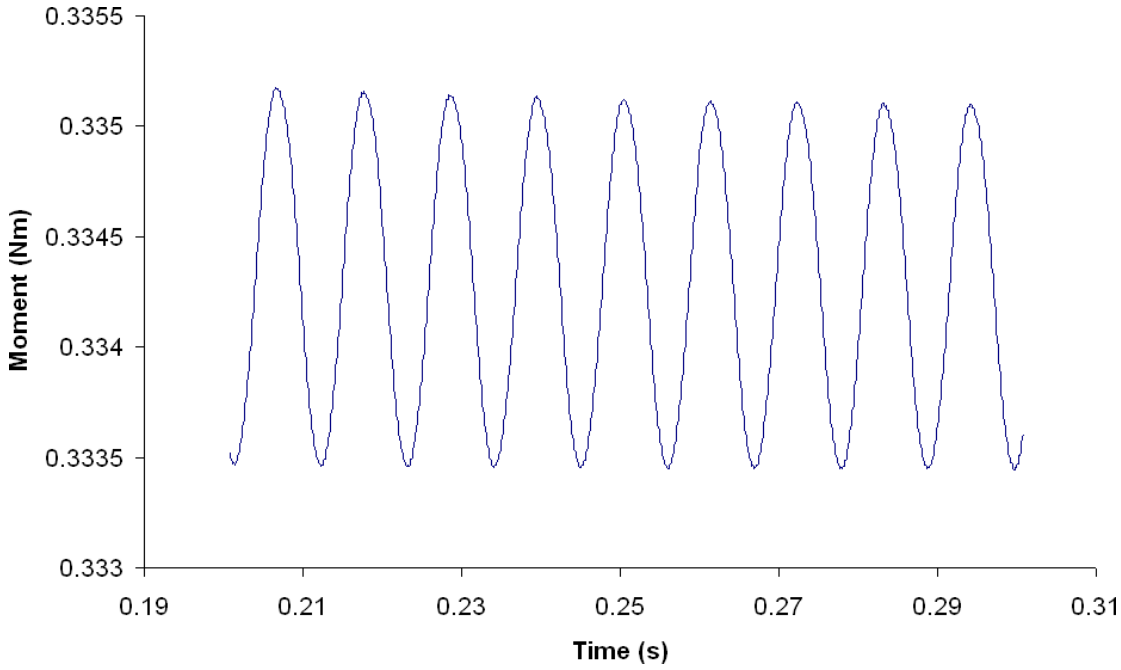

(a) Variation in torque levels over time.

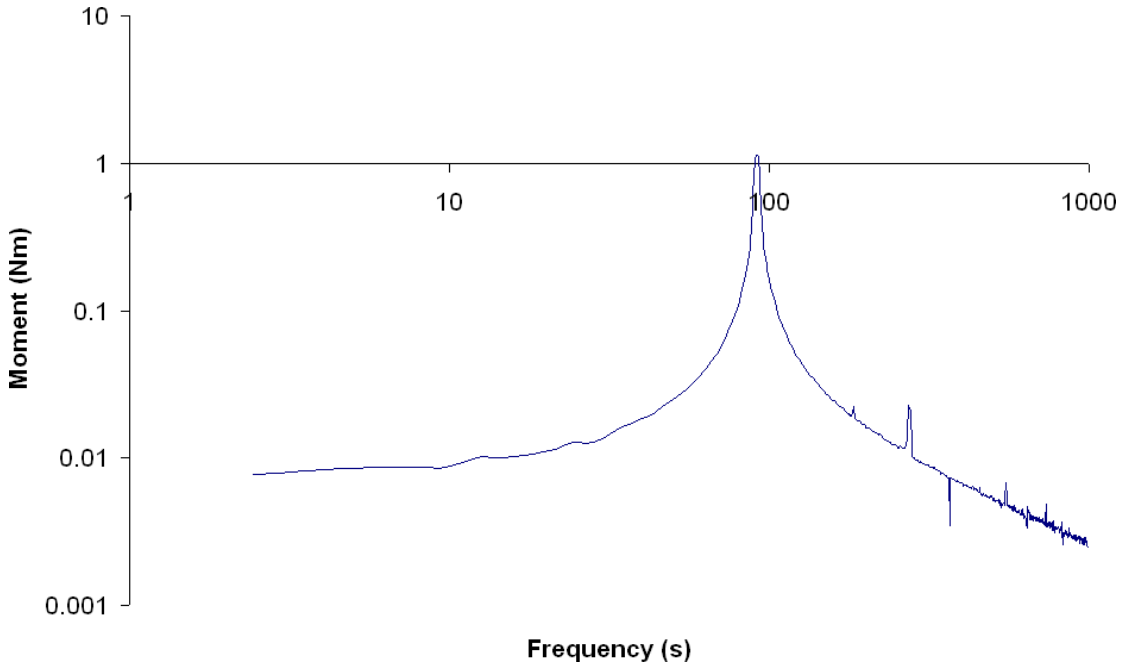

(b) Frequencies present in Fig. 5.15(a)

Figure 5.15: Graphs of Time Variance in the Moment Coefficient for the two dimensional model, and Fourier analysis of the variance.

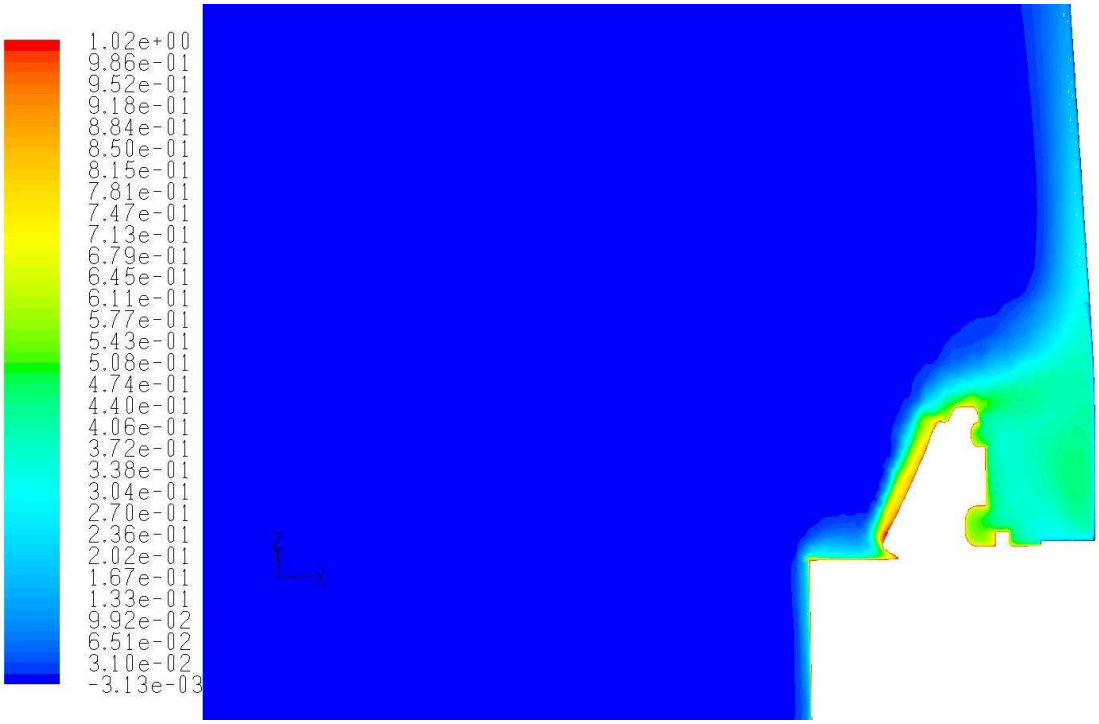

(a) 6708 RPM

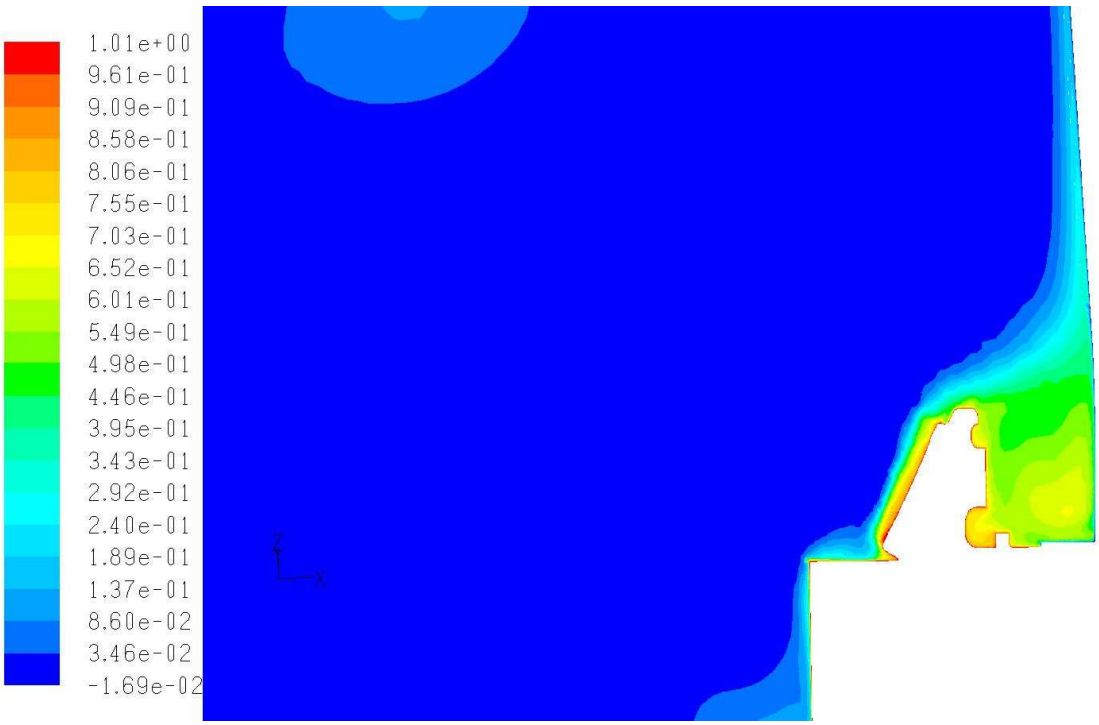

(b) 15000 RPM

Figure 5.16: Contours of swirl coefficient, clockwise rotation.

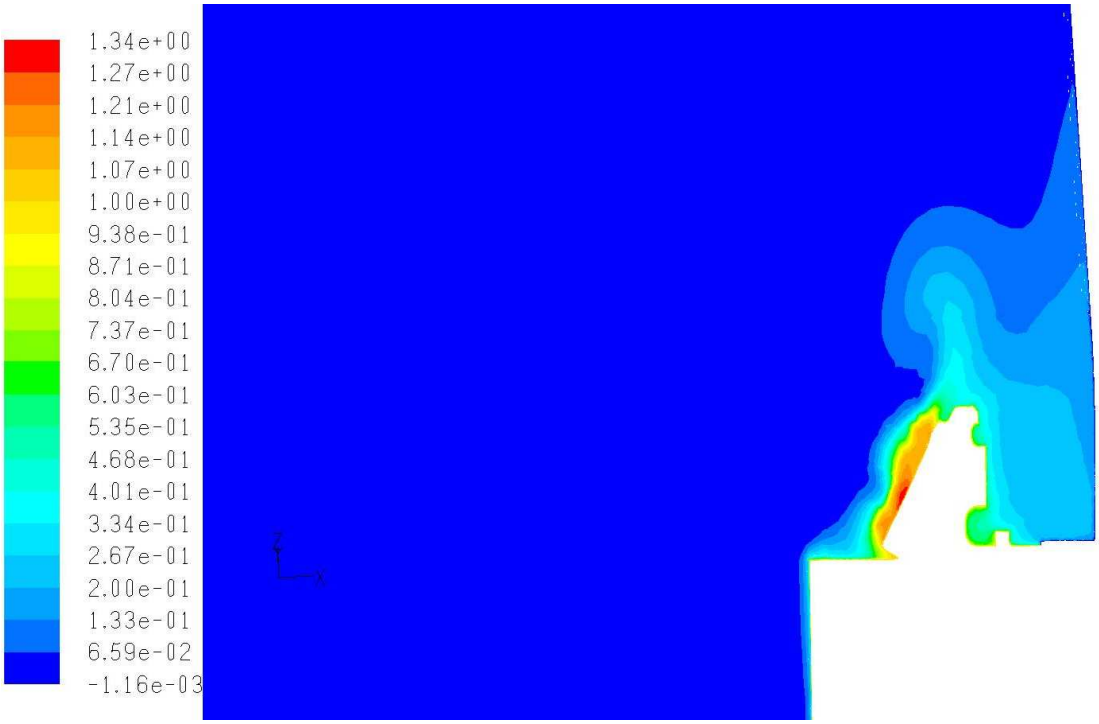

(a) 8203 RPM

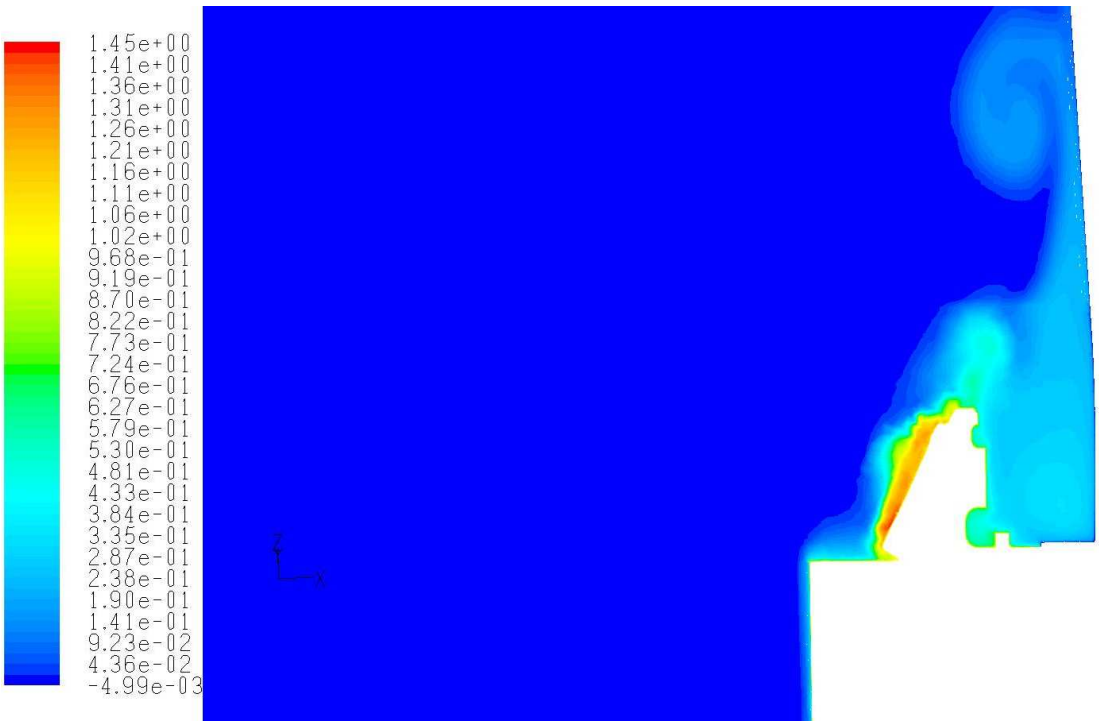

(b) 15000 RPM

Figure 5.17: Contours of swirl coefficient, anticlockwise rotation

with tangential velocities reaching values higher than tip velocity. The flow through the teeth appears far less smooth and this is probably evidence of the time-varying nature of the flow in the anticlockwise direction that cannot be adequately resolved by the steady-state calculation. More importantly, there appears to be far more flow through the teeth for rotation in the clockwise direction compared to the anticlockwise direction and this is undoubtedly significant when accounting for the lower windage power loss in the anticlockwise direction.

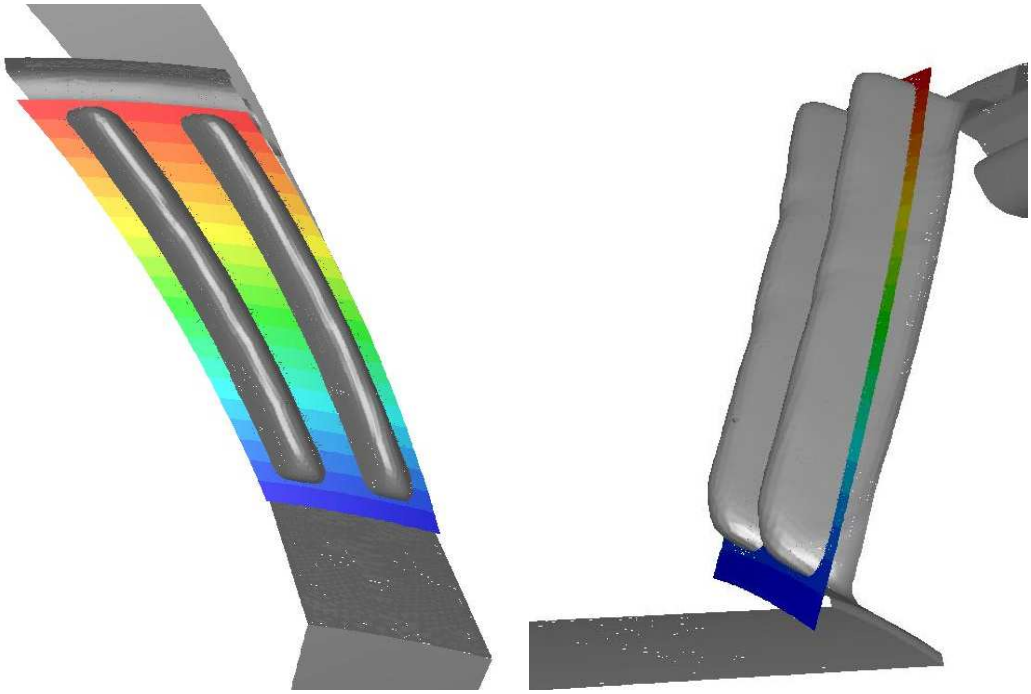

(a) x plane (b) y plane

Figure 5.18: Orientation in plane upon which velocity vectors are plotted in Figures 5.19-5.24

Figures 5.19 & 5.20 shows vectors relative to the rotating reference frame, showing a clear difference in the flow structure in both directions (the views are aligned with the axis to the right of the image). The flow in the clockwise direction (Fig. 5.19) is very 'smooth', with the vectors aligned with the tooth curvature, and very little sign of any recirculation visible. Much more complex is the flow for anti-clockwise rotation (Fig. 5.20), in which a vortex can be seen in the lower half of the tooth gap. If attention is turned to the transient flow, this vortex can be seen to be processing up the tooth valley

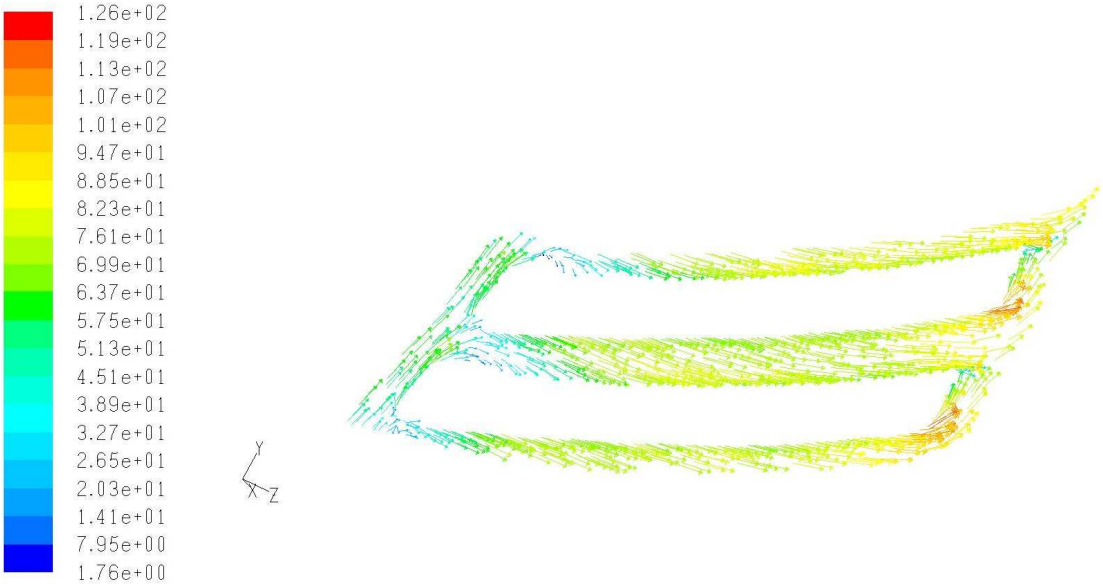

Figure 5.19: Vectors relative to reference frame in plane $1/3^{\text{rd}}$ of way up tooth flank, coloured by relative velocity magnitude ($m\ s^{-1}$), +8203 RPM. Orientation given in Fig. 5.18

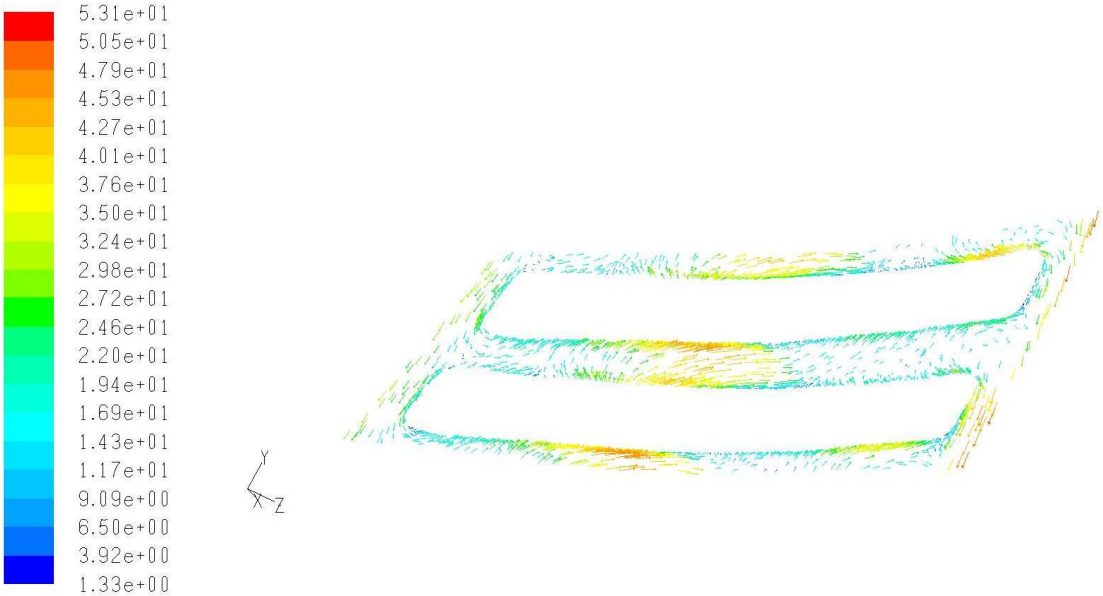

Figure 5.20: Vectors relative to reference frame in plane $1/3^{\text{rd}}$ of way up tooth flank, coloured by relative velocity magnitude ($m\ s^{-1}$), −8203 RPM. Orientation given in Fig. 5.18

(Fig. 5.21-5.24). Through the use of animations of the flow, it has been observed that vortices are being shed off the gear teeth, as shown in Figure 5.21-5.24. The dominant frequency, 730Hz, matches the rate that these vortices are shed off the gear teeth.

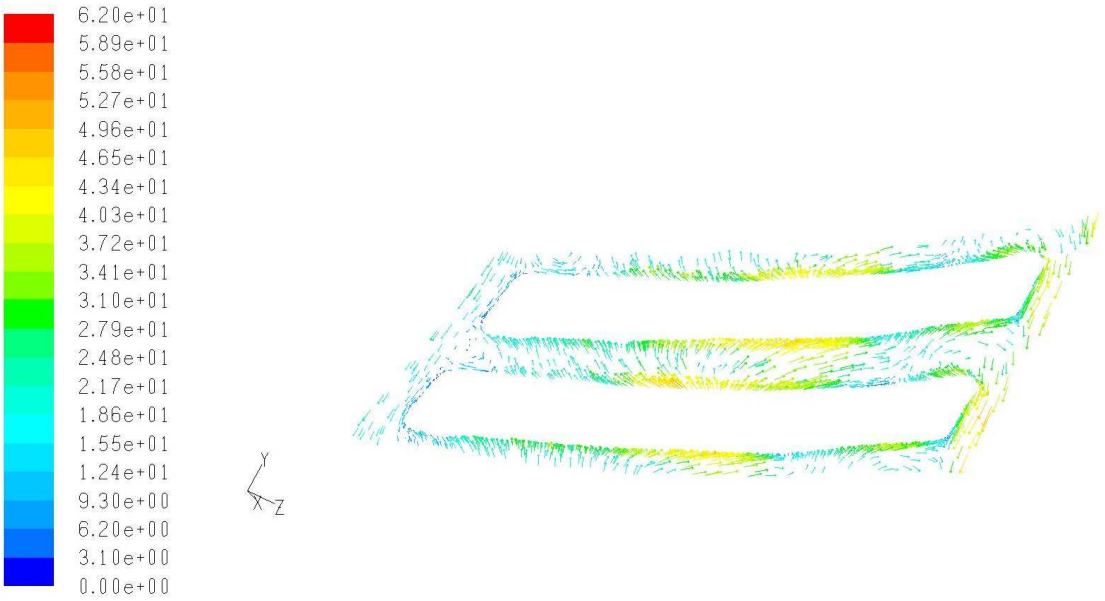

Figure 5.21: Vectors relative to reference frame in plane $1/3^{\text{rd}}$ of way up tooth flank, coloured by relative velocity magnitude ($m\ s^{-1}$), -8203 RPM, $t = t_0$. Orientation given in Fig. 5.18

Figure 5.25 shows tangential velocity, plotted on a plane through the centre of the tooth valley, at different times during the transient calculation. Taking the initial plot (5.25(a)) at t_0, subsequent plots are at intervals of $\simeq 9.64 \times 10^{-5}$ms, which represents $\simeq 60\%$ of the tooth passing time length. From these, clear signs of a structure passing up the valley can be observed. Over all, it appears that there is transience in the flow behaviour in the anticlockwise direction of rotation. It is also useful to understand how the vortices are linked to variations in the pressure close to the gear. By studying the static pressure at 7 locations close to the gear (Fig. 5.26), the time varying nature of the pressure levels can be seen (Fig. 5.27(a)-5.29(b)). Figures 5.3.4-5.3.4 present plots of pressure variation over time at 7 locations near to the gear surface, along with Fourier analyses of the variations, for anti-clockwise rotation at $15,000$ RPM. It can be seen that at the three points upstream of the gear (A, B and C in Figures 5.3.4 & 5.3.4) there is fluctuation in the static pressure that is dominated by a frequency of $\simeq 1300$ Hz, which is $\simeq 1/17^{\text{th}}$ of tooth passing frequency. A secondary frequency is also apparent

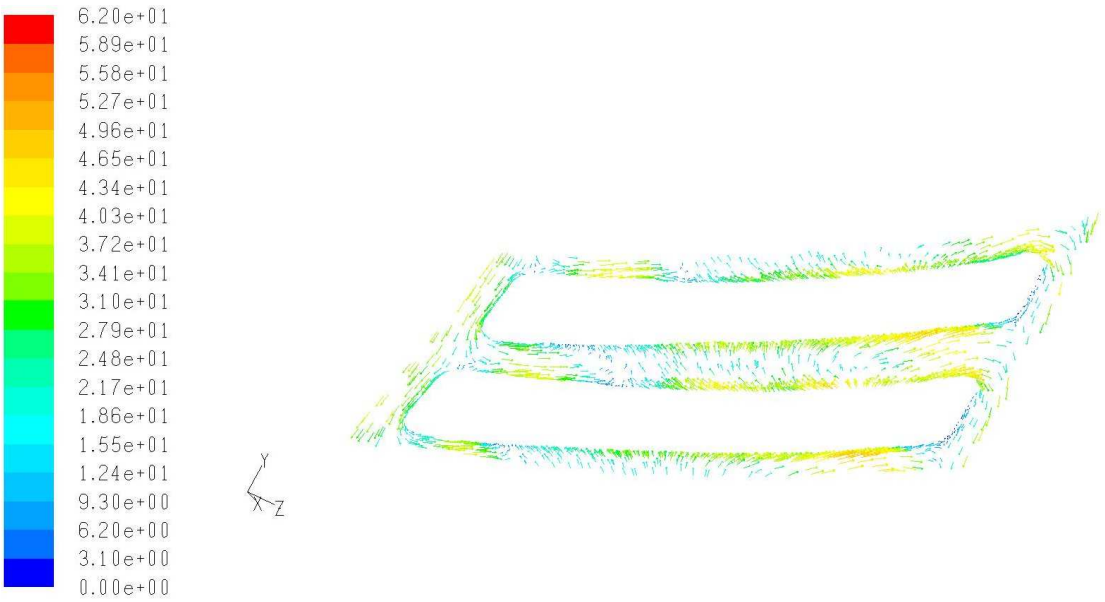

Figure 5.22: Vectors relative to reference frame in plane $1/3^{\text{rd}}$ of way up tooth flank, coloured by relative velocity magnitude ($m\ s^{-1}$), -8203 RPM, $t = t_0 + 0.402ms$. Orientation given in Fig. 5.18

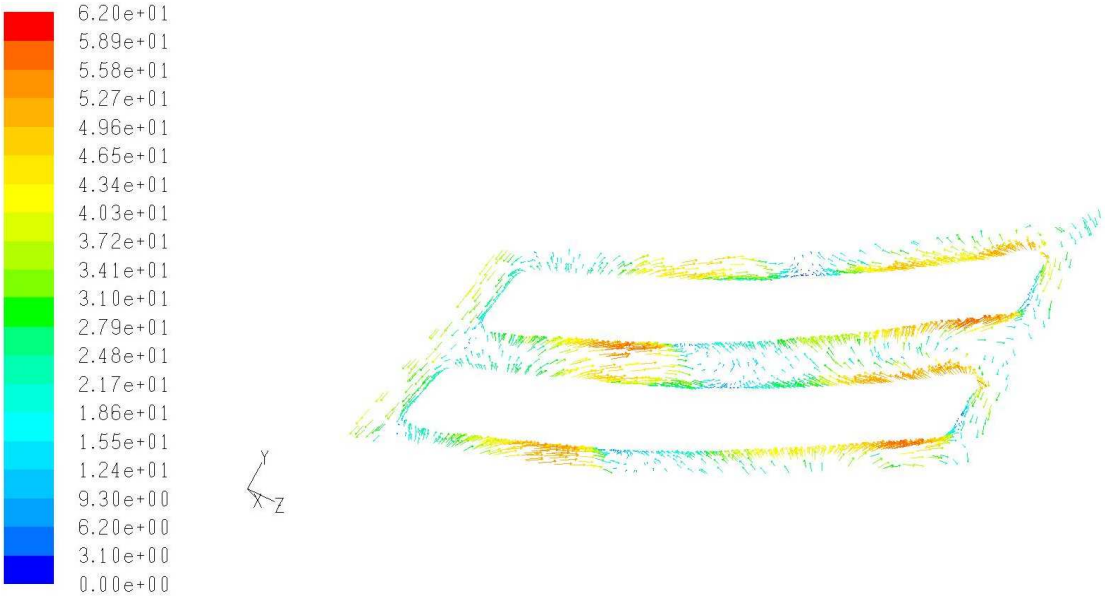

Figure 5.23: Vectors relative to reference frame in plane $1/3^{\text{rd}}$ of way up tooth flank, coloured by relative velocity magnitude ($m\ s^{-1}$), -8203 RPM, $t = t_0 + 0.804ms$. Orientation given in Fig. 5.18

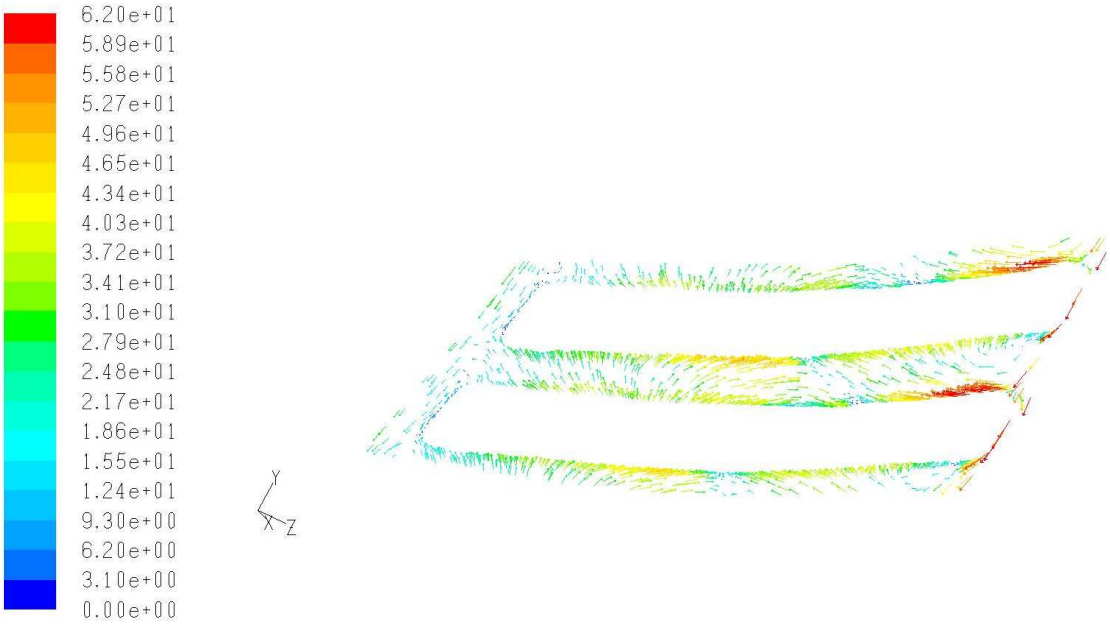

Figure 5.24: Vectors relative to reference frame in plane $1/3^{\text{rd}}$ of way up tooth flank, coloured by relative velocity magnitude ($m\ s^{-1}$), -8203 RPM, $t = t_0 + 1.206ms$. Orientation given in Fig. 5.18

at a value of $\simeq 2280$ Hz, which is $\simeq 1/10^{\text{th}}$ of tooth passing frequency. For the points further along the gear (D-G in Figures 5.3.4 & 5.3.4), more fluctuations are present, with a dominant frequency again at $\simeq 1/17^{\text{th}}$ of tooth passing frequency. The secondary frequency increases as consideration moves from point C to D, changing from $\simeq 1/10^{\text{th}}$ to $\simeq 1/9^{\text{th}}$ of tooth passing frequency. Secondary frequencies of $\simeq 1/9^{\text{th}}$ and $\simeq 1/6^{\text{th}}$ of tooth passing frequency are present at points E and F. These have dissipated at point G, with the only clear secondary frequency being at $\simeq 1/12^{\text{th}}$ of tooth passing frequency.

For the open gear case the windage power loss is lower when the gear rotates in the clockwise direction compared to the anticlockwise direction. Examination of Fig. 5.1 shows that for clockwise rotation the curvature of the teeth is such that the flow through the tooth valley is encouraged, whereas in the anticlockwise direction this flow is discouraged. In normal operation therefore one might expect lower friction losses in the anticlockwise direction. Comparison of Figures 5.16 and 5.17 confirms this with Fig. 5.16 (anticlockwise) showing more swirl and a less dominant throughflow.

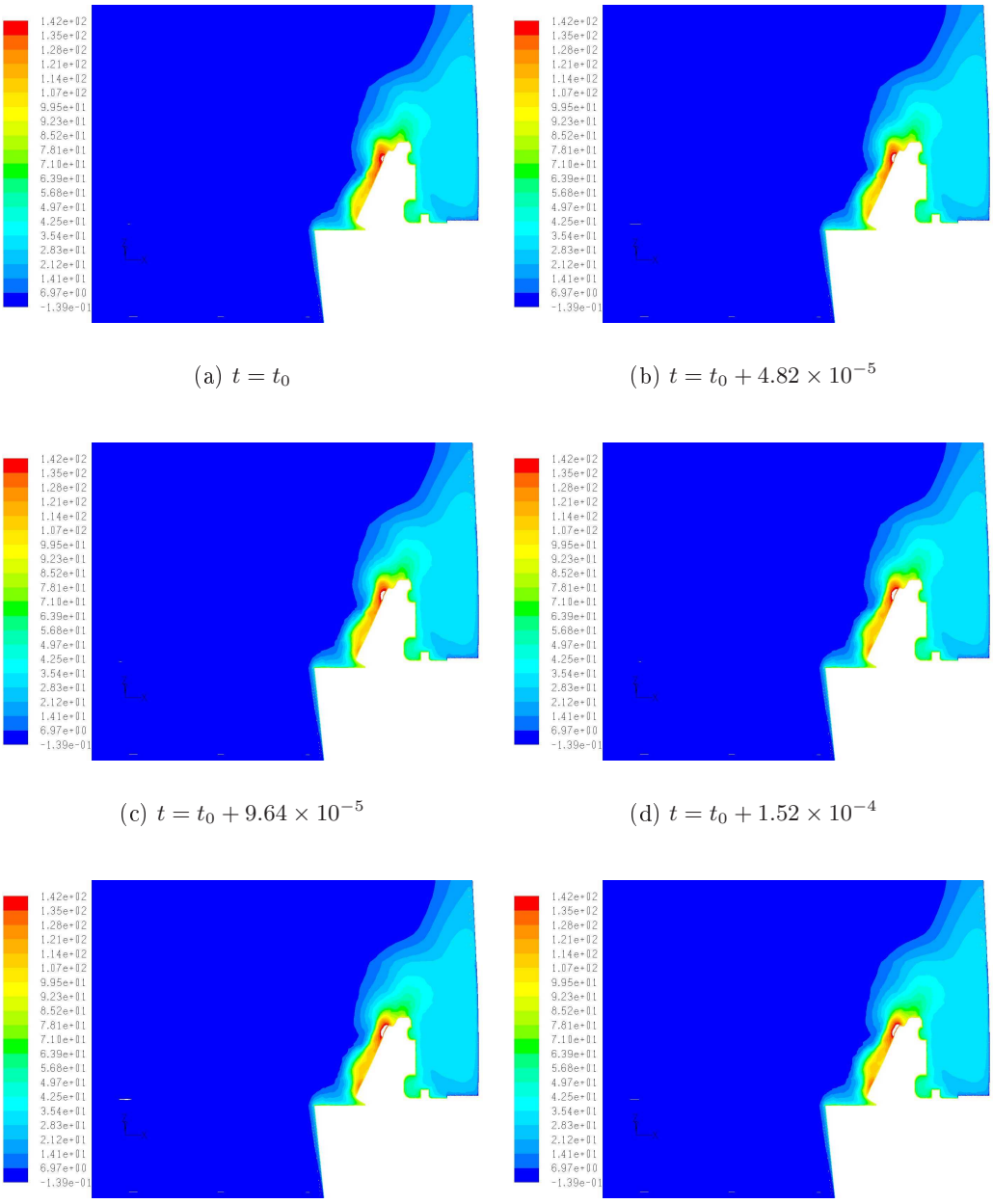

(a) $t = t_0$

(b) $t = t_0 + 4.82 \times 10^{-5}$

(c) $t = t_0 + 9.64 \times 10^{-5}$

(d) $t = t_0 + 1.52 \times 10^{-4}$

(e) $t = t_0 + 2.00 \times 10^{-4}$

(f) $t = t_0 + 2.49 \times 10^{-4}$

Figure 5.25: Contours of tangential velocity ($m\ s^{-1}$) on periodic boundary, 8203 RPM. Figure 5.25 continues.

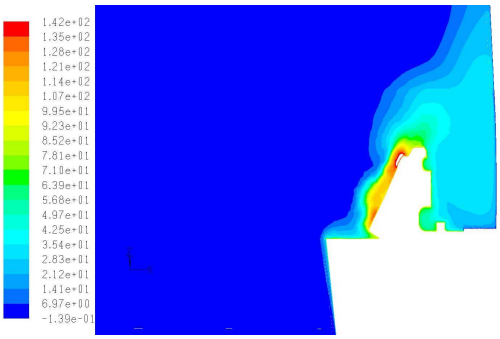

(g) $t = t_0 + 2.97 \times 10^{-4}$

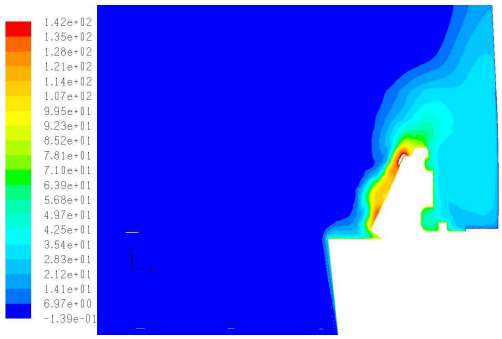

(h) $t = t_0 + 3.46 \times 10^{-4}$

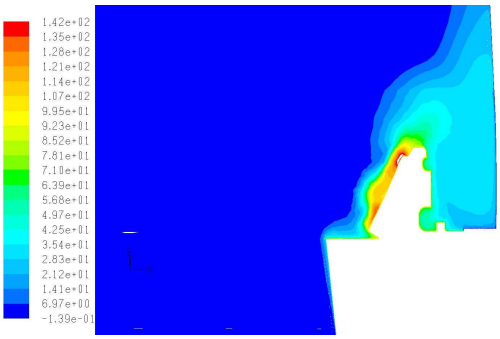

(i) $t = t_0 + 3.94 \times 10^{-4}$

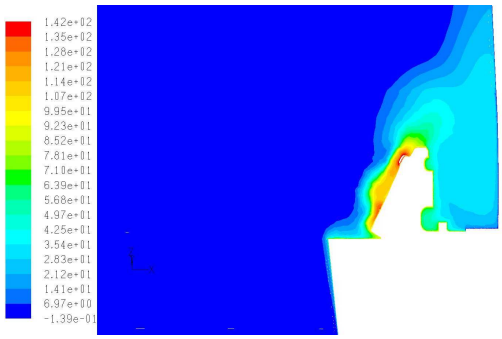

(j) $t = t_0 + 4.42 \times 10^{-4}$

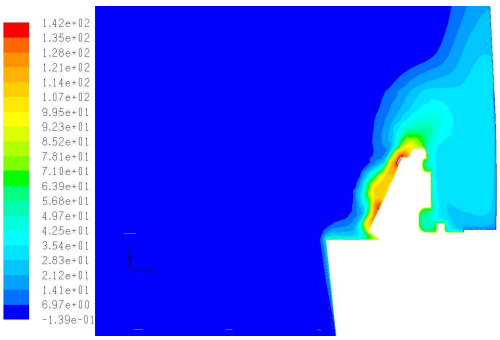

(k) $t = t_0 + 4.90 \times 10^{-4}$

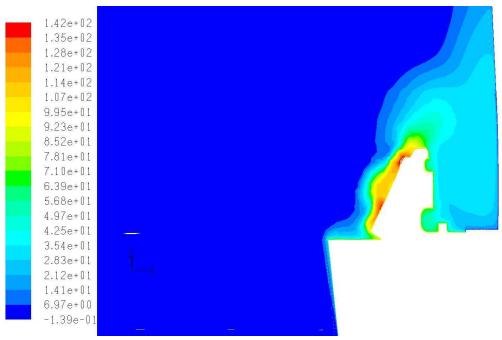

(l) $t = t_0 + 5.39 \times 10^{-4}$

Figure 5.25: Contours of tangential velocity ($m\ s^{-1}$) on periodic boundary, 8203 RPM. Figure 5.25 continues.

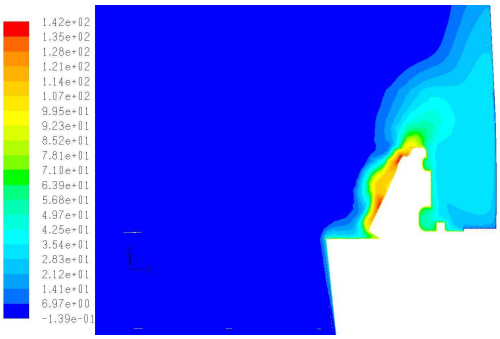

(m) $t = t_0 + 5.87 \times 10^{-4}$

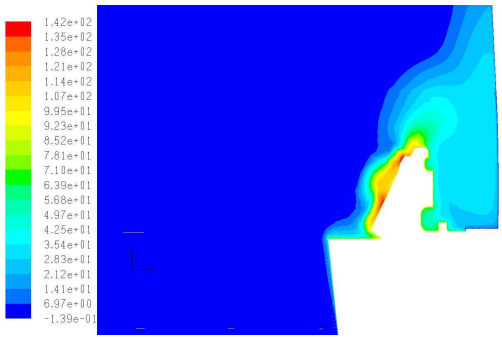

(n) $t = t_0 + 6.19 \times 10^{-4}$

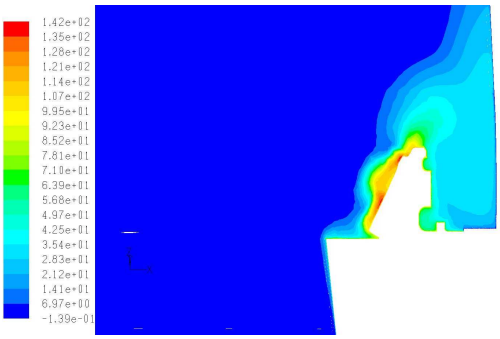

(o) $t = t_0 + 6.67 \times 10^{-4}$

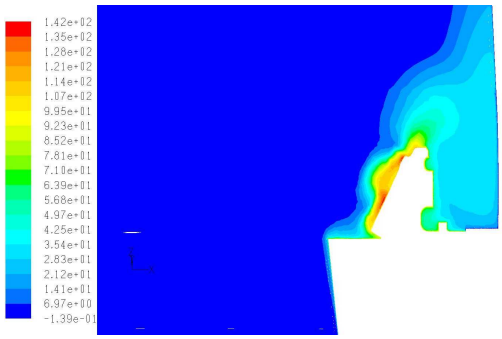

(p) $t = t_0 + 7.07 \times 10^{-4}$

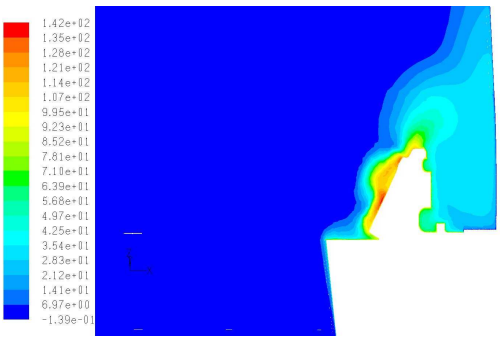

(q) $t = t_0 + 7.56 \times 10^{-4}$

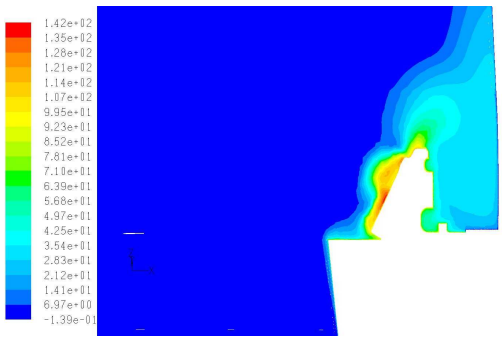

(r) $t = t_0 + 8.04 \times 10^{-4}$

Figure 5.25: Contours of tangential velocity ($m\ s^{-1}$) on periodic boundary, 8203 RPM. Figure 5.25 continues.

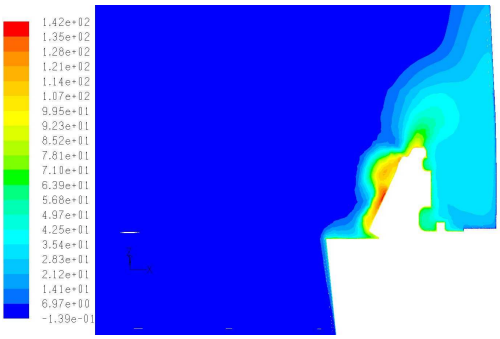

(s) $t = t_0 + 8.52 \times 10^{-4}$

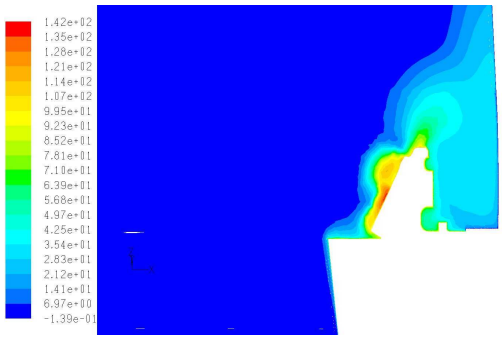

(t) $t = t_0 + 9.00 \times 10^{-4}$

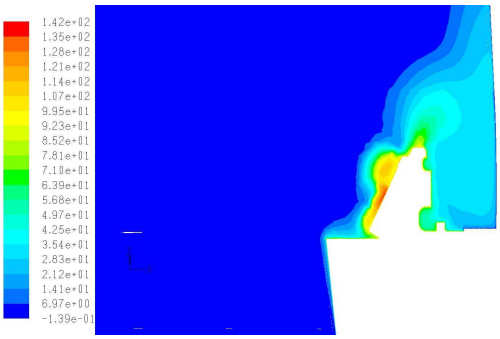

(u) $t = t_0 + 9.48 \times 10^{-4}$

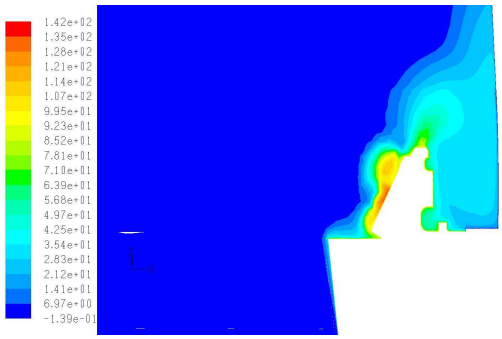

(v) $t = t_0 + 9.97 \times 10^{-4}$

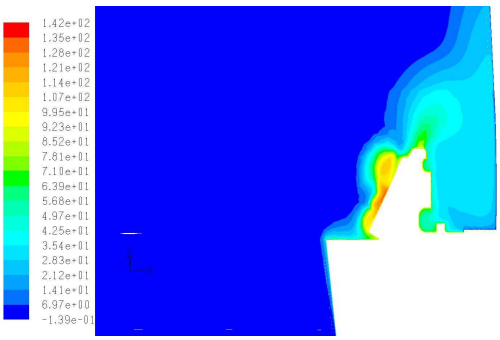

(w) $t = t_0 + 1.04 \times 10^{-3}$

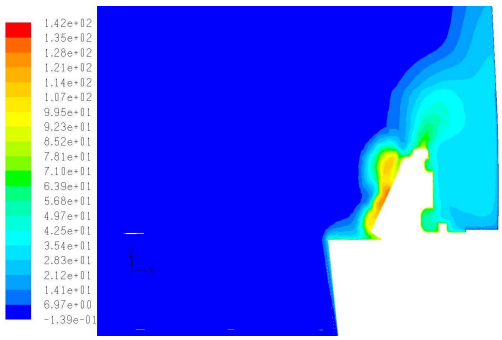

(x) $t = t_0 + 1.09 \times 10^{-3}$

Figure 5.25: Contours of tangential velocity ($m\ s^{-1}$) on periodic boundary, 8203 RPM. Figure 5.25 continues.

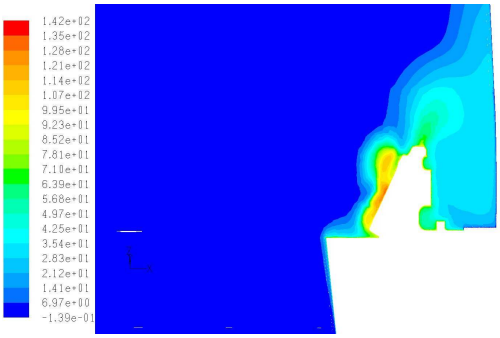

(y) $t = t_0 + 1.14 \times 10^{-3}$

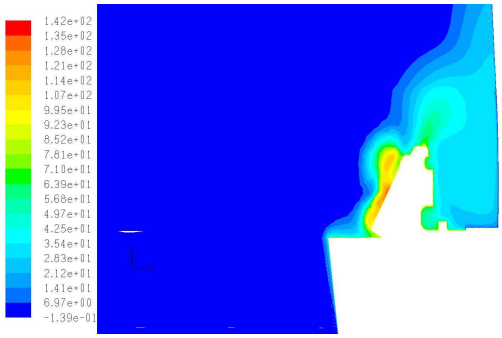

(z) $t = t_0 + 1.19 \times 10^{-3}$

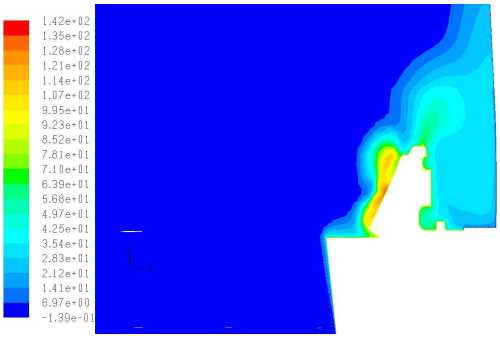

(Aa) $t = t_0 + 1.24 \times 10^{-3}$

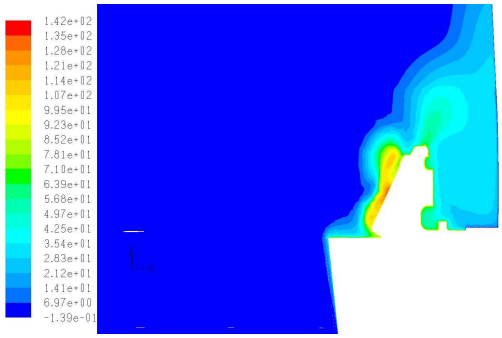

(Ab) $t = t_0 + 1.29 \times 10^{-3}$

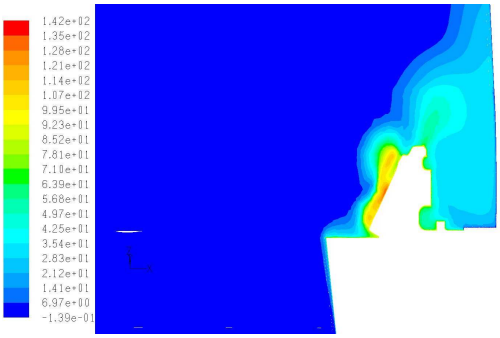

(Ac) $t = t_0 + 1.33 \times 10^{-3}$

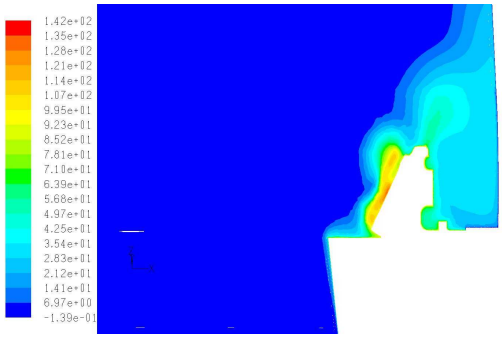

(Ad) $t = t_0 + 1.38 \times 10^{-3}$

Figure 5.25: Contours of tangential velocity ($m\ s^{-1}$) on periodic boundary, 8203 RPM.

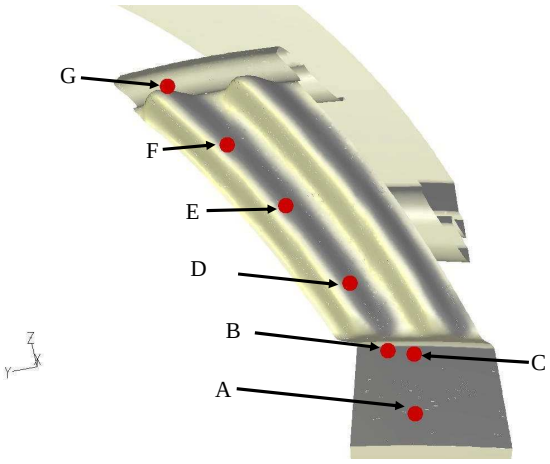

(a) x view

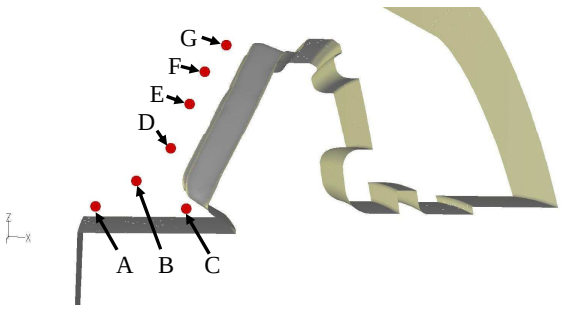

(b) y view

Figure 5.26: Locations for which pressure is monitored in Figures 5.27(a) to 5.29(b)

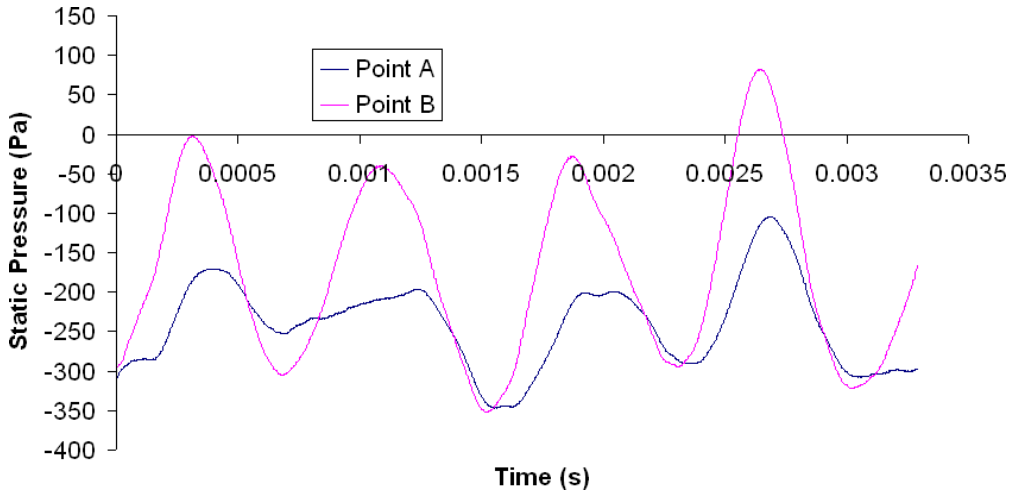

(a) Graph of Static Pressure at points A and B against Time, in anti-clockwise direction, 15000 RPM, showing variation in static pressure levels over time.

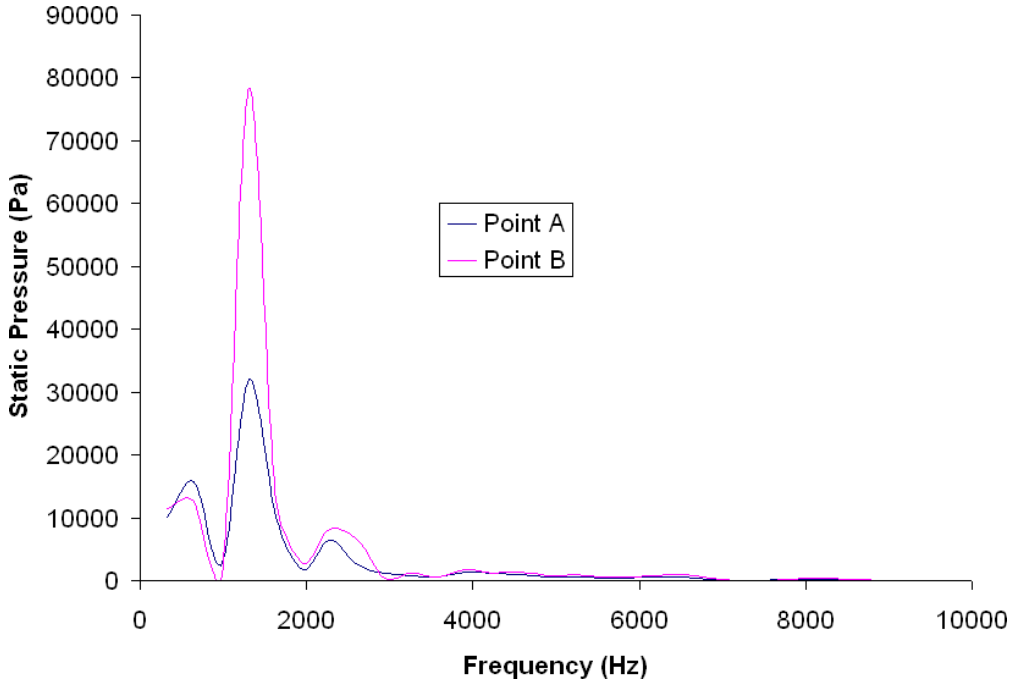

(b) Graph of Frequency against Power Spectral Density, in anti-clockwise direction, 15000 RPM, showing frequencies present in Fig. 5.27(a).

Figure 5.27: Static pressure variation at A and B over time, $\Omega = -15000$ RPM

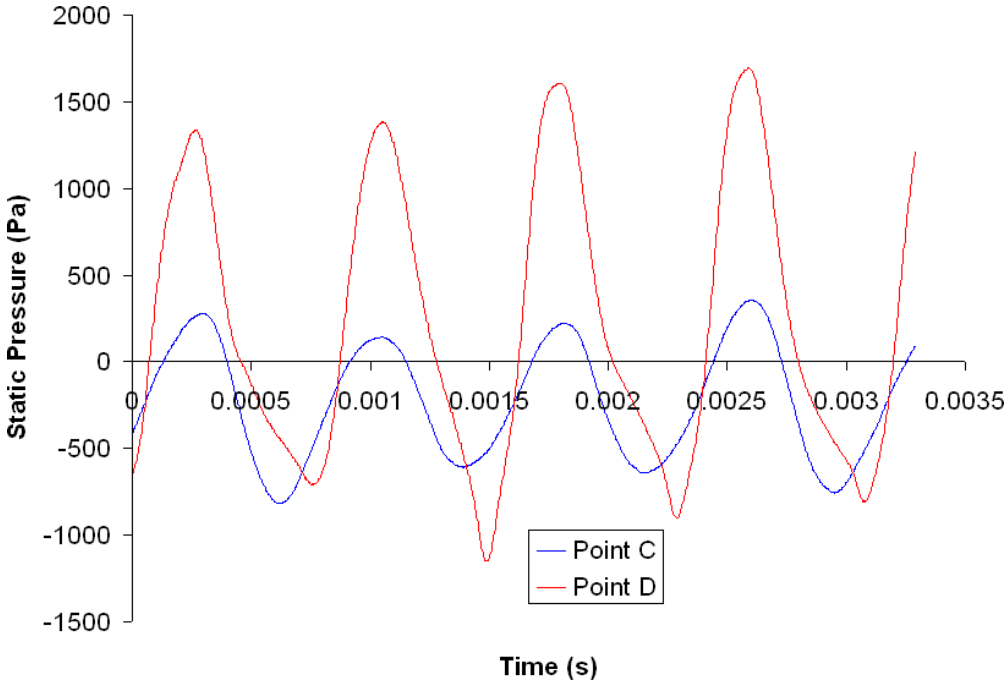

(a) Graph of Static Pressure at points C and D against Time, in anti-clockwise direction, 15000 RPM, showing variation in static pressure levels over time.

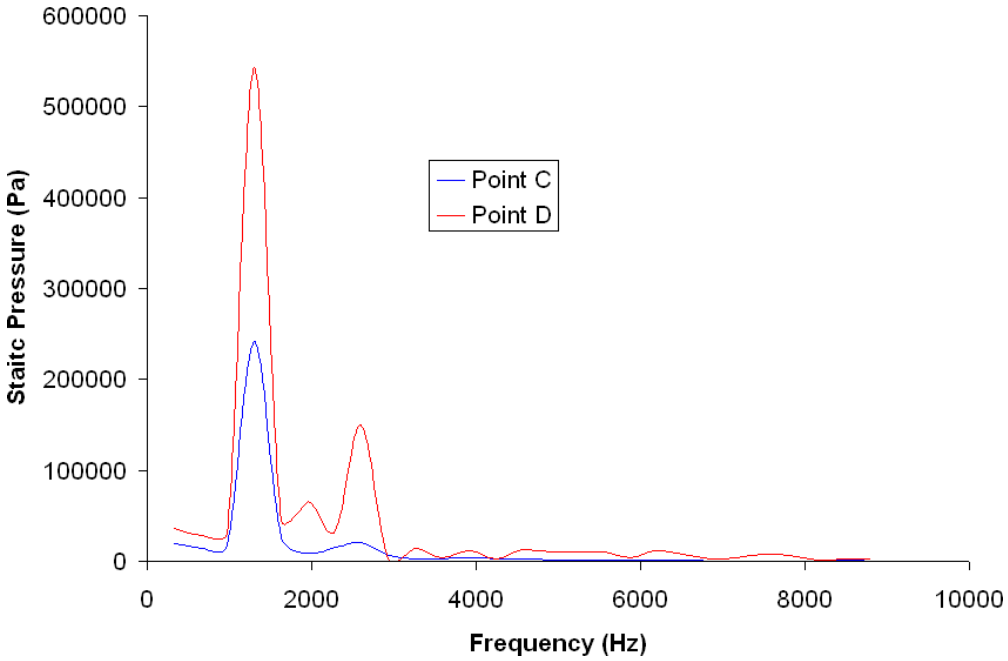

(b) Graph of Frequency against Power Spectral Density, in anti-clockwise direction, 15000 RPM, showing frequencies present in Fig. 5.28(a).

Figure 5.28: Static pressure variation at C and D over time, $\Omega = -15000$ RPM

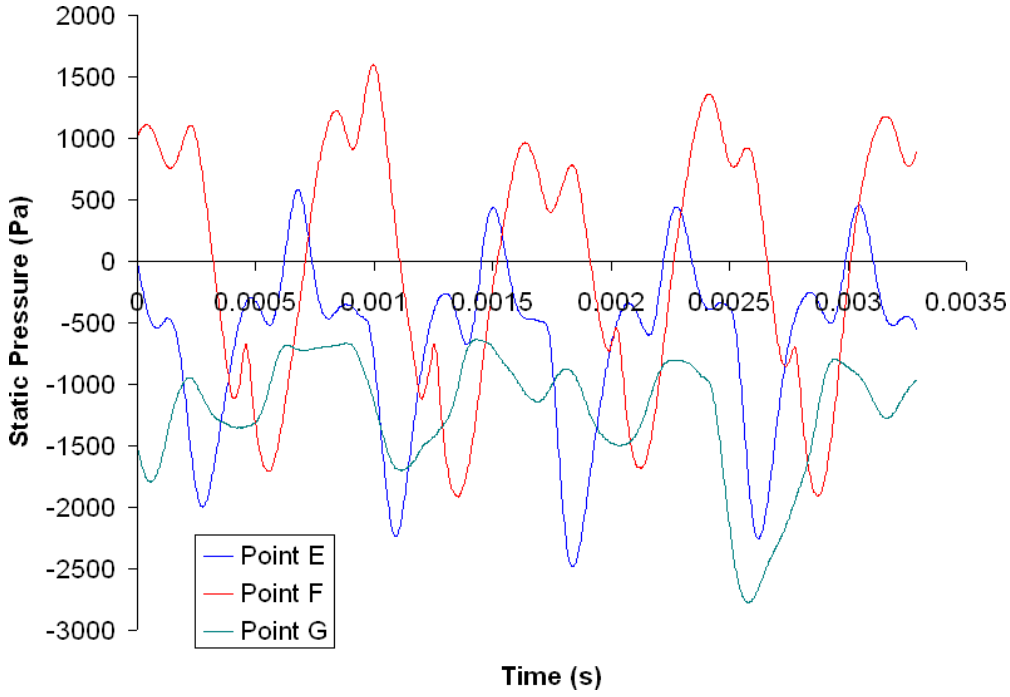

(a) Graph of Static Pressure at points E, F and G against Time, in anti-clockwise direction, 15000 RPM, showing variation in static pressure levels over time.

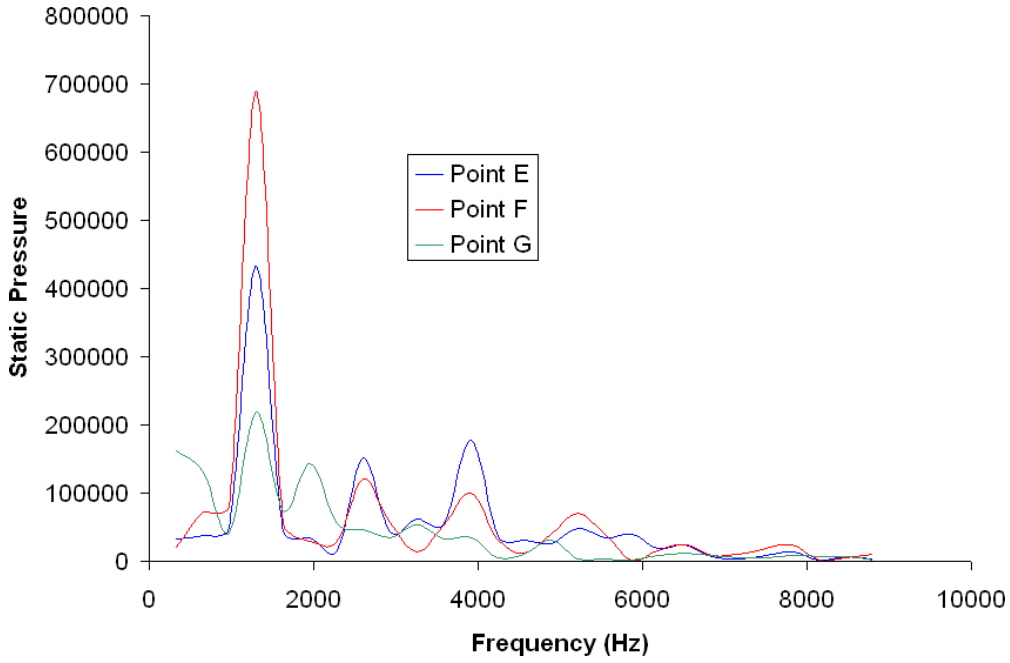

(b) Graph of Frequency against Power Spectral Density, in anti-clockwise direction, 15000 RPM, showing frequencies present in Fig. 5.29(a).

Figure 5.29: Static pressure variation at E, F and G over time, $\Omega = -15000$ RPM

5.4 Summary

Numerical models for the flow around an un-shrouded spiral bevel gear have been presented, studying the effect the direction of rotation may have upon the flow. In the clockwise direction, results have been presented in a steady state formulation using a RNG $k-\epsilon$ turbulence model. Two different models for near-wall flow have been used (a standard wall function and an enhanced wall treatment). Little difference has been observed between the results from these two models (Fig. 5.11), both of which under-predict experimental torque values by approximately 24%.

For anti-clockwise rotation, steady-state results have been presented using a RNG $k-\epsilon$ turbulence model with a standard wall function and also with an enhanced wall treatment. The standard wall function under-predicting torque levels by approximately 31% and the enhanced wall treatment predicting to within approximately 3.8% of the experimental value. In this case, the results from the steady-state formulation using the enhanced wall treatment were showing signs of transience, and so transient modelling of the flow was conducted. Transient results have been presented for the anti-clockwise direction at 8203 and 15,000 RPM, under-predicting torque levels by 2% and 11% respectively. Computations were conducted at 8203 RPM initially, as the flow is outside the region where compressibility effects would be significant. Further computations were conducted at 15,000RPM, as it represented the extreme of the velocity range. Interestingly, the average of the torque obtained using a steady-state formulation in both cases is a better prediction of the torque levels than those obtained using a transient formulation. At both speeds, time variance could be seen in torque levels on the gear surface, and in pressure levels with in the flow close to the gear surface.transient flow, with scalable dominant and secondary frequencies present in both cases at approximately $1/17^{\text{th}}$ and $1/10^{\text{th}}$ of tooth passing frequency, or $1/1547^{\text{th}}$ and $1/910^{\text{th}}$ of angular frequency. Results have also been presented for a two dimensional model of a toothless gear, modelled transiently. This showed far lower frequencies present within the flow, at approximately $1/12000^{\text{th}}$ of the angular frequency. Analysis of the flow structure has been presented, showing that the transience in torque levels is due to vortices being shed off of the gear teeth, a phenomenon which occurs at the same frequencies as the

dominant and secondary frequencies in the torque signal.

The work presented in this chapter has aided the development of the modelling strategy. At the start of this chapter, two clear questions remained for the strategy: how to model the near-wall flows, and whether the flow needs to be modelled in a transient setting. The results presented could be used to support the use of either approach studied for the near-wall flow. Standard wall functions show greater consistency when looking at effects due to rotation direction, whilst the enhanced wall treatment shows greater accuracy for anti-clockwise rotation. This implies the standard approach is good for qualitative analysis, whereas the enhanced approach may be better for quantitative analysis. As the second aim of this thesis is to apply the developed to strategy to a series of parametric variations of the shroud parameters to determine which produces the 'best' performance, that is the lowest power loss, which is a qualitative problem, it may be that the standard wall function is the 'better' model to use. However, it is felt that this question is still open, so further investigations will be conducted on this issue in the following chapter.

The second question of whether to model transience is much clearer. Results in this chapter have shown clear transience visible for anti-clockwise rotation, although no signs of this were apparent for clockwise rotation. It suggests that the flow should be modelled transiently for a bevel gear, as transience may well be evident. The fact that the behaviour seen for anti-clockwise rotation scales with speed implies that a 'test' case can be run for a geometry to investigate whether transience is evident, before running at all desired speeds.

The work presented in this chapter allows the following points to be added to the strategy:

- if the steady-state solution fails to converge after a significant amount of iterations, without diverging, the flow may well be transient, and should be modelled as such to confirm (or deny) this
- complex geometries can be meshed using unstructured meshes with size functions to capture the boundary layer

Chapter 6

Shrouded Gear

In this chapter a computational study of the flow around a shrouded spiral bevel gear is presented and the data is compared to available experimental data [24, 25][1]. The models are generated using the modelling strategy developed in chapters 4 & 5. Results are compared for clockwise and anticlockwise rotation with two experimental shrouded configurations. Reasonable agreement of the computational data with the experimental data is obtained. For the shrouded configuration, static pressure profiles along the shroud are compared to experimental data. The effect of different computational wall treatments is examined. The strategy is then applied to a series of parametric variations of the shroud geometry to investigate their affects on windage power loss. These variants highlight the effects that changing the geometry can have, and lead to suggestions for improvements in shroud design.

6.1 Experimental Setting

The gear is as shown in the previous chapter in Fig. 5.1. It has 91 teeth, an outer radius of 133.5mm, and a module of 2.92mm. In this study, the flow is single phase, operating at atmospheric pressures. A single gear is modelled. Rotational speeds vary from 0 to 15,000 RPM, in either rotational direction, giving tip velocities of up to 210ms^{-1}.

[1] Parts of this chapter have been published within [47, 48]

6.2 CFD Geometry and Boundary Conditions

The geometry modelled computationally was chosen to be as close as possible to that investigated experimentally. On the experimental test facility, illustrated in Fig. 5.2, the gear is mounted on a shaft which is connected through a series of bearings and a gearbox to a motor. The shaft passes through a back plate that isolates the test region from the driving section. In the shrouded configuration, Figure 6.1, in front of the gear is a flow-conditioning bullet. Consideration has been made to directional dependence within the flow, so calculations have been performed for both directions of gear rotation. A definition of rotational direction as used in this chapter is given in Fig. 5.1. This study is on a different to setting to that of §5 in that the gear is now enclosed in a shroud. A full description of the experimental apparatus is given by Johnson *et al.* [24]

In the experimental study two shrouded configurations were studied, one in which the inlet and outlet to the shroud were open to the atmospheric air within the room, and another in which air was supplied to the shroud at a controlled mass flow rate. In this latter configuration conditioning was applied to the air upstream of the shroud to encourage even entry to the shroud. It is this configuration that is illustrated in Fig. 6.1. Fig. 6.2 illustrates the geometry and boundary conditions for the single-tooth shrouded

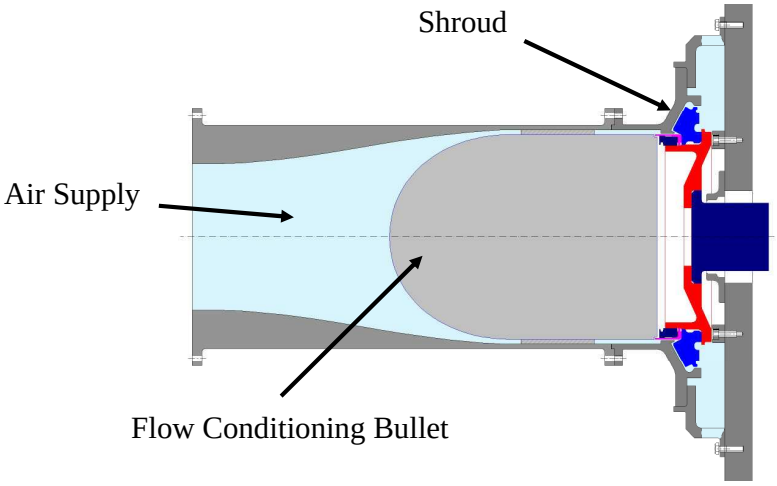

Figure 6.1: Shrouded configuration with air supply

cases. Referring to Fig. 6.2, air enters the computational domain through the mass flow inlet located 0.1m upstream of the gear in the axial direction. Flow conditions are approximated by specifying a mass flow rate. After passing through the gear system

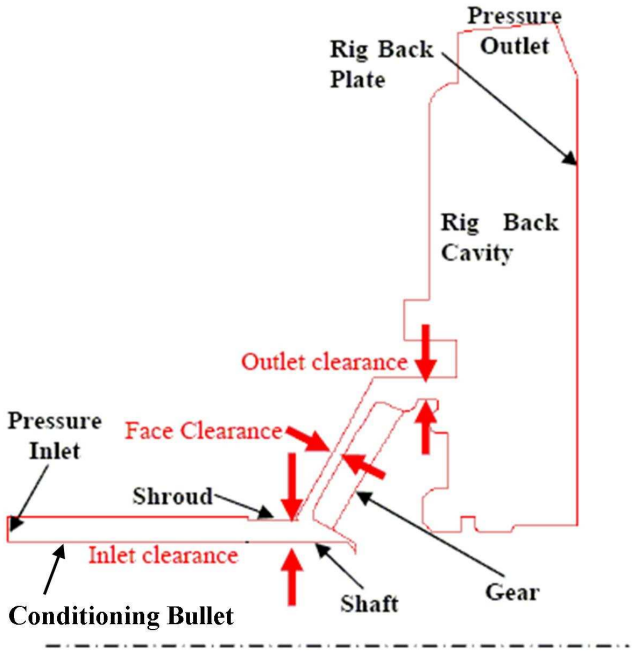

Figure 6.2: Boundary conditions for shrouded geometry. For the cases where a mass-flow rate is imposed, the pressure-inlet is replaced with a mass-flow inlet.

(past the section marked 'outlet clearance') the air, deflected radially outwards by the back plate, and leaves the computational domain through the pressure outlet. Ambient conditions at the outlet are represented by specifying a zero total gauge pressure. The turbulence quantities at the mass-flow/pressure inlet are calculated using

$$I = 0.16\mathrm{Re}_{D_H}^{-0.125} \tag{6.1}$$

where

$$\mathrm{Re}_{D_H} = \frac{\rho u_x D_H}{\mu} \tag{6.2}$$

The turbulence quantities at the pressure outlet (for backflow) are calculated from an imposed turbulence intensity of 10% (typical of room conditions) and a length scale appropriate to the outlet geometry. The gear and shaft are modelled as rotating walls with a no-slip condition applied. The stationary walls (the conditioning bullet, shroud, and back-wall) also have a no-slip condition imposed. In the azimuthal direction, a pair of periodic boundaries has been used. These pass along the bottom of the tooth valley, following the curvature of the teeth.

6.3 CFD Methodology

Single phase calculations of the air flow field and associated torques are obtained for a single crown gear using the commercial CFD code FLUENT (releases 6.2.16 & 6.2.17). The study uses three-dimensional CFD to calculate the air-flow and subsequent friction and turbulence losses. Computations have been carried out using a rotationally periodic volume. Models for the shrouded gear have one tooth, and contain up to $2,200,000$ cells. All models use unstructured, tetrahedral meshes, with hex cores, constructed using the commercial meshing program Gambit. Solutions for the single-phase airflow field, both steady state and transient, have been obtained. Simulations are performed using a rotating reference frame and an absolute velocity formulation. Computations correspond to shaft speeds between 3000 RPM and $15,000$ RPM, resulting in a Mach number in the vicinity of the gear teeth reaching values of the order of 0.7. For this reason, at the higher rotational rates ($\Omega \geq 10,031$ RPM) a compressible calculation has been performed taking air as an ideal gas. Convergence of the solution has been monitored in two manners. Primarily, in the manner described in §3.12. The convergence has also been monitored in the steady-state cases by monitoring the torque levels on the rotating surfaces. Convergence has been deemed to be achieved when the torque levels over 200 iterations vary by less than 3% and all the residuals have values less than 10^{-4}, with the residuals of the turbulent quantities have values less than 10^{-6}. Turbulence is modelled using the RNG $k-\epsilon$ model [63, 64] as the work in proceeding chapters has shown this to be the optimum two-equation turbulence model for this work, as well as being a two-equation model widely used in industry. A second order upwind differencing scheme has been used to discretise the governing equations.

6.4 Experimental Validation

Experimental data obtained on the test rig in Fig. 5.1 will be used for validation of the CFD models [24, 25] as described previously (§5.3.1) In the following sections, unless stated otherwise, all results are obtained using the RNG $k-\epsilon$ turbulence model, with enhanced wall treatment, and are steady state, isothermal, and incompressible.

In this section, the results from the shrouded calculations are presented. The mass flow rate through the shroud is an independent variable in these calculations as it is an imposed boundary condition and has been non-dimensionalised using a throughflow coefficient, C_Q:

$$C_Q = \frac{Q}{\Omega R_i^3} \tag{6.3}$$

Results will be plotted for the throughflow coefficient against the moment coefficient. To recap, the moment coefficient is:

$$C_M = \frac{M}{1/2\rho\Omega^2 R_o^5} \tag{6.4}$$

Two different shrouds were modelled for the purpose of the experimental validation as experimental data was collected on these two geometries, which have been referred to experimentally as Shrouds 1 and 2. More experimental data exists for Shroud 2 than Shroud 1, so the majority of the experimental validation has been conducted with this shroud, with the methodology then being applied to Shroud 1, to assist the parametric variation.

6.4.1 Shroud 2

Before looking at the results produced for shroud 2, details of the mesh will be given. An overview of the mesh on the rotating boundary is given in Fig. 6.3. The tetrahedral structure of the mesh can be seen clearly. Figures 6.4 and 6.5 show in greater detail the mesh structure in the region around the gear. Referring to Fig. 6.2, the inlet clearance, face clearance, and outlet clearance are, respectively, 4 mm, 1.5 mm, and 1.5 mm.

Fig. 6.6 shows the variation of C_M (calculated from computed torque values) against C_Q at a rotation rate of $\pm$8203 RPM. Both standard and enhanced wall treatments have been applied to the same mesh, for which y^* is around 25 on the gear teeth. The question of which near-wall approach to use is still open at this point, as such both approaches have been used, in an attempt to try and address the issue. Fig. 6.6 shows that the effect of wall treatment is less significant in this shrouded model than for the unshrouded cases (for example, Fig. 5.12). It is clear that both wall treatments are significantly over-

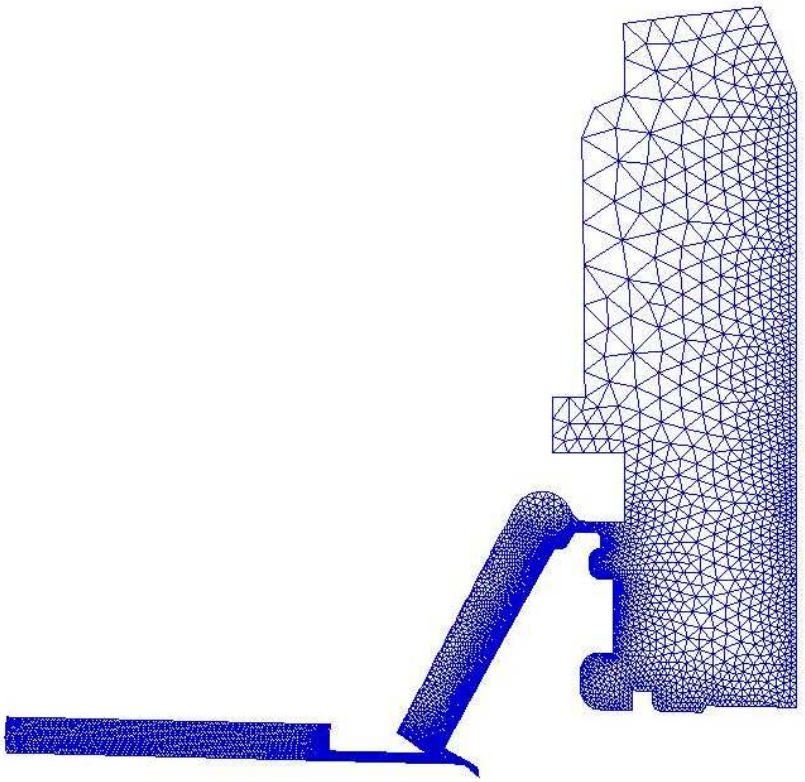

Figure 6.3: Mesh on rotating boundary for Shroud 2

predicting the torques compared to those measured experimentally (between 25% and 42% for clockwise rotation, and between 8% and 80% for anti-clockwise rotation).

A key design feature of the single-phase shrouds designed for the experimental programme is that they were fitted with 36 static pressure tappings arranged as four radial lines of nine located at $\theta = 45°$, 135°, 225° and 315° from top dead centre [25]. There was some tangential variation in pressure recorded for each of the sets of tappings and in analysis the four individual figures were averaged for each location. It was felt that this approach was an adequate treatment of the circumferential variation for the purposes of making broad trend comparisons. Figure 6.7 shows the location of the pressure tappings upstream of, and along, the shroud.

In Fig. 6.8, gauge static pressure data (normalised with point I) at points A to I from the experimental study are compared to those obtained numerically, for a shaft speed of 8203 RPM (clockwise) and a throughflow value for C_Q of 5230. On the whole agreement is very encouraging with the difference between the CFD and the experimental results across A-B being very similar, and the pressure values between points C to I showing

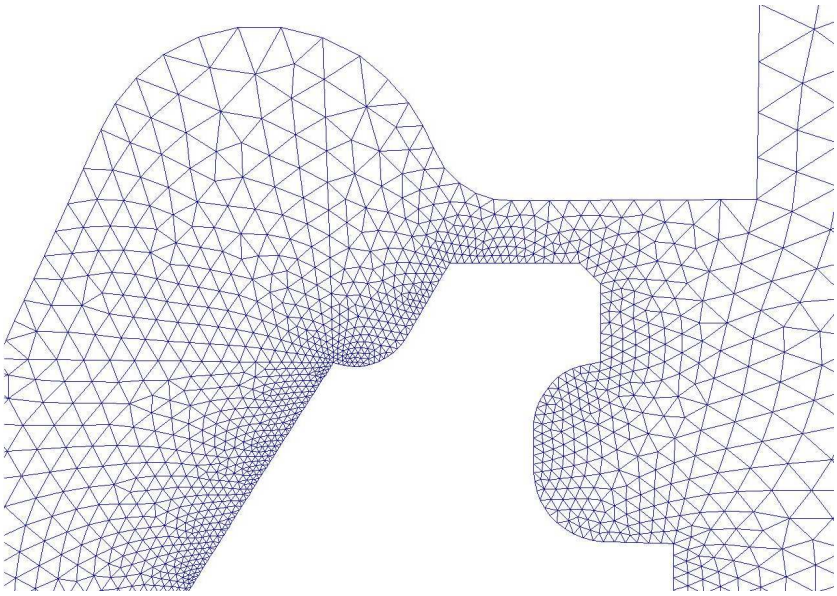

Figure 6.4: Close up of Mesh on rotating boundary at outlet from gear section, for Shroud 2

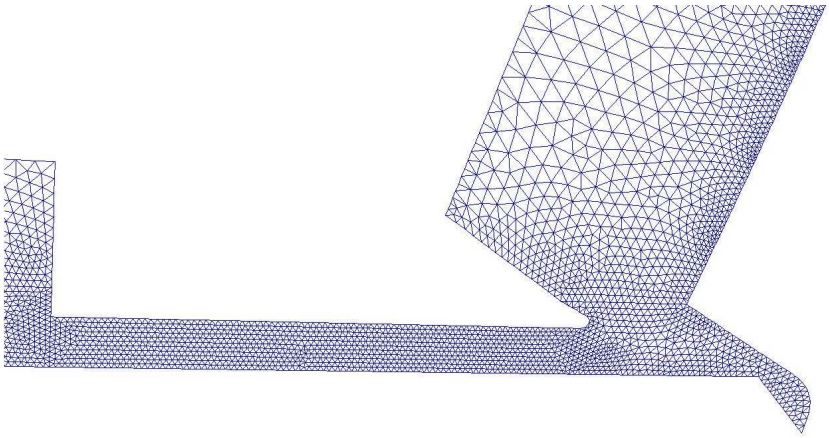

Figure 6.5: Close up of Mesh on rotating boundary at inlet to gear section, for Shroud 2

reasonable agreement. The main difference is between points B and C where the CFD indicates that pumping gains exceed losses whereas experimentally the pressure reduces.

Summary

In this section, experimental validation of the strategy obtained in Chapters 4 & 5 has been performed. The simulations conducted are shown to consistently over-predict the torque levels obtained experimentally. Little difference is seen between the results from the two different near-wall approaches used is found. The only reason that can be given

from the work presented in the section for using one approach over the other is that it has been found easier to converge solutions using the standard wall function than with the enhanced wall treatment. Recalling the greater consistency shown in Chapter 5 by the standard wall function to capture rotational direction effects, the decision can be made to use a standard wall function for the near wall flow. The work presented in this section has allowed the modelling strategy to be finalized. The strategy is as follows:

1. Model turbulence using an RNG $k-\epsilon$ turbulence model
2. Model as much of the computational domain as resources allow until you have established no azimuthal variation. A single tooth model will then suffice
3. A standard wall function should be used for the near-wall flows
4. If the steady-state solution fails to converge after a significant amount of iterations, without diverging, the flow may well be transient, and should be modelled as such to confirm (or deny) this
5. For closely shrouded gears, the flow should be modelled transient
6. Complex geometries can be meshed using unstructured meshes with size functions to capture the boundary layer

6.4.2 Shroud 1

Following on from the work on Shroud 2, which has been used to finalize a modelling strategy, this strategy has been used on a model of Shroud 1, which will also form one of the parametric variants used in §6.5. The geometry of shroud 1, although representative of engine geometry is not an actual engine geometry but rather a generic shroud capturing key features. This work establishes the accuracy of the meshes used in the variation, as the mesh style is consistent throughout the variations. Experimental data (as yet unpublished) has been produced for this shroud utilizing the in-house gear windage rig by Dr G. Johnson, in the same manner as by Johnson *et al.* [24, 25]. For this baseline shroud configuration experimental data has been collected for clockwise rotation at 8203 RPM, 10031 RPM and 12266 RPM, with 3 different forced through-flow rates of air at each speed.

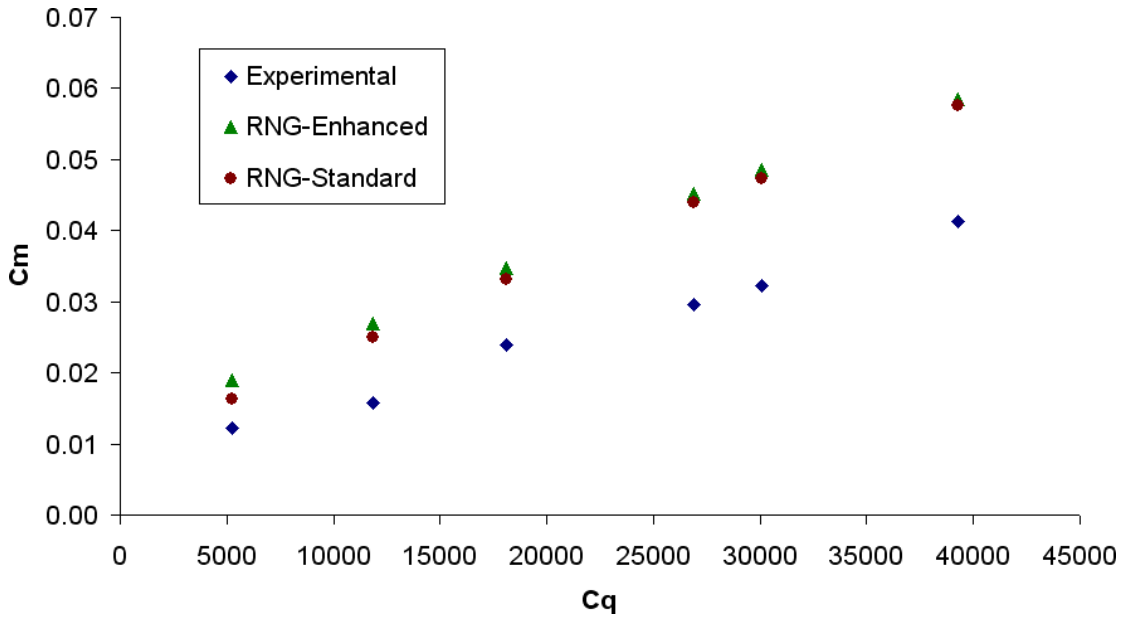

(a) Effect on torque of increasing air mass flow rate through Shroud 2 for 8203 RPM clockwise rotation.

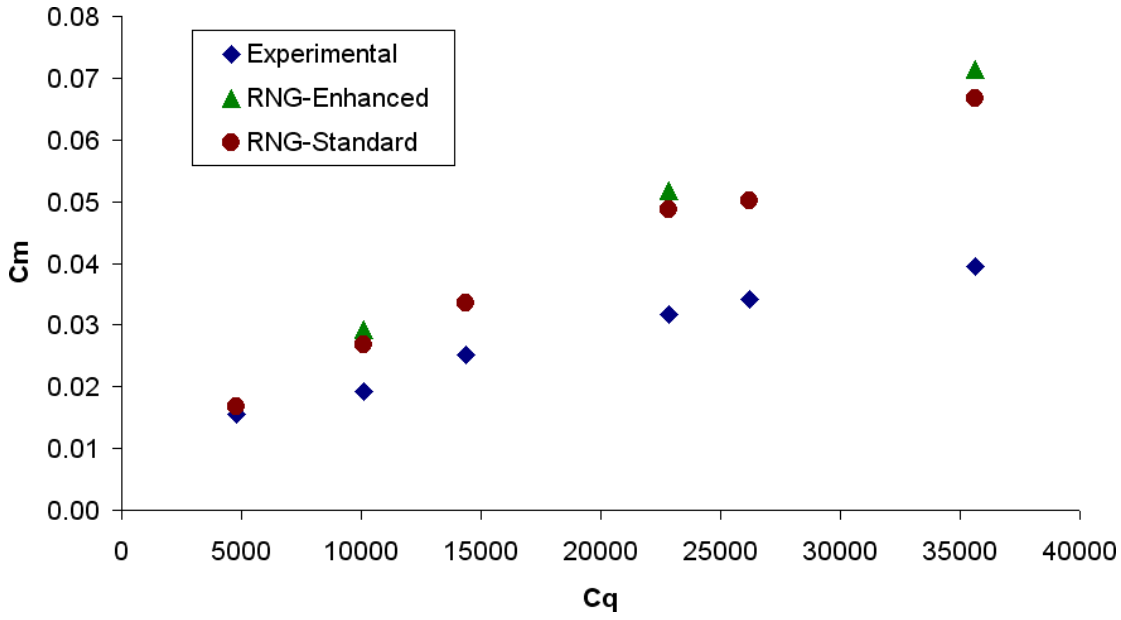

(b) Effect on torque of increasing air mass flow rate through Shroud 2 for 8203 RPM anticlockwise rotation

Figure 6.6: Effect on torque of increasing air mass flow rate through Shroud 2 for 8203 RPM.

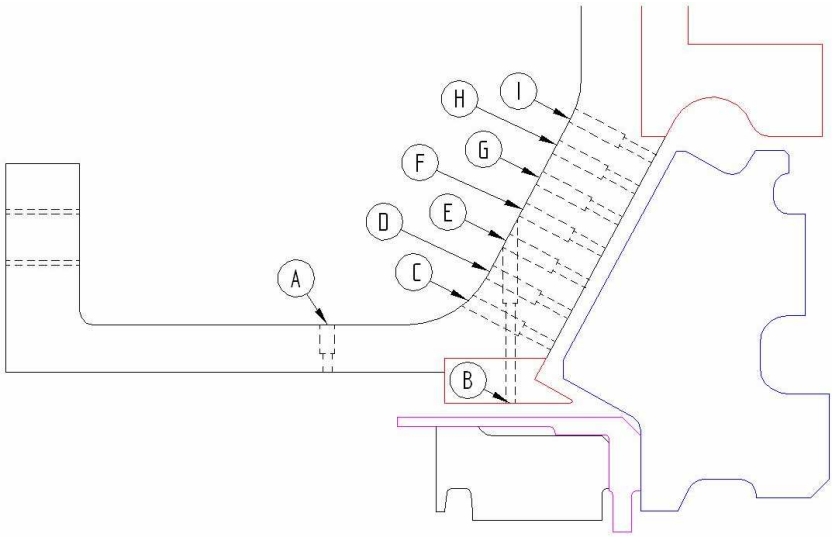

Figure 6.7: Illustrating location of pressure tappings along the shroud

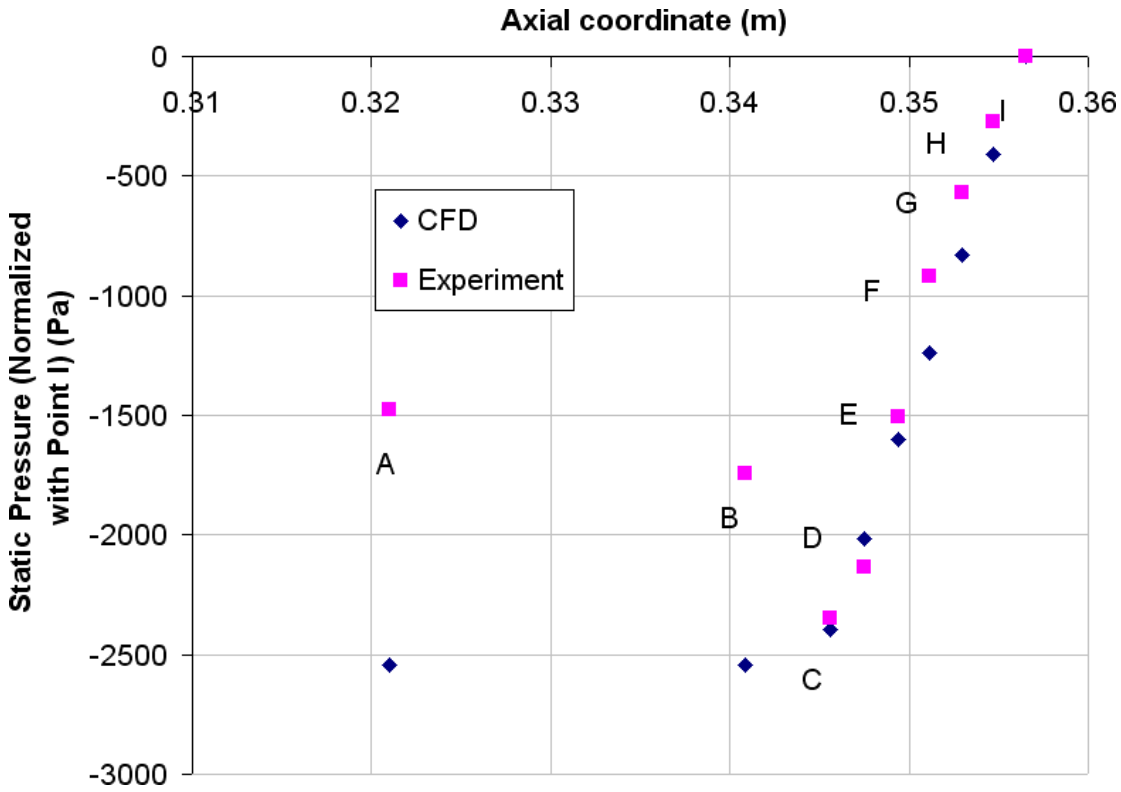

Figure 6.8: Comparison of Experimental and CFD gauge static pressure profile, for 8203 RPM, $C_Q = 5230$, Enhanced Wall treatment

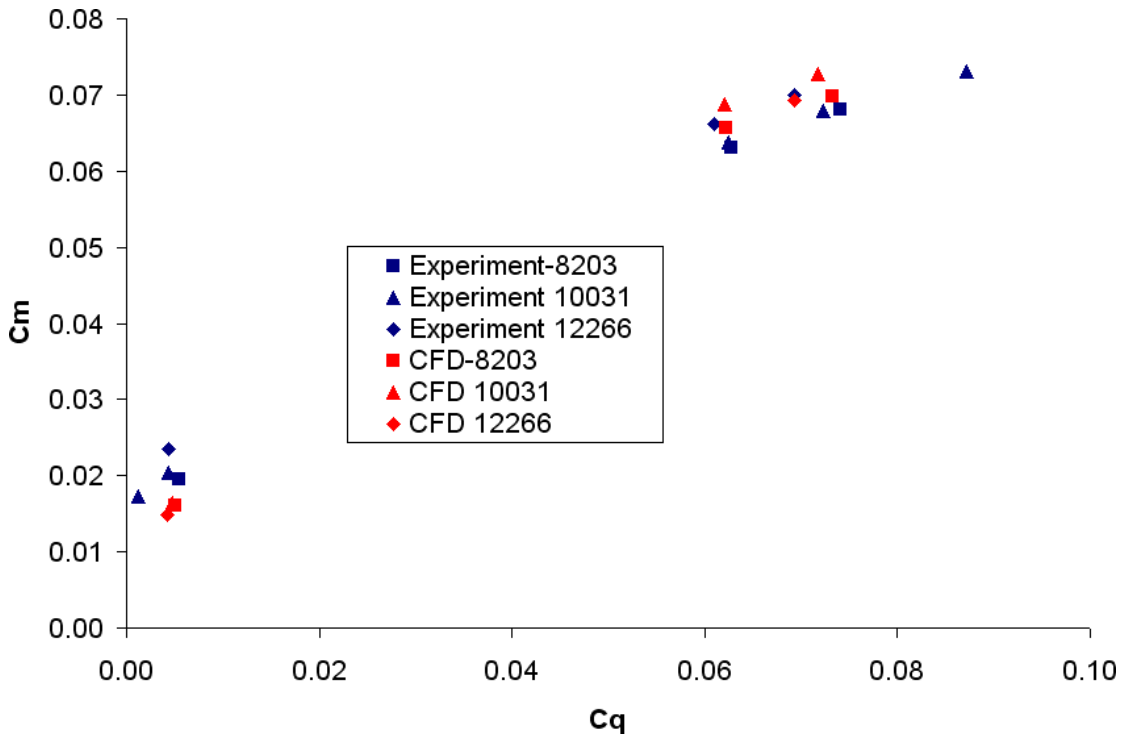

Figure 6.9: Graph of C_M against C_Q for Shroud 1, forced throughflows, for three different rotational rates, comparing experimental results with CFD.

Figure 6.9 presents a graph of Moment Coefficient (C_M) against Flow Coefficient (C_Q), for the baseline case, showing CFD and experimental values. There is strong agreement between the CFD and the experimental values. The worst agreement is for $C_Q = 0.004$, where the torque levels are under predicted by 37%. The best agreement is for $C_Q = 0.07$, where the torque levels are under predicted by 0.9%. This is encouraging, as it demonstrates that the modelling techniques utilized in this study are capable of replicating the torque levels seen experimentally to within an acceptable margin of error. Additionally, the agreement is greater for larger values of C_Q which allows greater confidence in the results of the parametric variations that will be presented here, for which the flow coefficients (in this setting) are 0.056.

6.5 Parametric Variations

In this section, the results from the parametric variations will be presented. This study is carried out for variants based around Shroud 1. Twenty-seven variations have been produced, by varying the inlet clearance, face clearance, and outlet clearance, each in 3 variants. Numerical simulations have been conducted with all 27 cases for clockwise rotation, and for 7 of the cases for anti-clockwise rotation. The cases are all run with no throughflow imposed, for speeds of 6708 and 12266 RPM, and up to 2 intermediate speeds. Whilst no throughflow is imposed, due to the use of a pressure inlet and pressure outlet as boundary conditions, along with the windage effect, a natural throughflow develops

Details of the variation of the three parameters are given in Table 6.1. The meshes used contain common elements, so the mesh for the variation with the smallest volume is included in the mesh with the largest volume. Three plots of the mesh on the rotating boundary are given in Figures 6.10-6.12. Figure 6.10 provides an overview of the overall mesh structure, showing the difference in mesh density between the mesh in the gear section and the mesh in the back cavity. Close-ups of the section of most interest are given in Figures 6.11 & 6.12.

Spacing	Inlet (mm)	Face (mm)	Outlet (mm)
Narrowest	1.56	0.25	2.52
Medium	3.19	1.5	3.013
Widest	4.00	2.12	4.00

Table 6.1: Parametric variation parameters.

Figure 6.13 presents a graph of flow coefficient (C_Q) against moment coefficient (C_M) for the 27 parametric variations. Data points plotted with the same geometrical shape have the same configuration of face and outlet clearance, with the different colours demonstrating the inlet clearance, with red representing a 1.56 mm clearance, green representing a 3.187 mm clearance, and blue representing a 4.00 mm clearance. Each variation has up to 4 data points, as each of the cases have been run at up to 4 different rotational speeds. The scatter seen is due to varying face and outlet clearances, as well as the different rotational rates imposed. Grouping the data in this manner makes it clear

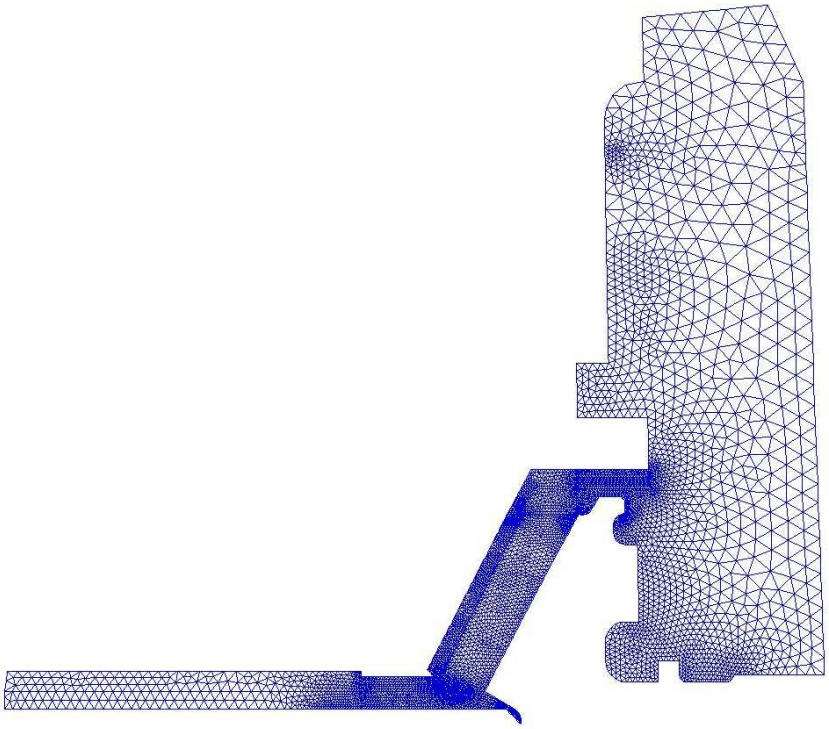

Figure 6.10: Mesh on rotating boundary for the largest domain in the Parametric Variations

that the inlet clearance has a significant impact on the torque levels seen, as all the cases with a narrow inlet clearance have a lower moment coefficient and a lower flow coefficient. If the average moment coefficient $\overline{C_M}$ is defined as the sum of the average moment coefficient for each configuration ($\overline{C_{M_{i,j,k}}}$) divided by the number of configurations (27):

$$\overline{C_M} = \frac{\sum_{i,j,k=1}^{3} C_{M_{i,j,k}}}{27}$$

the relative performance of each shroud can be determined. Compared to this average moment coefficient, these cases give an average 15.3% reduction in moment coefficient. The change from the medium to the widest inlet clearance is not as clear, with the two data sets occupying the same solution space. Compared to the average moment coefficient, the cases with a medium inlet give an average 6.5% reduction in moment coefficient, whilst those with the widest inlet give an average 11.3% increase. The same data is presented again in a different manner in Figure 6.14, this time emphasising the effect of the outlet clearance. The different geometrical shapes of the data points give

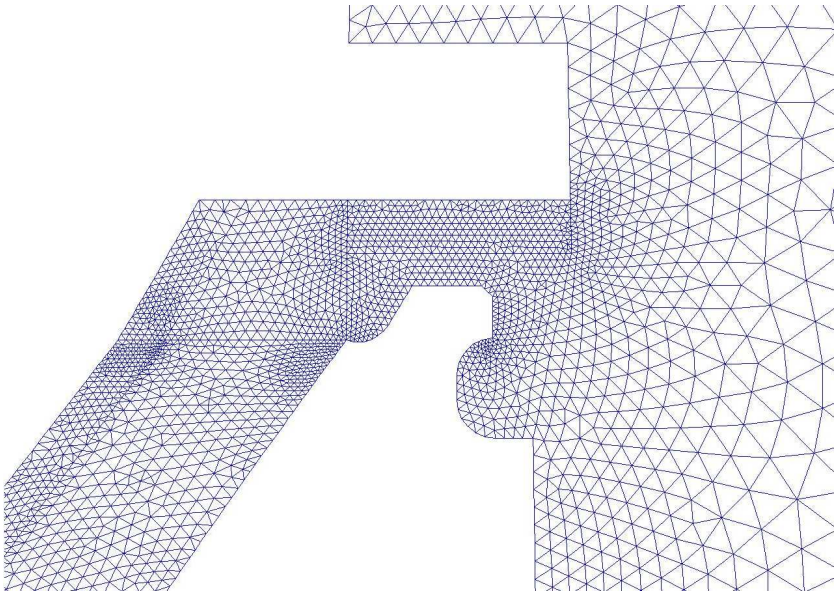

Figure 6.11: Close up of mesh on rotating boundary for the largest domain in the Parametric Variations, outlet region

the combination of inlet and face clearances, with the colour of the data points giving the outlet clearance. Red represents a 2.52 mm clearance, green represents a 3.013 mm clearance, and blue represents a 4.00 mm clearance. Each variation has up to 4 data points, as each of the cases have been run at up to 4 different rotational speeds. Data points plotted with the same geometrical shape have the same configuration of inlet and face clearance. The scatter seen is due to varying inlet and face clearances, as well as the different rotational rates imposed. Grouping the data in this manner makes it clear that the outlet clearance has a significant impact on the torque levels seen. It can be seen that, in general, the cases with a narrow outlet clearance have a lower moment coefficient and a lower flow coefficient. Compared to the average moment coefficient, these cases give an average 6.0% reduction in moment coefficient. However, it can also be seen that if the outlet is wide, the torque level can occupy any region of the solution space. Indeed, if a wide outlet is combined with a narrow inlet, torque levels can reduced to a level below that of a wide inlet with a narrow outlet. This suggests that whilst the outlet clearance has an influence on the moment and flow coefficients, the effect of the inlet clearance is more significant.

The effect of the face clearance on the moment coefficient is not as clear as the effect from the inlet or outlet, as can be observed in Fig. 6.15. It presents a graph of flow

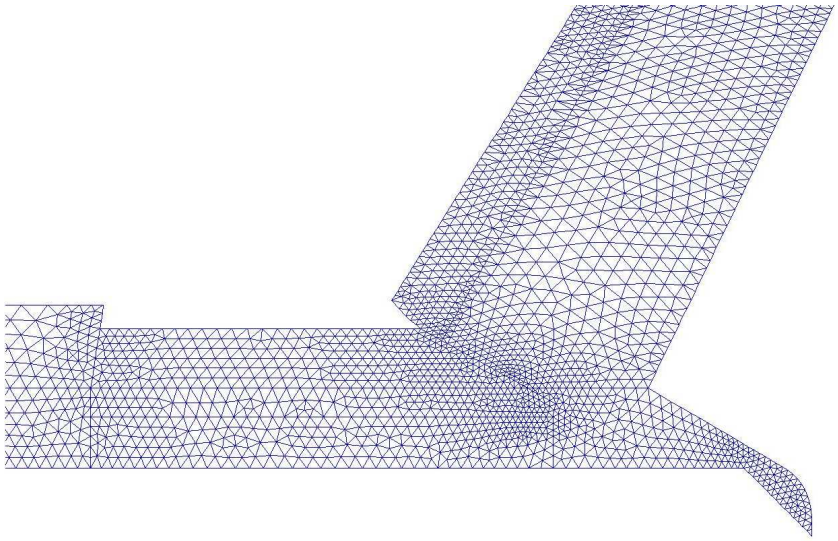

Figure 6.12: Close up of mesh on rotating boundary for the largest domain in the Parametric Variations, inlet region

coefficient (C_Q) against moment coefficient (C_M) for the 27 parametric variations. The geometrical shape of the data point specifies the inlet and outlet clearance, with the colour representing the face clearance. The narrowest clearance is represented by red points, representing a 0.25 mm clearance, green represents the medium clearance of 1.50 mm clearance, and blue represents a 2.12 mm clearance, the widest clearance. Each variation has up to 4 data points, as each of the cases have been run at up to 4 different rotational speeds. The scatter seen is due to varying inlet and outlet clearances, as well as the different rotational rates imposed. Grouping the data in this manner makes it clear that the face clearance can have an impact on the torque levels seen, as all the cases with a narrow face clearance have the higher moment coefficient and higher flow coefficient. Compared to the average moment coefficient, these cases give an average 12.8% increase in moment coefficient. This is in line with the findings of [68]. The widest face clearance gives the lowest values of moment coefficient. Compared to the average moment coefficient, these cases give an average 11.3% decrease in moment coefficient. The spread of the data, however, means that it is difficult to draw clear conclusions of the impact of the face clearance on torque levels in these cases, unlike the effects of inlet and outlet clearance.

Figure 6.16 presents a graph of flow coefficient (C_Q) against moment coefficient (C_M) for the 7 parametric variations, clockwise and anti-clockwise. Each variation has up to

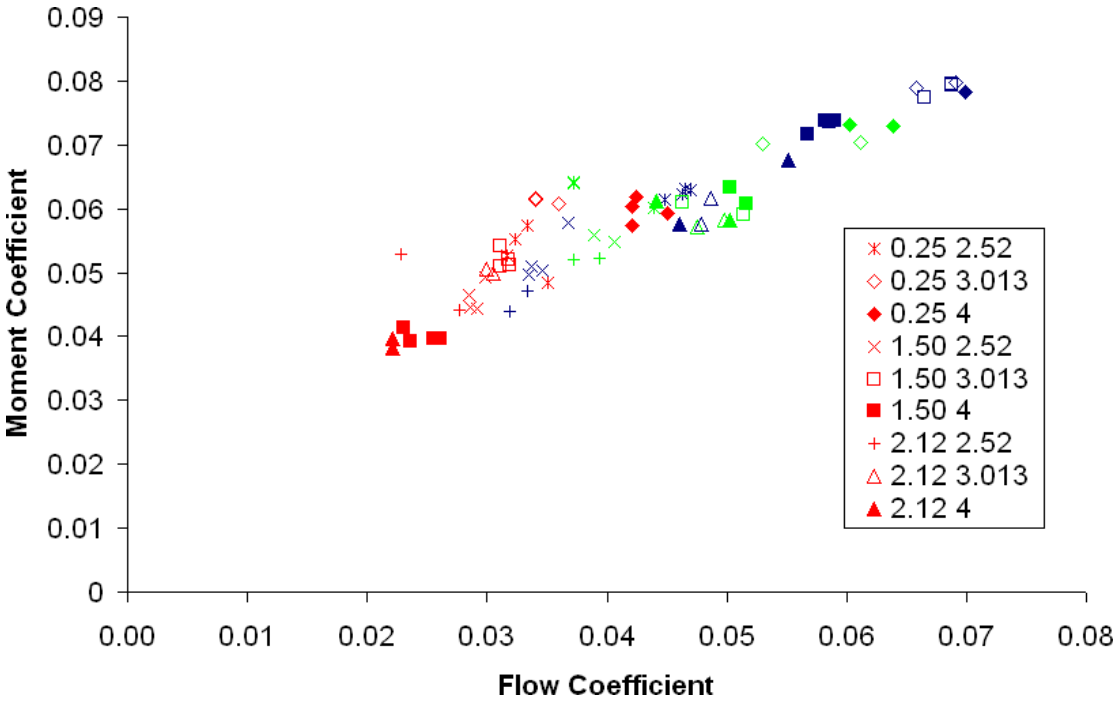

Figure 6.13: Graph of flow coefficient (C_Q) against moment coefficient (C_M) for the 27 parametric variations. The graph is coloured by the inlet clearance, with red representing a 1.56 mm clearance, green representing a 3.187 mm clearance, and blue representing a 4.00 mm clearance. Face and outlet clearances are given by the shape of the data point.

4 data points in each direction, as each of the cases have been run at up to 4 different rotational speeds. The crucial point to take from this figure is that whilst the direction of rotation affects the torque levels, it doesn't affect the relative performance of each of the shrouds. For this reason, directional dependence has not been investigated further.

Soon consideration will fall on where the various components of the moment coefficient originate from, so it is important to show how much of the torque is due to the pressure moment, and how much is due to the viscous moment. Figure 6.17 presents a graph of flow coefficient (C_Q) against pressure and viscous moment coefficients (C_M) for the 27 parametric variations. From this figure, it is clear that the pressure moment is not only greater than the viscous moment, but it also varies considerably. It is apparent that the viscous moment, which comes from the viscous drag, is essentially constant. This implies, therefore, that the pressure moment, which in turn is due to the pressure moment, is the term responsible for the change in behaviour between the different shrouds presented.

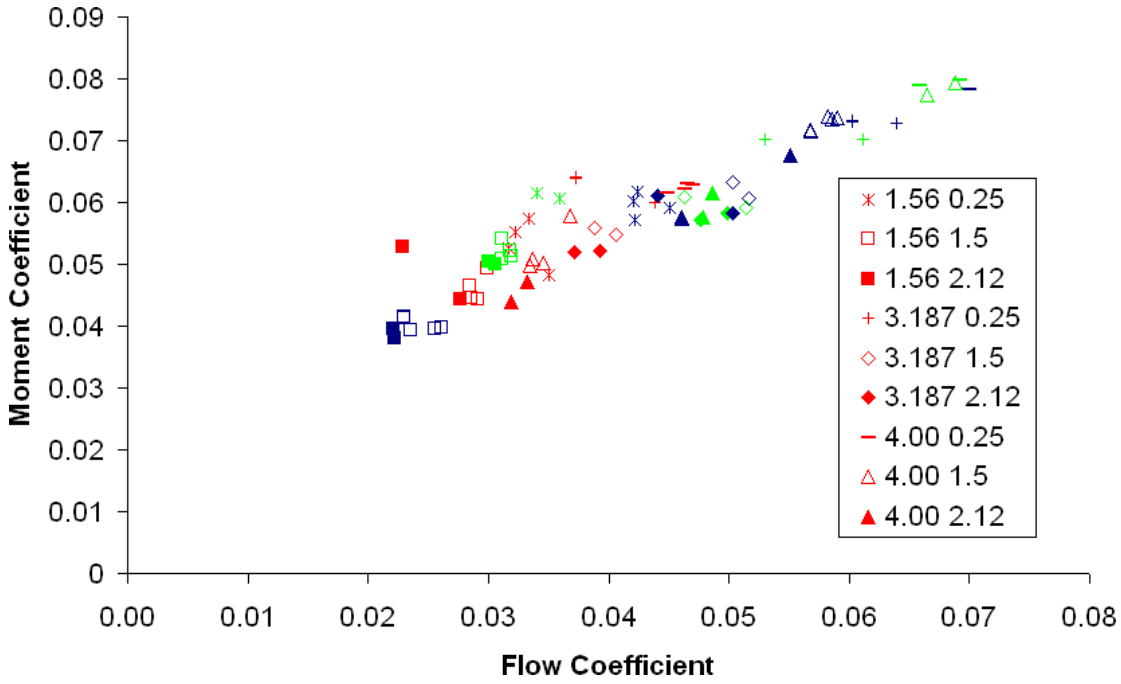

Figure 6.14: Graph of flow coefficient (C_Q) against moment coefficient (C_M) for the 27 parametric variations. The graph is coloured by the outlet clearance, red represents a 2.52 mm clearance, green represents a 3.013 mm clearance, and blue represents a 4.00 mm clearance. Inlet and face clearances are given by the shape of the data point.

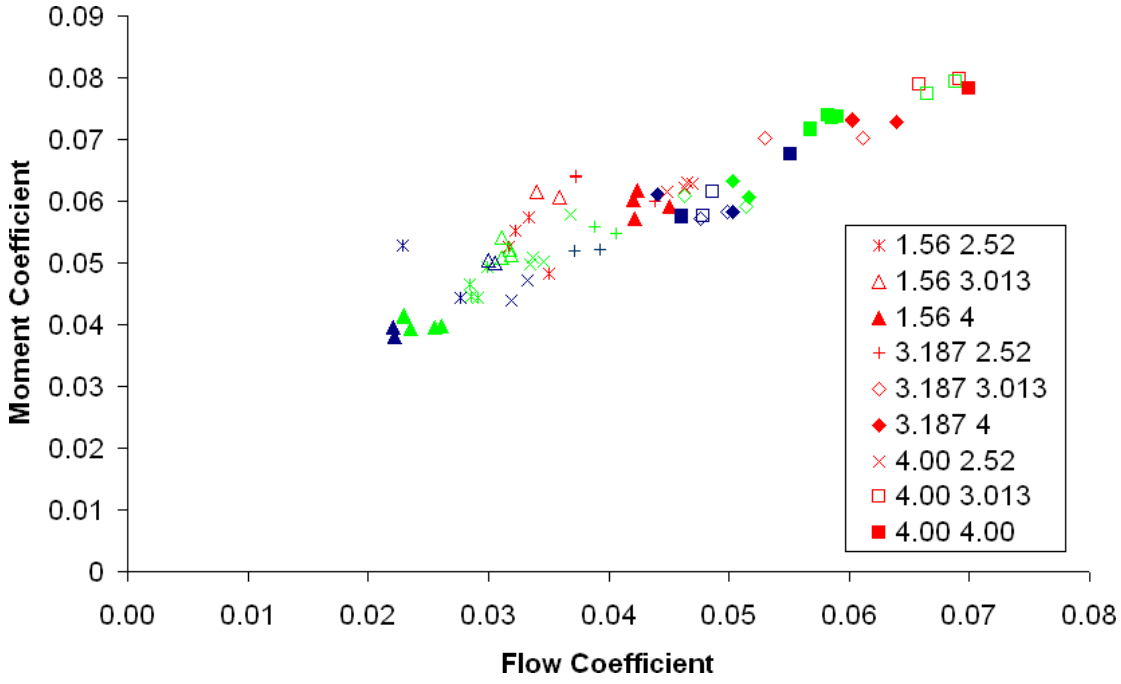

Figure 6.15: Graph of flow coefficient (C_Q) against moment coefficient (C_M) for the 27 parametric variations. The graph is coloured by the face clearance, red represents a 0.25 mm clearance, green represents a 1.50 mm clearance, and blue represents a 2.12 mm clearance. Inlet and outlet clearances are given by the shape of the data point.

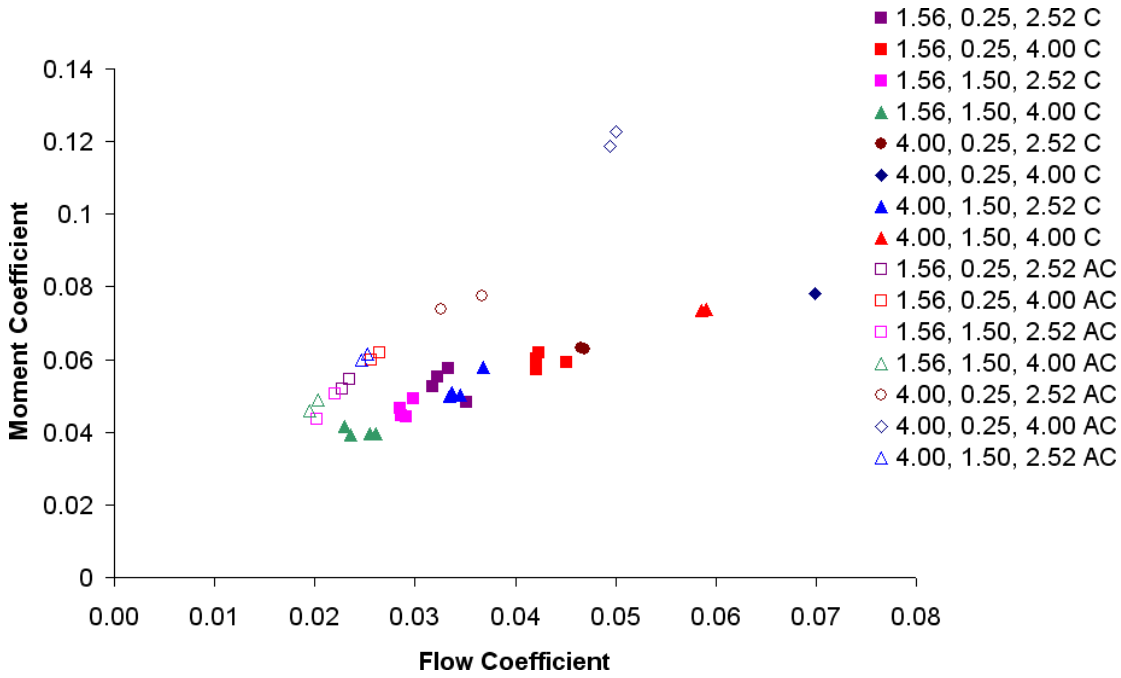

Figure 6.16: Graph of flow coefficient (C_Q) against moment coefficient (C_M) for 7 parametric variations, clockwise and anti-clockwise.

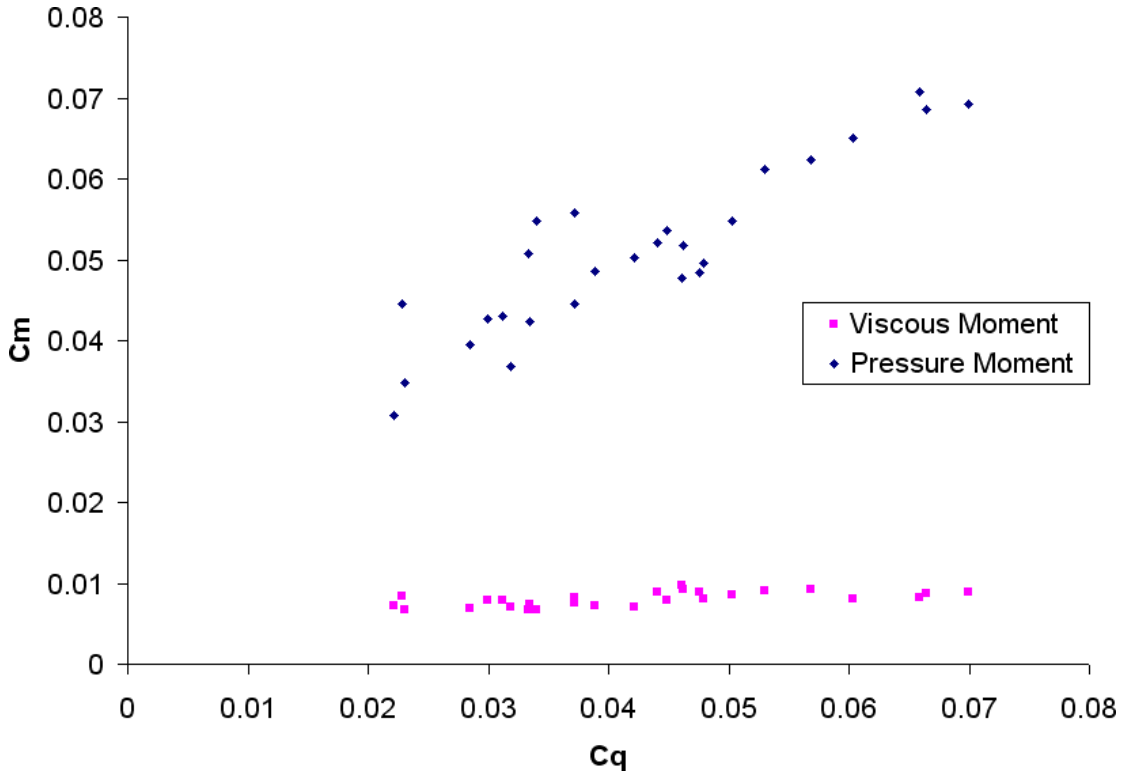

Figure 6.17: Graph of flow coefficient (C_Q) against pressure and viscous moment coefficients (C_M) for the 27 parametric variations.

6.5.1 Flowfield Investigation

In this section, a description of the flow structures present in the 'best' and 'worst' cases will be given. This will provide insight into the flow structures present, which will aid the discussion in §6.5.2-6.5.5 of the source of the higher moment coefficients seen in the worst cases.

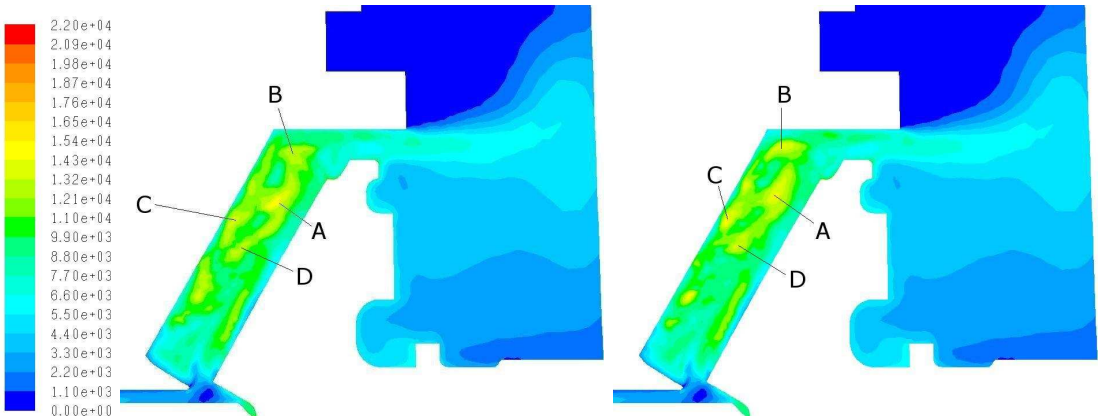

(a) t_0 (b) $t_0 + 5.375 \times 10^{-5}$

Figure 6.18: Contours of dynamic pressure (Pa) on the rotating boundary. 'Best' case shroud, $\Omega = 12266$ RPM. Figure 6.18 continues

Figure 6.18 shows contours of dynamic pressure on the rotating boundary for the best case shroud, rotating at $\Omega = 12,266$ RPM. In Fig. 6.18(a), 4 peaks of pressure can be seen, labelled A-D which, as will be shown, are on the outside of a recirculation within the flow. By showing these maxima, a description of the flow structure can be given. By studying these Figures, it can be seen that maximum A evolves from maxima C and D, and evolves into maximum B, which in turn evolves into maximum C. In Fig. 6.18(b), maximum A has moved along the gap between the teeth, and has started to rotate anti-clockwise, toward the shroud, though its motion is dominated by the bulk flow path. Maximum B has strengthened slightly, is rotating anti-clockwise, and is moving 'out-board' (toward the shroud). Maximum C is moving 'in-board' (toward the gear valley), and is being influenced by the bulk flow. Maximum D is moving in the direction of the bulkflow.

In Fig. 6.18(c), maximum A has continued to move along the gap between the teeth,

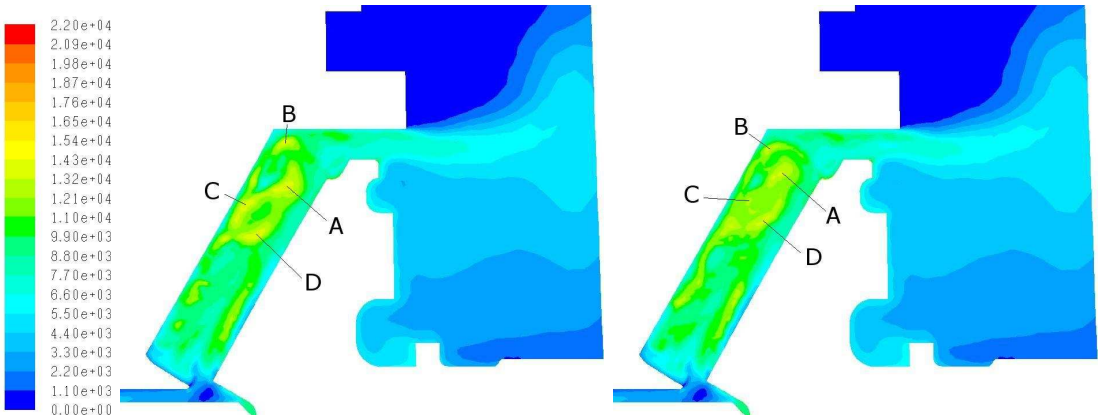

(c) $t_0 + 1.075 \times 10^{-4}$ (d) $t_0 + 1.613 \times 10^{-4}$

Figure 6.18: Contours of dynamic pressure (Pa) on the rotating boundary. 'Best' case shroud, $\Omega = 12266$ RPM. Figure 6.18 continues

is continuing to rotate anti-clockwise toward the shroud, although its motion is still dominated by the bulk flow path. It is now at the point of ejection from the tooth valley. Maximum B has weakened slightly, is still rotating anti-clockwise, and is now starting to move down the shroud. Maximum C is continuing to move in-board and is moving toward the original location of maximum A. Maximum D is continuing to move in the direction of the bulkflow, toward the original location of maximum A. Continuing to Fig. 6.18(d), maxima C and D can be seen to be at the first stages of merging, as both continue along the bulk flow path, toward the original location of maximum A. Maximum A has almost fully ejected from the tooth gap, continuing to rotate, heading toward the original location of maximum B. Maximum B has now started to move down the shroud.

In Fig. 6.18(e) maximum A has now ejected fully from the tooth gap, and continues to rotate, moving toward the shroud. Maximum B is now moving down the shroud, toward the original location of maximum C. Maxima C and D continue to move up the tooth gap, with maximum C moving inboard, both moving toward the original location of maximum A. Maximum A continues its out-board motion in Fig. 6.18(f), rotating at the same time. Maximum B is moving down the shroud face, toward the original location of maximum C. Maximum C continues to move in-board along the bulk flow path, with maximum D following it along the bulk flow path. In a similar manner

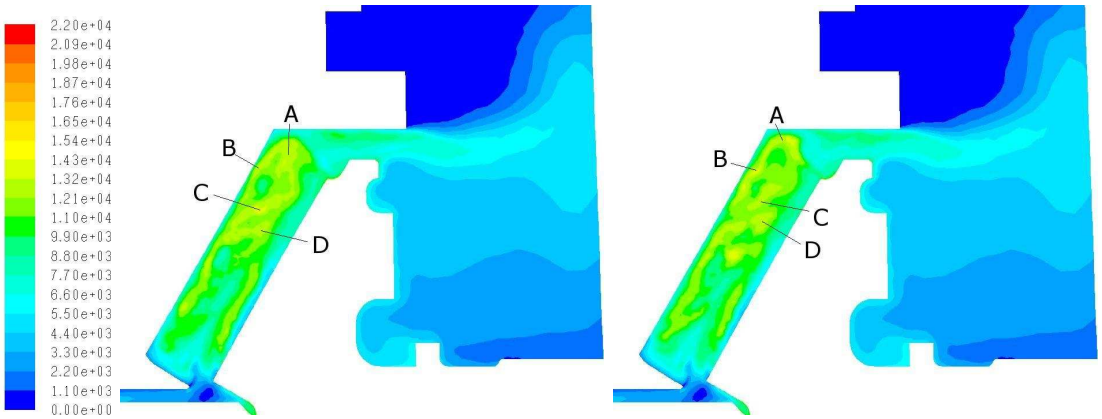

(e) $t_0 + 2.150 \times 10^{-4}$ (f) $t_0 + 2.688 \times 10^{-4}$

Figure 6.18: Contours of dynamic pressure (Pa) on the rotating boundary. 'Best' case shroud, $\Omega = 12266$ RPM. Figure 6.18 continues

to the behaviour of maximum B in Figures 6.18(a)-6.18(d), through Figures 6.18(g) & 6.18(h) maximum A has now started to weaken slightly, and is following a similar to that displayed earlier by maximum B. Maximum B continues to move down the shroud. Maximum C continues to move in-board and along the bulk flow path, and between Fig. 6.18(g) and Fig. 6.18(h) merges with maximum D, forming maximum C'.

The end of this sequence of figures (Fig. 6.18(i) & Fig. 6.18(j)) is similar to the beginning. Maximum A is now following the initial path of maximum B, and maximum C' has begun to follow the earlier path of maximum A. Maximum B is moving down the shroud, and will either continue this path, or follow the path of maximum C.

The path of the air flow can be seen to have potential problems when a second phase is introduced, as it would seem that whilst there is a clear motion of air travelling in-board along the shroud, it is unclear where this path then goes to. Experimental observations of the two-phase flow with shroud 2, which is very similar to the 'best' shroud shown in Fig. 6.18, show oil collecting at the end of this motion path.

Figure 6.19 shows the flow structure in one of the worst cases. As can be seen in these figures, the flow is dominated by the throughflow through the tooth valley. Vortices are being shed off the back of the gear, as can be seen by comparing Figure 6.19(g) & 6.19(h). To summarise, this section has shown two things: firstly for a 'good' shroud the bulkflow path is through the tooth valley, with recirculations present between the

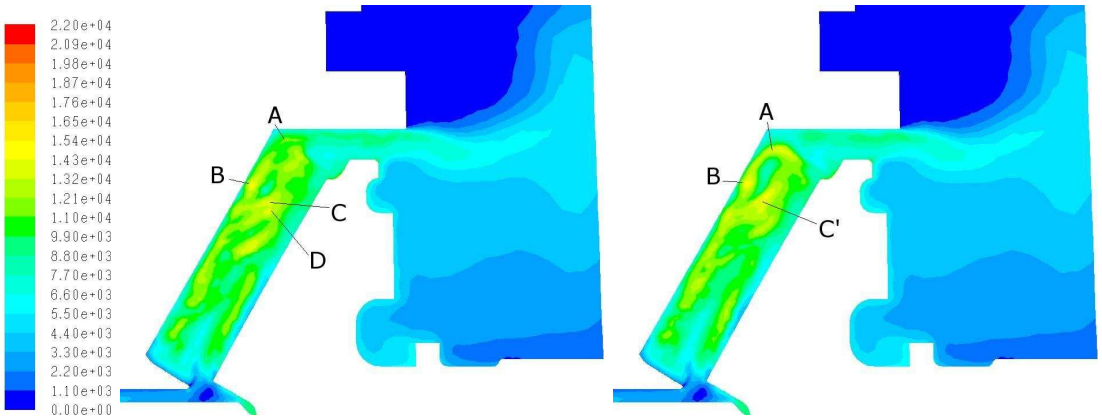

(g) $t_0 + 3.225 \times 10^{-4}$ (h) $t_0 + 3.763 \times 10^{-4}$

Figure 6.18: Contours of dynamic pressure (Pa) on the rotating boundary. 'Best' case shroud, $\Omega = 12266$ RPM. Figure 6.18 continues

tooth and the shroud. The bulkflow is slower than that seen in the 'worst' case. For a 'poor' shroud the recirculations are not present, and the bulkflow is higher. Changes in the magnitude of the velocity lead to higher values of dynamic pressure. The impact of this on windage power loss will be discussed further in subsequent sections.

6.5.2 Component-wise breakdown of torque contributions

In this section, details of the sources of the pressure and viscous moments will be expanded upon, showing the contribution that each face makes to the total moment. This will give insight into mechanisms for reducing windage power loss. The torque on the gear surface is due to the retarding forces which the surrounding air induces on the rotating gear. This torque can be split into two components: pressure forces and viscous forces. The pressure force is equal to the integral over the surface of the static pressure multiplied by the vectorial dot product between the normal vector to the surface ($\vec{n}$) and the direction vector, as below:

$$\mathbf{P} = \oint p\vec{n}.\vec{r}\mathrm{d}A \tag{6.5}$$

The viscous force is similar, being the integral over the surface of the wall shear-stress multiplied by the vectorial dot product between the normal vector to the surface ($\vec{n}$) and

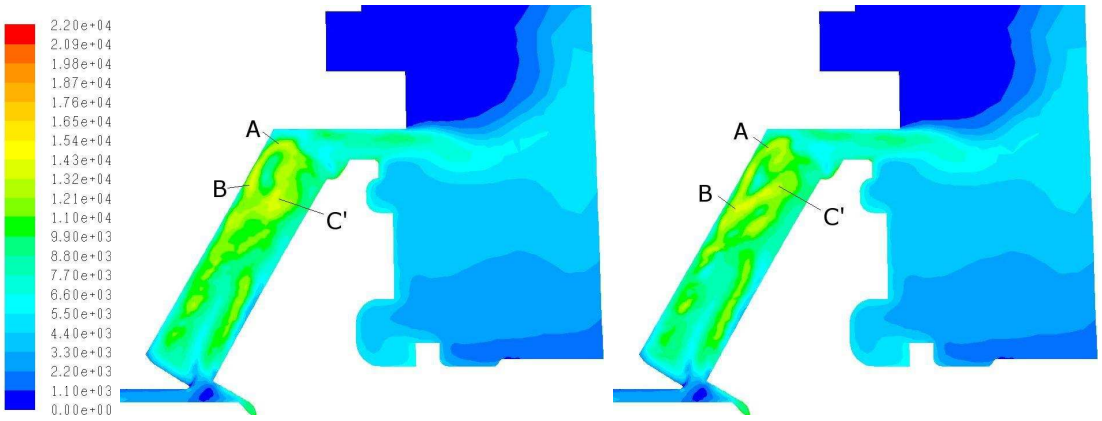

(i) $t_0 + 4.300 \times 10^{-4}$ (j) $t_0 + 4.838 \times 10^{-4}$

Figure 6.18: Contours of dynamic pressure (Pa) on the rotating boundary. 'Best' case shroud, $\Omega = 12266$ RPM.

the direction vector, as below:

$$\mathbf{V} = \oint \tau_w \vec{n}.\vec{r} \mathrm{d}A$$

Wall shear stress, commonly denoted as τ_w, is usually given as the magnitude in the direction normal to the wall, but it may be split vectorially, in order to give greater understanding of the effect of the flow structure upon τ_w. For the purposes of this study, the overall magnitude (τ_w), and the components in the azimuthal and streamwise directions, respectively τ_θ and τ_s (The azimuthal coordinate is identical to the angular coordinate, the streamwise direction is parallel to the teeth topland) are considered. These are given below

$$\tau_\theta = \sqrt{\tau_y^2 + \tau_z^2}$$

$$\tau_s = \cos\phi\tau_\theta - \sin\phi\tau_x$$

It may at this point seem logical to look at how the fraction of the total moment due to pressure or viscous forces varies. However, as the total moment is varying, this does not give much extra insight, but has been included in §B for completeness. It is now useful to consider how the moments are affected by the shroud geometry. To begin with, the effects of the geometry on the overall pressure moment are considered.

Figure 6.20 presents a graph of flow coefficient (C_Q) against pressure moment co-

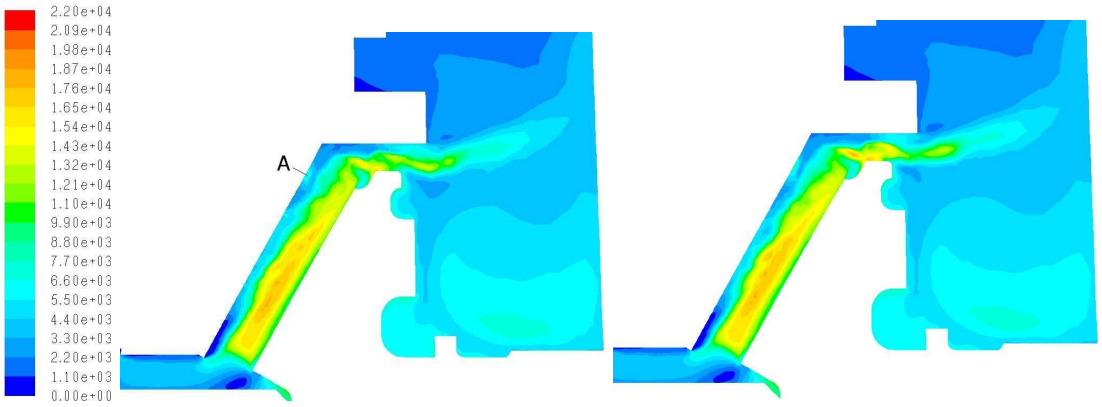

(a) t_0 (b) $t_0 + 5.375 \times 10^{-5}$

Figure 6.19: Contours of dynamic pressure (Pa) on the rotating boundary. 'Worst' case shroud, $\Omega = 12266$ RPM. Figure 6.19 continues.

efficient (C_{Mp}) for the 27 parametric variations. The graph is coloured by the inlet clearance, with red representing a 1.56 mm clearance, green representing a 3.187 mm clearance, and blue representing a 4.00 mm clearance. Data points plotted with the same geometrical shape have the same configuration of face and outlet clearance. The scatter seen is due to varying face and outlet clearances. As seen in Figure 6.17, the pressure moment accounts for a large fraction of the total moment, so it is no surprise that the variations in the pressure moment and the total moment due to the inlet clearance are very similar. For this reason, plots of the variation due to the face and outlet are not plotted here, although they are given in §B. Additionally, due to the small contribution the viscous moment has on the overall moment, plots of the variation of the viscous moment with inlet, face, or outlet clearance have not been plotted.

Having looked at the influence of the 3 shroud parameters on the pressure moment, it is useful to look at the amount of the moment which comes from each part of the gear, and how this varies (if at all) with shroud geometry. Figure 6.21 presents a graph of moment coefficient against pressure moment on teeth as a percentage of total pressure moment, coloured by the inlet clearance (1.56 mm, 3.187 mm, 4.0 mm). It shows that the cases where the moment coefficient is less, the percentage of the pressure moment due to the gear teeth is reduced. As the pressure moment is a significant fraction of the total moment, it is clear that any understanding of the mechanism behind the torque

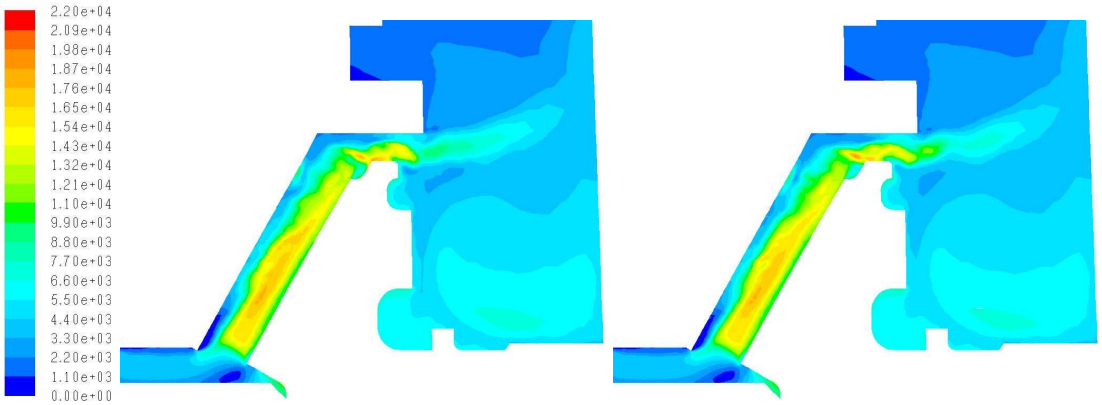

(c) $t_0 + 1.075 \times 10^{-4}$ (d) $t_0 + 1.613 \times 10^{-4}$

Figure 6.19: Contours of dynamic pressure (Pa) on the rotating boundary. 'Worst' case shroud, $\Omega = 12266$ RPM. Figure 6.19 continues.

experienced by the gear teeth will give an insight to methods of reducing windage power loss. The effect of the inlet upon this moment is the same as on the overall moment shown in Fig. 6.13 (reducing inlet clearance reduces torque).

Figure 6.22 presents a graph of moment coefficient against pressure moment on teeth as a percentage of total pressure moment, coloured by the face clearance (0.25 mm, 1.5 mm, 2.12 mm). The effect of the face upon this moment is much clearer than the effect on the overall moment shown in Fig. 6.15. It is clear that as the face clearance reduces the pressure moment on teeth as a percentage of total pressure moment increases. Figure 6.23 presents a graph of moment coefficient against pressure moment on teeth as a percentage of total pressure moment, coloured by the outlet clearance (2.52 mm, 3.013 mm, 4.0 mm). The effect of the outlet upon this moment is the same as on the overall moment shown in Fig. 6.14 (reducing outlet clearance reduces torque).

Summary

The work in this section has shown how the static pressure varies on the gear face. It has shown that it is the dominant parameter in the windage power loss, and is itself dominated by the pressure moment on the teeth themselves. This implies that minimising the pressure moment on the teeth will minimise windage power loss.

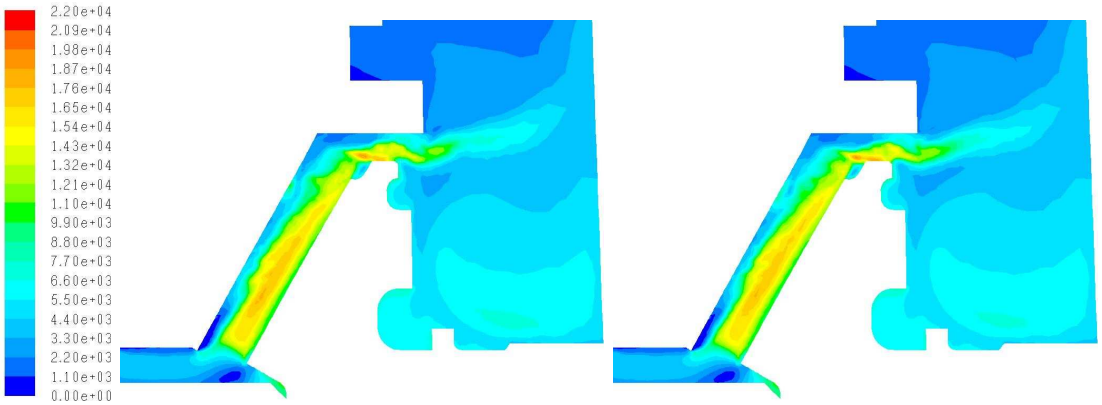

(e) $t_0 + 2.150 \times 10^{-4}$ (f) $t_0 + 2.688 \times 10^{-4}$

Figure 6.19: Contours of dynamic pressure (Pa) on the rotating boundary. 'Worst' case shroud, $\Omega = 12266$ RPM. Figure 6.19 continues.

6.5.3 Variation in Static Pressure

In this section the variation in the static pressure on the gear teeth shall be looked at. As has been shown in the previous section (§6.5.2), the cases where the moment coefficient is large see higher levels of static pressure on the gear teeth. So, it is useful to get a greater appreciation of how the static pressure varies across the gear-teeth, in order to gain some insight into how to reduce the windage power loss. Figure 6.24 shows the location of the 6 lines which are used for plotting the variation in various quantities across the gear face, including the static pressure and the fluid density. The lines are evenly spaced, 5 mm apart, starting 1.2 mm from the inner radius of the teeth, and finishing 1.8 mm from the outer radius.

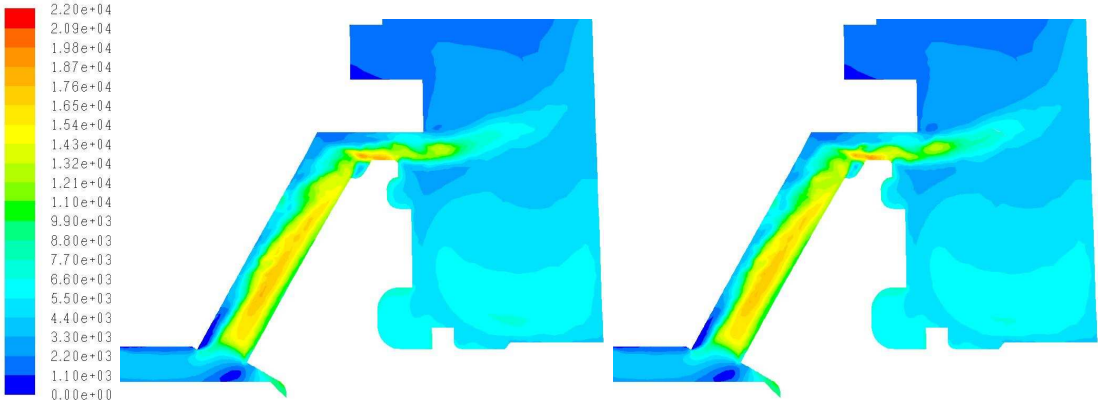

(g) $t_0 + 3.225 \times 10^{-4}$ (h) $t_0 + 3.763 \times 10^{-4}$

Figure 6.19: Contours of dynamic pressure (Pa) on the rotating boundary. 'Worst' case shroud, $\Omega = 12266$ RPM. Figure 6.19 continues.

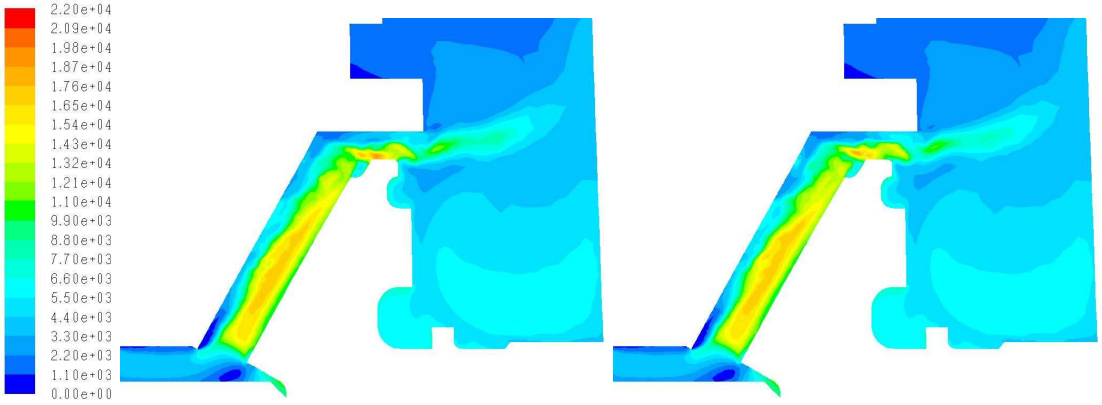

(i) $t_0 + 4.3 \times 10^{-4}$ (j) $t_0 + 4.838 \times 10^{-4}$

Figure 6.19: Contours of dynamic pressure (Pa) on the rotating boundary. 'Worst' case shroud, $\Omega = 12266$ RPM.

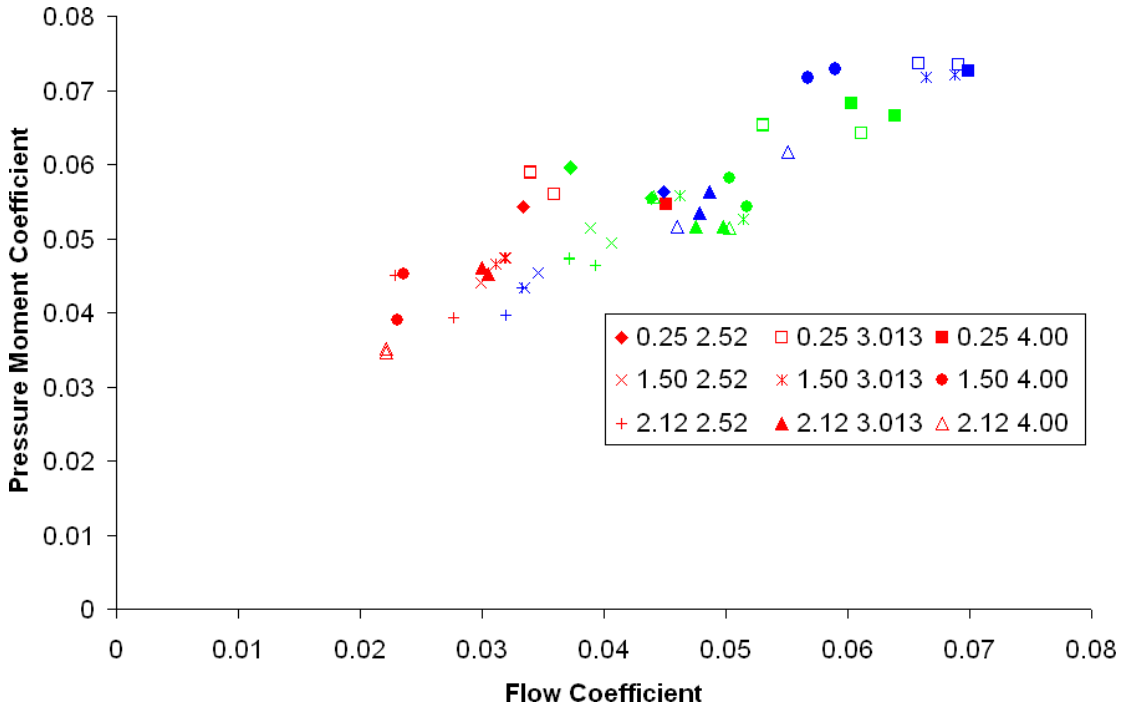

Figure 6.20: Graph of flow coefficient (C_Q) against pressure moment coefficient (C_{Mp}) for the 27 parametric variations. The graph is coloured by the inlet clearance, with red representing a 1.56 mm clearance, green representing a 3.187 mm clearance, and blue representing a 4.00 mm clearance.

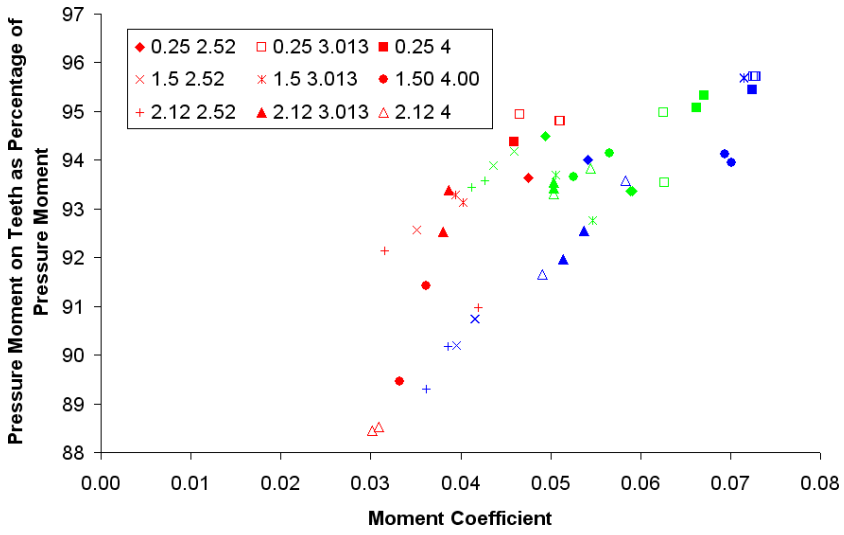

Figure 6.21: Graph of Moment Coefficient against Pressure moment on Teeth as Percentage of Total Pressure Moment, coloured by inlet clearance, with red representing a 1.56 mm clearance, green representing a 3.187 mm clearance, and blue representing a 4.00 mm clearance.

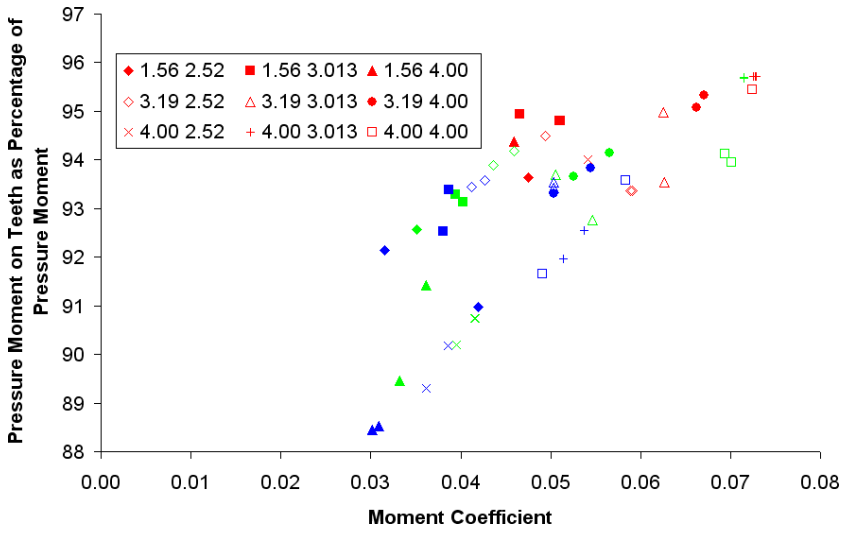

Figure 6.22: Graph of Moment Coefficient against Pressure moment on Teeth as Percentage of Total Pressure Moment, coloured by face clearance, with red representing 0.25 mm clearance, greeen representing 1.5 mm, and blue representing 2.12 mm.

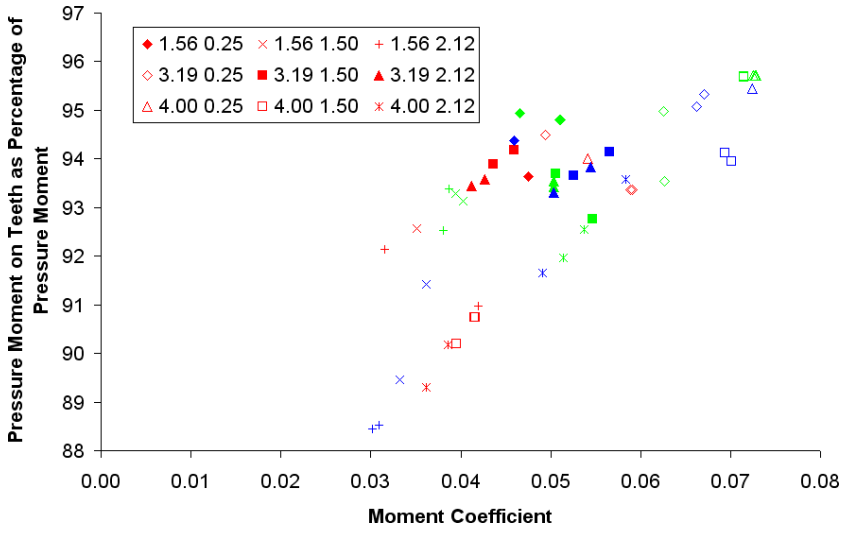

Figure 6.23: Graph of Moment Coefficient against Pressure moment on Teeth as Percentage of Total Pressure Moment, coloured by outlet clearance, with red representing 2.52 mm clearance, green representing 3.013 mm clearance, and blue representing 4.0 mm.

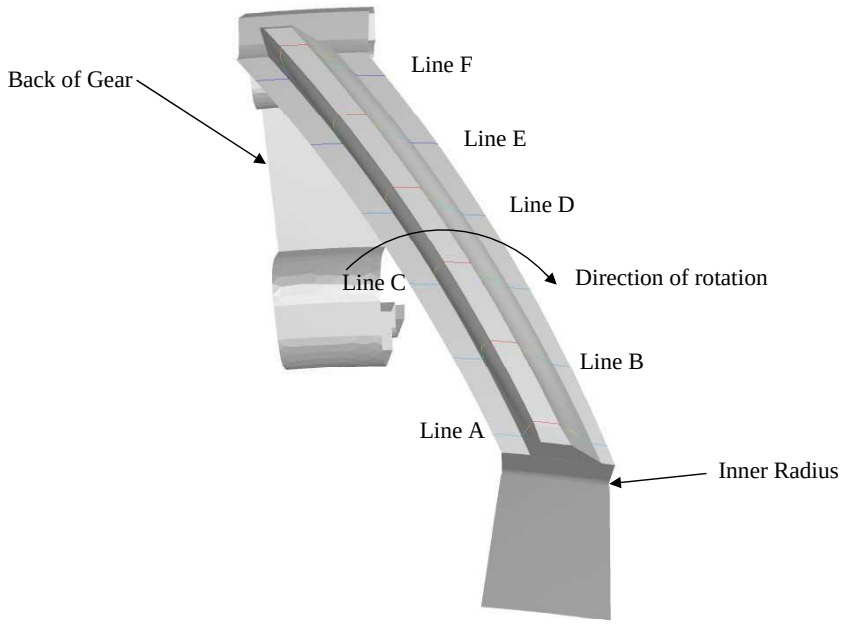

Figure 6.24: Position of Lines A-F on the gear teeth.

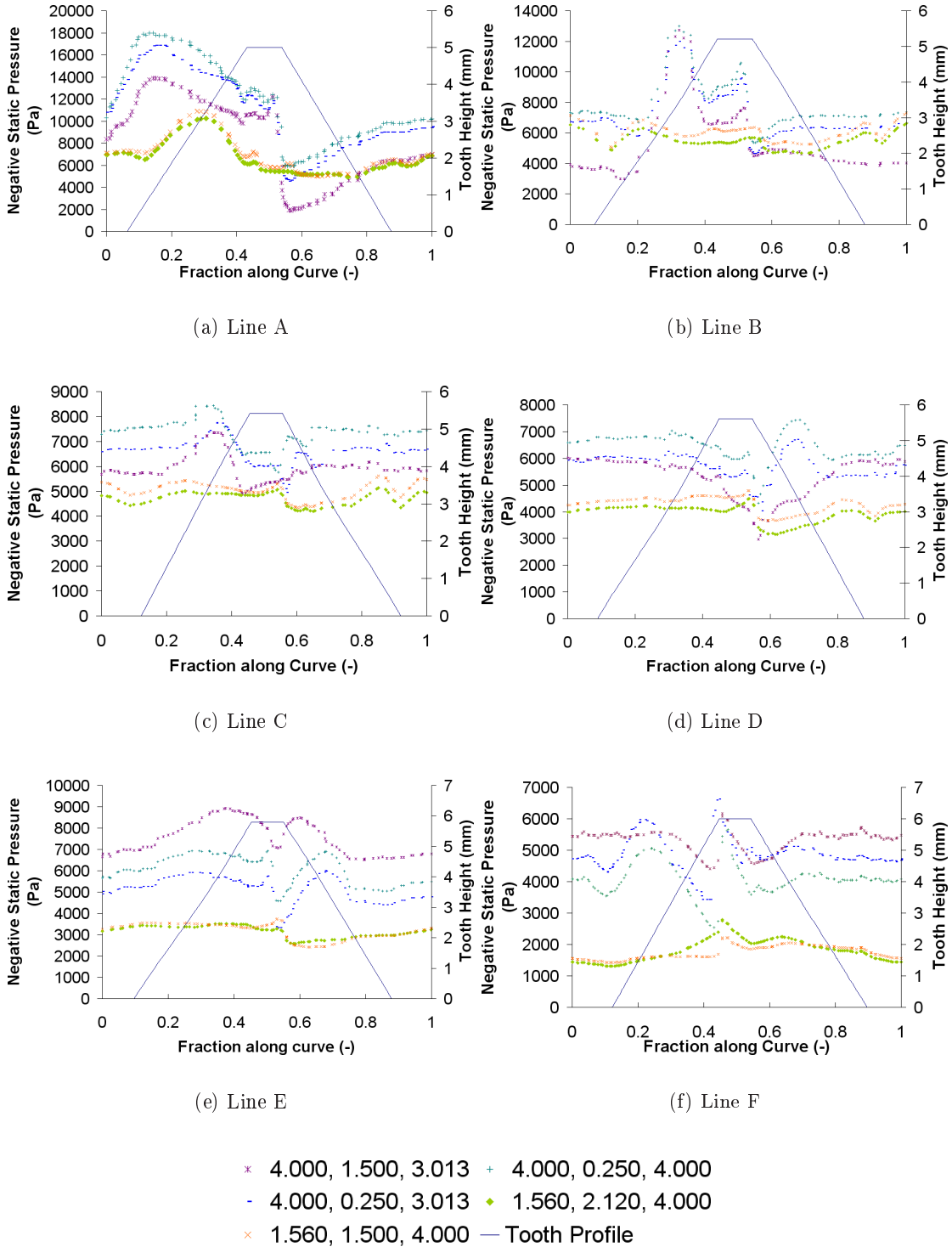

(a) Line A

(b) Line B

(c) Line C

(d) Line D

(e) Line E

(f) Line F

Figure 6.25: Negative Static Pressure on Lines A-F on the gear teeth, for the 3 worst (4.00 mm inlet) and 2 best (1.56 mm inlet) case shrouds. Legend refers to inlet clearance (mm), face clearance (mm), and outlet clearance (mm).

Figure 6.25(a) shows a plot of negative static pressure (NSP) across the gear teeth, at the point A, for the 3 worst ((4mm, 1.5 mm, 3.013mm), (4 mm, 0.25 mm, 4mm) and (4 mm, 0.25 mm, 3.013mm)) and 2 best case ((1.56 mm, 2.12 mm, 4mm) and (1.56 mm, 1.5 mm, 4mm)) shrouds. NSP has been plotted as it is proportional to the pressure force (see Eq. 6.5), and is equal in sign. The force is a retarding force, hence it is negative. It can be seen that there is much greater variation in the NSP in the three worst cases compared to the two best cases. The best cases show fairly constant NSP on the leading edge ($0.54 \leq x < 0.87$) and topland ($0.43 \leq x < 0.54$), with the only major change in NSP being on the trailing edge ($0.07 \leq x < 0.43$). This is different to the worst cases, which all see rising NSP on the trailing edge, with a sudden increase in NSP between the leading edge and the topland. The NSP rises on the trailing edge of the worst cases, and only recovers at the bottom of the valley ($0 \leq x < 0.43$).

Figure 6.25(b) shows a plot of NSP across the gear teeth, at the point B, for the 3 worst and 2 best case shrouds. In all 5 cases the NSP is almost constant on the leading edge of the teeth. However, as in Fig. 6.25(a), there is a shock between the leading edge and the topland in the 3 worst cases, causing a sudden rise in NSP. The NSP across the topland remains fairly constant in all 5 cases. In the 3 worst cases there are then two significant changes in NSP on the trailing edge, unlike the 2 best cases which show a much smoother transition to a similar NSP than the worst cases.

Figure 6.25(c) shows a plot of NSP across the gear teeth, at the point C, for the 3 worst and 2 best case shrouds. As with the two previous figures, it can be seen that the NSP in the 2 best cases is fairly constant across the leading edge and topland of the teeth, indeed, apart from two minor shocks at the extremes of the valley, the NSP shows little change across the entire tooth. The 3 worst cases show higher NSP on the leading edge and topland than the best cases, along with a sharp increase in NSP on the trailing edge of the tooth.

Figure 6.25(d) shows a plot of NSP across the gear teeth, at the point D, for the 3 worst and 2 best case shrouds. As with all these figures in this series, a clear difference can be seen between the NSP profile in the best and worst cases. Additionally, it is possible in this figure to determine how the varying face clearance can affect the NSP

on the teeth in two otherwise identical cases. The case (4mm, 1.5mm, 3.013mm) shows decreasing NSP on the leading edge of the teeth, where as the other 2 worst cases see a NSP which increases in the lower half of the leading edge, and then falls as well. The 2 best cases show slightly falling NSP on the leading edge. At the transition between the leading edge and the topland, all 5 cases now exhibit a sudden increase in NSP, although it is smaller in the best cases compared to the worst. After this change, the NSP on the teeth in the best cases is almost constant, slowing only a minor decrease. The previously identified case see this change over the entire topland after which, along with the other 2 worst cases, the NSP is seen to constantly rise.

Figure 6.25(e) shows a plot of NSP across the gear teeth, at the point E, for the 3 worst and 2 best case shrouds. It can be seen again that the NSP profile across the teeth in the best cases is relatively flat, with the only minor change being at the transition from the top land to the leading edge, where an increase in NSP occurs, which is recovered on the trailing edge. The worst cases display decreasing NSP across the trailing edge up to a much sharper decrease and then increase in NSP at the transitions from the top land to the trailing edge and from the top land to the leading edge, after which the NSP then decreases again.

Figure 6.25(f) shows a plot of NSP across the gear teeth, at the point F, for the 3 worst and 2 best case shrouds. In the best case, the NSP is seen to slowly rise across the leading edge and topland to a point of maximum NSP, at the transition from the top land to the trailing edge, after which there is a sudden decrease in NSP. This is followed by nearly constant NSP on the trailing edge. At this stage, the worst cases display near constant NSP on the leading edge, with a significant increase in NSP over the topland, up to the transition between the topland and the trailing edge. At this point there is again a decrease in NSP, followed by an increase in NSP over the rest of the trailing edge. If all 6 figures are looked at together, it can be observed that in moving 'up' the tooth (from A to F), the magnitude of the static pressure decreases. This can be seen clearer in Figure 6.26, which displays the azimuthal pressure drop (the difference between the maximum and minimum pressure) for the 5 cases. Although the pressure drops reduces as consideration moves away from the inner radius, it can be observed that the pressure

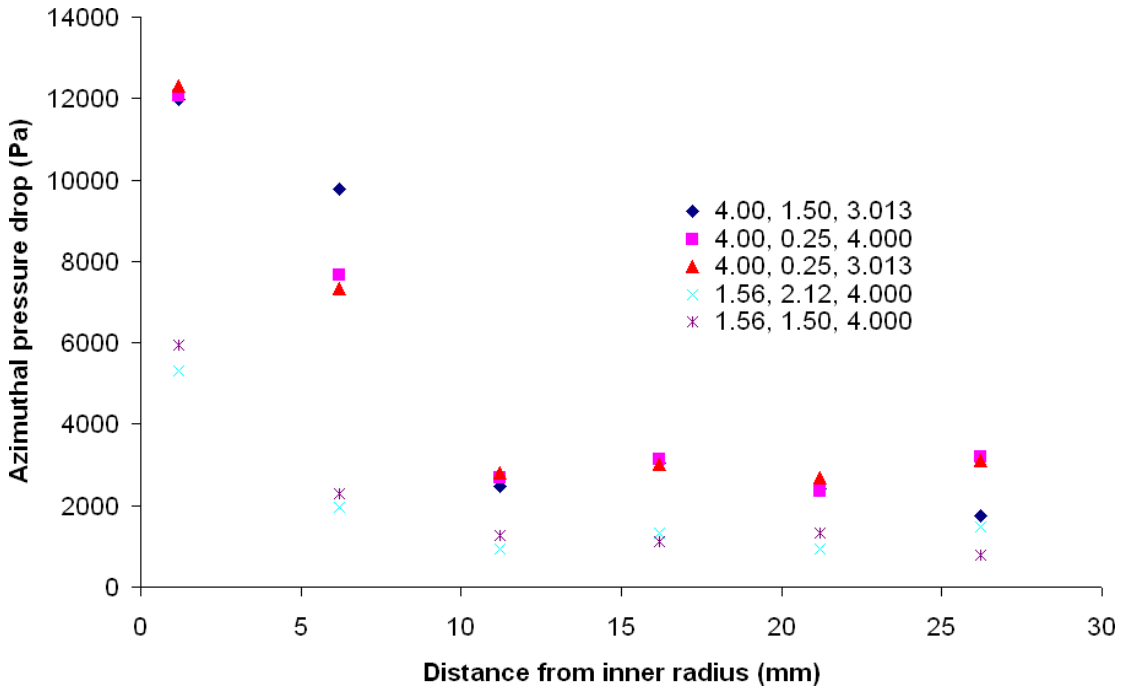

Figure 6.26: Azimuthal Pressure Drop across teeth, for the 3 worst and 2 best case shrouds, against distance from inner radius. Legend refers to inlet clearance (mm), face clearance (mm), and outlet clearance (mm).

drop is consistently higher in the 3 worst cases than the 2 best cases, being at least double the magnitude.

This section has shown how the static pressure varies over the tooth surface. To summarize, it has shown that the good shrouds show less variation in the static pressure across the tooth. This pressure converts into the pressure force, so an understanding of its origin is important in the understanding of the major component of bevel gear windage. For this reason, focus now shifts to Bernoulli's equation and variations in dynamic pressure across the gear tooth surface (§6.5.4).

6.5.4 Bernoulli's equation and Variations in Dynamic Pressure

The simulations have been conducted with the fluid modelled as being compressible. Figure 6.17 demonstrated that the viscous forces were an order of magnitude less than the pressure forces, so for a simple approximation (which will aid the understanding of the situation) the viscous effects can be discounted and the compressible form of

Bernoulli's equation can be used:

$$\frac{\rho v^2}{2} + \rho g h + \left(\frac{\gamma}{\gamma - 1}\right) p = \text{constant} \tag{6.6}$$

This implies that, subject to compressibility effects upon the ratio of specific heat capacity (γ), any significant changes in static pressure will be due to changes in dynamic pressure (hydrostatic effects can be discounted, as the simulation is rotationally periodic, with gravitational effects removed). For this reason, graphs of dynamic pressure across the gear surface are now given.

Figures 6.27(a)-6.27(f) show graphs of dynamic pressure on lines A-F of the gear teeth, for the 3 worst and 2 best shrouds. It can be seen immediately that there exists two distinct dynamic pressure profiles across the leading face of the gear, however the profile on the trailing face is very similar in all 5 cases. The worst cases show much larger gradients at the transition points between the faces in the pressure profile compared to the best cases. Figure 6.27(c) shows a graph of dynamic pressure on line C of the gear teeth, for the 3 worst and 2 best shrouds. Interestingly, the different face clearance shows a change in behaviour over the gear topland, with much higher dynamic pressures in the cases where the clearance is greater.

Figure 6.27(d) shows a graph of dynamic pressure on line D of the gear teeth, for the 3 worst and 2 best shrouds. In the worst case, the profile on the leading face shows some influence from the face clearance, with a different profile apparent.

This section has shown how the dynamic pressure varies across the gear tooth surface, for the 3 worst and 2 best cases (in terms of gear windage). The variations in dynamic pressure seen 'on' the gear can be linked back to the flowfield description. In the bad cases, the bulk of the throughflow is through the valley, leading to much higher dynamic pressures on the gear teeth, whilst longitudinal vortices are observed above the teeth in the good cases, with much smoother flow through the valley, causing smaller gradients of dynamic pressure across the teeth. Clear differences in the pressure profile are seen between the two sets. To understand greater the dynamic pressure variation, it is now useful to consider how the components of the dynamic pressure (density and velocity magnitude) vary across the gear surface.

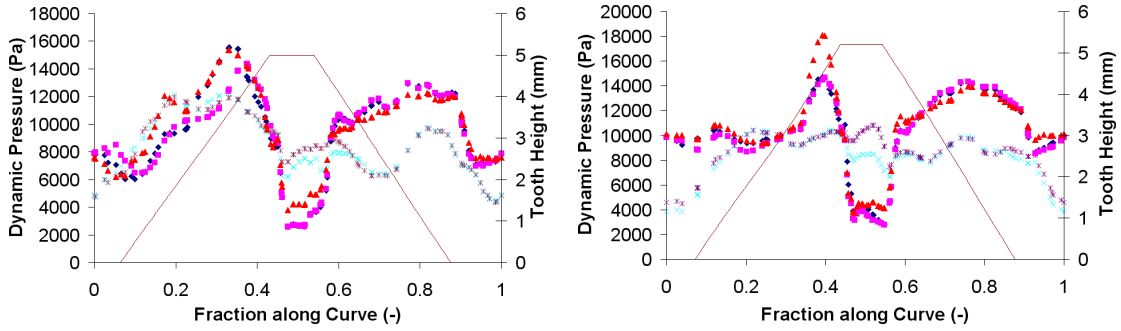

(a) Line A

(b) Line B

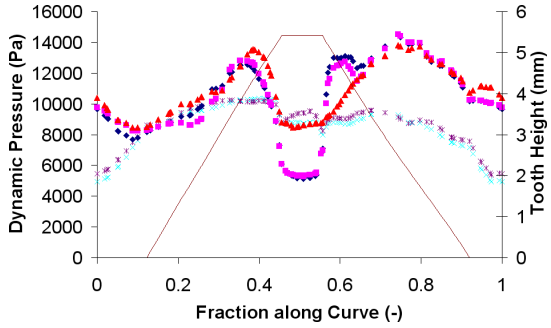

(c) Line C

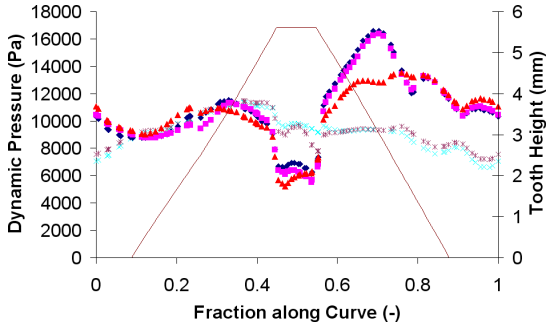

(d) Line D

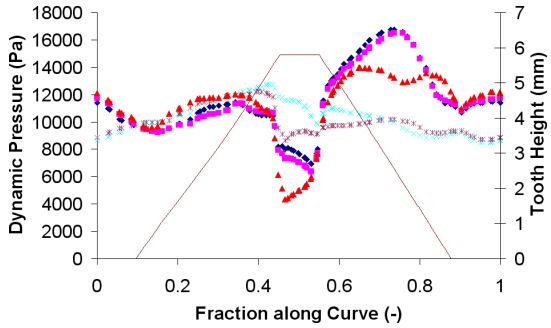

(e) Line E

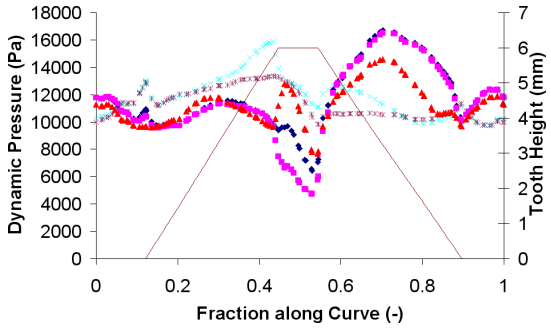

(f) Line F

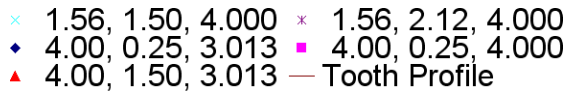

Figure 6.27: Dynamic Pressure on Lines A-F on the gear teeth, for the 3 worst (4.00 mm inlet) and 2 best (1.56 mm inlet) case shrouds. Legend refers to inlet clearance (mm), face clearance (mm), and outlet clearance (mm).

6.5.5 Variations in Density and Velocity Magnitude

By the definition of dynamic pressure, it becomes clearer that any increases in dynamic pressure must come from either an increase in density and/or an increase in velocity. For this reason, both of these in turn shall now be investigated. The density differences across the gear surface between the high and low cases can be seen in Figure 6.28. The trend in the density variation in these cases can be seen to be similar in form to the dynamic pressure variations at the same point, as seen in Figure 6.27.

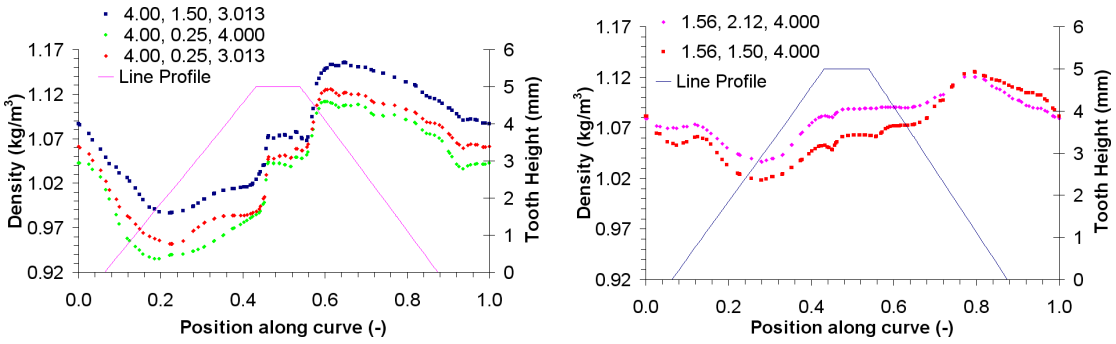

(a) High C_M (b) Low C_M

Figure 6.28: Graph of Density against Position across Teeth, Line A (as defined in Fig. 6.24)

Figure 6.28 shows a plot of air density over the tooth surface, at line A, for the three highest torque and two lowest torque cases, at a rotational speed of $\Omega = 12,266$ RPM. The leading edge of the teeth is on the right hand side of the graph. The cases (Fig. 6.28(a)) where the torque is higher show a larger variation in density compared to the cases (Fig. 6.28(b)) where the torque is lower (9% compared to 5%), although the average density at this point is lower (1.046kgm^{-3} compared to 1.071kgm^{-3}). Similar variations in density occur for the other 5 points (B-F), and are included for completeness within the appendix (§B). Whilst there is variation apparent in the density, it is not enough to account for the changes in dynamic pressure seen, so it should logically be due to changes in velocity magnitude. Figures 6.29(a)-6.29(f) show plots of velocity magnitude squared over the tooth surface, at lines A-F, for the three highest and two lowest torque cases. The value given is for the velocity at the centre of the cell nearest to the wall, and

not for the node values on the wall surface[2]. By comparing Fig. 6.29(a)-6.29(f) with Fig. 6.27(a)-6.27(f) it can be observed that the velocity squared profile and the dynamic pressure profiles are very similar, emphasising the concept that pressure variation is due mainly to the velocity variation and not the density variation (although the latter does have some effect). The profile has been discussed previously (§6.5.4). This section has focused on the variation of density and velocity magnitude squared (the components of dynamic pressure) across the gear teeth. The reason for considering these (especially the velocity) has been to show why and how the cases that induce greater air flow through the gear space will experience greater windage. It implies that by reducing the throughflow, the windage may also be reduced. Variation in density across the teeth has been seen to be minimal, and does not account for the large variations in dynamic pressure which are observed. This clearly implies that the bulk of the variation must be coming from changes in velocity (the only effect of the density variation is to 'smooth' the velocity profile within the dynamic pressure profile).

[2]These would clearly be identical for each of the 5 cases

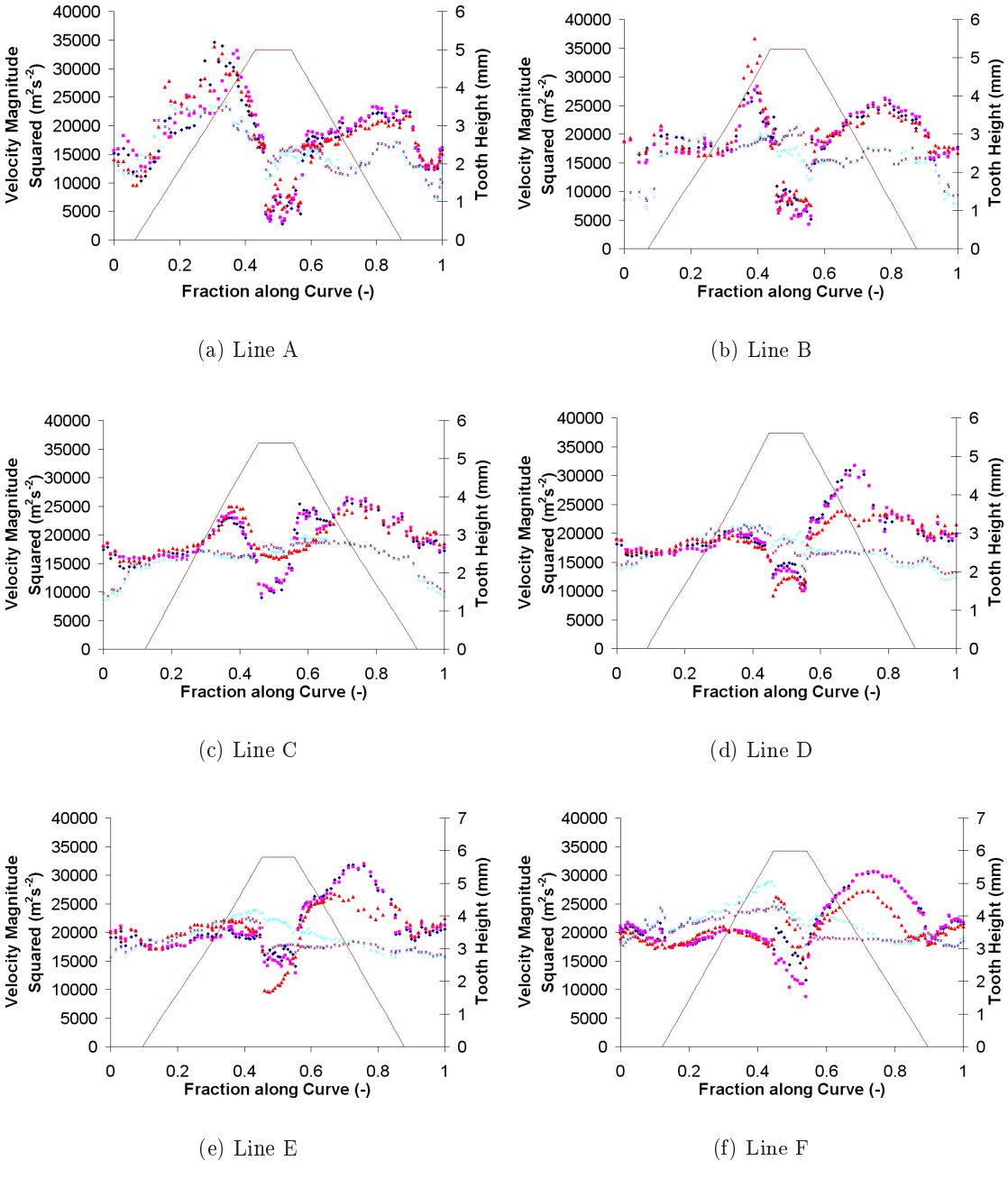

(a) Line A

(b) Line B

(c) Line C

(d) Line D

(e) Line E

(f) Line F

Figure 6.29: Velocity Magnitude Squared on Lines A-F on the gear teeth, for the 3 worst (4.00 mm inlet) and 2 best (1.56 mm inlet) case shrouds. Legend refers to inlet clearance (mm), face clearance (mm), and outlet clearance (mm).

6.6 Conclusion

In this chapter, the experimental setting has been described, which has been used to provide validation data for the numerical modelling (§6.4). By comparing the numerical and experimental results for a fixed angular velocity with increasing forced throughflow rate, it has been shown that the numerical modelling captures the same trend between the flow and moment coefficients (C_M and C_Q), although the levels are consistently over-predicted by between 25% and 42%. Pressure levels along the shroud are also over-predicted. If this is used to imply that the overall pressure within the domain is over-predicted, then it becomes clearer why the torque may be over-predicted. Using conservation of pressure on a streamline (Eq. 6.6), it can be seen that if the overall pressure is higher in the CFD than in the experiments, but the dynamic pressure is the same (which it will be if the flow rate imposed is the same as in the experiment), then the magnitude of the static pressure will be higher, causing a higher pressure force on the gear teeth.

Following on from the experimental validation, the focus then shifted to a series of parametric variants of the shroud geometry, altering the inlet, face, and outlet clearances. This variation highlighted the effects that these parameters can have on the gear windage in an unforced situation. Significant reductions in moment coefficient were achieved by reducing any of these parameters: however it was observed that the flow was sensitive to 'over' restriction in some areas. It has been shown that if the face clearance is reduced too much, the windage power loss will increase.

A flowfield investigation has been presented for one of the 'best' and one of the 'worst' cases, to give some insight into how the flow is developing. In these cases, the best case shows more recirculation, primarily between the gear teeth and the shroud. It also shows that the highest dynamic pressures are not in the tooth valley in the best cases, unlike the worst cases.

By analysing the components of the moment on the gear, more insight into the source of the windage can be obtained. The results shown in §6.5 attempt to explain the source of the higher torques in the cases where the flow coefficient is higher. The worst cases generate a higher throughflow than the best cases, which in turn causes higher

velocities throughout the domain. Higher dynamic pressures are then experienced by the gear. As it has been observed that the viscous forces are much smaller than the pressure forces, it can be assumed that the compressible form of Bernoulli's equation (Eq. 6.6) holds true. This equates changes in dynamic pressure with equal changes in the magnitude of the static pressure. Higher static pressures cause higher pressure forces (and hence moments) to be experienced, giving an explanation of the source of the higher moments experienced in the worst cases. The work presented in this chapter leads to the following recommendation for shroud design: a shroud geometry that encourages a reduced throughflow, possibly via higher recirculation, should be a better shroud design. For the variations studied here this equates to a narrow inlet (1.56 mm clearance), with wide face and outlet clearances (2.12 mm and 4 mm, respectively)

Chapter 7

Conclusion

In closing this thesis, this chapter provides a statement of what has been achieved by the work described in it.

7.1 Statement of the aims and objectives of the work

The work within this thesis is part of a larger project which has investigated how windage power loss can be affected by geometric features of gears and shrouds. This is important as for large diameter ($\sim$ 200mm) bevel gears running at high speeds ($\Omega > 10,000$ RPM) the windage power loss forms a substantial part of the total power loss [24]. To date the flow field around a shrouded spiral bevel gear is one that has received little research, either experimentally or numerically, despite the widespread use of bevel gears in high speed gear boxes. The aims of the work presented in this thesis were twofold:

- develop and validate a modelling strategy for the flow around a shrouded spiral bevel gear
- apply this modelling strategy to a series of parametric variations of the shroud parameters

It was expected that the work would deliver a strategy for the numerical modelling of a shrouded spiral bevel gear which could be used to aid shroud design.

7.2 Level of attainment of objectives

A methodology was developed for successfully modelling a shrouded spiral bevel gear. This strategy was applied to a series of parametric variations of 3 key shroud parameters (the inlet clearance, the face clearance, and the outlet clearance, as defined in Chapter 6).

7.2.1 Development of modelling strategy-Simple geometries

The modelling strategy was developed by modelling some approximations to the shrouded spiral bevel gear using the commercial CFD program FLUENT, with numerical meshes developed using the commercial mesh generation program GAMBIT. As a starting point, models of Taylor-Couette flow were developed, to simulate experimental data which is available in the open literature. For completeness, this work has been presented within an Appendix to this thesis (Appendix A).

Carrying on from this point, work moved to study a modification of Taylor-Couette flow, looking at the flow between a pair of cones. This has been called Conical Taylor-Couette flow. Simulations were conducted to replicate the experiments of Yamada & Ito [69–71]. The aim of this section was to look at the relative accuracy of various numerical turbulence models, to assess their applicability in the final setting. Comparisons were made between 4 turbulence models: the standard $k-\epsilon$ turbulence model, the RNG $k-\epsilon$ turbulence model, the SST $k-\omega$ turbulence model, and the Reynolds Stress Model. In cases where no-throughflow is present, the comparisons between the RNG $k-\epsilon$ and the SST $k-\omega$ turbulence models demonstrated slightly better predictions from the latter model. However, the former model performed more consistently, capturing the trend shown in the data from Yamada & Ito with greater fidelity.

In the cases that bore more relevance to the setting of the shrouded spiral bevel gear, where throughflow is present, comparisons were made between the standard $k-\epsilon$ and the RNG $k-\epsilon$ turbulence models, and the Reynolds Stress Model. These showed of the two $k-\epsilon$ turbulence models, the RNG $k-\epsilon$ turbulence model performed better. It also closely matched the results from the Reynolds Stress Model. This was of benefit, as the computational resources needed for the $k-\epsilon$ turbulence models are less than for the

Reynolds Stress Model. Comparisons were also made using the RNG $k-\epsilon$ turbulence model with two different wall treatments, by using a standard wall function and an enhanced wall treatment. These produced different results, neither of which accurately captured the full set of experimental data when using a two-dimensional model.

Another set of comparisons were made by comparing the results obtained using two-dimensional meshes with those obtained with a three-dimensional 'wedge' and a full three-dimensional simulation. The three-dimensional wedge model showed little improvement over the two-dimensional model, with the added drawback of an increase in run-time. The full three-dimensional model showed some improvement, with results obtained using the RNG $k-\epsilon$ turbulence model with a standard wall function showing a better match with the overall trend shown experimentally, although it was seen to smooth out a distinct transition which was apparent in the data of Yamada & Ito. The full three-dimensional model was required for the cone was because of the non-axisymmetric flow pattern. It was felt, in the case of the gear, that the teeth would impart a rotational periodicity on the solution, eliminating the need to model the gear in its entirety.

The work presented in Chapter 4 gave a significant step toward developing a modelling strategy. To recap, the (preliminary) strategy was

- model turbulence using an RNG $k-\epsilon$ turbulence model
- model as much of the domain as computational resources allow

It still left questions as whether to use a standard wall function or an enhanced wall treatment, whether to model the flow steady-state or transient. These questions would be addressed in the subsequent chapters.

7.2.2 Development of modelling strategy-Unshrouded gear

The strategy which had been developed was then applied to the flow around an unshrouded spiral bevel gear. This would give a complex domain upon which to trial the strategy. Data produced 'in-house' would provide experimental validation. A model was developed of the experimental setting, which incorporated a single spiral bevel gear attached to a rotating shaft. To reduce complex flow interactions between the gear and

other equipment, a backing plate was fitted behind the gear. This was modelled as one of the extremes of the computational domain, the others being the axis of revolutions, and pressure boundaries representing the room in which the gear was situated. Due to the sizes of the grids that would be required to accurately resolve the flow over the entire gear, models were developed that incorporated just two-gear teeth. This was in line with the preliminary strategy, as a balance had to be made between the resources available, and the computational times needed to model the entire gear. Simulations were conducted for both rotational directions, as experimental data was available for these. In line with the preliminary strategy, turbulence was modelled using the RNG $k-\epsilon$ turbulence model. The domain was modelled using a combination of structured and unstructured meshes. To capture the boundary layer without resorting to dividing the domain into many small volumes near the wall, size-functions were used, to cause the mesh size to change smoothly.

In an attempt to answer the first unanswered question in the strategy, comparisons were made in steady-state simulations between the standard wall function and the enhanced wall treatment, in both rotational directions. The standard wall function consistently under-predicted the torque levels in both rotational directions by approximately 24%. Changing the direction of rotation of the gear means that effectively a different gear is being modelled (due to the curvature and angle of the teeth). It is felt that this is a useful result: if the under-prediction is known to be a consistent margin, it means that this numerical modelling technique can be used for prediction of trends. The performance of the enhanced wall treatment was not as consistent: for clockwise rotation it under-predicted torque levels by a similar margin to the standard wall function, in anti-clockwise rotation the performance of the model improved dramatically, with torque levels 'under-predicted' by just 6% at worst. However, the steady-state results produced using the enhanced wall treatment for anti-clockwise rotation also showed a lot of 'noise', failing to settle to a converged solution, with the reported torque values being averaged over 5000 iterations to give a 'steady-state' torque level.

As the solution for the unshrouded gear with anti-clockwise rotation produced using the RNG $k-\epsilon$ turbulence model showed such variation in the steady-state solution, it was

deemed necessary to conduct transient solutions of the flow-field. These were conducted at two rotational speeds (8203 and 1500 RPM), in order to indicate at any scalability of the solution with speed. Transience was indeed seen to be present within the solution. Analysis of the torque on the gear showed a dominant frequency of $\simeq 1/17^{\text{th}}$ of tooth passing frequency in both cases, with a secondary frequency also present at $\simeq 1/11^{\text{th}}$ of tooth passing frequency in both cases. Animations of the flow structure, shown in Figure 5.25 indicated vortices being shed from the gear at the same rate as the dominant frequency.

The work presented in Chapter 5 allows the addition of the following points to the strategy:

- if the steady-state solution fails to converge after a significant amount of iterations, without diverging, the flow may well be transient, and should be modelled as such to confirm (or deny) this
- complex geometries can be meshed using unstructured meshes with size functions to capture the boundary layer

7.2.3 Development of model-Application to a Shrouded Gear

In order to validate the strategy that had been validated, numerical models were developed of two shrouds for which experimental data had been produced in-house [25]. The first of these had the gear rotating at a constant rate, with a varying through-flow rate forced through the domain. This was simulated for the gear rotating at 8203 RPM in both directions. Comparisons were made between the performance of the two different wall treatments. Little difference was seen between the results obtained with these, both treatments over-predicting the torque levels seen experimentally. The only difference found between the two was that numerical convergence was easier to obtain with the standard wall function. For this reason, when modelling the second experimental setting, the standard wall function was used. These simulations again mimicked an experimental setting, with 3 different clockwise rotational speeds ran with 3 different imposed mass flow rates. Good agreement was shown, with the agreement improving with increasing non-dimensional imposed mass flow.

As it finally stands, the modelling strategy is as follows:

1. Model turbulence using an RNG $k-\epsilon$ turbulence model
2. Model as much of the computational domain as resources allow until you have established no azimuthal variation. A single tooth model will then suffice
3. A standard wall function should be used for the near-wall flows
4. If the steady-state solution fails to converge after a significant amount of iterations, without diverging, the flow may well be transient, and should be modelled as such to confirm (or deny) this
5. For closely shrouded gears, the flow should be modelled transient
6. Complex geometries can be meshed using unstructured meshes with size functions to capture the boundary layer

7.2.4 Application of modelling strategy to a series of parametric variations of key shroud parameters

Having developed the modelling strategy, this was then applied to a series of parametric variations of key shroud parameters. Many aspects of the shroud design could be altered, it was decided within the scope of this project to focus on the inlet clearance, the face clearance, and the outlet clearance. Each of these parameters were varied in 3 variants, leading to 27 variants in total. The models would be run with no imposed throughflow, although throughflows would be allowed to develop, by using pressure boundaries at the inlet and outlet. Initial work looked at the effect of rotational direction on the relative performance of the shrouds by looking at 8 variants (the extremes of clearance for the inlet and outlet, and the narrower pair of face clearance). As shown in Figure 6.16, whilst directional dependence was shown in the torque values reported, the relative performance of the shrouds did not change. This allows the focus to be on the performance of the shrouds in just one rotational direction. Simulations were conducted for the 27 variants at up to 4 different clockwise rotational rates. For the gear in question, this allows the conclusion that the part of the geometry which has the greatest effect on windage power

loss is the inlet clearance to be made, followed by the outlet clearance and finally the face clearance. By looking at the flow structure seen in the best and worst cases, insight was gained into how the shroud geometry changed the flow structure. It showed that 'good' shrouds show low throughflow, with significant recirculations present under the shroud, whereas 'bad' shrouds show high throughflow, with little recirculation under the shroud. These high and low throughflows lead to high and low dynamic pressure, respectively, across the teeth. Analysing the torque components (pressure and viscous) on the 4 sections that the gear was numerically subdivided into indicated that the majority of the torque ($\simeq 85\%$) was coming from the pressure force on the gear teeth. Using Bernoulli's equation as an approximation to the conditions under the shroud, it was then possible to show how these high dynamic pressures lead to high pressure forces, which are due to the static pressure. This is an important result which has not been previously reported.

7.3 Statement of original contribution of the thesis

The most important novel aspect of the work contributed by this thesis is that it has demonstrated that numerical modelling of the flow around a shrouded spiral bevel gear is indeed possible. It can capture the performance trend of a shroud well, meaning that it can be used as an aid to shroud design.

Prior to this thesis, no modelling of a shrouded spiral bevel gear has been presented in the open literature, and only one previous model of an unshrouded spiral bevel gear [20] has been presented[1].

The parametric variations presented in this thesis are the first that have been presented for a shrouded spiral bevel gear, according to the literature survey. They have highlighted simple strategies to reduce windage power loss which can be easily applied to shroud design.

7.4 Future Work

The work presented in this thesis leaves questions which it would be interesting to answer in future work. The first of these is in the work on Conical Taylor-Couette flow (§4).

[1] The work of Farrall *et al.* was a precursor to this thesis

Results were produced to replicate the work of Yamada & Ito [69–71]. Over most of the experimental range, these accurately reproduced these results, except for the transition region. None of the different modelling techniques used, which are all Reynolds-averaged Navier-Stokes models, successfully captured this transition. It may be that, through the use of a Large eddy simulation (LES), the transition can be captured. The flow structures present (seen in Figures 4.20(a)-4.20(c)) show 'plumes' of higher velocity coming off of the vertex of the cone, which are seen to be affected by the rotation of the cone at higher speeds, but at lower speeds this effect is less pronounced. This suggests there is a point at which the angular momentum induced by the rotation of the cone overcomes the axial momentum of the throughflow, which may be better captured by a LES. Other effects which may contribute to this transition could be acceleration effects. Noui-Mehidi [40] showed that for a truncated cone this was an important mechanism, though Yamada & Ito do not given any indication of acceleration rate, so this would be difficult to replicate. Another possibility is the location and amount of the secondary flow vortices present at low speeds. It was shown that after the transition these vortices have disappeared. As vortices are a good method of transfer of energy and momentum, their non-existence/disappearance may explain the sudden increase in torques seen.

An area of work which could be studied when looking at windage power loss which hasn't been considered here is how the geometry of the gear affects the windage power loss. This would be easy to achieve numerically, by simple alterations of the gear model. Farrall *et al.* [20] briefly considered the effect of 'blocking' the entrance to the tooth valley, as did Winfree [68], but there are many other factors which could be studied numerically, such as the cone angle of the gear, the cutter radius of the tooth, the pressure angle, or the cutter angle. Insight to the likely impact of these effects can be gained from fan theory [9], although a spiral bevel gear is a poor fan.

The parametric variation has looked at the effect of reducing three parameters. Of these, the largest reductions in windage power loss came from reductions in the inlet clearance, with the outlet clearance also producing appreciable reductions in windage power loss. Future work could consider the effect of the shape of these restrictions. For example, the shape of the inlet restriction is such that any back-flow along the shroud

will be turned directly back into the mainflow. If this back-flow were introduced as a crossflow instead, this would cause a virtual restriction on the inlet flow. As this work has shown that restricting the amount of air that the gear drives through the domain reduces the windage power loss, redirecting this flow should cause reductions in windage power loss. Thus, a series of variations on the angle of this cross flow may yield further insight into mechanisms for reducing single-phase windage power loss.

The outlet restriction is another area that needs further work. The geometry used here has many sharp corners, which will increase the venutri effect through the outlet, increasing the pressure drop through the shroud. By the arguments contained in §6, this will cause higher windage power loss. By altering the geometry here, by either changing the angle of this restriction and/or by streamlining the geometry, the windage power loss will be affected, and further gains could be made in reducing windage power loss from this area.

All the work that has been reported in this thesis has been single-phase. Results published by Johnson *et al.* [24] show that the torque in a two phase environment can be calculated from the single-phase torque and a simple oil acceleration term, based on the oil flow rate. For this reason, it does not seem necessary to use CFD to predict two-phase torque levels. However, CFD could be used to give a clearer understanding into the oil flow paths. This would allow an understanding of how the oil interacts with the gear, which could be used to change the oil velocities without reducing the lubrication. If this change in velocity was combined with a change in flow rate, it becomes clear that a reduction in windage power loss would result.

Finally another area which could be considered (numerically) would be that of meshing gears. This has been achieved, two-dimensionally, for spur gears by Strasser [53]. Modelling meshing gears would need far more computing resources to be dedicated to the work than has been available during this thesis, but would give dramatic insight into the flow structures as the two gears mesh. If this were to be conducted in two phase, it would allow greater understanding of the oil flow paths which occur under meshing.

7.5 Contribution to Science

The extent to which the work in this thesis has contributed to science can be measured by the publications that have arisen from it. Material from Chapter 4 has been published in the Journal of Fluids Engineering [49]. The two chapters on the flow around a spiral bevel gear (§5 and §6) have had material from them published at ASME TurboExpo 2007 [48] and ASME TurboExpo 2008 [47].

Appendix A

Computational Investigation of Taylor Couette Flow

A.1 Introduction

The motivation for the work contained in this chapter was to provide a starting point for developing a methodology for modelling the flow around a shrouded spiral bevel gear, as the geometrical setting of Taylor-Couette flow is a crude approximation of the target setting. Models would be developed which replicated an experimental set-up in the available literature [8]. Taylor-Couette flow is the flow that exists around a rotating cylinder/disc housed in a stationary chamber, as shown in Fig. A.1. Taylor-Couette flow begins when the inner cylinder in Fig. A.1 is rotated whist the outer cylinder remains stationary. For low angular velocities (Ω) the flow is laminar, with a linear velocity gradient between the two cylinders. Above a critical angular velocity, for which $\mathrm{Ta}_C < \mathrm{Ta} < 400$, the flow becomes unstable, though it is still laminar. Due to an imbalance between the centripetal and viscous forces, pairs of vortices appear between the two cylinders. As the rotation speed increases, the vortices become smaller and the flow becomes turbulent. A 'pluming' effect is known to occur at the ends of the cylinder, with a rotating flow being driven out from the top of the cylinder. This impinges on the stationary cylinder wall, driving the first vortex, as well as causing a secondary flow along the wall of the outer cylinder away from the inner cylinder. There are various

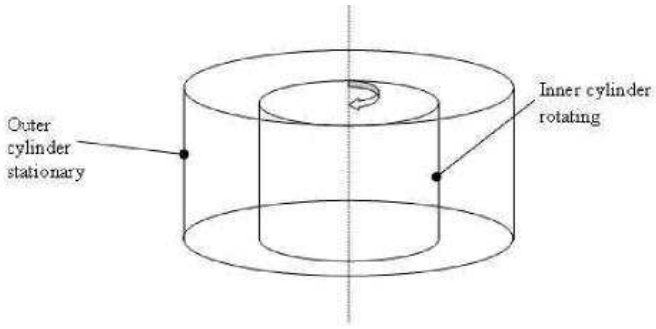

Figure A.1: Sketch of the setting

forces that can be looked at within the flow. From a mechanical viewpoint, of particular significance is the moment seen by the disc due to the retarding force from the fluid surrounding it. This moment can be considered to be a power loss and is referred to as windage loss.

Figure A.1 shows a sketch of the setting modelled. The rotating inner cylinder and stationary outer cylinder are both highlighted. A brief summary of the open literature that is available is presented in §A.2. In §A.3 the three different model configurations that have been used are presented, as well as the various turbulence models that have been applied. §A.4 presents the results, which are then discussed in §A.5, with appropriate conclusions presented.

A.2 Previous work

Much work has been conducted on basic Taylor-Couette flow, that is the flow between two right cylinders[1] where the inner cylinder rotates and the outer cylinder remains stationary, see Wild *et al.* [62], Lathrop *et al.* [28], Dubrulle & Hersant [17], Shiomi *et al.* [52], these are discussed below.

Wild *et al.* [62] performed an experimental and computational assessment of windage losses in rotating machinery. This was achieved by studying Taylor-Couette flow experimentally and computationally, utilizing an earlier version of Fluent (circa 1992). Their calculations made use of three turbulence models, the standard $k-\epsilon$ model [32], the RNG $k-\epsilon$ model [63, 64], and the RSM model [30]. Wild *et al.* found that good agreement

[1] A 'right' cylinder is one where the angle between the sides of the cylinder is 90°, a right angle.

could be found between the standard $k-\epsilon$ model with their own experimental data.

Lathrop *et al.* [28] looked experimentally at Taylor-Couette flow at large Reynolds number, $10^3 < \mathrm{Re} < 10^6$. They observed a transition in the flow at $\mathrm{Re} = 1.3 \times 10^4$, and that whilst approximate relationships between the torque and Reynolds Number could be given above and below this transition (respectively $M_{disc} \sim \mathrm{Re}^{1.3}$ and $M_{disc} \sim \mathrm{Re}^{1.73}$), no global relationships could be defined.

Dubrulle & Hersant [17] looked at momentum transport and torque scaling in Taylor-Couette flow from an analogy with turbulent convection. They present two predictions as to the relationship between torque and Reynolds Number for both low values of Re,

$$M_{disc} = 1.46 \frac{T^{3/2}}{(1-T)^{7/4}} \mathrm{Re}^{3/2},$$

and larger values of Re,

$$M_{disc} = 0.5 \frac{T^2}{(1-T)^{3/2}} \frac{\mathrm{Re}^2}{\ln\left[T^2(1-T)\mathrm{Re}^2 \times 10^{-4}\right]^{3/2}}.$$

Dubrulle & Hersant demonstrate good agreement between the predictions and experimental data.

To summarise, the literature indicates that basic Taylor-Couette flow can be modelled accurately, with torque levels relatively easy to predict. Whilst global relationships between torque levels and Reynolds number may not exist, approximate relationships can be found.

A.3 CFD Methodology

Calculations of the fluid flow field (the fluid in question being water) and associated torques are obtained for a shrouded cylinder. The study uses two and three dimensional computational fluid dynamics (CFD) to calculate the fluid flow and subsequent friction and turbulence losses for a shrouded cylinder. Computations have been carried out using two-dimensional and three-dimensional models. The two-dimensional models assume

axisymmetry within the flow. Two different three dimensional models were developed, one representing a rotationally periodic volume incorporating a 1° wedge on the cylinders, whilst the other representing a 1° wedge of a pair of infinite cylinders. The geometry (Fig. A.1) matches that used in Bilgen & Boulos [8]. Steady state solutions for the single-phase fluid flow field have been obtained using the commercial CFD codes FLUENT 6.2.16 & 6.3.26. Simulations are performed using a rotating frame of reference and the absolute velocity formulation. Computations correspond to rotation rates, Ω, within the range 0.4 rad $s^{-1} \leq \Omega \leq 150$ rad s^{-1}. Turbulence is modelled using the standard $k-\epsilon$ model [31], as well as the RNG version [63, 64] and the Realizeable version [51]. The governing equations were discretized using a second order upwind differencing scheme. Near-wall behaviours were captured through the standard wall function [32].

A.3.1 Infinite Cylinder.

The first model used is an infinite cylinder. Due to the rotational symmetry incorporated in the problem, it is not necessary to model the full 360° of the model, indeed in this case only a one-degree segment has been used. In all the models, end effects shall be discounted, and so the use of a model where there are no ends is fairly intuitive. A schematic diagram of the model is shown in Fig. A.2. The outer cylinder has been omitted from the view, so as to make the orientation clearer. The total number of cells in the model, before any grid adaptation is performed, is 770. The amount of cells across the gap is low to start with so as to assess the abilities of the grid adaptation built into FLUENT.

A.3.2 Rotating Slice

This model was developed to make use of the rotational symmetry in the problem to reduce the size of the mesh, whilst incorporating end effects. Whilst it is true that the interesting flow in Taylor-Couette flow is not in the region between the faces, the contribution of that region to the overall flow is important, especially in how the flow at the corner of the cylinder develops (the pluming described in §A.1). Computationally, including these regions does increase the overall computing time, as 8/9 of the total

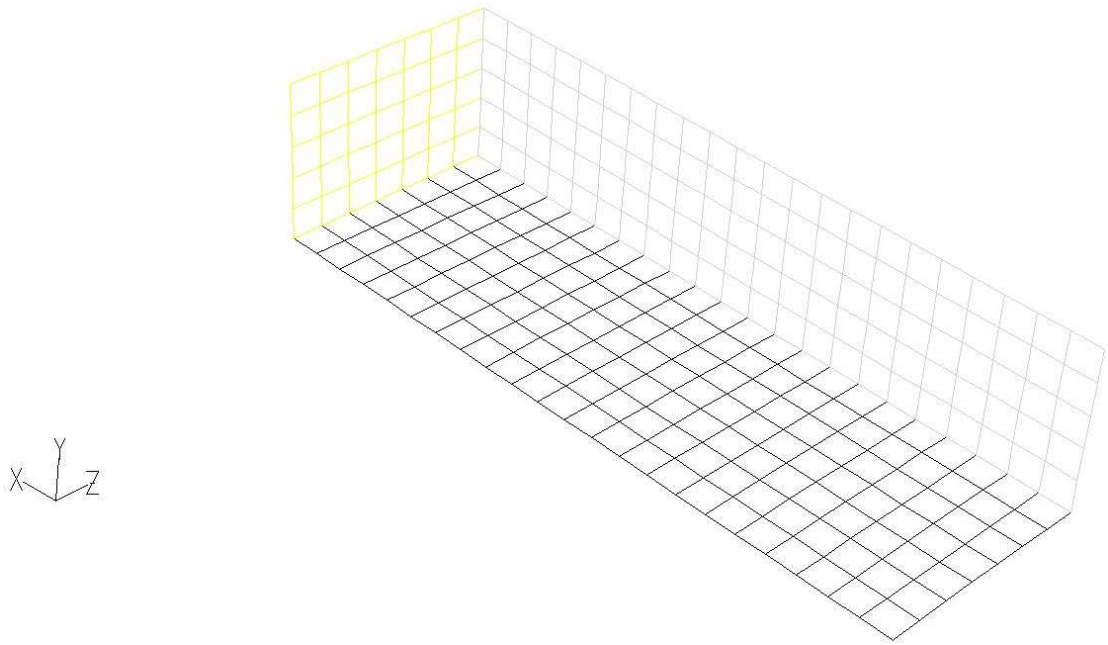

Figure A.2: Infinite cylinder model

volume considered in this situation is not in the annulus region. The model is shown in Fig. A.3. Fig. A.3(a) gives an overview of the mesh, with Fig. A.3(b) focusing on the top right corner, so as to give better detail of the mesh in the corner. The mesh is symmetric about the centreline of the cylinder, and rotationally symmetric about the x-axis.

A.3.3 Two-dimensional Slice

This model makes use of the fact that the flow should be two-dimensionally axi-symmetric and so the CFD model should be able to be simplified to two-dimensions. We can see that there is also another symmetry plane between the top and bottom of the cylinder which could be exploited. Following the work of Wild et al. [62], however, we see that it is necessary to model the entire situation, primarily so that, if the Taylor vortices are present, that they are the 'correct' size and quantity. A view of the model is shown in Fig. 5. In fact, two models of this configuration have been run, one having the inner cylinder surface identified separately into its three component parts, so as to deduce the contribution that end effects have in the moment calculated.

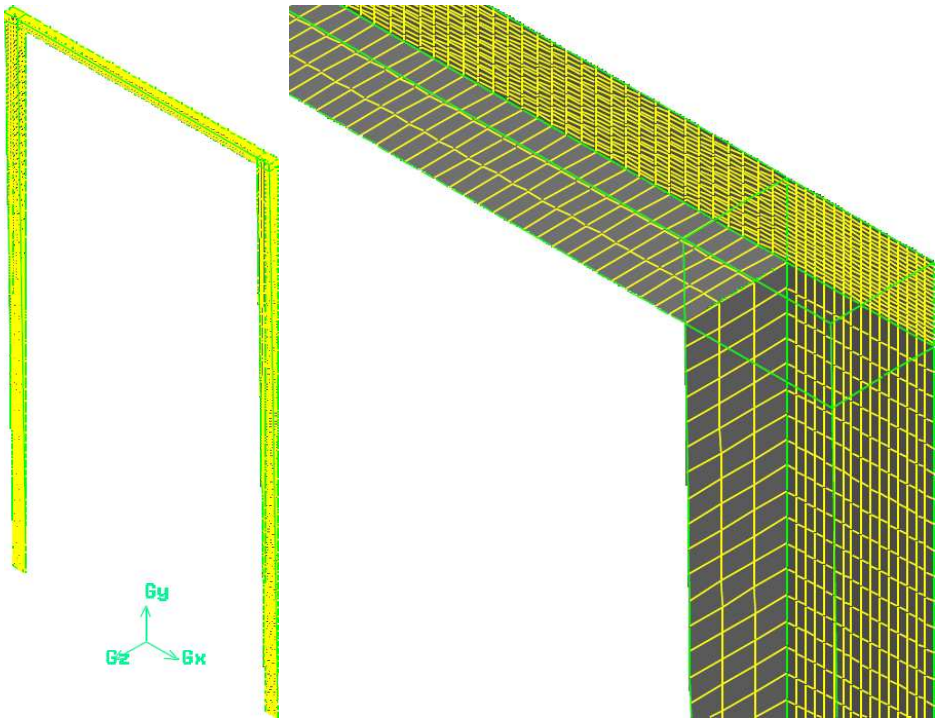

(a) Entire Mesh (b) Close up of top-right corner.

Figure A.3: Three-dimensional Rotating Slice model, as described in §A.3.2

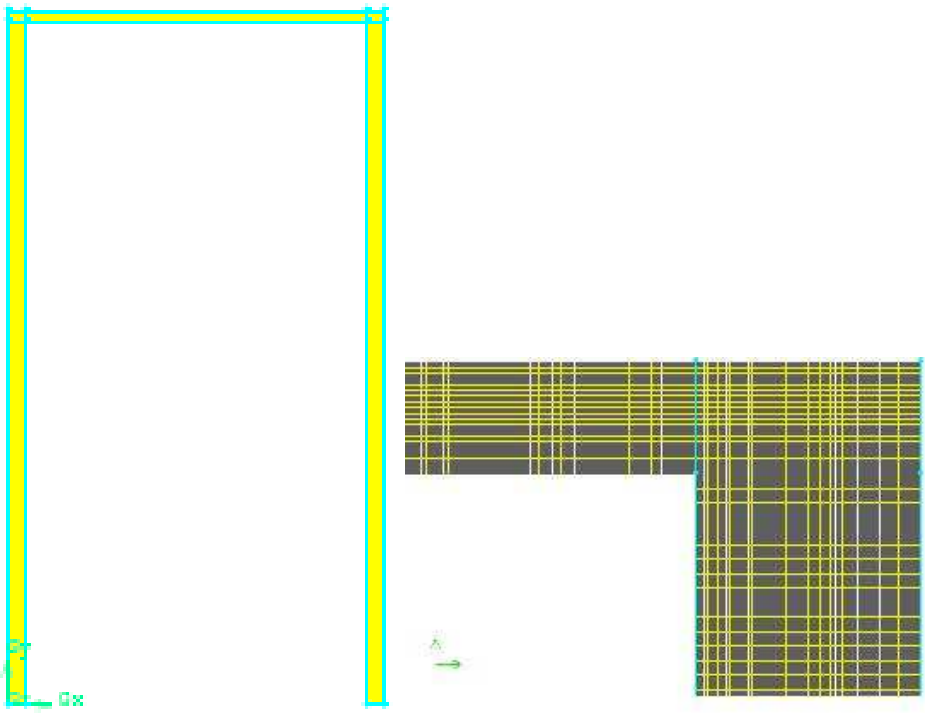

(a) Entire Mesh (b) Close up of top-right corner.

Figure A.4: Rendering of the two-dimensional complete model, as described in §A.3.3. Model contains 16,800 cells.

A.3.4 Viscous Models

In this section the 3 types of viscous model used will be described. These are the $k-\epsilon$ turbulence models (Standard, RNG, and Realizeable).

Standard $k-\epsilon$ Turbulence Model

The standard $k-\epsilon$ turbulence model [31] has the form:

$$\frac{\partial}{\partial t}(\rho k)+\frac{\partial}{\partial x_i}(\rho k u_i)=\frac{\partial}{\partial x_i}\left[\left(\mu+\frac{\mu_t}{\sigma_k}\right)\frac{\partial k}{\partial x_i}\right]+G_k+G_b-\rho\epsilon-Y_M, \tag{A.1}$$

and

$$\frac{\partial}{\partial t}(\epsilon k)+\frac{\partial}{\partial x_i}(\epsilon k u_i)=\frac{\partial}{\partial x_i}\left[\left(\mu+\frac{\mu_t}{\sigma_\epsilon}\right)\frac{\partial \epsilon}{\partial x_i}\right]+C_{1\epsilon}\frac{\epsilon}{k}\left(G_k+C_{3\epsilon}G_b\right)-C_{2\epsilon}\rho\frac{\epsilon^2}{k}. \tag{A.2}$$

In these equations, G_k represents the generation of turbulent kinetic energy due to the mean velocity gradients. G_b is the generation of turbulent kinetic energy due to buoyancy. Y_M represents the contribution of the fluctuating dilatation in compressible turbulence to the overall dissipation rate. $C_{1\epsilon}$, $C_{2\epsilon}$, and $C_{3\epsilon}$ are constants. σ_k and σ_ϵ are the turbulent Prandtl numbers for k and ϵ, respectively.

RNG $k-\epsilon$ Turbulence Model

The RNG $k-\epsilon$ turbulence model [63, 64] has a similar form to the standard $k-\epsilon$ turbulence model:

$$\frac{\partial}{\partial t}(\rho k)+\frac{\partial}{\partial x_i}(\rho k u_i)=\frac{\partial}{\partial x_i}\left(\alpha_k\mu_{\text{eff}}\frac{\partial k}{\partial x_i}\right)+G_k+G_b-\rho\epsilon-Y_M, \tag{A.3}$$

and

$$\frac{\partial}{\partial t}(\epsilon k)+\frac{\partial}{\partial x_i}(\epsilon k u_i)=\frac{\partial}{\partial x_i}\left(\alpha_\epsilon\mu_{\text{eff}}\frac{\partial \epsilon}{\partial x_i}\right)+C_{1\epsilon}\frac{\epsilon}{k}\left(G_k+C_{3\epsilon}G_b\right)-C_{2\epsilon}\rho\frac{\epsilon^2}{k}-R. \tag{A.4}$$

In these equations, G_k represents the generation of turbulent kinetic energy due to the mean velocity gradients. G_b is the generation of turbulent kinetic energy due to buoyancy.

Y_M represents the contribution of the fluctuating dilatation in compressible turbulence to the overall dissipation rate. The quantities α_k and α_ϵ are the inverse effective Prandtl numbers for k and ϵ, respectively.

Realizeable $k-\epsilon$ Turbulence Model

The modelled transport equations for k and ϵ in the realizable $k-\epsilon$ model are [51]

$$\frac{\partial}{\partial t}(\rho k) + \frac{\partial}{\partial x_j}(\rho k u_j) = \frac{\partial}{\partial x_j}\left[\left(\mu + \frac{\mu_t}{\sigma_k}\right)\frac{\partial k}{\partial x_j}\right] + G_k + G_b - \rho\epsilon - Y_M + S_k \tag{A.5}$$

and

$$\frac{\partial}{\partial t}(\rho \epsilon) + \frac{\partial}{\partial x_j}(\rho \epsilon u_j) = \frac{\partial}{\partial x_j}\left[\left(\mu + \frac{\mu_t}{\sigma_\epsilon}\right)\frac{\partial \epsilon}{\partial x_j}\right] + \rho C_1 S\epsilon - \rho C_2 \frac{\epsilon^2}{k+\sqrt{\nu\epsilon}} + C_{1\epsilon}\frac{\epsilon}{k}C_{3\epsilon}G_b + S_\epsilon \tag{A.6}$$

where

$$C_1 = \max\left[0.43, \frac{\eta}{\eta+5}\right]$$

$$\eta = S\frac{k}{\epsilon}$$

$$S = \sqrt{2S_{ij}S_{ij}}$$

In these equations, G_k represents the generation of turbulence kinetic energy due to the mean velocity gradients. G_b is the generation of turbulence kinetic energy due to buoyancy. Y_M represents the contribution of the fluctuating dilatation in compressible turbulence to the overall dissipation rate. C_2 and $C_{1\epsilon}$ are constants. σ_k and σ_ϵ are the turbulent Prandtl numbers for k and ϵ, respectively. S_k and S_ϵ are user-defined source terms.

A.3.5 Wall Treatment

The standard wall functions in FLUENT are based on the proposal of Launder and Spalding [31], and have been most widely used for industrial flows. It utilizes two formulae for the stress-strain relationship, one a log-law for the mean velocity (the so-called

'law of the wall', Eqn. A.7),

$$U^* = \frac{1}{\kappa} \ln(9.793 y^*), \tag{A.7}$$

(where κ is von Kármáns constant ($= 0.4187$).), the other a laminar stress-strain relationship (Eqn. A.8),

$$U^* = y^*. \tag{A.8}$$

The log-law is employed when $y^* > 11.225$, the laminar law is employed when $y^* < 11.225$. Reynolds' analogy between momentum and energy transport gives a similar logarithmic law for mean temperature.

The standard wall functions work reasonably well for a broad range of wall-bounded flows. However, they tend to become less reliable when the flow situations depart too much from the ideal conditions that are assumed in their derivation. Among others, the constant-shear and local equilibrium hypotheses are the ones that most restrict the universality of the standard wall functions.

A.3.6 Boundary and Operating Conditions

In all cases, the flow is assumed to be incompressible, steady state and isothermal. The inner cylinder is modelled as a rotating wall with a no-slip condition applied. The outer cylinder is modelled as a stationary wall with a no-slip condition applied. For all cases, the flow is initialized to be stationary. All the simulations were computed on a computer with a Pentium 4, 3.40GHz with 2.0 GB of RAM.

A.4 Results

To compare the efficiency of the models used, torque coefficients have been calculated.

Fig. A.5 shows an overview of the performance of the three models, compared with experimental data and theoretical curves (Eq. 2.11a & Eq. 2.11b) from [8]. Firstly it can be seen that three different numerical models are producing similar results, with little variation shown. If we dismiss the CFD result produced using the infinite cylinder model at $\mathrm{Re} = 2.4 \times 10^4$, it can be seen that with increasing Reynolds number, the accuracy of the CFD improves. Moment coefficients are over-predicted by 28% for $\mathrm{Re} = 2.3 \times 10^4$,

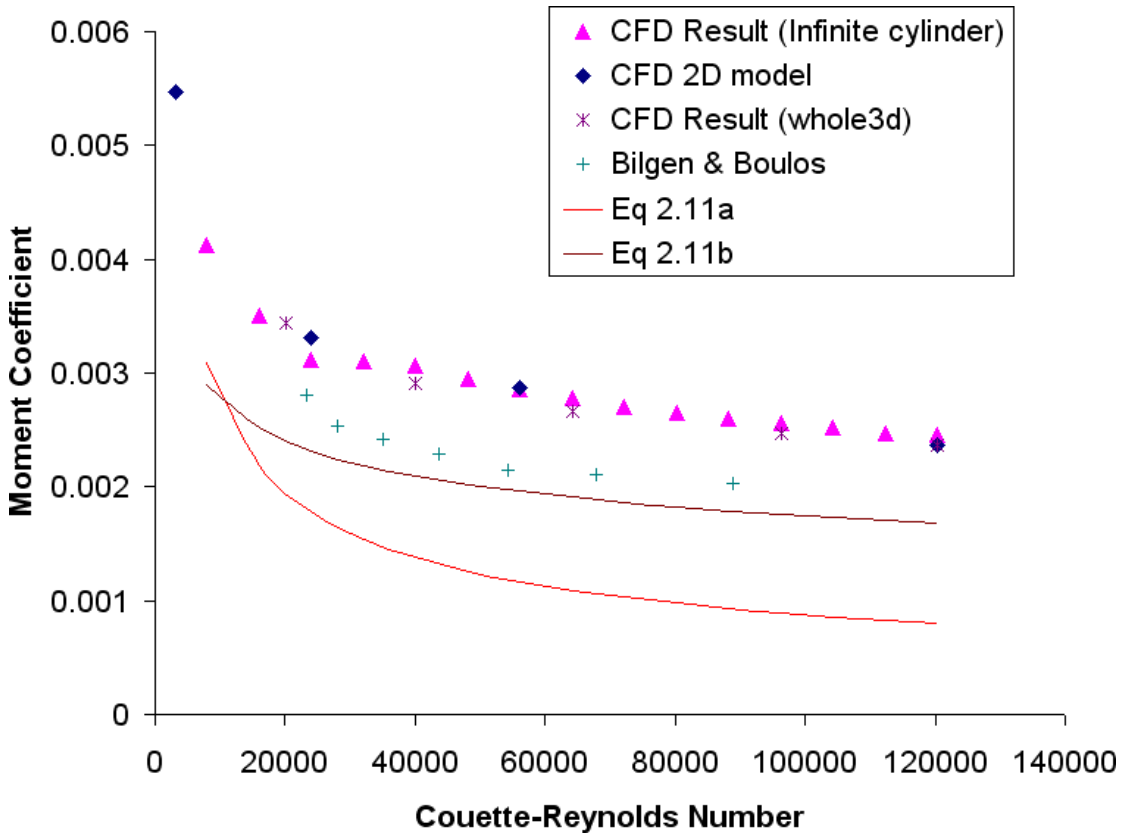

Figure A.5: Plot of moment coefficient against Couette-Reynolds Number.

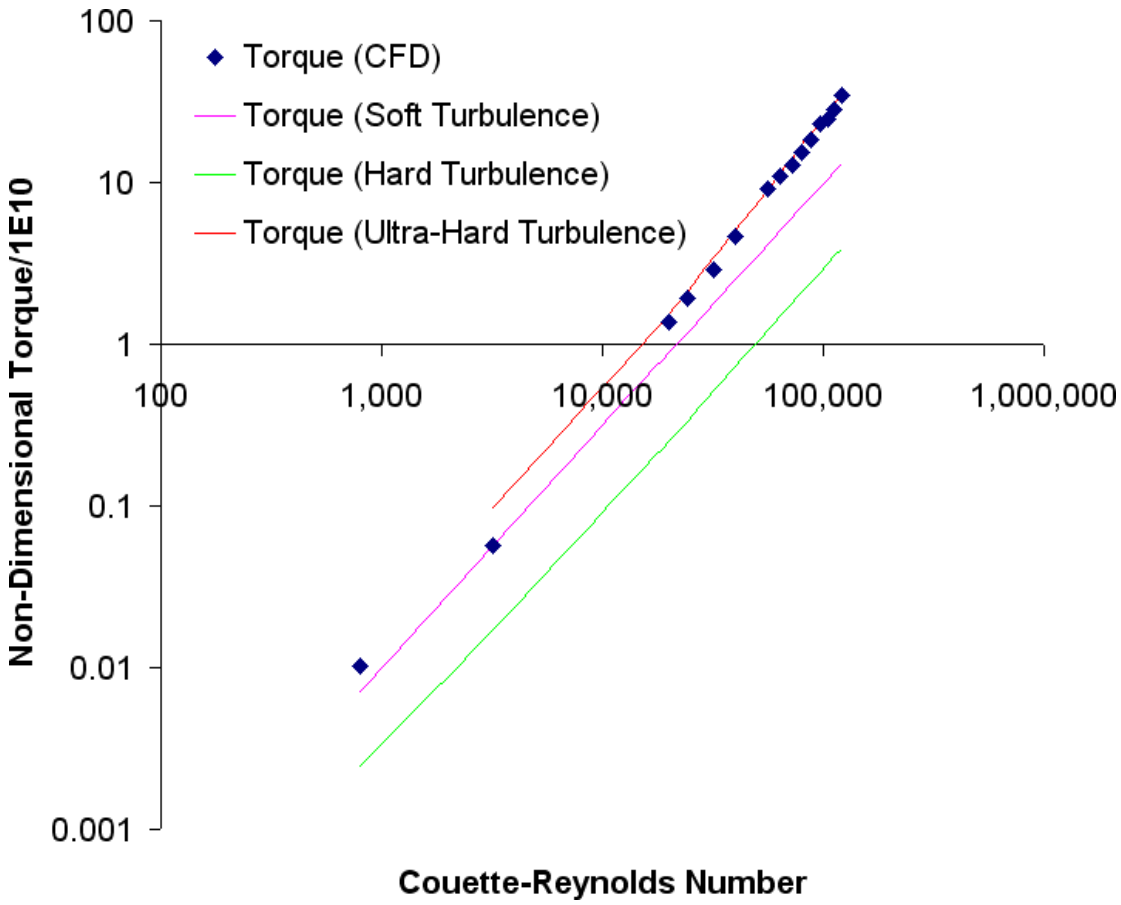

Figure A.6: Non-dimensional torque against Couette-Reynolds number.

reducing to an over-prediction of 18% for $\mathrm{Re} = 8.9 \times 10^4$. Compared to the equations given in [8], however, the performance is less satisfactory, with the CFD producing moment coefficients 44% higher than those given by Eq. 2.11b.

Fig. A.6 demonstrates how the results from the CFD compare with Eq. 2.17, from Dubrulle & Hersant [17]. For low values of Couette-Reynolds the agreement between the CFD and the 'soft' turbulence equation (Eq. 2.17a) is good, with the moment coefficient from the CFD being within 20% of the soft equation. When the Couette-Reynolds number is $\geq 2 \times 10^5$, the agreement with the 'ultra-hard' turbulence equation (Eq. 2.17c) is also good, with the moment coefficient on average under-predicted by 8%. These results agree with the findings of [17].

Fig. A.7 shows how the CFD compares with data from Daily & Nece [11]. The curves **Laminar** and **Turbulent** refer to Eq. 2.14a and Eq. 2.14c, respectively. We see close agreement between the Turbulent Equation, Eq. 2.14c, and the CFD data, with

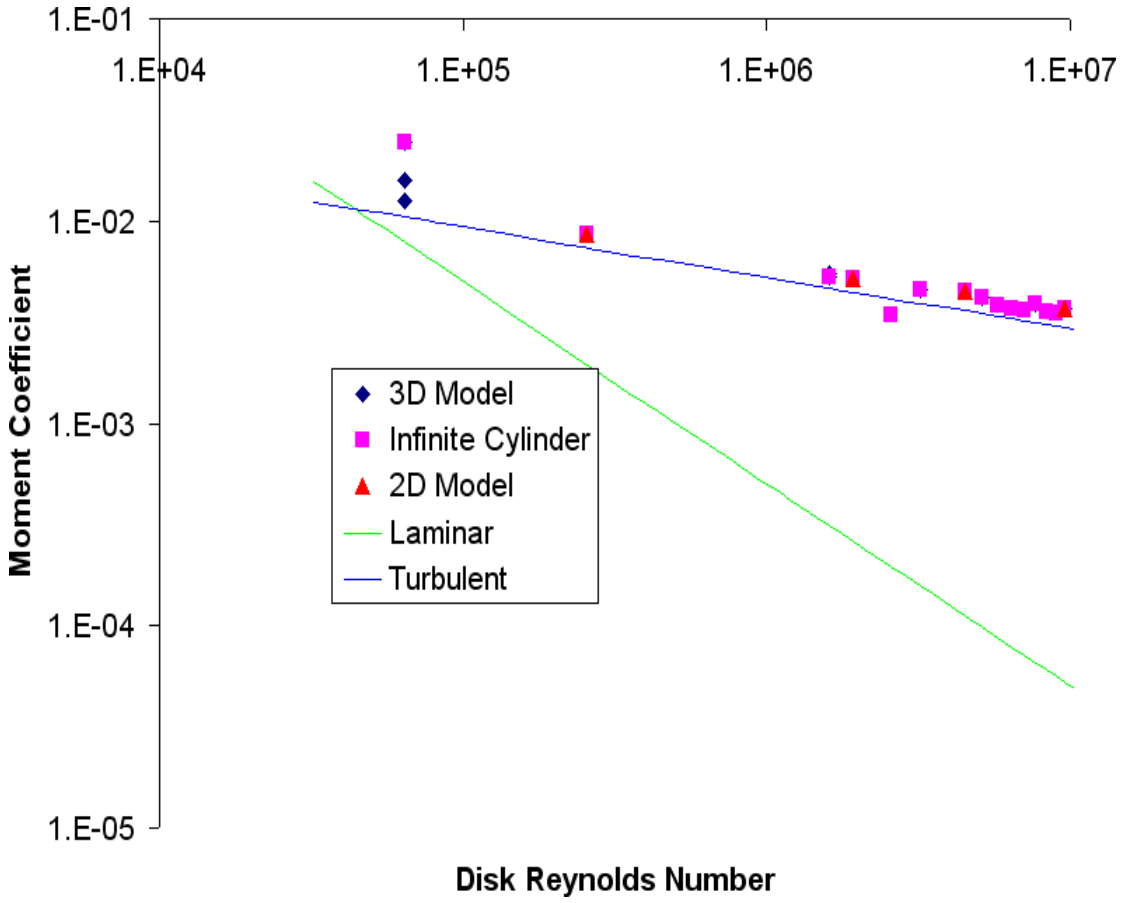

Figure A.7: Plot of moment coefficient against Disk Reynolds number, as defined in [11].

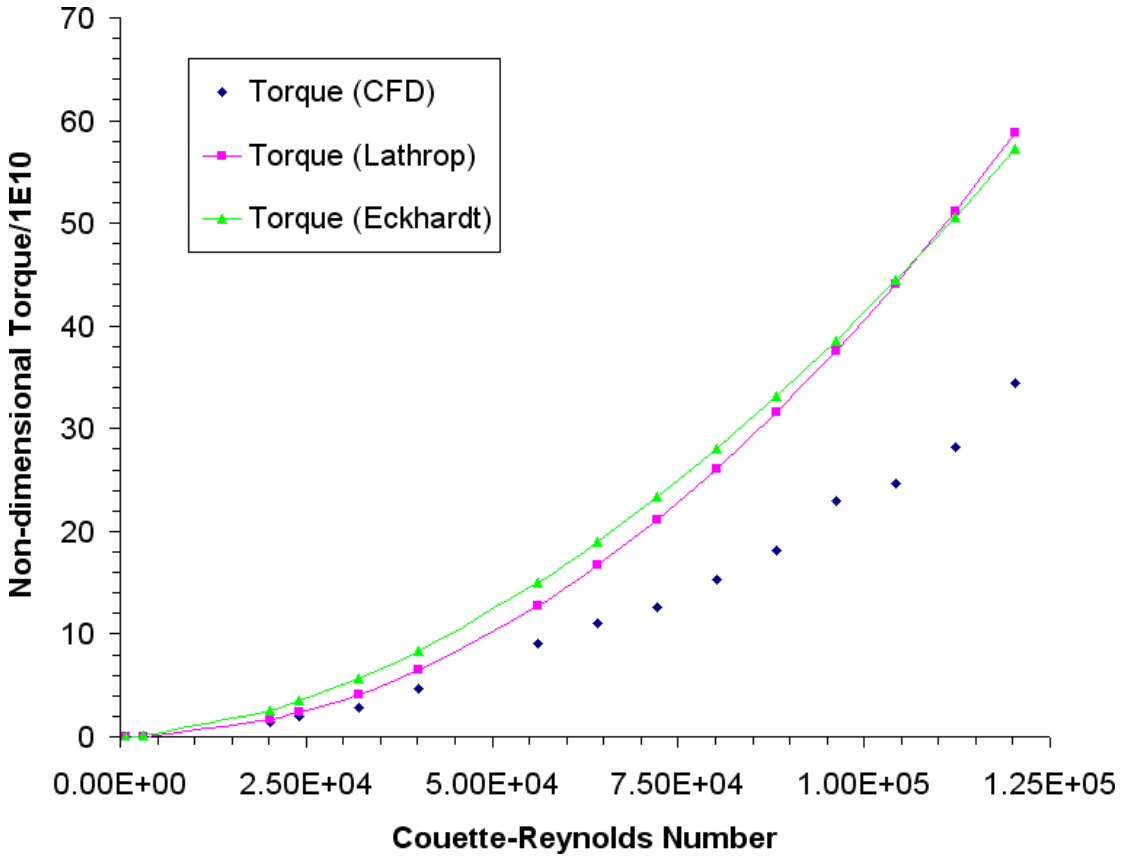

Figure A.8: Plot of Couette-Reynolds number, Re_c, against non-dimensional torque.

the CFD being within ±20% of the curve. The closest agreement is for $\mathrm{Re} = 5.8 \times 10^6$, where the CFD is 12% higher than Eq. 2.14c. The worst agreement is for $\mathrm{Re} = 4.5 \times 10^6$, where the CFD is 25% higher than Eq. 2.14c.

Fig. A.8 looks at how well the models of [19, 28] compare with the CFD data. It can be seen that these models significantly over-predict the torque levels seen. Compared to the equation from [28] (Eq. 2.18), the best agreement is for $\mathrm{Re} = 2 \times 10^4$, where the equation over-predicts the torque by 20%, with the agreement worsening with increasing Re, the worst value being for $\mathrm{Re} = 1.1 \times 10^5$, where the over-prediction is 82%. Similarly, compared to the equation from [19] (Eq. 2.19) the best agreement is for $\mathrm{Re} = 5.6 \times 10^4$, where the equation over-predicts the torque by 65%, the worst value being for $\mathrm{Re} = 3.2 \times 10^4$, where the over-prediction is 99%.

It is also useful to look at how well the models replicate the flow structure itself. Figure A.9 shows contours of radial velocity on the rotational boundary for the infinite cylinder model (§A.3.1). The rotational axis is the x axis. As can be seen, the classic flow

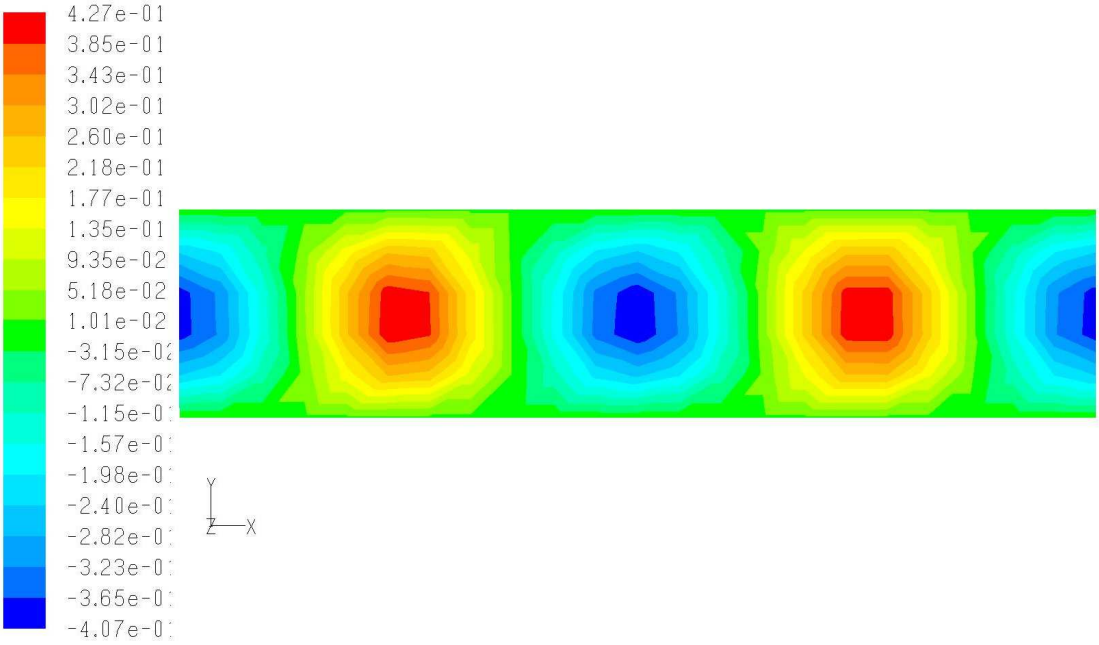

Figure A.9: Contours of radial velocity on the rotational boundary for the infinite cylinder model (§A.3.1). $\Omega = 96 \text{rad} s^{-1}$ (turbulent flow with Taylor Cells)

structure of Taylor-cells has developed, with alternating values of positive and negative radial velocity in the axial direction.

We can look at the velocity profile in the gap. Figure A.10 shows a plot of tangential velocity in the radial gap, for the model described in §A.3.2, shown in Fig. A.3, for an angular velocity of $96 \text{rad} s^{-1}$. Boundary layers can be seen close to the two walls. The overall profile is similar to that shown in [11], although the bulk flow profile is different. The flow in this region is influenced by the non-dimensional gap width as well as the Reynolds number, which are different in this investigation to those used by Daily and Nece [11], which explains the difference in velocity profile seen.

Figure A.11 shows a contour plot of velocity magnitude in the entire domain for the two-dimensional model (§A.3.3).

A.4.1 Summary

Overall, there is very little difference between the results obtained from the different models although the data from the 3D model is slightly closer to the experimental data. However, this model is the most computationally expensive as it requires more cells and it would be difficult to justify modelling 3D on the basis of these results alone. In all

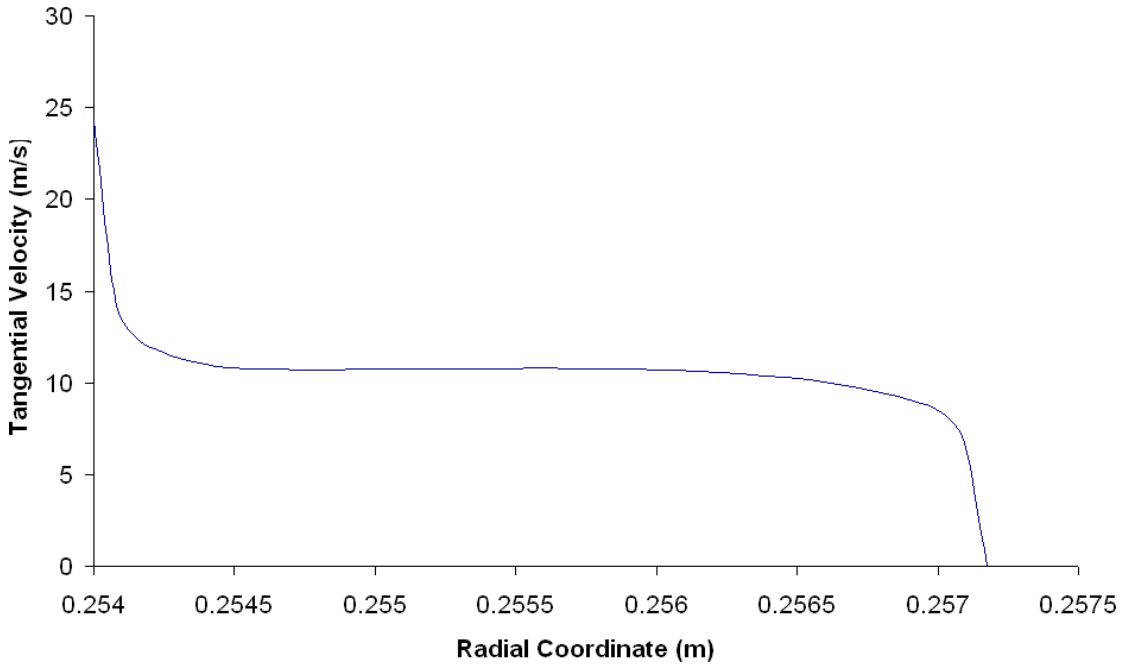

Figure A.10: Plot of tangential velocity in the radial gap, for the model described in §A.3.2, shown in Fig. A.3, for an angular velocity of 96rads^{-1}.

cases the retarding torque obtained from the CFD models is significantly higher than that obtained experimentally (between 13% & 61% higher than experimental data). The model that deviates most from the experimental data is that from the infinite cylinder model, which is understandable, as it is the most simplified version of the problem. This suggests that the effects of the ends of the cylinders must be considered in this problem, and should be included in any similar situations. A limited investigation into the effect of the turbulence models was conducted, with the standard, RNG and realizable $k-\epsilon$ models being applied. Generally the RNG model was found to be the most accurate of the three forms used, though the Realizable model did produce very similar results to those from the RNG.

A.5 Conclusions

This investigation has highlighted some of the positive aspects of using FLUENT. The results achieved with the models are satisfactory, though they do highlight the fact that the more accurate results required, the more accurate the model must be. In the trade off between computing time, and accurate modelling some compromise must evidently

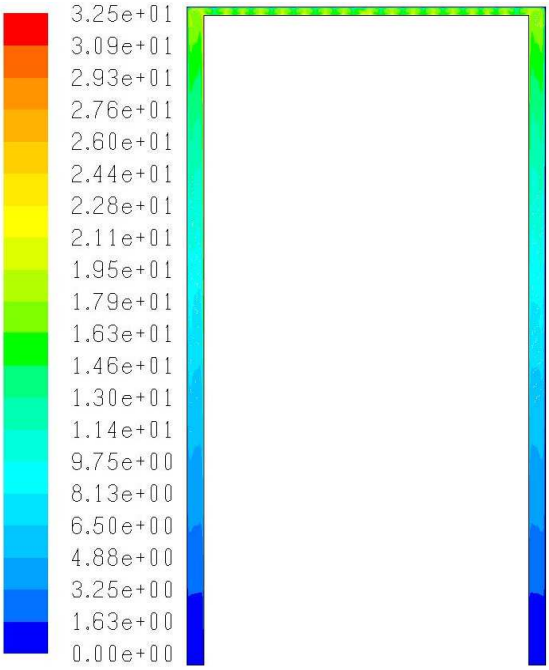

Figure A.11: Contours of velocity magnitude in the entire domain for the two-dimensional model (§A.3.3). $\Omega = 128 \text{rad} s^{-1}$ (turbulent flow with Taylor Cells). Axis of revolution is the x-axis, at the bottom of the figure.

be reached. Using the Kolmogorov length scaling, we find that the number of cells we would need for Direct Numerical Simulation of this flow is in the order of 10^{11}, so we can see that using models like those shown in §A.3, along with the turbulence models used, is entirely appropriate. The use of Reynolds-Stress models, or Large Eddy Simulations has not be investigated, primarily to concentrate on one kind of model, as well as the fact that these models have a longer computing time. The possible increase in accuracy is worth considering, but again, a balance has to be reached between accuracy and computing time. This investigation has shown that the use of the variations on the $k-\epsilon$ model are sufficient for rotating flows that are similar to Taylor-Couette flow. The $k-\omega$ turbulence model was tried, but the results were not as accurate as $k-\epsilon$, due to $k-\omega$ only really being suitable for low-Re flow, which is not what was considered here. Other considerations for improving the accuracy of the grid's would be to use denser grids, and grids that are not based around quadrilaterals. It would also be worth considering using Reynolds Stress models, to see how much more accurate the results are in comparison with $k-\epsilon$.

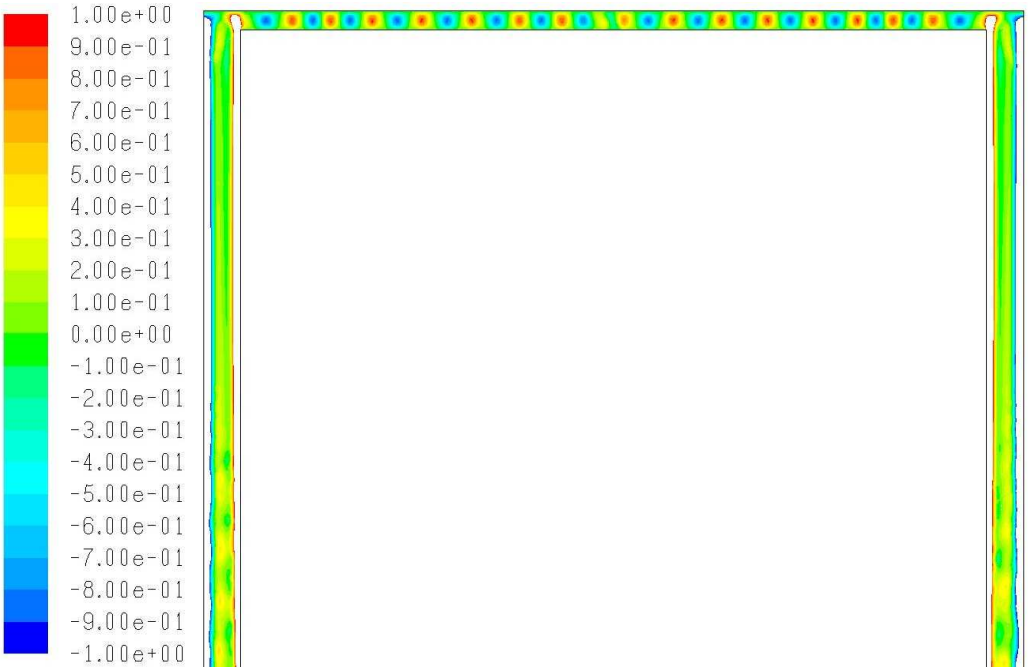

Figure A.12: Contours of radial velocity (clipped to a scale of $-1 \leq v_r \leq 1$), close up of Taylor-Cells. $\Omega = 128 \text{rad} s^{-1}$ (turbulent flow with Taylor Cells)

Appendix B

Shrouded Gear-Extra plots

The figures included in this section are placed here for completeness. In general they are used to support figures in the main body of the thesis in Chapter 6 which show little of interest happening in certain situations.

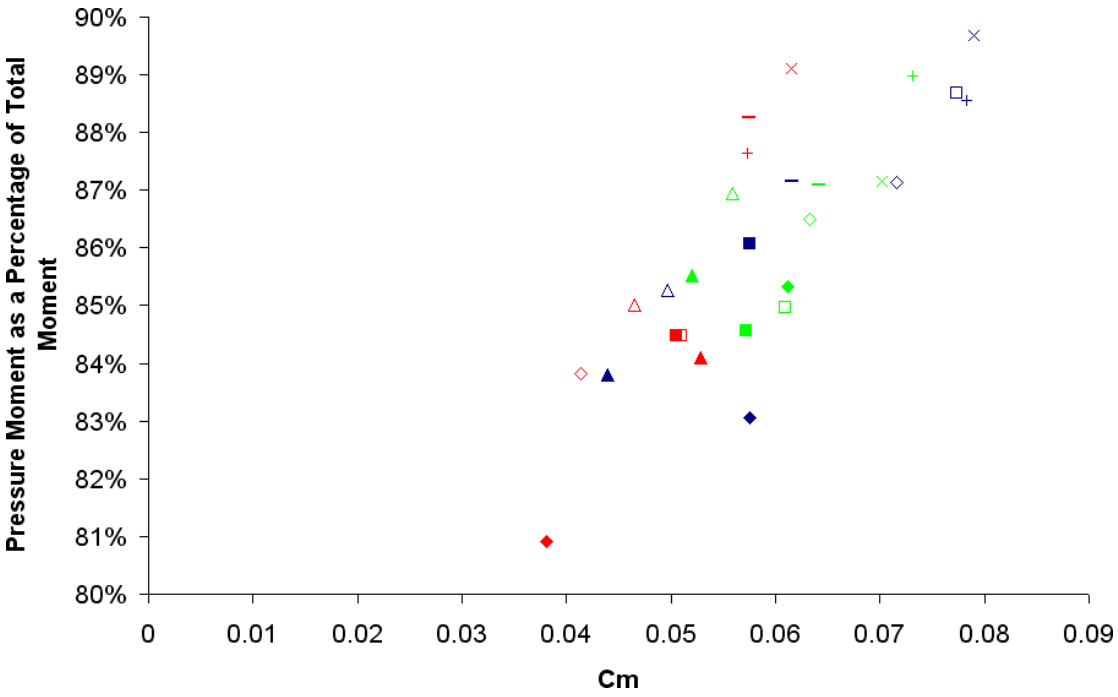

Figure B.1: Graph of moment coefficient (C_M) against pressure moment as a percentage of total moment for the 27 parametric variations. Coloured by inlet clearance

Figures B.1 and B.2 present graphs of moment coefficient (C_M) against, respectively, pressure moment and viscous moment as a percentage of the total moment for the 27 parametric variations. The graphs are coloured by the inlet clearance, with red represent-

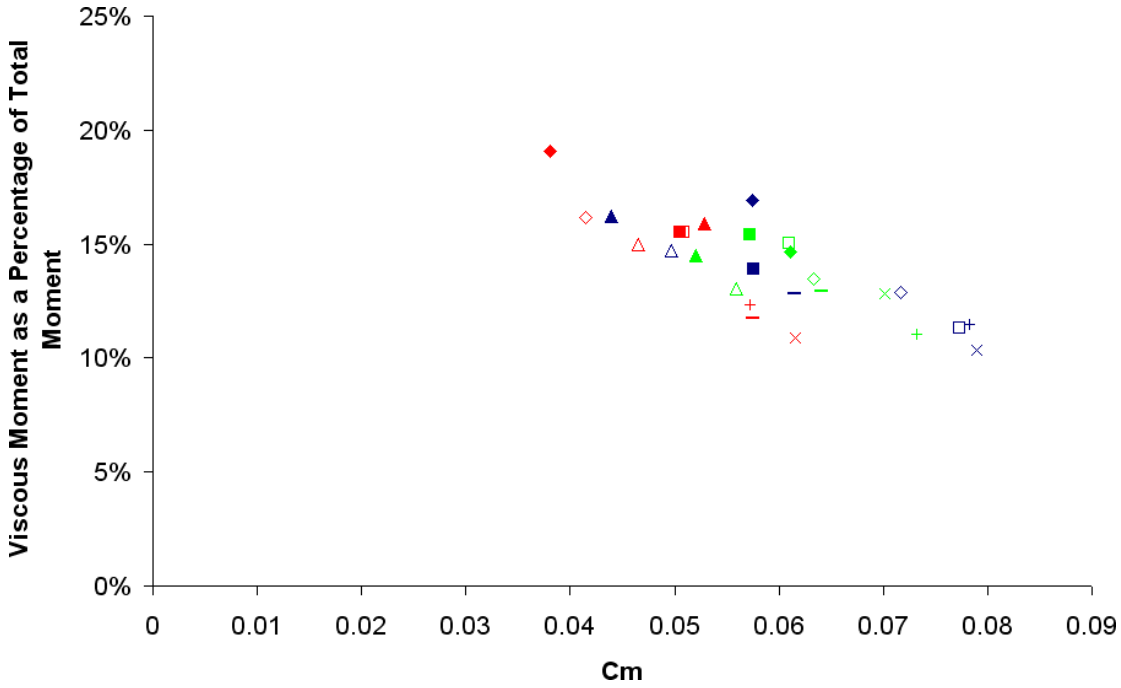

Figure B.2: Graph of moment coefficient (C_M) against viscous moment as a percentage of total moment for the 27 parametric variations. Coloured by inlet clearance

ing a 1.56 mm clearance, green representing a 3.187 mm clearance, and blue representing a 4.00 mm clearance. These graphs show that the pressure moment accounts for between 80.9% & 89.7% of the total moment, and varies by up to ±39%. The viscous moment, whose contribution is between 10.3% and 19.1% of the total moment, varies by up to 21%.

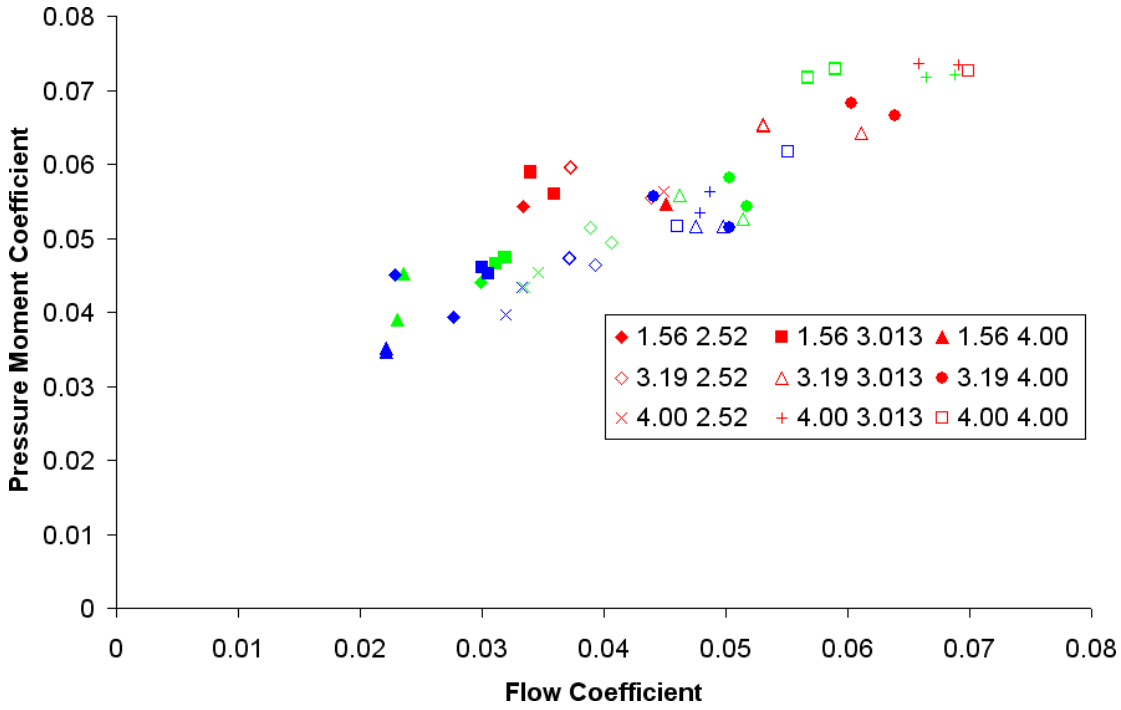

Figure B.3: Graph of flow coefficient (C_Q) against pressure moment coefficient (C_{Mp}) for the 27 parametric variations. The graph is coloured by the face clearance.

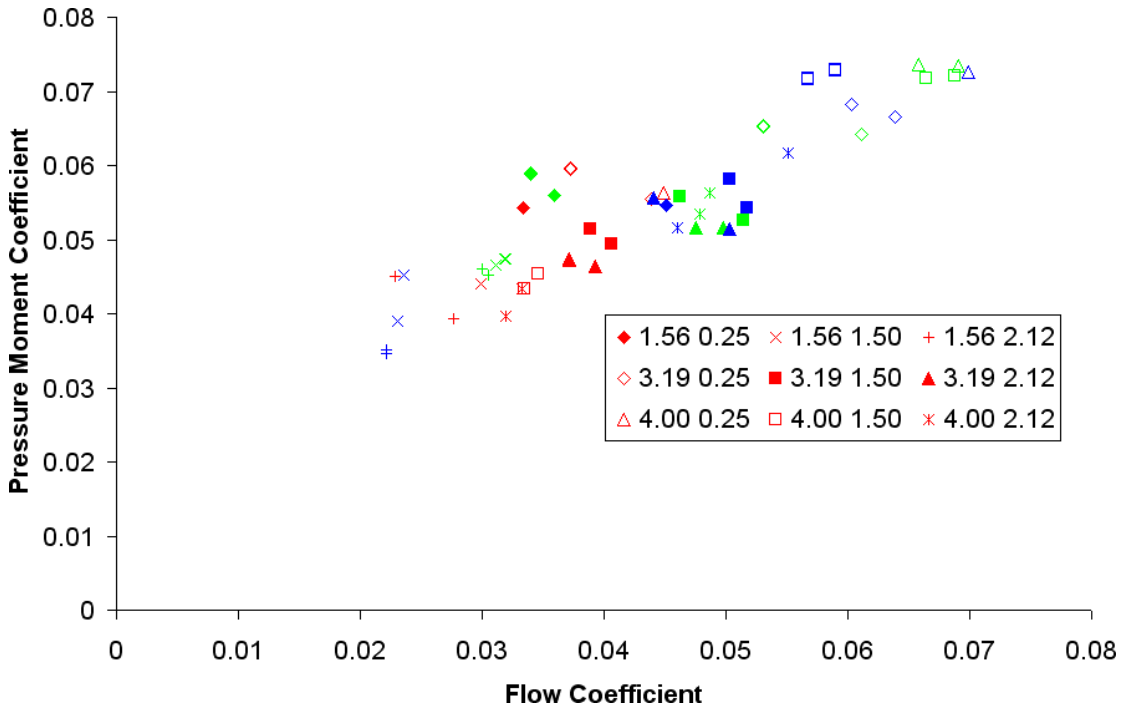

Figure B.4: Graph of flow coefficient (C_Q) against pressure moment coefficient (C_{Mp}) for the 27 parametric variations. The graph is coloured by the outlet clearance.

Figure B.3 presents a graph of flow coefficient (C_Q) against pressure moment coefficient (C_{Mp}) for the 27 parametric variations. The graph is coloured by the face clearance, with red representing a 0.25 mm clearance, green representing a 1.5 mm clearance, and blue representing a 2.12 mm clearance. Data points plotted with the same geometrical shape have the same configuration of face and outlet clearance. The scatter seen is due to varying inlet and outlet clearances. Grouping the data in this manner makes it clear that the face clearance has an impact on the pressure moment seen, as all the cases with a wide face clearance have a lower pressure moment coefficient and a lower flow coefficient. The change from the medium to the narrowest inlet clearance is not as clear, with the two data sets occupying the same solution space.

Figure B.4 presents a graph of flow coefficient (C_Q) against pressure moment coefficient (C_{Mp}) for the 27 parametric variations. The graph is coloured by the outlet clearance, with red representing a 2.52 mm clearance, green representing a 3.013 mm clearance, and blue representing a 4.0 mm clearance. Data points plotted with the same geometrical shape have the same configuration of face and outlet clearance. The scatter seen is due to varying face and inlet clearances. Grouping the data in this manner makes it clear that the outlet clearance has an impact on the pressure moment seen, as all the cases with a narrow outlet clearance have a lower pressure moment coefficient and a lower flow coefficient. The change from the medium to the widest outlet clearance is not as clear, with the two data sets occupying the same solution space.

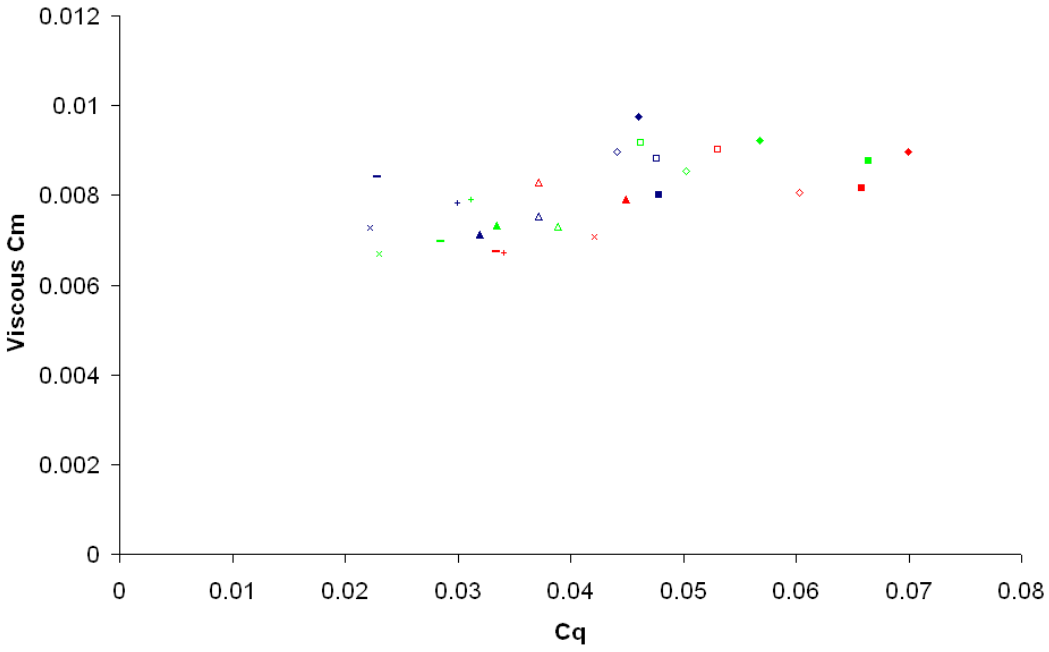

Figure B.5: Graph of flow coefficient (C_Q) against viscous moment coefficient (C_{Mv}) for the 27 parametric variations. The graph is coloured by the face clearance.

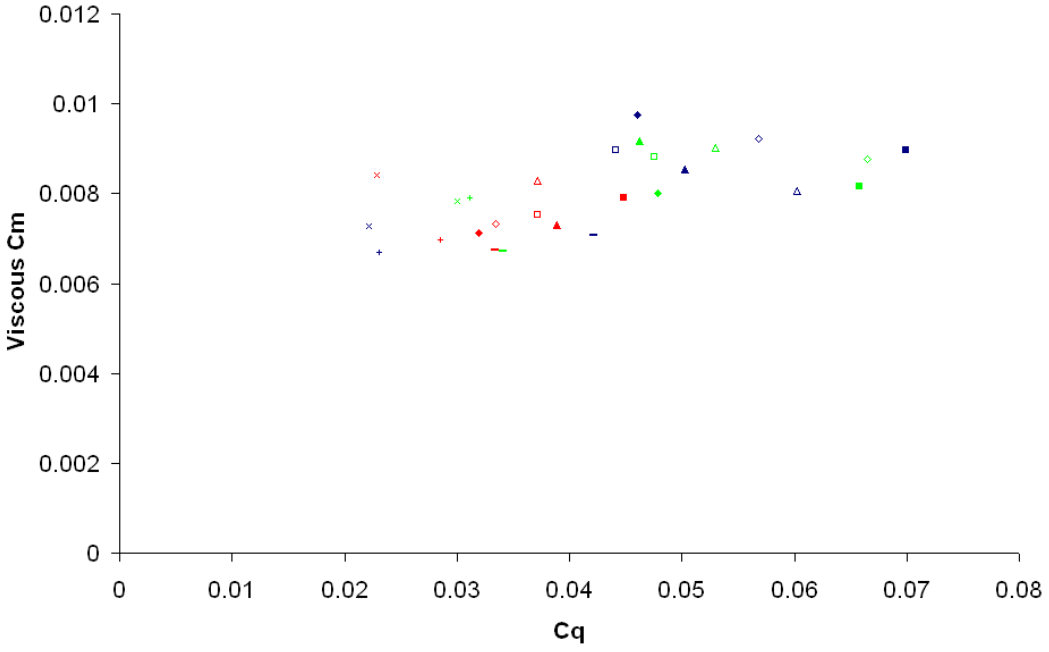

Figure B.6: Graph of flow coefficient (C_Q) against viscous moment coefficient (C_{Mv}) for the 27 parametric variations. The graph is coloured by the outlet clearance.

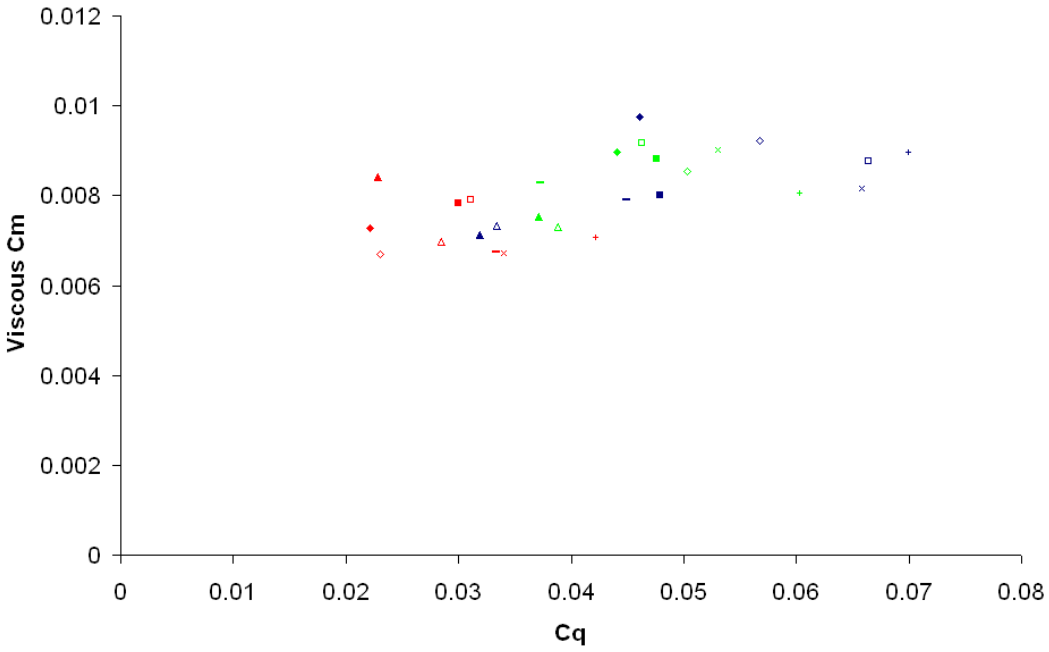

Figure B.7: Graph of flow coefficient (C_Q) against viscous moment coefficient (C_{Mv}) for the 27 parametric variations. The graph is coloured by the inlet clearance.

Figure B.7 presents a graph of flow coefficient (C_Q) against viscous moment coefficient (C_{Mv}) for the 27 parametric variations. The graph is coloured by the inlet clearance, with red representing a 1.56 mm clearance, green representing a 3.187 mm clearance, and blue representing a 4.00 mm clearance. Data points plotted with the same geometrical shape have the same configuration of face and outlet clearance. The scatter seen is due to varying face and outlet clearances. It can be seen that the change in the viscous moment with flow coefficient is not as great as the change in pressure moment, with a variation in the moment of $+21\%/-16\%$ from the average, compared to the $\pm 39\%$ variation seen in the pressure moment. This aside, grouping the data in this manner makes it clear that the inlet clearance has an impact on the viscous moment seen, as all the cases with a narrow inlet clearance have a lower pressure moment coefficient and a lower flow coefficient. The change from the medium to the widest inlet clearance is not as clear, with the two data sets occupying the same solution space.

Figure B.5 presents a graph of flow coefficient (C_Q) against viscous moment coefficient (C_{Mv}) for the 27 parametric variations. The graph is coloured by the face clearance, with red representing a 0.25 mm clearance, green representing a 1.5 mm clearance, and

blue representing a 2.12 mm clearance. Data points plotted with the same geometrical shape have the same configuration of inlet and face clearance. The scatter seen is due to varying inlet and face clearances. It can be seen that varying the face clearance has an impact on the overall viscous moment, with the narrow face clearance produces higher viscous moments than the widest face clearance.

Figure B.6 presents a graph of flow coefficient (C_Q) against viscous moment coefficient (C_{Mv}) for the 27 parametric variations. The graph is coloured by the outlet clearance, with red representing a 2.52 mm clearance, green representing a 3.013 mm clearance, and blue representing a 4.0 mm clearance. Data points plotted with the same geometrical shape have the same configuration of face and outlet clearance. The scatter seen is due to varying inlet and face clearances. It can be seen that varying the outlet clearance has some impact on the overall viscous moment, with the narrowest outlet clearance producing lower viscous moments, although the effect of the other two outlet clearances on the overall viscous moment is not as obvious.

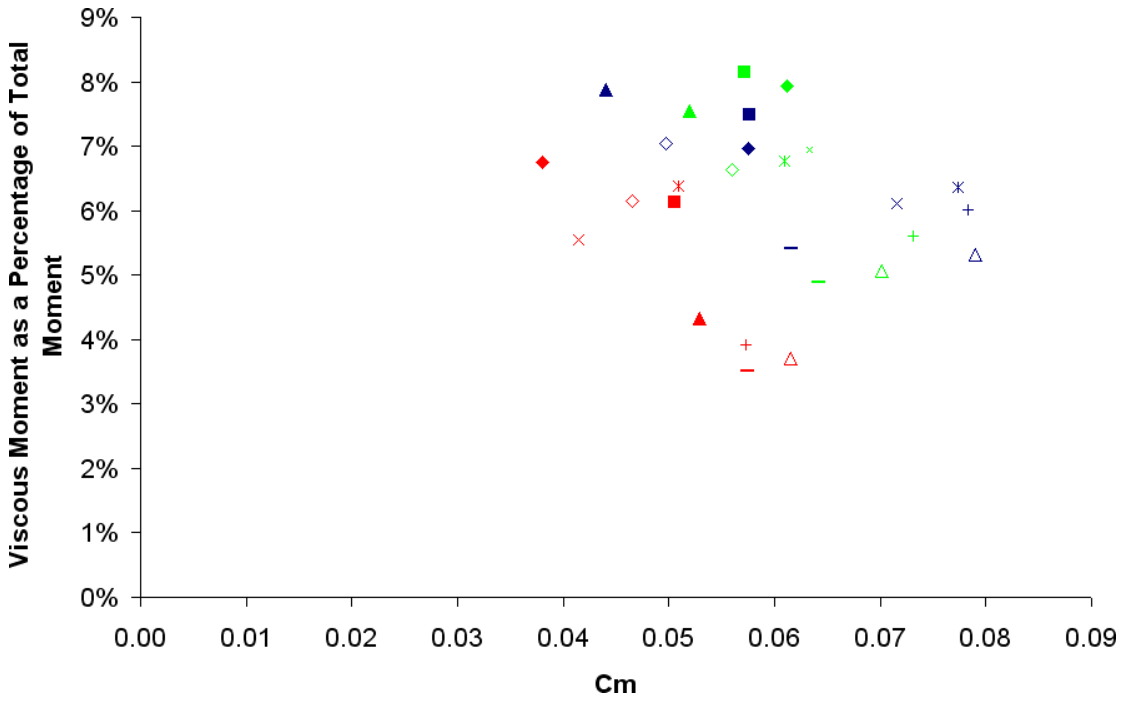

(a) Coloured by inlet

Figure B.8: Graph of Moment Coefficient against Viscous Moment on Gear Teeth as a Percentage of Total Moment, coloured by inlet.

Figure B.9 presents graphs of moment coefficient against Viscous Moment on Gear Teeth as a Percentage of Total Moment. Figure B.8(a) is coloured by the inlet clearance (1.56 mm, 3.187 mm, 4.0 mm), Fig. B.9(a) is coloured by face clearance (0.25 mm, 1.5 mm, 2.12 mm), and Fig. B.9(b) is coloured by the outlet clearance (2.52 mm, 3.013 mm, 4.0 mm). The inlet clearance is seen to have an effect on both the moment coefficient and the percentage of the moment that is due to the viscous moment on the gear teeth, with the narrowest inlets having the smaller moment coefficient *and* percentage moment. Similarly the face clearance is seen to affect the moment coefficient and the percentage, with the narrowest face clearance having higher moments and lower percentages. The outlet clearance does not show any clear effect on the percentage moment.

Figure B.10 presents graphs of moment coefficient against viscous moment on back of gear as a percentage of total moment. Figure B.10(a) is coloured by the inlet clearance (1.56 mm, 3.187 mm, 4.0 mm), Fig. B.10(b) is coloured by face clearance (0.25 mm, 1.5 mm, 2.12 mm), and Fig. B.10(c) is coloured by the outlet clearance (2.52 mm, 3.013 mm, 4.0 mm). The flow structure in the back cavity is not affected greatly by the changes in shrouding, as these graphs show, although each of the parameters can reduce the percentage moment. Medium inlet clearance (Fig. B.10(a)) is seen to have the lowest percentage moment. The outlet clearance does appear to have some effect on percentage of the moment which the viscous moment on the back of the gear represents, as can be seen in Fig. B.10(c), with the medium clearance having the lowest percentage moment. Face clearance also has some an affect on the viscous moment seen on the back curves of the gear, with the tightest clearance seeing the lowest percentage moment.

Figure B.11 presents graphs of moment coefficient against viscous moment on top of gear as a percentage of total moment. Figure B.11(a) is coloured by the inlet clearance (1.56 mm, 3.187 mm, 4.0 mm), Fig. B.11(b) is coloured by face clearance (0.25 mm, 1.5 mm, 2.12 mm), and Fig. B.11(c) is coloured by the outlet clearance (2.52 mm, 3.013 mm, 4.0 mm). This moment represents a minimal amount of the total moment (less than 1%), and there appears to be no clear influence on it due to the varying shroud geometry.

Figure B.12 presents graphs of moment coefficient against viscous moment on front

curves of gear as a percentage of total moment. Figure B.12(a) is coloured by the inlet clearance (1.56 mm, 3.187 mm, 4.0 mm), Fig. B.12(b) is coloured by face clearance (0.25 mm, 1.5 mm, 2.12 mm), and Fig. B.12(c) is coloured by the outlet clearance (2.52 mm, 3.013 mm, 4.0 mm). A clear relation between the inlet clearance and the viscous moment percentage can be seen (Fig. B.12(a)), where the narrowest inlet shows a 25% increase in the moment fraction. The other two parameters, as can be expected, show little effect on the viscous moment on the front curves of the gear.

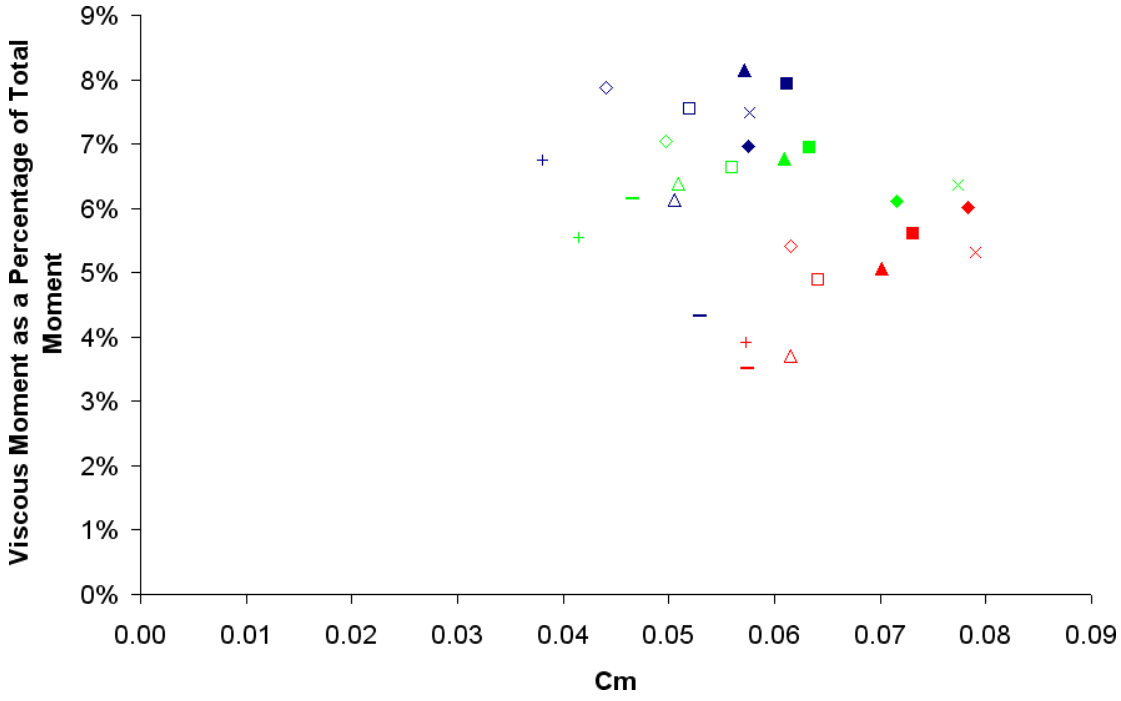

(a) Coloured by face

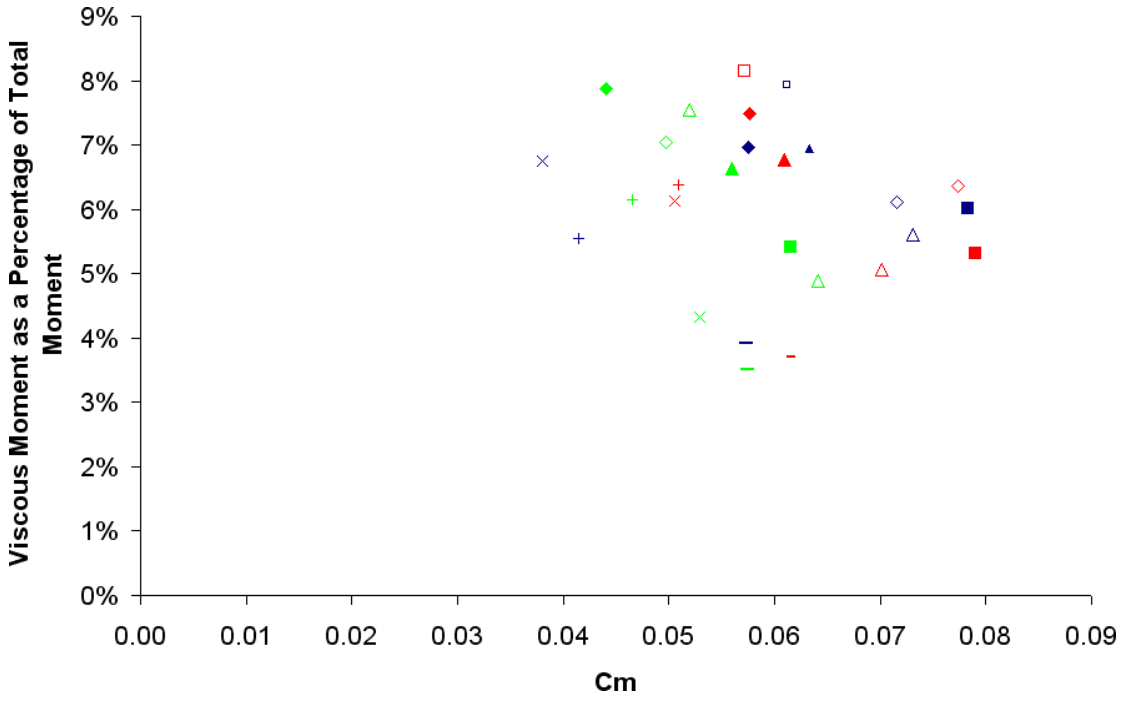

(b) Coloured by outlet

Figure B.9: Graph of Moment Coefficient against Viscous Moment on Gear Teeth as a Percentage of Total Moment.

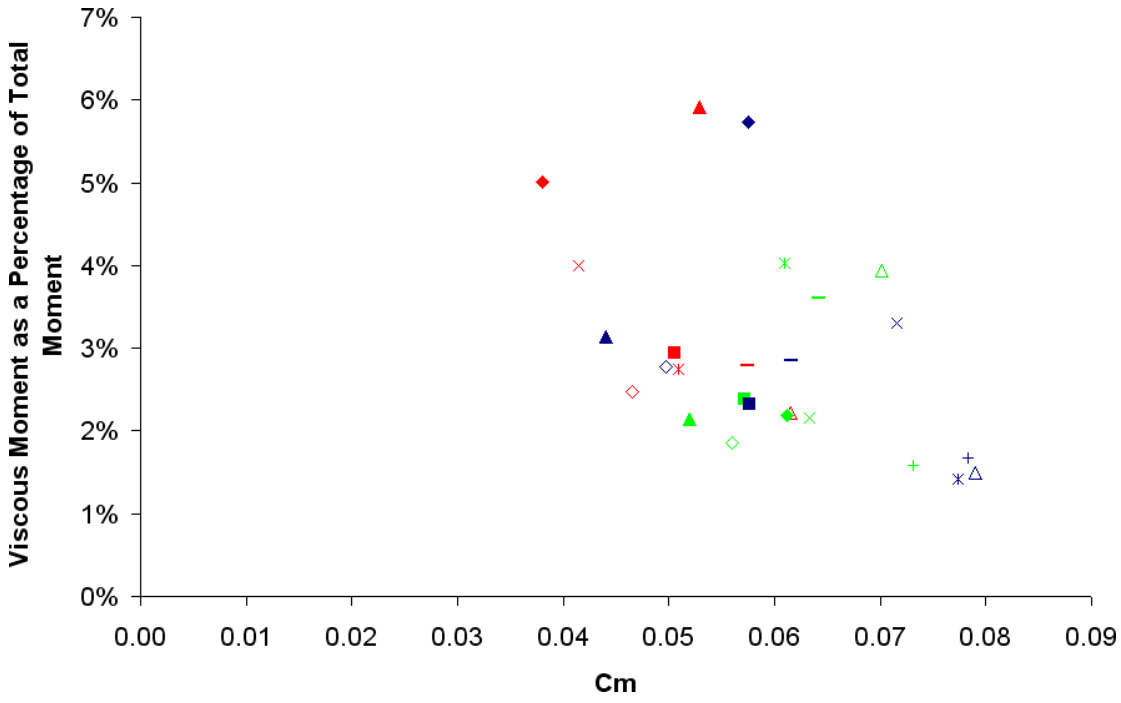

(a) Coloured by inlet

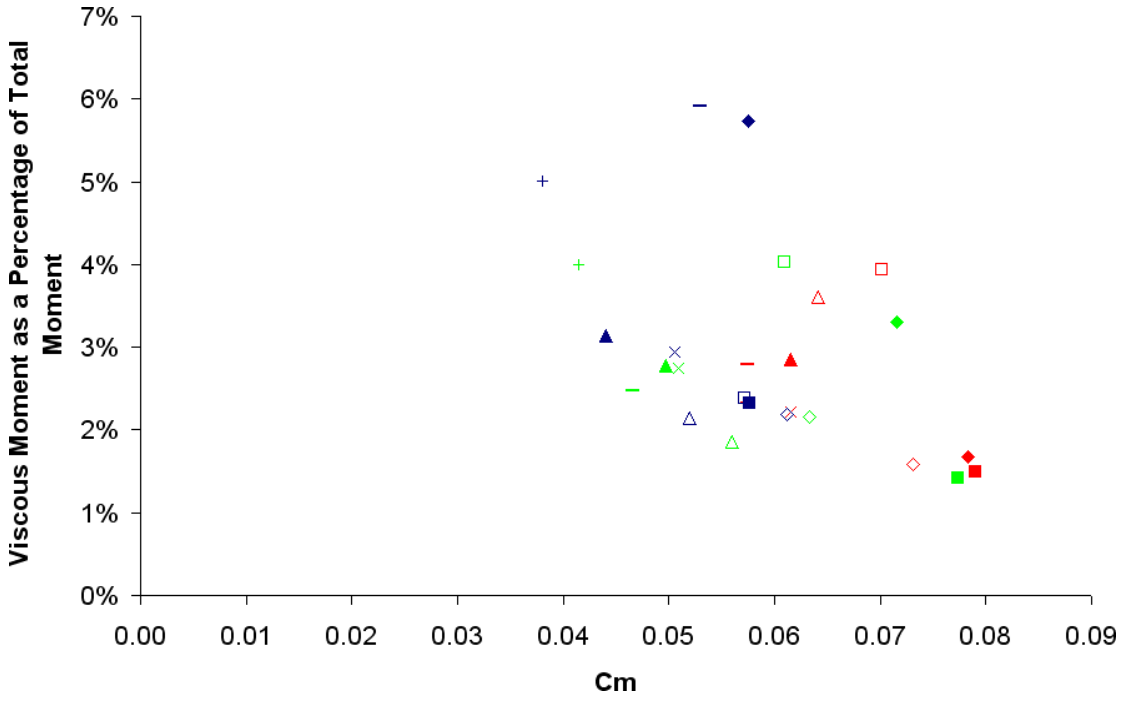

(b) Coloured by face

Figure B.10: Graph of Moment Coefficient against Viscous Moment on Back of Gear as a Percentage of Total Moment. Fig. B.10 continues.

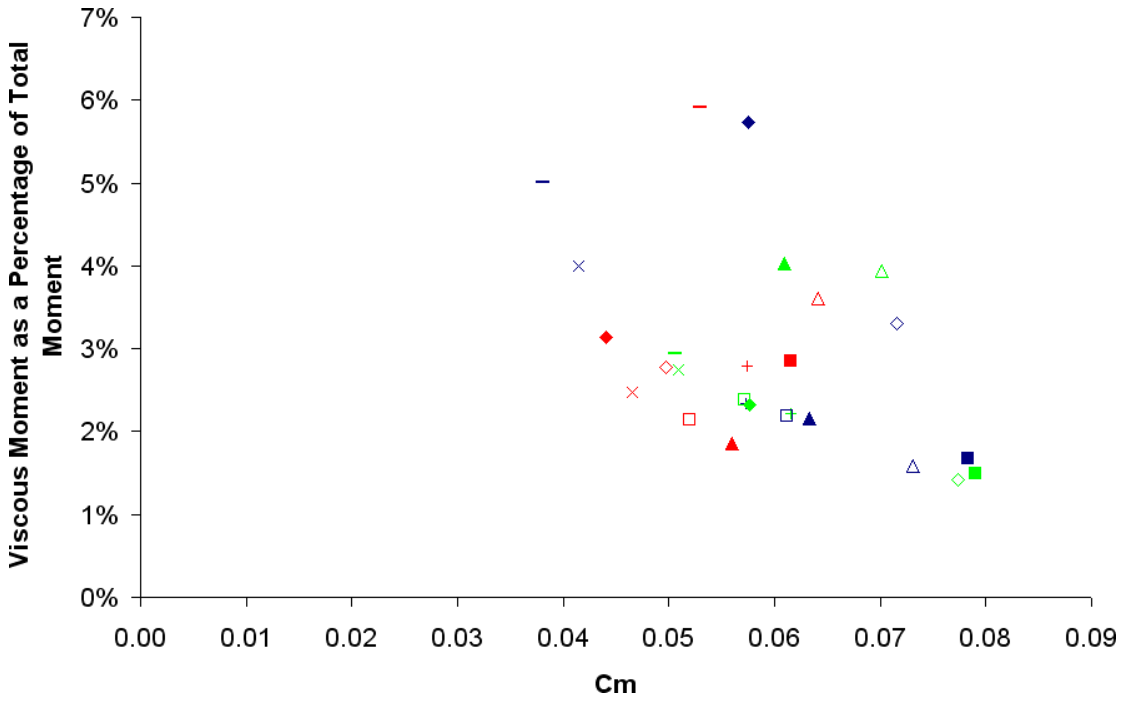

(c) Coloured by outlet

Figure B.10: Graph of Moment Coefficient against Viscous Moment on Back of Gear as a Percentage of Total Moment.

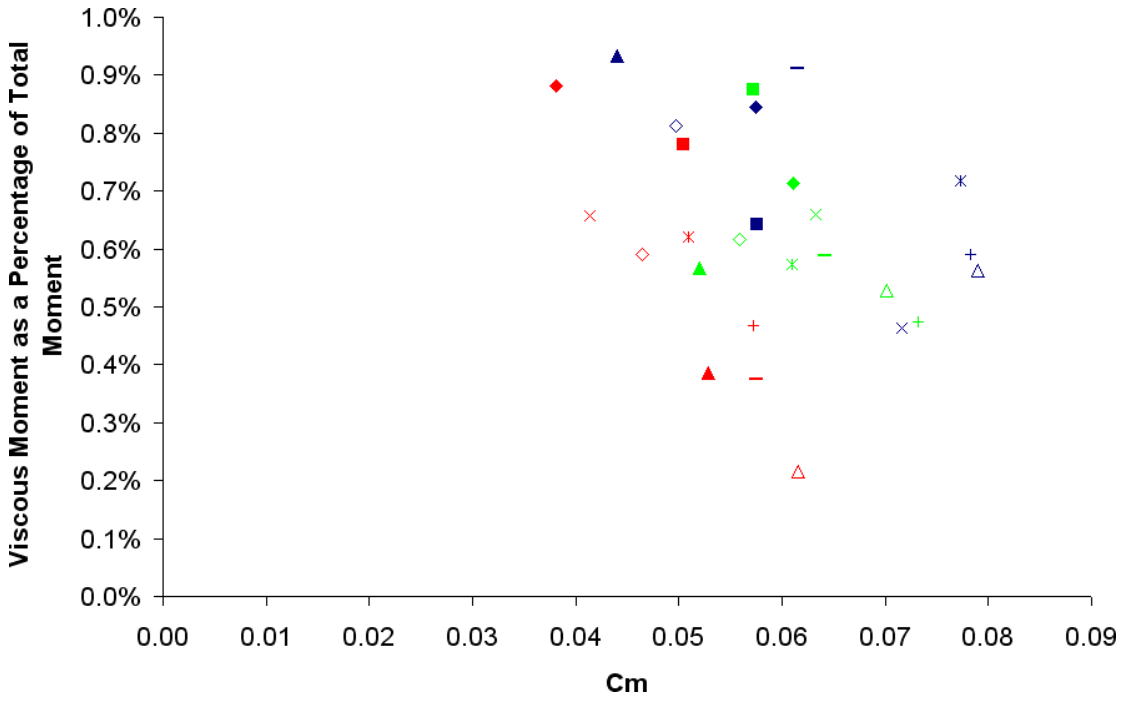

(a) Coloured by inlet

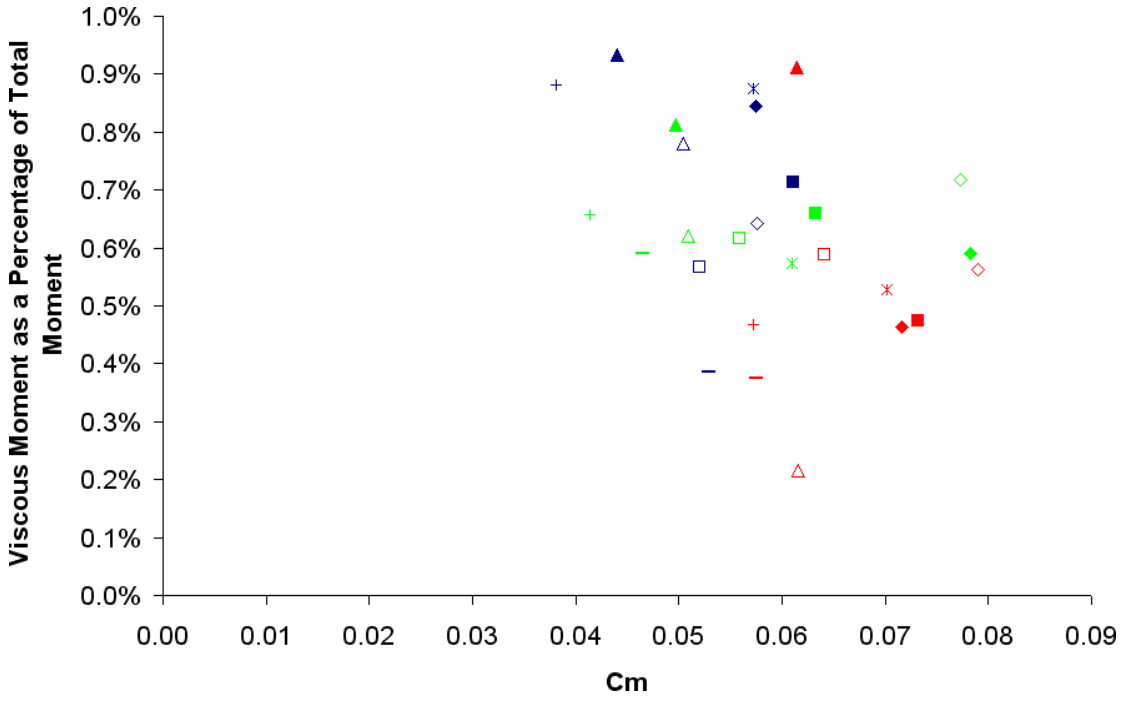

(b) Coloured by face

Figure B.11: Graph of Moment Coefficient against Viscous Moment on Top of Gear as a Percentage of Total Moment.

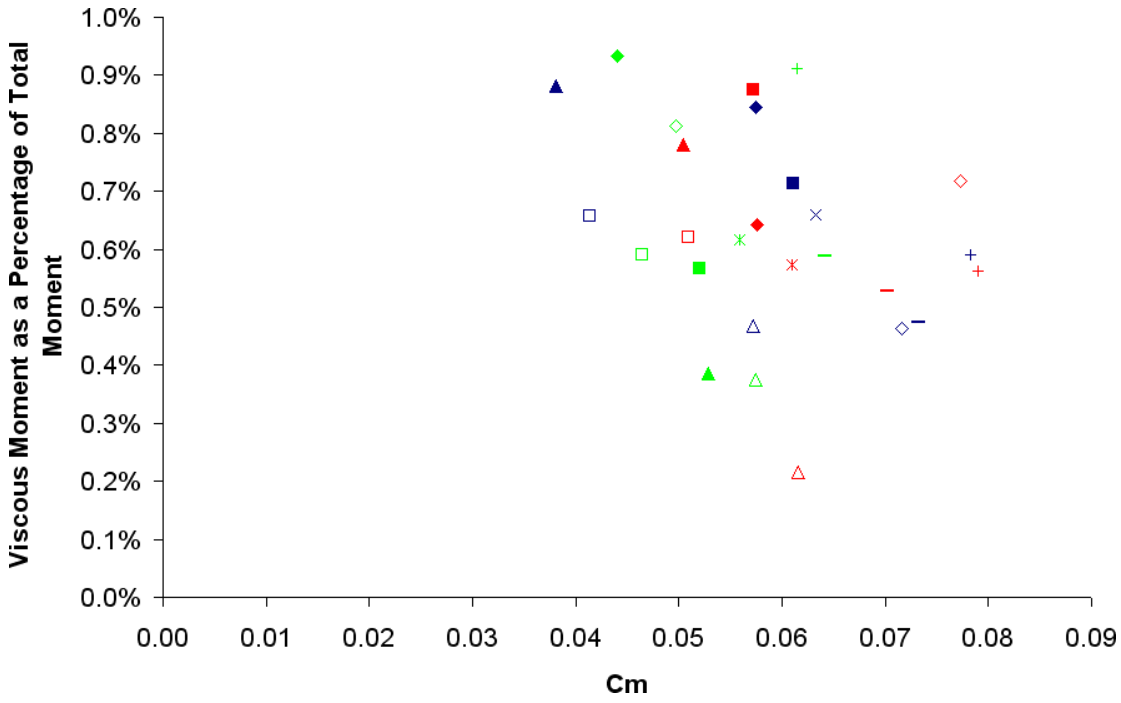

(c) Coloured by outlet

Figure B.11: Graph of Moment Coefficient against Viscous Moment on Top of Gear as a Percentage of Total Moment.

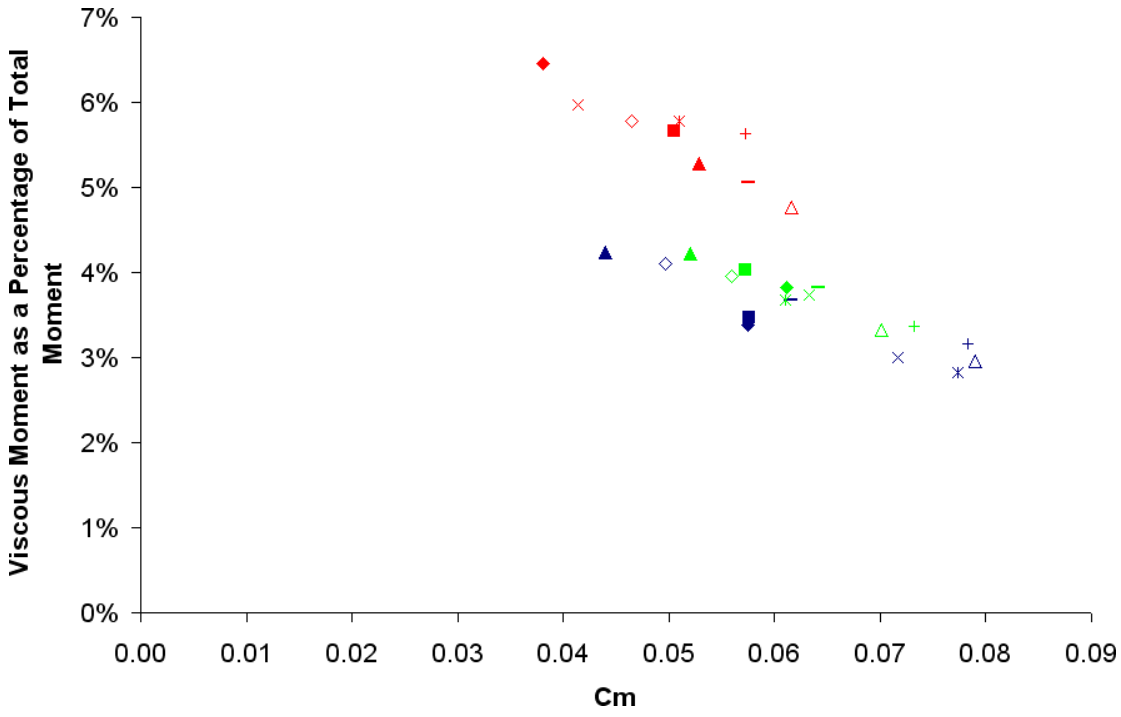

(a) Coloured by inlet

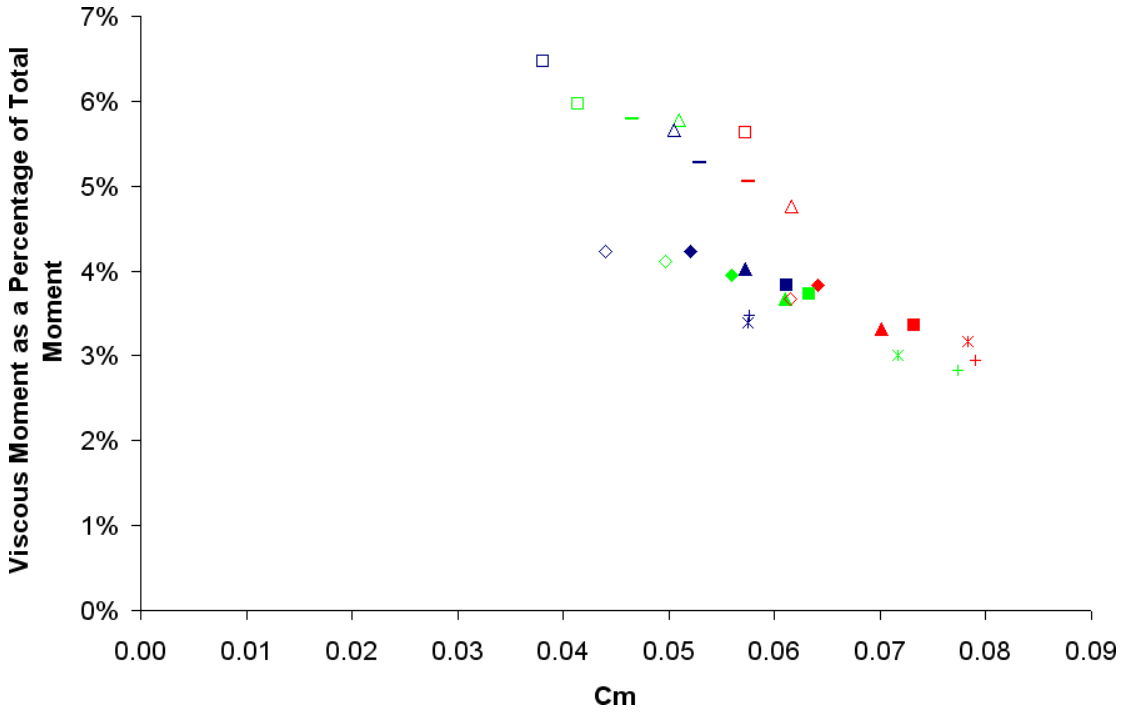

(b) Coloured by face

Figure B.12: Graph of Moment Coefficient against Viscous Moment on Front Curves of Gear as a Percentage of Total Moment. Fig. B.12 continues.

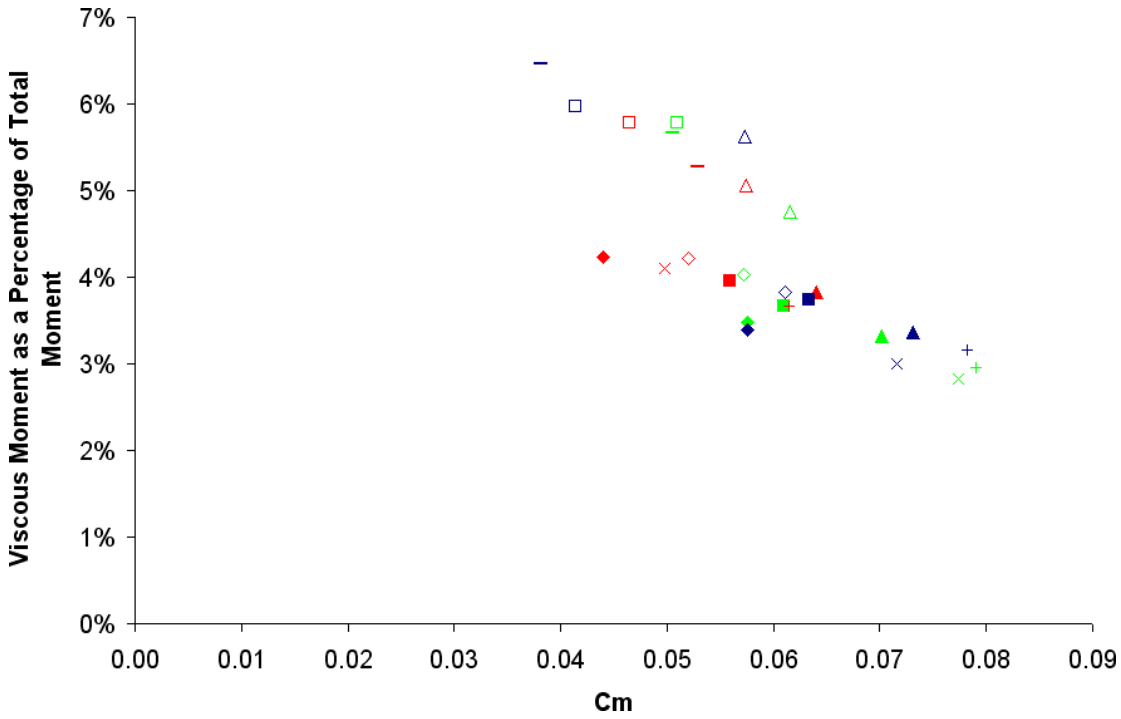

(c) Coloured by outlet

Figure B.12: Graph of Moment Coefficient against Viscous Moment on Front Curves of Gear as a Percentage of Total Moment.

Figure B.13 shows a plot of air density over the tooth surface, at line B, for the three highest torque and two lowest torque cases, at a rotational speed of $\Omega = 12,266$ RPM. The leading edge of the teeth is on the right hand side of the graph. The cases (Fig. B.13(a)) where the torque is higher show a larger variation in density compared to the cases (Fig. B.13(b)) where the torque is lower (between 5.4% and 6%, compared to between 2.3% and 3.3%), although the average density at this point is slightly lower (1.08kgm^{-3} compared to 1.084kgm^{-3}).

Figure B.14 shows a plot of air density over the tooth surface, at line C, for the three highest torque and two lowest torque cases, at a rotational speed of $\Omega = 12,266$ RPM. The leading edge of the teeth is on the right hand side of the graph. The cases (Fig. B.14(a)) where the torque is higher show a smaller variation in density compared to the cases (Fig. B.14(b)) where the torque is lower (2% compared to 3%), although the average density at this point is higher (1.083kgm^{-3} compared to 1.082kgm^{-3}).

Figure B.15 shows a plot of air density over the tooth surface, at line D, for the three highest torque and two lowest torque cases, at a rotational speed of $\Omega = 12,266$ RPM. The leading edge of the teeth is on the right hand side of the graph. The cases (Fig. B.15(a)) where the torque is higher show a smaller variation in density compared to the cases (Fig. B.15(b)) where the torque is lower (2.1% compared to 2.7%), although the average density at this point is higher (1.087kgm^{-3} compared to 1.084kgm^{-3}).

Figure B.16 shows a plot of air density over the tooth surface, at line E, for the three highest torque and two lowest torque cases, at a rotational speed of $\Omega = 12,266$ RPM. The leading edge of the teeth is on the right hand side of the graph. The cases (Fig. B.16(a)) where the torque is higher show a similar variation in density compared to the cases (Fig. B.16(b)) where the torque is lower (2.5%), although the average density at this point is lower (1.079kgm^{-3} compared to 1.086kgm^{-3}).

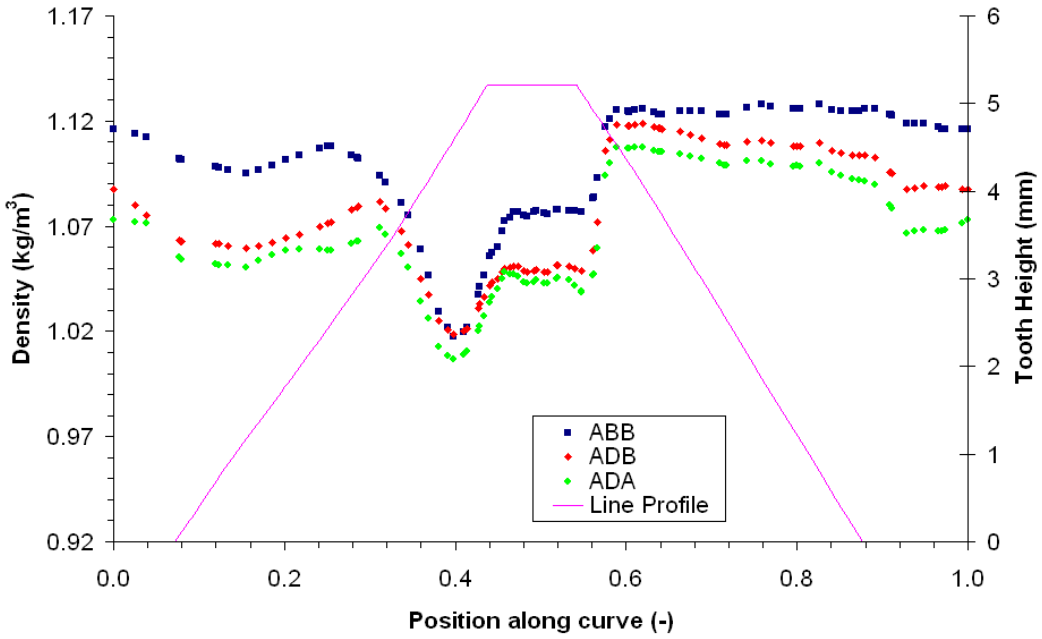

(a) High C_M

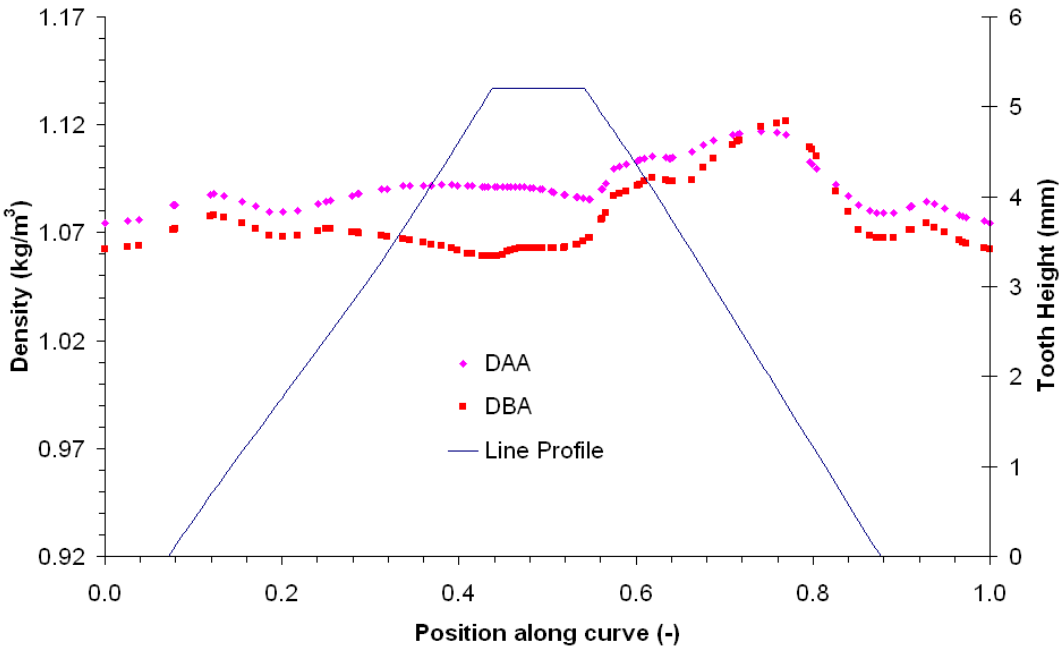

(b) Low C_M

Figure B.13: Graph of Density against Position across Teeth, Line B (as defined in Fig. 6.24)

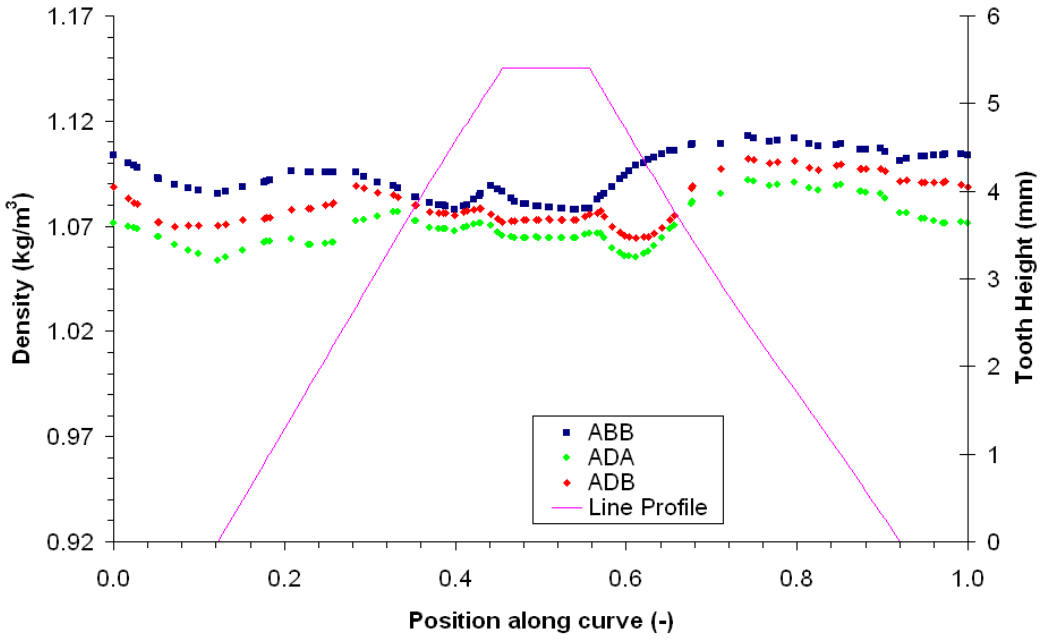

(a) High C_M

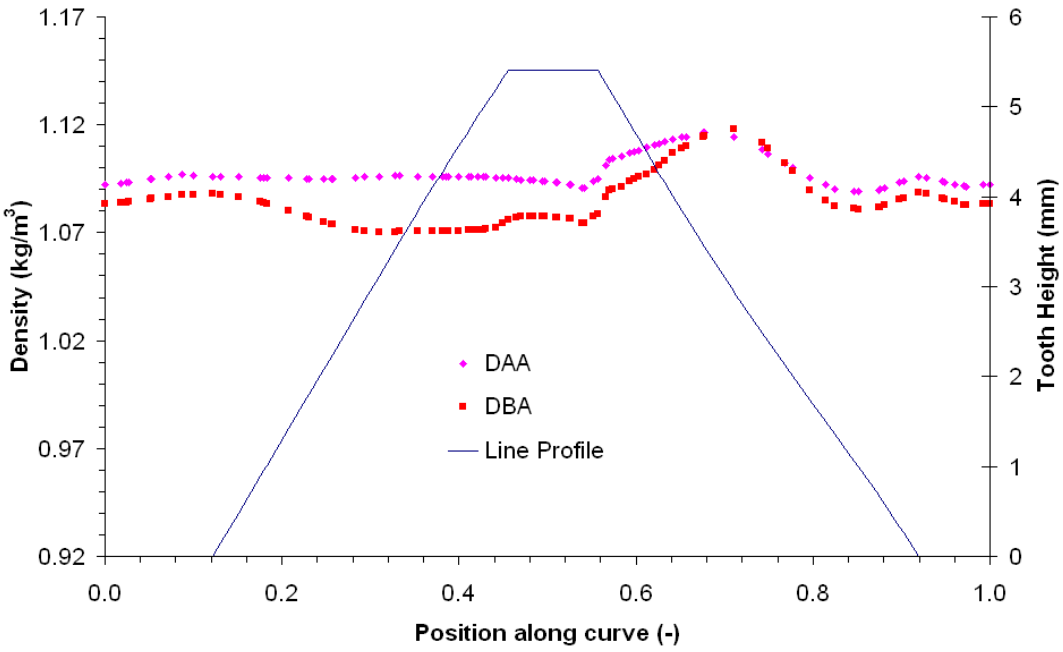

(b) Low C_M

Figure B.14: Graph of Density against Position across Teeth, Line C (as defined in Fig. 6.24)

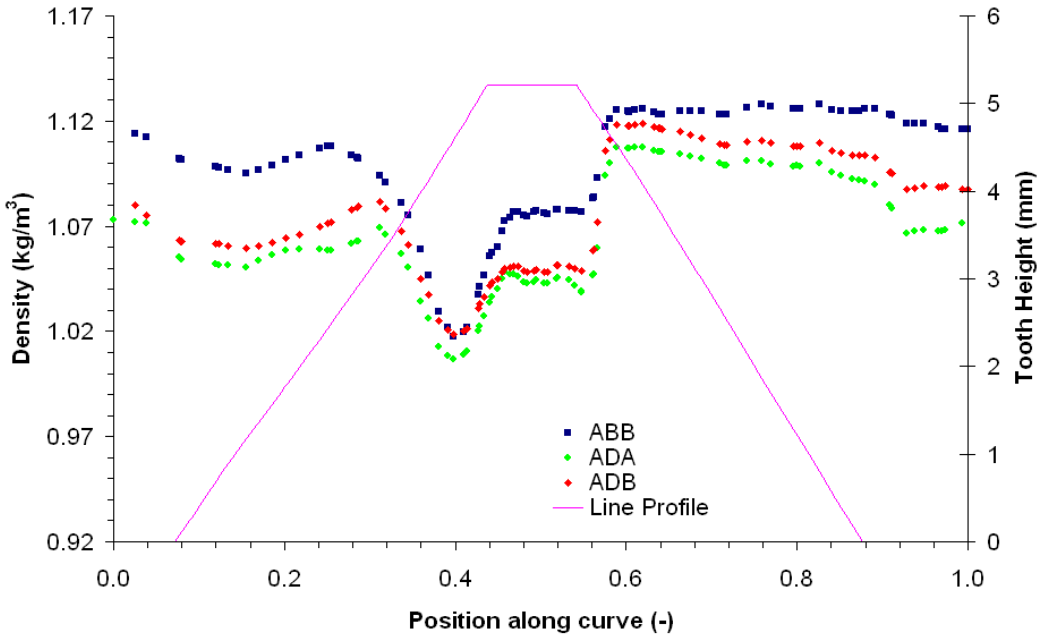

(a) High C_M

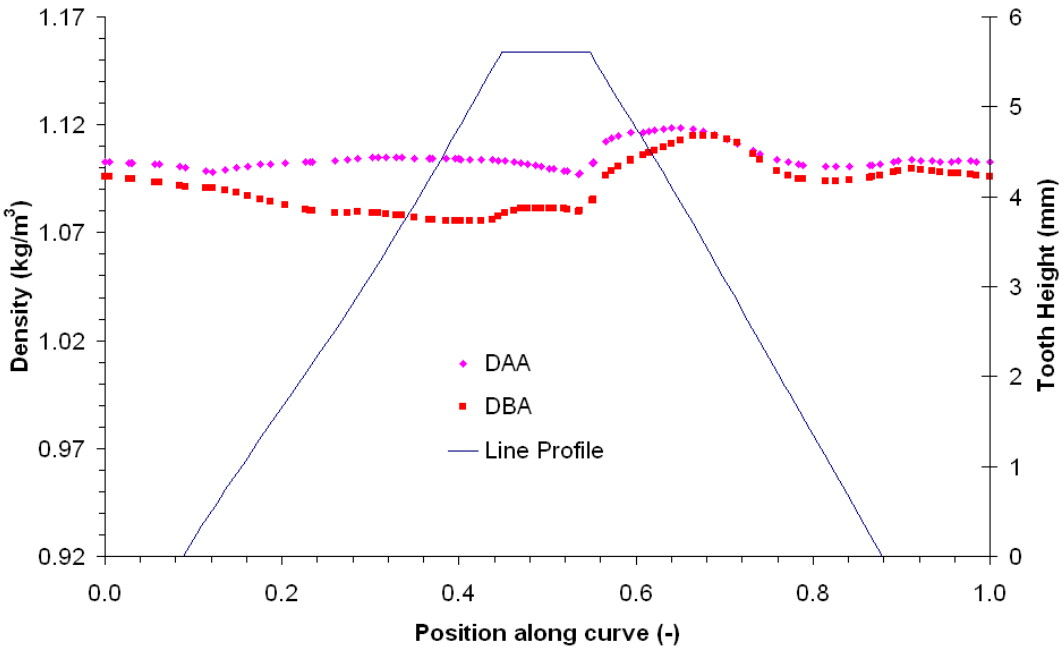

(b) Low C_M

Figure B.15: Graph of Density against Position across Teeth, Line D (as defined in Fig. 6.24)

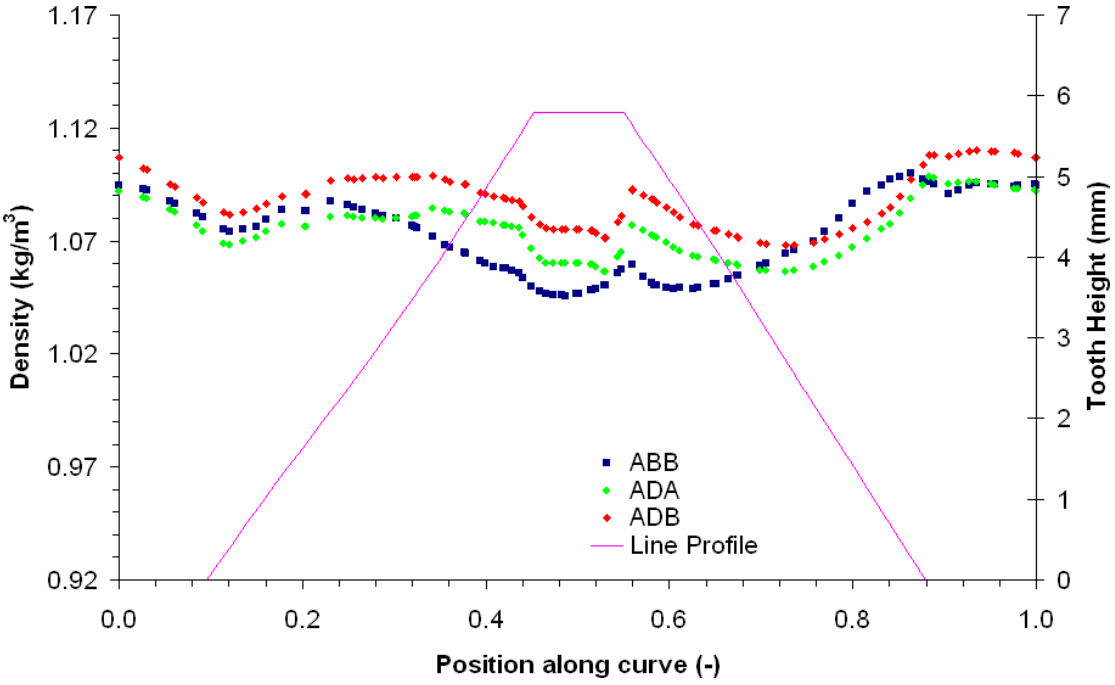

(a) High C_M

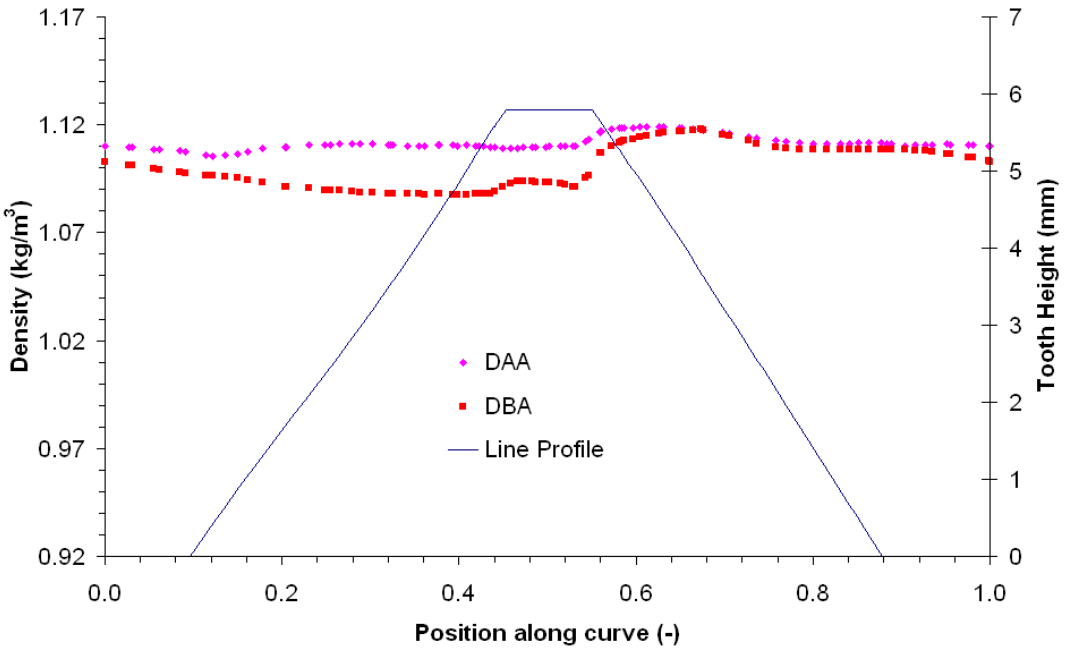

(b) Low C_M

Figure B.16: Graph of Density against Position across Teeth, Line E (as defined in Fig. 6.24)

Bibliography

[1] *FLUENT 6.2 User's Guide.* Fluent Inc, 2005.

[2] L. Akin and J. Mross. Theory for the Effect of Windage on the Lubricant Flow in the Tooth Spaces of Spur Gears. *Journal of Engineering for Industry*, 97(4):1266–1273, Nov 1975.

[3] K. Al-Shibl, K. Simmons, and C. Eastwick. Modelling Windage Power loss from an Enclosed Spur Gear. *Proceedings of the IMech E, Part A: Journal of Power and Energy*, 221:331–341, 2007.

[4] N. Anderson and S. Loewenthal. Spur-gear-system efficiency at part and full load. In *AVRADCOM Technical Report 79-46*, number 1622. NASA, 1980.

[5] N. Anderson and S. Loewenthal. Effect of geometry and operating conditions on spur gear system power loss. *Journal of Mechanical Design*, 103:151–159, January 1981.

[6] N. Anderson and S. Loewenthal. Efficiency of nonstandard and high contact ratio involute spur gears. *Journal of Mechanisms, Transmissions, and Automation in Design*, 108:119–126, March 1986.

[7] Y. Ariura, T. Ueno, T. Sunaga, and S. Sunamoto. The lubricant churning loss in spur gear systems. *Bulletin of the JSME*, 16(95):881–892, May 1973.

[8] E. Bilgen and R. Boulos. Functional dependence of torque coefficient of coaxial cylinders on gap width and reynolds number. *Journal of Fluids Engineering*, 95:122–126, March 1973.

[9] F. Bleier. *Fan Handbook*. McGraw-Hill, 1997.

[10] R. Boness. Churning Losses of Discs and Gears Running Partially Submerged in Oil. In *Proceedings of the 1989 Power Transmissions and Gearing Conference, Chicago, USA, ASME*, pages 355–365. ASME, 1989.

[11] J. Daily and R. Nece. Chamber Dimensional Effects on Induced Flow and Frictional Resistance of Enclosed Rotating Disks. *Journal of Basic Engineering*, March 1960.

[12] P. Dawson. Windage Loss in Large High-Speed Gears. *Proc. of the Inst. Mech. Engineers*, 198:51–59, 1984.

[13] P. Dawson. High Speed Gear Windage. *GEC Review*, 4, 1988.

[14] Y. Diab, F. Ville, C. Changenet, and P. Velex. Windage Losses in High Speed Gears - Preliminary Experimental and Theoretical Results. volume 4, pages 941–947. ASME 2003 Design Engineering Technical Conferences and Computers and Information in Engineering Conference, 2003.

[15] Y. Diab, F. Ville, C. Changenet, and P. Velex. Windage Losses in High Speed Gears - Preliminary Experimental and Theoretical Results. *Journal of Mechanical Design*, 126:903–908, September 2004.

[16] Y. Diab, F. Ville, C. Changenet, and P. Velex. Simulations and Experimental Investigation on Windage Losses in High-Speed Gears. *VDI Berichte*, 1904:1435–1450, 2005.

[17] B. Dubrulle and F. Hersant. Momentum transport and torque scaling in taylor-couette flow from an analogy with turbulent convection. *The European Physical Journal B*, 26:379–386, 2002.

[18] C. Eastwick and G. Johnson. Gear Windage - A Review (Technology Review). *Journal of Mechanical Design*, April 2008.

[19] B. Eckhardt, S. Grossmann, and D. Lohse. Scaling of global momentum transport in Taylor-Couette and pipe flow. *European Physical Journal B*, 18:541–544, 2000.

[20] M. Farrall, K. Simmons, and C. Hibberd, S. Young. Computational Investigation of the Airflow Through A Shrouded Bevel Gear. Reno-Tahoe, Nevada, USA, 2005. ASME Turbo Expo 2005, ASME.

[21] M. M. Gibson and B. Launder. Ground Effects on Pressure Fluctuations in the Atmospheric Boundary Layer. *Journal of Fluid Mechanics*, 86:491–511, 1978.

[22] P. Heingartner and D. Mba. Determining Power Losses in The Helical Gear Mesh; Case Study. pages 965–970, Chicago, Illinois, USA, September 2003. ASME DETC 2003.

[23] N. P. Hoffman and F. H. Busse. Instabilities of Shear Flows between Two Coaxial Differentially Rotating Cones. *Physics of Fluids*, 11:1676–1678, 1999.

[24] G. Johnson, B. Chandra, C. Foord, and K. Simmons. Windage Power Losses from Spiral Bevel Gears with Varying Oil Flows and Shroud Configurations. Berlin, Germany, 2008. ASME Turbo Expo 2008, ASME.

[25] G. Johnson, K. Simmons, and C. Young. Experimental Investigation into Windage Power Loss from a Shrouded Spiral Bevel Gear. May 2007.

[26] B. Kader. Temperature and Concentration Profiles in Fully Turbulent Boundary Layers. *International Journal of Heat and Mass Transfer (Elsevier)*, 24:1541–1544, 1981.

[27] R. Kobayashi, Y. Kohama, and M. Kurosawa. Boundary-layer transition on a rotating cone in axial flow. *Journal of Fluid Mechanics*, 127:341–352, 1983.

[28] D. P. Lathrop, J Fineberg, and H. L. Swinney. Turbulent flow between concentric rotating cylinders at large reynolds number. *Physical Review Letters*, 68(10):1515–1518, 1992.

[29] B. Launder. Second-Moment Closure: Present... and Future? *International Journal of Heat and Fluid Flow*, 10:282–300, 1989.

[30] B. Launder, G. Reece, and W. Rodi. Progress in the Development of a Reynolds-Stress Turbulence Closure. *Journal of Fluid Mechanics*, 68:537–566, 1975.

[31] B. Launder and D. Spalding. *Lectures in Mathematical Models of Turbulence*. Academic Press, 1972.

[32] B. Launder and D. Spalding. The Numerical Computation of Turbulent Flows. *Computer Methods in Applied Mechanics and Engineering (Elsevier)*, 3:269–289, 1974.

[33] A. Lord. *An Experimental Investigation of Geometric and Oil Flow Effects on Gear Windage and Meshing Losses*. PhD thesis, University of Wales, Swansea, UK, 1998.

[34] N. E. May, J. W. Chew, and P. W. James. Calculation of Turbulent Flow for an Enclosed Rotating Cone. *Journal of Turbomachinery (ASME)*, 116:548–554, July 1994.

[35] F. Menter. Improved Two-Equation $k - \omega$ Turbulence Models for Aerodynamic Flows. *NASA Technical Memorandum 103975*, 1992.

[36] F. Menter, M. Kuntz, and R. Langtry. *Heat and Mass Transfer 4*. Begell House Inc., 2003.

[37] C. Milian, J. Distretti, P. Leoni, and P. Velex. A Model of the Pumping Action Between the Teeth of High-Speed Spur and Helical Gears. *VDI Berichte*, 1665:627–637, 2002.

[38] C. Milian, J. Distretti, P. Leoni, and P. Velex. A Model of the Pumping Action Between the Teeth of High-Speed Spur and Helical Gears. *Gear Technology*, pages 50–54, May 2004.

[39] J. Moureh, D. Flick, and P. L. Larrieu. Etude hydrodynamique et thermique d'un échangeur de chaleur à noyau tournant conique. *Revue Générale de Thermique*, 35(414):402–407, 1996.

[40] M. N. Noui-Mehidi. Effect of acceleration on transition properties in a conical cylinder system. *Experimental Thermal and Fluid Science (Elsevier)*, 29:447–456, 2005.

[41] M. N. Noui-Mehidi, N. Ohmura, and K. Kataoka. Gap Effect on Taylor Vortex Size Between Rotating Conical Cylinders. *15th Australasian Fluid Mechanics Conference, The University of Sydney, Sydney, Australia*, December 2002.

[42] M. N. Noui-Mehidi, N. Ohmura, and K. Kataoka. Mechanism of Mode Selection for Taylor Vortex Flow between Coaxial Conical Rotating Cylinders. *Journal of Fluids and Structures*, 16:247–262, 2002.

[43] M. N. Noui-Mehidi, N. Ohmura, and K. Kataoka. Numerical Computation of Apex Angle Effects on Taylor Vortices in Rotating Conical Cylinder Systems. *Journal of Chemical Engineering of Japan*, 35:22–31, 2002.

[44] M. N. Noui-Mehidi, N. Ohmura, and K. Kataoka. Dynamics of the helical flow between rotating conical cylinders. *Journal of Fluids and Structures*, 20:331–344, 2005.

[45] M. N. Noui-Mehidi, A. Salem, P. Legentilhomme, and J. Legrand. Apex Angle Effects on the swirling flow between cones induced by means of a tangential inlet. *International Journal of Heat and Fluid Flow (Elsevier)*, 20:405–413, 1999.

[46] J. C. F. Pereira and J. M. M. Sousa. Confined vortex breakdown generated by a rotating cone. *Journal of Fluid Mechanics*, 385:287–323, 1999.

[47] S. Rapley, C. Eastwick, and K. Simmons. Effect of variations in shroud geometry on single phase flow over a shrouded single spiral gear. Berlin, Germany, 2008. ASME Turbo Expo 2008.

[48] S. Rapley, K. Simmons, and C. Eastwick. The Application Of CFD To Model Windage Power Loss From A Spiral Bevel Gear. Montréal, Canada, May 2007. ASME Turbo Expo 2007.

[49] S. Rapley, K. Simmons, and C. Eastwick. Computational Investigation of Torque in Coaxial Rotating Cones. *Journal of Fluids Engineering*, 2008.

[50] H Schlichting. *Boundary Layer Theory*. McGraw-Hill, 1979.

[51] T-H. Shih, W. Liou, A. Shabbir, Z. Yang, and J. Zhu. A New $k-\epsilon$ Eddy-Viscosity Model for High Reynolds Number Turbulent Flows. *Computers Fluids*, 24(3):227–238, 1995.

[52] Y. Shiomi, S. Nakanishi, and H. Kutsuna. CFD Calculation for Two-Phase Flow in Concentric Annulus with Rotating Inner Cylinder. Luxembourg, May 2000. PHOENICS Users Conference Proceedings, Phoenics.

[53] Strasser. CFD Investigation of Gear Pump Mixing Using Deforming/Agglomerating Mesh. *Journal of Fluids Engineering*, 129:476–484, Apr 2007.

[54] J. Stuart. On the non-linear mechanics of hydrodynamic stability. *Journal of Fluid Mechanics*, 4(1):1–21, May 1958.

[55] G. Taylor. Fluid friction between rotating cylinders I. - torque measurements. *Proceedings of the Royal Society (London)*, 157:546–564, Dec 1936.

[56] J. Tevaarwerk. Traction Calculations and Design Data for Two Traction Fluids. *Advanced Power Transmission Technology*, pages 285–298, June 1981.

[57] D. Townsend and L. Akin. Gear lubrication and cooling experiment and analysis. *Advanced Power Transmission Technology*, pages 477–490, June 1981.

[58] D. Townsend and L. Akin. Study of lubricant jet flow phenomena in spur gears-Out of mesh condition. *Advanced Power Transmission Technology*, pages 461–476, June 1981.

[59] S. T. Wereley and R. T. Lueptow. Velocity field for Taylor-Couette flow with an axial flow. *Physics of Fluids*, 11:3637–3649, December 1999.

[60] F. White. *Fluid Mechanics*. McGraw Hill, 5^{th} edition, 2003.

[61] D. Wilcox. Turbulence Modeling for CFD. *DCW Industries, Inc., La Canada, California.*, 1998.

[62] P. M. Wild, N. Djilali, and G.W. Vickers. Experimental and computational assessment of windage lossed in rotating machinery. *Journal of Fluids Engineering (ASME)*, 118:116–122, 1996.

[63] K. Wilson. Renormalization Group and Critical Phenomena. I Renormalization Group and the Kandoff Scaling Picture. *Physical Review B*, 4:3174–3183, 1971.

[64] K. Wilson. Renormalization Group and Critical Phenomena. II Phase-Space Cell Analysis of Critical Behaviour. *Physical Review B*, 4:3184–3205, 1971.

[65] M. Wimmer. An experimental investigation of Taylor vortex flow between conical cylinders. *Journal of Fluid Mechanics*, 292:205–227, 1995.

[66] M. Wimmer. Taylor vortices at different geometries. *Lecture Notes in Physics (Springer-Verlag)*, 549:194–212, 2000.

[67] M. Wimmer and J. Zierep. Transition from Taylor vortices to cross-flow instabilities. *Acta Mechanica*, 140:17–30, 2000.

[68] D. Winfree. Reducing Gear Windage Losses from High Speed Gears. Baltimore, Maryland, USA, September 2000. ASME Power Transmission and Gearing Conference, ASME.

[69] Y. Yamada and M. Ito. On the Frictional Resistance of Enclosed Rotating Cones (1st Report, Frictional Moment and Observation of Flow with a Smooth Surface). *Bulletin of the JSME*, 18:1026–1034, September 1975.

[70] Y. Yamada and M. Ito. On the Frictional Resistance of Enclosed Rotating Cones (2nd Report, Effects of Surface Roughness). *Bulletin of the JSME*, 19:943–950, August 1976.

[71] Y. Yamada and M. Ito. Frictional Resistance of Enclosed Rotating Cones With Superposed Throughflow. *Journal of Fluids Engineering*, 101:259–264, 1979.